The Dissertation Committee for Sean Matthew Lewis
certifies that this is the approved version of the following dissertation:

Characterizing Laser-Heated Plasma Energy Density Distributions for Magnetized Liner Inertial Fusion

Committee:

Todd Ditmire, Supervisor

J. Craig Wheeler

John Keto

Boris Breizman

Roger D. Bengtson

Characterizing Laser-Heated Plasma Energy Density Distributions for Magnetized Liner Inertial Fusion

by

Sean Matthew Lewis,

DISSERTATION

Presented to the Faculty of the Graduate School of

The University of Texas at Austin

in Partial Fulfillment

of the Requirements

for the Degree of

DOCTOR OF PHILOSOPHY

THE UNIVERSITY OF TEXAS AT AUSTIN

August 2018

Acknowledgments

I would like to thank the folks that have supported my efforts to create this thesis. First to my peers, most notably Matthew Wisher and Nathan Riley. Matt spent several years working with the magnetic field device used for some of these experiments, and Nathan helped develop the gas cells. Nathan was helpful for me to understand some physics for this work. Next, my supportive coworkers in the Z-Beamlet laser group at Sandia, including Matthias, Mark, Patrick, Marius, Ella, Jens, Ian, Jon, and Shane. In particular, Mark and Shane have both been responsible for large aspects of the hardware required for these experiments. Everything I have done has been a collaborative effort and I had the benefit of some world class facilities with top-notch people running them. Most of the data I worked with toward the end of the project required no work on my part, I only analyzed the data.

John Porter has been a strong proponent for my work and an inspirational leader. He supported my time at Sandia and was the visionary force behind much of the new experimental capabilities that enabled this work.

At UT, Thanks to Boris for answering some of my dumb questions. Roger and Todd supported me and provided the infrastructure and funding I needed to move forward. I'd like to thank Roger most of all, for taking personal time to advise me as an emeritus professor. His patience and generosity are

an inspiration for me. His dedication to his students is a model for mentorship that I will aspire to follow for those that come after me.

Characterizing Laser-Heated Plasma Energy Density Distributions for Magnetized Liner Inertial Fusion

Publication No. _____

Sean Matthew Lewis, Ph.D.
The University of Texas at Austin, 2018

Supervisor: Todd Ditmire

Magnetized Linear Inertial Fusion (MagLIF) is an inertial confinement fusion (ICF) concept being pursued at Sandia National Laboratories [1]. It uses fusion fuel preheating via a laser. A subsequent cylindrical liner implosion and magnetic flux compression brings this fuel to fusion conditions. Experiments on the Z-facility at Sandia have produced compelling neutron yields in the range of 10^{12} $n/shot$ [2]. Maximal and axially uniform energy density in the preheat plasma is important for MagLIF yield [1] [3]. We developed a preheat test platform at the Z-beamlet laser facility that includes surrogate helium gas cell targets. We fielded 2D multi-frame imaging diagnostics including shadowgraphy and x-ray pinhole cameras (PHC). Sound speed and blast wave plasma expansion provide methods for temperature and energy per unit length measurements, giving distributions across the axial length of the plasma. We used these measurements to compare energy density beyond a benchmark of 4 mm across a range of laser parameters, enabling comparisons between preheat

configurations. Initial preheat configurations with a 2 ns early prepulse and a 3 ns long heating pulse produced very low energy densities of less than 200 J beyond 4 mm axially. We observed approximately a factor of 4 improvement in coupled energy beyond 4 mm from implementation of a 20 ns early prepulse. Combining a magnetic field, early prepulse, and 5 ns main heating pulse produced an approximate factor of five improvement in coupled energy beyond 4 mm. Without a magnetic field, the energy per unit length descends steeply with axial length. With a 17 T axially-oriented magnetic field, the axial energy density and temperature distribution becomes more uniform up to 6-8 mm, and total coupled energy beyond 4 mm increases by a factor in the range of 1.5-2. Transverse x-ray PHC images on magnetic field shots indicate that the laser heated region is narrower than the laser width. This is evidence for cross-field electron thermal conduction suppression and self-focusing. A Gaussian radial temperature distribution solves the diffusion equation with a diffusion coefficient that is a constant function of temperature, which is approximately the case for electron conduction above a certain temperature across magnetic field lines. This approximate temperature distribution produces a qualitatively similar x-ray profile to data if peak temperatures exceed 1.5 keV during heating. To our knowledge, we have the first indirect measurements of temperatures and energy densities in surrogate preheat plasmas, both with and without a magnetic field. The energy density and temperature distributions we have measured will provide a valuable comparison to simulations and inform both the design simulators of MagLIF and the experimental planners.

Table of Contents

List of Figures

Chapter 1

Introduction to Magnetized Liner Inertial Fusion and Motivation for this Work

1.1 Introduction and Forward Outline for this Dissertation

Controlled fusion remains a daunting laboratory challenge. Magnetized Liner Inertial Fusion (MagLIF) presents a promising approach for inertial confinement fusion, with a hot plasma initially heated by a laser that is compressed and confined with a magnetic field. Initial results are promising, but simulations indicate that they can be improved significantly by increasing the delivered energy in the laser-initiated preheat plasma. This dissertation work will cover methods and results from measurements of preheat plasma energy, temperature, and spatial extent that will be informative to further develop MagLIF.

In this chapter, we introduced some of the concepts that will be expounded on in later chapters related to MagLIF and laser heating. We will motivate the connection between preheat concepts and their importance to fusion via MagLIF.

Extensive experimental capability development was required to make

the measurements we present here. The experimental setup and diagnostics are explained in chapters two and three as well as Appendix A. Chapter three describes the physics needed to understand the shadowgraphy diagnostic we used, while Appendix A outlines the physics of x-ray emission imaging.

To fully understand preheat, we will need an arsenal of physics terminology in higher energy density ranges of plasma transport based on plasma physics ordinarily carried out at lower densities for magnetic confinement fusion experiments. The laser heats the plasma via the collisional absorption process. Since collisional absorption is a strong decreasing function of temperature, laser absorption is affected by heat conduction and hydrodynamic motion. The laser can be focused or diverged and the plasma's heated radius is greatly impacted by radial energy transport. Chapter four will describe thermal conductivity in some detail, and outline the major forms of radial heat transport we expect. We will solve the diffusion equation in cylindrical geometry and provide solutions for electron and radiative diffusive conduction as well as conductivity in the presence of a magnetic field.

One of these areas which will be explored later is the hydrodynamic transport of the heated plasma column following preheat. We will use our understanding of transport to infer the preheated energy deposition. We will extract an energy per unit length across the axial length of the plasma compare axial energy distributions. These methods will be described in chapters five and six. We will use energy distributions to see how various laser parameters change the overall energy deposited in the gas. We will see that improvements

in deposited energy arise from extending the duration of the main heating pulse length, adding an earlier prepulse to help remove the gas-containing vessel window, and adding a magnetic field. These topics will be the focus of chapter seven.

Another topic for this dissertation is the influence of the seed magnetic field on the preheat plasma. We expect to find a narrower and longer laser-heated plasma with a magnetic field present. This is a result of radial thermal conduction reduction, which increases the central peak temperature, thus augmenting axial conduction and reducing plasma expansion via thermal waves. Since the length of the plasma is important, namely that it should be about the same length as the 1 cm liner, our measurements provide some measurements for the length of energy deposition over which heating is uniform. We will attempt to answer some of these questions in chapter eight.

Finally, we will wrap things up and summarize the results in chapter nine.

1.2 Motivation in the context of MagLIF

This chapter covers an inertial confinement fusion (ICF) approach called Magnetized Liner Inertial Fusion (MagLIF) [1]. MagLIF combines three main steps: magnetization, laser preheating, and electromagnetic implosion within a liner. I will very briefly mention aspects of fusion research including ICF, then expound on the physics of MagLIF. Our experiments presented in this dissertation attempt better measurements of laser heated plasmas in configurations

similar to MagLIF, although there are important differences. In particular, the laser preheating phase is the most relevant to this dissertation. We will discuss the physics of MagLIF preheat and why it is so important to MagLIF. There are strong motivation for further experimental study of preheat energy and energy density distributions within the plasma. In many cases we were able to make statements about experimental parameters that can be optimized to improve energy deposition. Exploring aspects of MagLIF preheat will be the focus of this dissertation.

1.3 Controlled Laboratory Fusion

Controlled laboratory-scale fusion energy and research has been an elusive goal for decades. Fusion is energetic, releasing as much as 3 MeV per nucleon due to the difference in nuclear binding energy. It is also a significant source of potentially useful neutrons. Popular descriptions of fusion have touted it as a clean energy source, with little radioactive waste and abundant natural fuel supply in the form of natural deuterium and lithium. The reality is in the practicality- controlled fusion remains elusive after 70 years of research and will likely continue to do so for a long time.

Unlike fission, fusion requires a high temperature plasma state. Basically, hydrogen isotope plasmas needs to kept at a high enough density in a large enough volume and time and at temperatures of about 100 million degrees kelvin for reactions to occur. The very hot and either very large or very dense plasmas required are tremendous technical challenges to create and

maintain. Because fusion reactions produce heat, it is conceivable to initiate a fusion plasma that has achieved "ignition", in which the reaction heat drives further reactions. Thermonuclear burn will be achieved when reactions self-heat the plasma and maintain the high temperature required for further reactions. This is the ultimate goal of most fusion research.

Fusion research split early in the 1960s into the magnetic confinement (MCF) and inertial confinement (ICF) approaches. Magnetic confinement fusion uses large magnetic fields to confine charged plasma particles along magnetic field lines. It aims for a burning plasma with large volumes with a reactant density of about $10^{14}\ cm^{-3}$. For burning plasmas these conditions must be maintained at plasma kinetic temperatures of 10's of keV for many seconds or ideally in continuous operation. Magnetic confinement of plasmas has been a tremendous challenge. The main motivation is that properly magnetically confined plasma could achieve ignition of a burning plasma that self-heats indefinitely. ICF instead seeks to achieve fuel burn in a short, rapid burst. ICF is fundamentally a transient process; it must achieve net fusion energy output before the fuel has had time to thermally disassemble. In the absence of a containment pressure from a magnetic field, ICF uses only the inertial mass of the fuel and surrounding tamping material to increase reaction time. ICF also must compress the fuel to more than a thousand times solid density. Traditionally this approach uses nanosecond-timescale lasers to drive spherical implosions. Magnetized ICF such as MagLIF uses a magnetic field and the inertia of a liner to contain the plasma during a few nanoseconds of

high fusion reactivity. In such schemes, pulsed power instead of a laser system is the driver for an electromagnetic implosion.

1.3.1 Fusion Reactions and Reactivity

Fusion is challenging because reactant nuclei must overcome the Coulomb repulsion between like-charges (the Coulomb Barrier) in order for the strong nuclear force to bind them. This is a strong barrier, so the nuclei require significant kinetic energy. The fusion cross section has units of surface area, and describes size and effectively the probability for a collision to produce a reaction. Fusion cross sections depend on each nuclei's kinetic energy, and ultimately depend on the quantum mechanics involved in the strong force. Cross sections for hydrogen increase steeply with temperature until the individual kinetic energy approaches the 10 keV range. Fusion reactivity is another important concept; it is related to fusion cross section. The difference is that reactivity takes into account the likelihood of a collision, given the velocity of the fuel. Higher velocities have a higher flux of particles per second. Reactivity is the time-averaged product of cross section and velocity, in base units of volume per second. It is the basic measure of how many fusion reactions you expect per reactant pair. It is only a function of temperature, and when you multiply by density and integrate over time you can calculate the total number of reactions.

Reactions involving heavy Isotopes of hydrogen are the main focus of fusion research. Deuterium and tritium (DT) fusion is by far easiest to achieve

because it has the highest available fusion cross section by an order of magnitude and a maximum reactivity at a lower temperature than other reactions. DT undergoes the following reaction:

$$D + T =^4 He(3.5MeV) + n(14.2MeV) \tag{1.1}$$

The peak cross section occurs around 64 keV, which is close to the ideal for MCF. Ideal operating temperature for ICF is lower because there is a optimization balance between higher cross section at higher temperature and having a slower thermal-pressure-driven disassembly. Importantly, DT fusion produces a 14 MeV neutron that will most likely escape the reaction vessel or region. For fusion power, the neutrons are the critical medium by which heat is transferred out of the reaction area to be used for energy. They can also be absorbed by a medium such as lithium, which breeds tritium and can release additional energy upon fission. The charged helium nuclei remain in the fusion reaction area and must deposit their kinetic energy via collisions in order for a plasma to achieve ignition. These alpha particles are confined by MCF's magnetic fields, but they have meter-scale cyclotron orbits in fields of 1-10 T, so a magnetic device must have length scales of many tens of meters.

Instead of DT it is often convenient to work with the DD reaction, since tritium is radioactive and has no natural abundance. The cross sections of all of the fusion reactions are well understood, so DD can demonstrate the physics necessary for fusion. The two DD reactions looks like the following [4]:

$$D + D = \begin{cases} T(1.01MeV) + p^+(3.03MeV), & 50\% \\ {}^3He(0.82MeV) + n(2.45MeV), & 50\% \end{cases} \tag{1.2}$$

For a fusion plasma of finite dimensions, the reactivity as a function of temperature can be used to calculate the expected number of fusion reactions. The other only other parameter is the product density of each of the reactants. The time-integral of the reactivity and the densities will give the number of reactions.

$$yield = \int_0^t < \sigma v > n_1 n_2 \, \mathrm{d}t\mathrm{d}V \tag{1.3}$$

In the case of the DD reaction, the two reactant species are the same so the integral depends on the density squared. The integral is over volume and time for which fusion-relevant temperatures and densities are present. This integral, combined with knowledge of the energy output of the reaction, can be used to calculate total energy yield of power of bulk fusion reactions. The most important thing to remember for fusion scalings is that it is varies rapidly with temperature, goes like density squared, and roughly linearly with time and volume until ignition physics becomes relevant.

1.3.2 Magnetic Confinement Fusion

Most MCF concepts are not as relevant to this dissertation, but some of them are important to convey. In particular the β factor, which compares thermal pressure to magnetic pressure, will be important later. The goal of MCF is to create a magnetically insulated, burning plasma spanning very large volumes. The primary avenue for pursuing MCF has favored Tokamaks, which are toroidal magnetic geometries that use a time-varying poloidal magnetic

field to generate a current in the plasma. The plasma currents generate an encircling toroidal magnetic field that also helps to confine the plasma. Electrons and ions orbit the magnetic field lines along cyclotron orbits (Larmor orbits) with radius given by $r_c = mv_{th}/eB$. These particle trajectories can drift from collisions as well as large and small scale instabilities, and this leads to particle loss.

To achieve ignition in a MCF, a triple product called the Lawson Criterion must be satisfied. This is a product of reactivity, density, and confinement time $< \sigma v > n\tau_c$. These criteria are conditions necessary for a plasma to become self heated via hot fusion products. MCF needs to optimize reactivity so it requires temperatures of about 25 keV. The Lawson criteria can be satisfied at any density, but require larger and larger volumes and times for burning plasma operation. MCF operates around approximately 10^{14} ions per cubic centimeter, for reasons described soon. This is a low enough density that radiative cooling via bremsstrahlung is not prohibitive. However the Lawson Criterion can only be achieved at these densities if the confinement time is relatively long and volumes very large. Thus magnetic confinement fusion aims to maintain a hot, stable "burning" plasma on timescales of seconds up to continuous operation [5].

In MCF, plasma density is constrained such that thermal pressures can be balanced by magnetic field pressures with technically viable superconducting field coils achieving about 10 T. The size of such fields determine the scale of the rest of the machine. Beta is given by $2\mu_0 nkT/B^2$. This ratio of thermal

pressure to magnetic pressure is called β and it is one of the primary metrics for a MCF experiment or reactor [5]. For us later it will quantify scenarios in which pressure is sufficiently balanced to inhibit plasma transport, but in most of the work described in this dissertation $\beta >> 1$ and plasma hydrodynamic expansion is uninhibited.

β effectively determines the size scale and energy density of a MCF reactor device, because higher fields permit higher energy densities. Larger magnetic fields than those created by superconducting coils would permit smaller reaction volumes for the same fusion power output. Because of surface loss to volume scaling, a smaller reactor has to operate at higher powers. Unfortunately, producing higher magnetic fields than about 10 T is not really feasible on large size scales and times. The higher power density for smaller reactors, plasma physics limits on continuous operation, and the higher thermal neutron flux all combine to make smaller MCF designs less optimal. These factors combined with magnet technology essentially set the physical size of a continuously operating DT-based MCF reactor to ITER-Scale or larger. This ultimately sets the size and cost of potential continuously operating magnetic fusion reactors to be very high [5].

1.3.3 ICF

Laser-driven Inertial confinement fusion requires compressing a solid fuel pellet to a thousand times solid density with an final temperature of several kilovolts. The spherical implosion must be spatially symmetric which

is a defining challenge of this approach. The implosion must also occur at a high velocity, and such that its trajectory follows closely along an adiabat in PV space. Such an implosion will minimize the heat lost from the fuel and maximize the PdV work done to heat and compress it. If an ICF implosion achieves ignition, a substantial fraction of the fuel undergoes fusion reactions before it can significantly expand and drop in density. Burn fraction is a more important criteria for ICF than metrics like the Lawson Criteria for MCF, which depend on confinement time. The ignition region is intended to begin in a hot spot in the center of the compressed fuel, and propagate as a burn wave outward. The traditional approach to ICF has been to use lasers to implode a spherical fuel pellet of DT fuel. The two approaches are direct drive and indirect drive. These use either lasers or secondary radiation pressure, respectively, to ablate a layer of plasma from the surface of the fuel pellet. The momentum transferred to the pellet from the ablated plasma drives the inward implosion. The National Ignition Facility (NIF) was designed to achieve fusion via this indirect-drive method of secondary pressure of ablation within a Hohlraum capsule.

A number of challenging physics regimes apply to imploding ICF capsules that make them difficult to predict. One of these is the 3D Rayleigh-Taylor instability. This happens when pressure is applied from a lower-density fluid interfacing with a higher-density fluid, causing the interface to become unstable. Another difficulty is the physics of non-thermal electron heat transport. Electrons with high velocities can transport energy away from the cen-

trally heated region in ways that are difficult to model and understand. The ICF plasmas can have regions of "warm dense matter" where atomic physics at high densities and temperatures become important. Converging shock waves must be aimed and timed properly. To understate things, imploding an ICF fuel pellet is a complex physics problem!

1.3.4 Ignition and Burn in ICF

ICF ignition requires hot fusion by-product α ions to re-deposit their energy in a small area. Optimal temperatures are lower than the peak in fusion reactivity because higher temperatures result in higher pressures, causing the fuel to disassemble faster. Ignition in ICF requires temperatures above 4.3 keV. This is the temperature at which alpha particle product heating outstrips bremsstrahlung losses [4]. The confinement parameter, by analogy to MCF, is a product of number density n_0 and an effective inertial confinement time τ_{conf}. The confinement time can be re-expressed, since the fuel will expand to a lower density at a speed similar to the ion sound speed. Using this fact and an equation for the ion acoustic speed, the confinement parameter is re-expressed using the radius of the dense plasma region and the mass density. So $\tau_{conf} = \frac{R_f}{c_s}$. The plasma sound speed c_s is given by $c_s = \sqrt{\gamma Z k T_e / m_i}$. Here, the adiabatic index γ is usually taken as one, and since we have hydrogen Z=1. The electron temperature T_e determines the outward pressure driving sound speed expansion. Our confinement parameter is now $n_0 R_f / \sqrt{\gamma Z k T_e / m_i}$. Given a temperature in the right range and noting that m_i is a constant ion mass,

we now have a threshold criteria for ignition quantified by a density and a radius. The result is an expression for the effective confinement of fusion heating simply called areal density or ρR. For ICF ignition, the criteria will ultimate goal is achieving necessaryρR with necessary temperatures and while maintaining symmetry. [4].

The dynamic of an ICF implosion are important. Once the fuel has achieved the necessary density, fusion burn is desired to be achieved in a central "hot spot". Stagnation is a word for conditions in which the outward thermal pressure balances inward implosion pressure, and burn must be timed to coincide with stagnation which requires a high degree of implosion symmetry. The concept of stagnation will be important later.

1.3.5 Magneto-Inertial Fusion

Alternative ICF schemes aim for intermediate burn times and densities by combining magnetic confinement with fuel compression and heating. Magneto-Inertial Fusion (MIF) and Magnetized target fusion (MTF) use a magnetic field for plasma confinement. However they use a shorter confinement time and higher density fuel than traditional MCF, and are fundamentally transient like ICF. Some very early ICF papers described adding an external magnetic field to augment ICF's neutron yield.

In MTF, a target plasma with an embedded magnetic field is launched into or created inside an imploding liner. The plasmas are typically field-reversed configuration (FRC) plasmas, or plasmoids, which are toroidal plas-

mas maintained in shape by their own internal currents. These FRC plasmas are compressed to fusion temperatures and densities with their frozen-in magnetic field via compression inside a conducting liner. The timescales for FRC plasmas is microseconds to milliseconds and they have electron densities from 10^{17} to 10^{19} cm^{-3}. Because of these longer plasma timescales, MTF liner implosion speeds can be much slower than many other MIF schemes and require much less energy, but they require large compression ratios to achieve desired densities. The triple-product Lawson Criteria from MCF are still an applicable metric for MTF experiments. Thus, since Magnetized target fusion uses densities and collision times are mid-range between MCF and initially solid-density implosions in ICF, reaction times are also necessarily longer than non-magnetized ICF.

Concepts for MIF vary widely, including simply seeding a 10 T magnetic field into the NIF Hohlraum for subsequent laser-driven implosion. Most of these approaches use some type of magnetic flux compression to achieve much higher fields in the kiloTesla range [6]. MIF often uses such high fields, to help suppress electron heat losses and enhance stability even at very high thermal pressures. Flux compression uses an imploding electrically conductive media such as a metal liner to surround and compress a magnetic field. Since a magnetic field is excluded from a moving conductor, the magnetic field flux density will increase as the internal volume decreases. MagLIF is a type of Magneto-Inertial Fusion [1].

1.4 Magnetized Liner Inertial Fusion

MagLIF starts as a cylindrical liner containing an externally-generated magnetic field (10-30 T) and an initially high pressure (4-10 atmospheres range) fusion reactant gas. The MagLIF process then goes through three steps [1]. First, a Helmholtz coil surrounding the 1 cubic centimeter vessel volume pulses on a millisecond timescale to create an embedded magnetic field. Existing systems on integrated MagLIF experiments can deliver 10 T. Next, a Terawatt class laser heats a plasma column in the center of the liner to a desired temperature approaching keV. Ideally many kJ of laser energy is delivered to the gas. Finally, a pulsed-power z-pinch implosion is initiated in the liner surrounding the vessel. This compresses the fuel, doing pdV work to increase temperature and density to fusion-relevant conditions. The electrically conducting liner also increases the intensity of the magnetic field in the vessel via magnetic flux compression to the kilotesla range. This kilotesla field helps to inhibit thermal conduction losses and should dramatically improve retention of hot fusion by-product ions [1].

The geometry of choice for a magnetized plasma is cylindrical symmetry. A cylindrical implosion geometry is less favorable for achieving ICF ignition compared to a spherical geometry, because the fuel is not compressing as fast, due to r_0/r^2 scaling versus r_0/r^3 [1]. The radial compression ratio necessary to achieve a stagnation temperature from a thermalized preheat temperature is given by:

$$C_R = \left(\frac{T_{stag}}{T_{preheat}} \right)^{3/2g} \tag{1.4}$$

Where C_R is the convergence ratio $R_{stagnation}/R_0$ and g is the volumetric geometry factor that is either 2 for cylinders or 3 for spheres. The desired temperature at stagnation is about 4-5 keV. C_R of 120 is required for cylindrical geometry and about 25 for spherical geometry if temperature starts in the eV range [1].

One of MagLIF's key steps is laser preheating. Preheat significantly reduces the compression ratio necessary to achieve ignition conditions. Slutz estimated that a C_R of 20-30 is all that is needed in cylindrical geometry from an initial density of approximately 1-5 mg/cc to a final density of 0.5-5 g/cc [1]. That is a final density of 1.5 to $3 * 10^{23}$ cm^{-3}. Compare this to spherical-geometry laser driven ICF, which needs to achieve symmetrical implosions with a compression ratio of about 100. A C_R of about 25 in cylindrical geometry is achievable on Z with implosion speeds of about 1/10 mm/ns or 100 km/s, so initial temperature must be much higher than an eV range ionization temperature.To achieve fusion temperatures, cylindrical compression ratios of 20-30 require that the fuel starts at about 200 eV when the liner begins to implode. Maintaining this high initial temperature following laser preheat and during implosion is an important requirement for achieving fusion conditions. With a fixed C_R determined by the driver, the initial temperature determines the stagnation temperature and whether it will reach the ideal range of 4-5

keV for ignition. This early-time temperature behavior will be a key topic of this dissertation, and we see that it is important for MagLIF fusion yield [1].

In order for ignition to be practical the cylindrical plasma length has to be long enough that energetic fusion products don't all escape axially before a significant fraction of the fuel has time to react. This sets an aspect ratio for the converging cylindrical geometry. It turns out that aspect ratios of about 1:1, with centimeter length scales are sufficient [1].

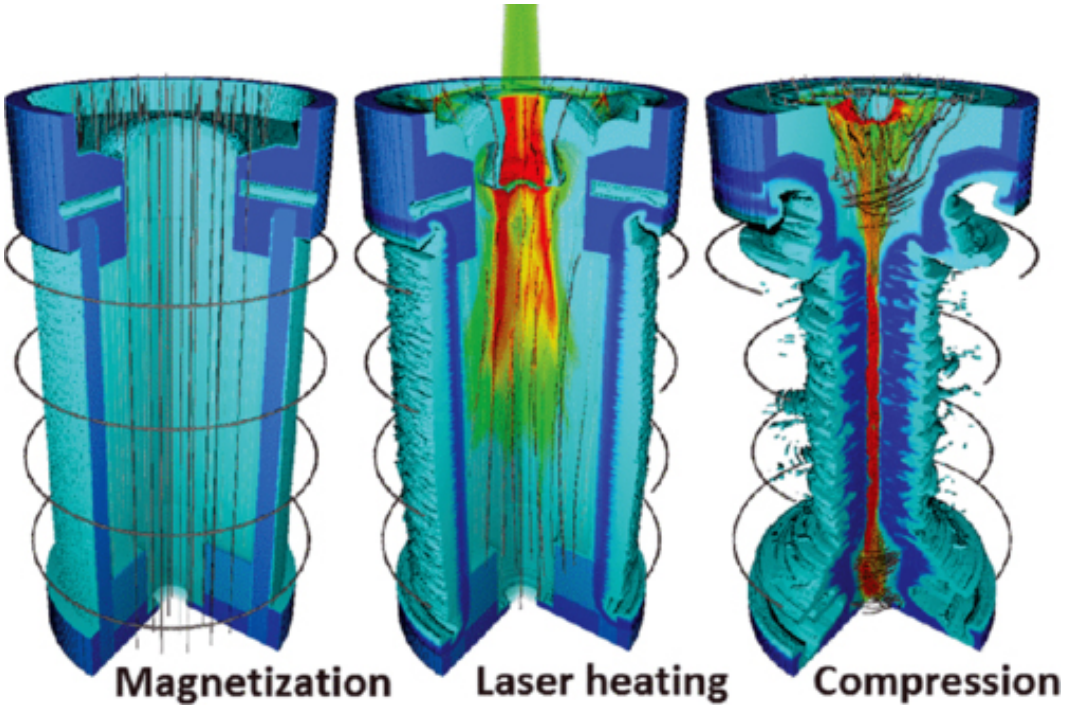

Figure 1.1: The MagLIF fusion scheme illustrated in three streps, including magnetization, laser preheat, and pulsed power driven implosion and stagnation [1].

Designs by Slutz and others indicate that MagLIF could be particularly

promising in the future [7]. Design improvements call for cryogenic targets with deuterium ice on the walls of the liner. A follow-up paper by Slutz indicates that high-gain Q=1000 might be available on a 60 MA pulsed power driver and with many kJ of initial laser preheat energy. Such facilities are not available currently, but the large increase in gain points to a large parameter space for improvement in MagLIF [7].

1.4.1 Z Machine

The Z Pulsed Power Facility at Sandia National Laboratories is the world's largest pulsed power facility by stored energy and discharge power. Over several decades Sandia researchers have used the Z-machine to explore high energy density physics with widely varying applications including stockpile stewardship physics, astrophysics, and inertial confinement fusion. The Z-machine's technical capabilities are globally unmatched. The facility uses a 36 module Marx bank with a maximum discharge current of about 24 MA at a voltage of 6 MV. The total stored energy is about a megajoule. The discharge waveform is tunable, allowing for optimization of a wide range of target packages. The Z-machine also has a host of diagnostic options, including most notably for this thesis the Z-Beamlet laser which will be described in chapter two.

For MagLIF experiments the Z facility can deliver currents exceeding 20 MA, and thus the magnetic pressures exceed megabars. The facility is capable of driving implosion velocities on the order of 100 km/s in cylindrical liners

surrounding the plasma. Decades of experience with imploding liners, wire arrays, and other Z-pinch concepts led to an understanding of the dynamics of such a imploding liner. In particular, Z-pinch geometries are susceptible to instabilities such as sausage instability, blowout or kink instability, and Rayleigh-Taylor instabilities. However, Slutz and others were able to conclude that magneto-RT and other instabilities might be mitigated sufficiently to allow axisymmetric and nearly homogenous hot plasmas at stagnation, and in fact this has been shown to be the case experimentally.

1.4.2 Magnetic Field and Magnetic Flux Compression

MagLIF initially contains a background axial seed magnetic field. A pair of Helmholtz coils pulsed on millisecond timescales currently generates this 10 T seed field. As mentioned earlier, the seed field undergoes flux compression as the liner implodes. The 20 MA axial current from the Z-machine generates an azimuthal B-field external to the liner, so it should not have any influence on the field inside the fuel volume. The primary role of the liner is not to directly implode and compress the pre-heated fuel, but rather to act as an imploding electrical conductor for magnetic flux compression. The seed magnetic field is expected to be "frozen in" to the preheat plasma following laser heating and ionization. Thermal pressure causes the sound speed expansion of the initial laser plasma column, as will be discussed in detail later, so the field strength in the plasma actually decreases as it expands. The expanding hot plasma will also exclude and compress the magnetic field between the hot boundary and

the liner as it expands following laser heating. Fortunately, the magnetic field between the liner and the heated plasma region will be increasing in intensity as the liner implodes.

The magnetic field is strength is increased by the ratio of the square of initial to final radii $\left(\frac{r_s}{r_0}\right)^2$. For a $C_R = 25$ this produces a magnetic field that is expected to be on the order of kiloTesla, eg. 6 kT for a 10 T seed field. This field magnetizes the hot electrons to inhibit radial thermal losses from the laser heating column even during stagnation, insulating it from the liner. Also, as mentioned previously, such strong fields are crucial for containing the MeV-energy fusion byproducts for both D-D fusion and future D-T fusion reactions and keeping their energy within the fusion column, thus increasing effective fuel ρr by orders of magnitude. In fact it turns out that ρr is not the most relevant confinement criteria, but rather the product of stagnation B-field and stagnation plasma radius BR. Initial MagLIF experiments are thought to have achieved a $BR > 0.3MG * cm$, which is about half of what is required for fusion by-products to be fully confined [8]. If the stagnation column were larger in radius this would help with this issue, but the initial energy deposited is believed to be too low, resulting in a narrow plasma column. Other results suggest that the magnetic field is already strong enough for trapping of daughter products, suggesting that increasing the initial preheat energy density should be an important goal [9].

Although Knapp's argument about daughter product confinement parameters is correct, inertial confinement is still provided by the combination

of the flux-compressed field and the liner. The magnetic field is not providing the bulk of the inertial confinement for the MagLIF plasma during stagnation, because the areal density of the liner is much greater, with the magnetic field as an intermediary. The ρr of the fuel alone is about 0.01 g/cm^2 while that of the liner is about 1.1 g/cm^2 based on Slutz's simulations [1]. Without the liner areal density tamping the stagnation plasma, and the compression of the seed field to act as an insulating medium between the fuel and the liner, the parameter space for a cylindrical geometry inertial confinement scheme would be significantly more demanding.

Another benefit of magnetization that seems to occur from the magnetic field was not anticipated in the MagLIF design. Results from Z-machine experiments with an empty liner show that a pre-existing axial magnetic field may alleviate the Magneto-Rayleigh-Taylor (MRT) instabilities on the liner surface. In a recent paper from 2014, Awe describes how the addition of the background axial magnetic field in a MagLIF-like setup imparts a helicity to the MRT instability, along with tamping its overall amplitude [10]. This effect should aid in maintaining plasma stability as conditions approach stagnation in MagLIF.

1.4.3 MagLIF Integrated Results

The best results so far from integrated experiments on MagLIF are presented in a 2015 paper by Gomez et. al [2]. These results show a neutron yield of $2 * 10^{12}$ for DD fusion. Time integrated x-ray pinhole imagers sensitive

to emission in the correct energy range to penetrate the aluminum liner show a narrow 100 micron radius slightly helical plasma on stagnation. Emissions are consistent with a 2 kV helical plasma column about 100 microns in diameter with several nanosecond duration. The x-ray emissions coincide in time with the peak neutron emissions. Neutron yields for most integrated MagLIF experiments were around 10^{11} or 10^{10} [2]. Follow-up work indicates that these experiments were producing thermonuclear fusion conditions, meaning that fusion is a result of a high temperature and density plasma rather than some sort of non-thermal ion kinetic collisions [11].

As mentioned previously, the magnetic field helps confine charged DD fusion daughter products ^3He, p^+, and ^3T nuclei within the plasma column. The MeV-energy secondary tritium has a chance to fuse with nearby D via the higher cross section DT reaction. These secondary reactions have been observed through 14 MeV neutrons in MagLIF experiments, indicating that significant magnetic retention of DD reaction daughter products via magnetic confinement had occurred. Recent work on the secondary DT yield from these integrated experiments has provided strong evidence that the stagnation plasma is strongly magnetized and is effective at increasing fuel ρR by trapping MeV energy fusion by-products. The anisotropy of these neutrons also gives us information about the temperature of the plasma. This could only be possible if magnetic flux compression produced fields in kiloTesla range near the stagnated column [9].

The results of these MagLif experiments are no small achievement, but

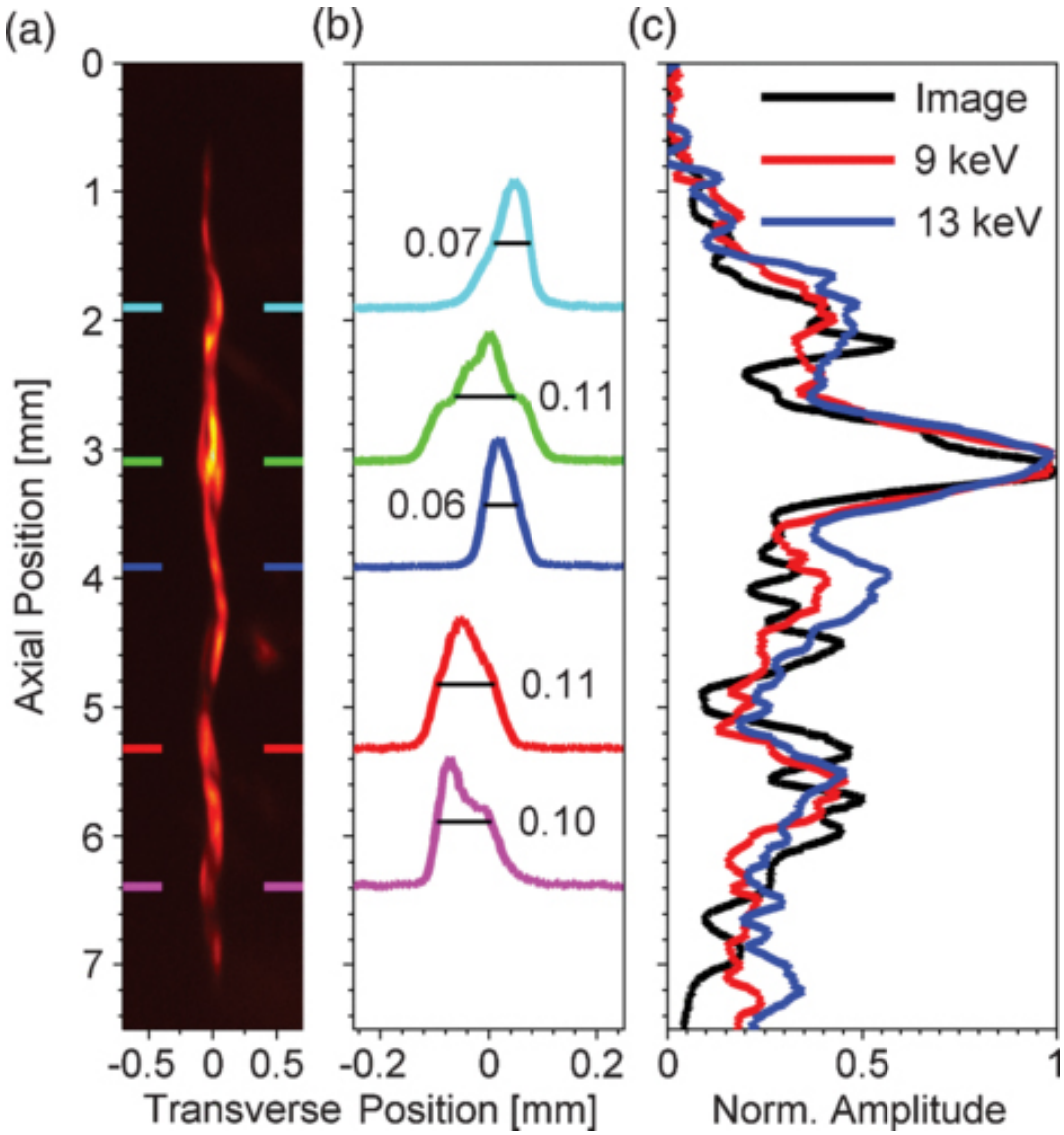

Figure 1.2: This x-ray emission image shows the stagnating plasma column from a MagLIF integrated shot. The image shows a helical structure and sub-100-micron diameter. The image demonstrates that a high degree of implosion symmetry is possible in stagnating plasma columns, which is encouraging [2]

they fall short of the predictions for what MagLIF could do with present parameters. The fusion reactivity for deuterium at 3 keV is about $3 * 10^{-26}$ m^3/s. This is significantly lower than what DD reactivity could be at higher temperatures. For example, at 30 keV the reactivity increases by a factor of 500, and temperatures of above 25 keV are required for DD reactions to achieve ICF ignition [4]. DT reactivity is about $3 * 10^{-24}$ m^3/s at 3 keV, or about 100 times higher than DD. Thus we might expect similar conditions with DT fuel to produce about 10^{14} neutrons per shot. Scientific breakeven with MagLIF would happen when the neutron energy approaches the order of the driver energy coupled to the target. The Z driver consumes megajoules and delivers about 0.5 MJ. For DT fusion this corresponds to a neutron yield in the 10^{18} range, so there is a ways to go for experimental realization of scientific break-even.

Some aspects of these initial integrated MagLIF results are puzzling. The experiment parameters of these initial experiments as reported by Gomez did not match Slutz's target designs of MagLIF. These integrated MagLIF experiments had a 10 T magnetic field, 2 kJ laser energy, a low $2 * 10^{20} 1/cc$ electron density. The Z-beamlet heating laser was not smoothed, for example with a distributed phase plate (DPP), which would allow the experimental laser parameters to more closely match simulations [2]. Integrated MagLIF experiments are unable to make any measurements of the energy or temperature of the laser-heated channel prior to the implosion, since no visible or x-ray diagnostics can pass through the MagLIF liner.

1.5 MagLIF Preheat

Here and throughout the rest of this work I will focus on the fuel pre-conditioning, which is the process of preparing the fuel for implosion. In particular I will focus on the preheating process of pre-conditioning, following seed field magnetization. In our experiments we explored laser heating with the 2ω in helium in a setup similar to MagLIF.

The preheating laser deposits energy in the fuel via inverse bremsstrahlung (IB) (also called collisional absorption). This process heats electrons in cold plasma much more efficiently than in a hot plasma, resulting in a transparency increase as the plasma is heated. This means that at any one time the laser deposits the most energy near the edge of the heated plasma that is farthest downstream. This heating process can be described as a "bleaching wave" because once a region is heated, the continuing laser pulse propagates to the next region and heats it, creating a propagating heating front. [1]. The solution to the differential equation for the axial distribution of temperature deposited via this process was originally derived in a paper by Denavit and Phillion and independently by Slutz sometime later during design work on MagLIF [12].

There are several intuitive reasons to suspect the laser heating behavior might be more complex than the bleaching wave solution to the collision absorption equations. Hydrodynamics are not included in the bleaching wave model. Radial and axial electron thermal transport are actively occurring, generating a diffusive thermal wave radially outward from the heated region as well as smoothing the bleaching wave axial profile [1]. The plasmas are also

radiating energy at a rate that is dependent on the temperature to the fourth power as well as the presence of contaminants in the plasma. We also suspect that self-focusing laser plasma interactions may be important in determining the volume of heated plasma. All of these effects will be discussed in a future chapter.

The gaseous hydrogen fuel in MagLIF is contained behind a thin film or window that resides at the top of the vessel. The laser enters the volume through an aperture called the Laser Entrance Hole, or LEH. The LEH window must be converted to a plasma by a short laser pulse preceding the main laser pulse. The goal is to cause this window material to be removed from the vessel area by heating it and driving an exploding plasma away. Ideally this plasma should drop at least a factor of 10 below the 2ω critical density of $3 * 10^{21}$ cm^{-3} in order for various tricky nonlinear processes to sap energy away from the preheated fuel. Early MagLIF experiments used a 2 ns early pre-pulse of an energy around 100-200 J to blow away a 3 μm thick polyimide window. Density gradients and radiation effects are important at that interface. There are also nonlinear processes even in the bulk plasma that couple the laser energy to plasma waves or electron pressure imbalances and are broadly known as laser-plasma interactions (LPI). Parasitic laser energy loss mechanisms and instabilities due to LPI are expected and must be mitigated if they cause substantial energy to be radiated or transported from the desired heating region.

1.5.1 Motivation for MagLIF Preheat Studies

MagLIF yields are expected to scale more strongly than linearly with initial preheat energy up to about 2 kJ, as shown in figure 1.3. Yet there is no way to make a measurement of the overall laser energy coupled to the fuel during MagLIF preheat on an integrated experiment. Nor is there a reliable way to say exactly what distribution of energy density can be expected for preheating with a given distribution.

We are motivated by diagnosing the energy content of the preheat plasma. There is some speculation in the MagLIF literature that early integrated experiments could have performed better with more preheat energy. With too little thermal energy density in the preheat plasma channel, the convergence of the liner will be too high; implosion pressure will be too high compared to the stagnation pressure and the resulting stagnation column will be too narrow. This will result in a small volume in which fusion conditions prevail, lowering the yield.There are many possible explanations for the energy content of the laser-heated channel to be low.

Sefkow et al. described simulations of integrated MagLIF experiments with parameters in the results reported by Gomez [2]. Those parameters included a seed field of 10 T, peak Z current of 18 MA, and total laser energy preheat energy of 2 kJ. These simulations produced a higher yield than those reported by Gomez et. al. It was speculated in Sefkow's paper that shortfalls in the preheated plasma energy would explain the discrepancy with experiments, for example if only a few hundred Joules were coupled to the gas. Sefkow

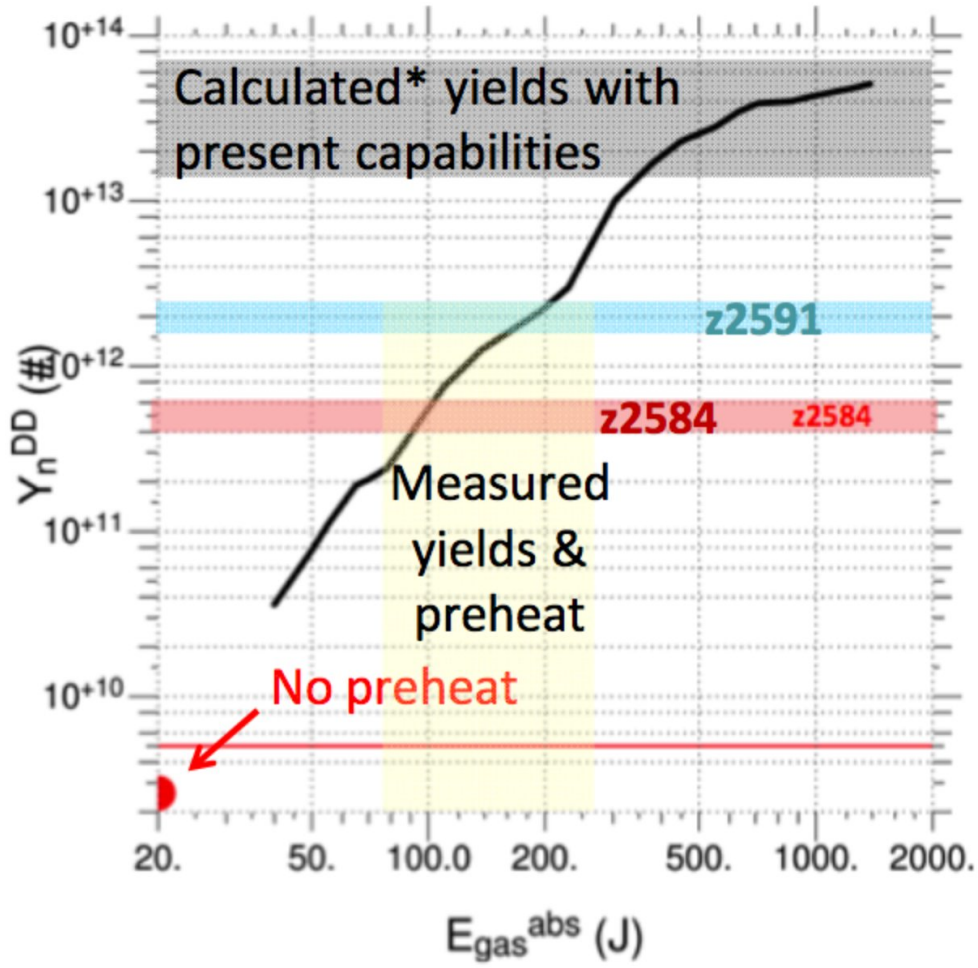

Figure 1.3: Neutron yield scales roughly like the preheat energy squared according to simulation work by Sefkow. On this log scale, the slope is between 1 and 2, suggesting that the yield scales strongly with preheat energy up to the kJ range. These were from follow-up work via 2D Hydra simulations from Sefkow after publishing [13]

suggested that simulations exploring lower laser preheat energies would be the topic of a follow-up paper, but this never came to fruition [3]. So the work of

Sefkow and others suggest that overall energy in the preheated gas is lower than ideal, but there are few direct measurements of this preheat energy. Indeed there are x-ray imaging results from some integrated MagLIF experiments to show that on some shots did not see substantial energy in the plasma in the later 5 mm of the target. We seek a direct measurement of the energy density profiles in preheat plasmas during and after laser heating.

1.5.2 Ideal Preheat Conditions

There are several important preheat plasma column parameters to optimize for MagLIF. First, ideally, the plasma column would have an energy density, measured in energy per unit length, that is as high as is achievable. At a fixed density this means the laser raises the fuel temperature as high as possible within the central half-radius. Slutz initially described an ideal design space for MagLIF with a laser diameter that has a particular size for a given preheat temperature, as shown by the yield scaling depicted in figure 1.4. Subsequent experiments have typically operated in the range of laser radii between 0.4 mm and 0.7 mm.

Additionally, the temperature of the preheated fuel must also remain high during and after laser heating. Thermal energy density must be maintained for approximately 20-30 ns during the time in which the liner is energized by the pulsed power apparatus, but does not implode significantly. Heat may be that transported away from the laser heated plasma column even during laser heating. Mechanisms for heat loss are primarily hydrodynamic ion

density transport via ion acoustic waves and recoil at the liner, electron thermal heat conduction to liner walls, and electromagnetic radiation transmitted through the fuel region. Radiation losses from impurities can rapidly cool the plasma, even possibly on timescales comparable to laser heating. Very strong radiative loss would result in an energy density distribution that is strongly bias towards the LEH, since the plasma would cool rapidly and the IB bleaching wave would not penetrate very far. Any impurity material which mixes in the bulk gas, for example from the LEH window, should be avoided. The details of radiative transport and electron thermal heat waves will be discussed separately in future chapters.

Together with an overall high temperature, heating uniformity with small axial temperature gradient through the one centimeter axial length scale also may be important [1]. It is important that most of the energy be delivered to the 1 cm axial depth and not beyond, so the length of the plasma is important also. If the heated region is too long, laser energy is wasted being deposited in a region that will not implode. 2D Rad-hydro models describe thermal condition homogenizing the energy density axially on timescales faster than the implosion, so within nanoseconds after heating [3]. However, initially axially biased energy deposition may be problematic even if it is not manifest during stagnation 30-40 ns later. We will see evidence in future chapters for significantly more laser energy being deposited close to the LEH region than deeper into the plasma in certain situations. Preferential heating near the LEH region may be related to undesirable contaminants in the plasma and higher

radiation rates that deplete the overall energy density before implosion.

A higher fuel density will also benefit the energy per unit length. Unfortunately there is a tradeoff here, because an initially higher gas pressure requires a thicker LEH window and contributes to LPIs. Increasing the fuel density closer to critical density makes thermal self-focusing more likely, for example. Thermal self-focusing occurs when radial gradients in laser heating drive thermal gradients, which subsequently push a density gradient. The density gradient causes a change in the plasma's index of refraction, which can create an instability where the laser is focused into regions of lower density, heating them further and driving more density depletion. This is the primary mechanism of laser filamentation and will be important for us to describe later. There may be a particular initial fuel density that can deliver the highest preheated energy per unit length with a given laser parameters.

Also, the density of the fuel must be maintained within the liner following preheat, which means axial losses through the LEH region and out the bottom of the liner prior to implosion should be minimal. The heated fuel mass is transported at the sound speed on nanosecond timescales, so the radial ion sound wave will certainly impact the liner in less than 10 ns. McBride et. al. describe this as a blast wave, but an ion acoustic wave would be a more accurate description if the heating laser diameter approaches a millimeter [14]. The inward shock of the liner as it implodes may also meet and collide with the outward shock of the preheated fuel, with the flux-compressed magnetic field insulating between, as was originally intended in the design [1]. Although no

fuel mass is lost radially, heat conduction losses may occur with the liner if the flux-compressed magnetic pressure is not sufficient to insulate the hot plasma core from the liner wall. The main avenue for ion density (and coulomb-bound electrons) loss will also transport axially. Fortunately the motion along the z-axis near the LEH is tamped by the ion sound wave and blast wave emerging from the LEH region. On the lower end of the vessel is the cold gas of the vessel fill line, into which a shock unfortunately can readily propagate.

Finally, the laser heats a plasma channel with a finite diameter. While increasing the diameter of the beam can increase the energy per unit length present in these plasma columns by increasing the heated cross sectional area, there is a practical limit. The aspect ratio of the liner in MagLIF sets maximum diameter of the beam. Ideally the laser heating radius is up to half the inner liner radius. This ratio is based on parameters that Slutz explored during the initial design phase [1].

1.5.3 Laser Preheat Parameters

There are several tunable parameters of the fuel preheat that could be explored. This list is long, but it does not include everything: 1) the energy and power of the main heating beam laser 2) prepulse energy 3) prepulse delay 4) Laser timing relative to liner implosion, which is set by delay between Z and ZBL. 5) fuel density (higher is better for fusion yield but not necessarily for mitigating LPI or for ease of target fabrication) 6) laser radii, with certain restrictions 7) thickness and composition of LEH window material 8)

background magnetic field 9) position of best focus of beam.

Optimizing these parameters to achieve ideal preheat conditions is difficult because of our incomplete understanding of the physics of the preheat process. It is not clear what the right configuration of the heating laser parameters achieves the best energy deposition and uniform energy density. Slutz, Sefkow, and others designers worked to optimize many of these things via analytical work and simulations in the original design. In order to validate our physics models and simulation packages, it would be valuable to have an empirical scaling of preheat energy density as some of these parameters are varied. One chapter of this dissertation will attempt to do that.

The timing of laser preheat relative to the liner implosion is certainly important. Slutz mentions that there is an optimum time which minimizes axial loss of fuel and lost fuel temperature but still optimizes the liner implosion ratio. Basically the plasma column temperature begins decreasing immediately following laser heating, and after several nanoseconds fuel mass begins to transport axially and radially. By his estimates the fuel mass loss is acceptable on timescales of 100 nanoseconds or less, but the optimum time for the preheat seems to be just before the liner begins to implode. We will not explore laser timing in this work as it does not work well with preheat-only experiments.

Livermore carried out a number of experiments in the past several decades related to transmitting laser energy through a thin window, as this is a often a necessary scenario in laser inertial fusion. Their results suggest that

in order to deliver maximal laser energy, improvements can be made by operating at 3ω. Total energy can also be increased by using a distributed phase plate (DPP) and temporal smoothing by spectral dispersion (SSD) [15]. We will explore the results of implementing a DPP, which in our case did not seem to translate to a significant improvement in uniformity of energy distributions. We did not implement SSD or 3ω conversion due to the significant hardware changes required.

One related work on laser energy Harvey-Thompson et. al. report experiments on the OMEGA-EP laser with 0.35 μm light [16]. These experiments demonstrate a very high laser coupling efficiency into the target gas: as much as 0.82 of the laser energy delivered, for long pulses over 3 ns in duration. Harvey-Thompson's paper explored the strongly nonlinear affect of LPI at intensities in the range of 1-2 10^{14} w/cm^2, similar to the intensity regime we operate in. We will be able to further explore energy density in experiments similar to those reported in Harvey-Thompson et. al with a 2ω heating beam more relevant to recent MagLIF experiments [16] [17].

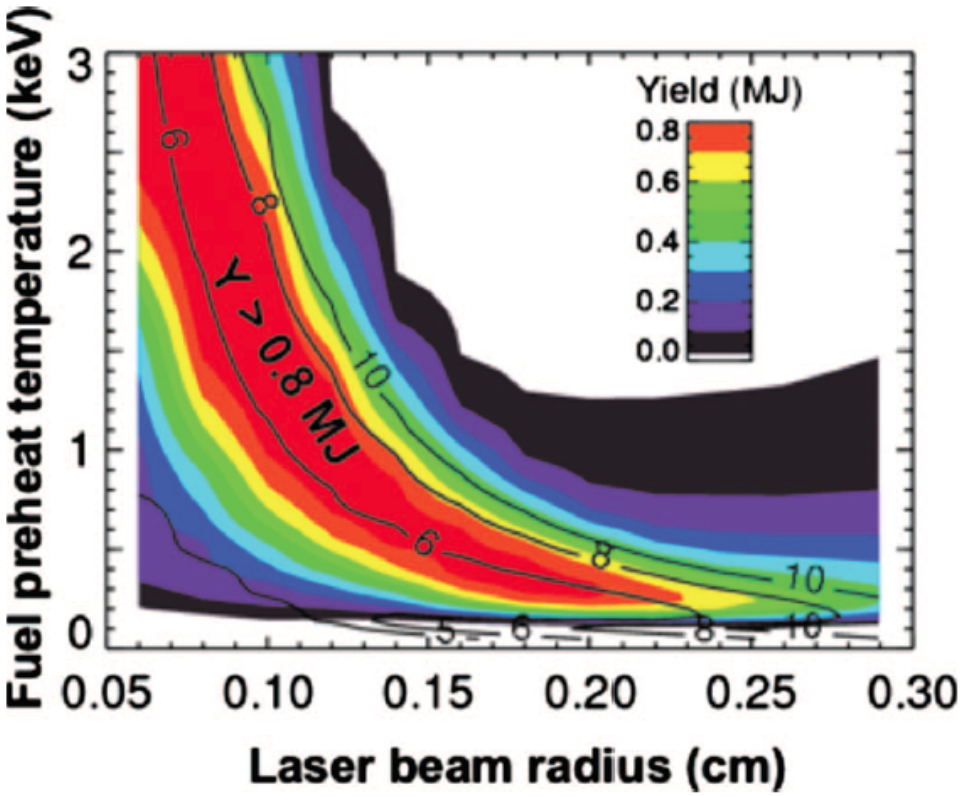

FIG. 15. (Color) Contours of the fusion yield for magnetized liners (colors) are plotted as a function of the laser beam radius and the fuel preheat temperature. The black lines are curves of the required preheat energy in kilojoules. The results are for a beryllium liner with A_R=6 and length =0.5 cm. The initial magnetic field was 30 T and the convergence ratios are fixed at 25 by adjusting the fuel density.

Figure 1.4: This figure and caption from Slutz's 2010 paper describes how a heated radius of about 1 mm with a maximal temperature is highly advantageous to MagLIF yield [1]. The optimum radius seems to be about 0.8 mm as preheat temperature approaches the keV temperature range. If preheat temperatures are too low, then a still wider plasma is better to optimize energy density. Unfortunately the optimum preheat energy total of six kilojoules is more than Z-beamlet can deliver presently.

Chapter 2

Experimental Setup and Diagnostics

This chapter will describe the hardware that we developed to be able to support plasma transport measurements on surrogate MagLIF-like targets. The hardware crucially includes the Z-Beamlet laser system itself, which is shared with the Z-facility and thus supports the same MagLIF experiments we are interested in replicating or experimentally simulating. We implemented new target chambers, new gas cell targets, magnetic field delivery hardware, and gas fill delivery systems. There were also a new set of diagnostics to capture laser-heated plasma transport. All of these capabilities have been in development since approximately 2014 and some are still being developed. I will describe the facility and target chambers that we used for this work, including a newly adapted target chamber called Conchas.

Besides the existing facility, significant hardware had to be assembled for these experiments to be possible. In terms of historical development, we did not start out with all of this hardware intending to use it for the experiments that I will describe. Some machinery, such as the B-field driver, were originally constructed for other purposes and adapted. We needed time to install a target area with a new target chamber that had all of the required capabil-

ities adapted to work together. Several elements including the gas cells and magnetic field drivers required considerable engineering development. More specifically related to the experiments are the diagnostics we used for exploring plasma heating and expansion. These include shadowgraphy and x-ray diagnostics combined with the Gila laser system on the newly re-purposed Conchas target chamber. The integrated experimental platform became fully operational in 2017.

2.1 Z-Beamlet Laser Facility

2.1.1 Z-Beamlet

The Z-Beamlet laser (ZBL) was originally a prototype laser system developed at Lawrence-Livermore National Laboratories (LLNL) as a prototype for the National Ignition Facility. At that time it was called Beamlet. It was transported to Sandia National Laboratories in the 1990s and re-tasked as a system for generating short-duration x-ray point sources for radiographic imaging of targets on the Z-machine [18]. ZBL worked extremely well as a radiography source, but turned out to be useful for a number of other reasons also. ZBL is a terawatt-class Nd:glass solid state laser with nanosecond timescale pulse durations. The timescale and power were developed for ICF so they are well suited for delivering significant plasma heating before mass transport can occur on nanosecond timescales, so this timescale and power is relevant for MagLIF also.

The ZBL system capabilities include delivering multiple kilojoules of

frequency-doubled 527 nm green light with a maximum irradiance of $10^{16} W/cm^2$. Pulse durations and energies are tunable in a 6 ns window via a custom waveform on an automatic waveform generator (AWG). Maximum energy currently attainable is about 4 kJ. The laser amplifier cooling cycle after a shot is about 3 hours. This permits a maximum practical full system shot rate of about three shots a day [18].

Several innovations were required to make Z-beamlet possible. Primarily, Beamlet included an advancement enabling multi-passing the main Nd:glass amplifiers versus passing through multiple successively larger amplifiers as was done in the NOVA laser. This allowed the laser to take up less space and require less energy. The advance that allowed this to be possible was the Plasma Electrode Pockels Cell, or PEPC. This is a large polarization-switching optic similar to a conventional Pockels cell. For such a large optic size with a large 30 cm aperture very high electric fields would normally be required for Pockels cell operation in transverse mode. Alternatively, undesirable concentric ring electrodes would be required on both sides of the optic to impose a longitudinal electric field. In the PEPC a plasma on the surface of the optic creates a longitudinal electric field with minimal laser distortion or losses. The PEPC thus permits controlling the multi-passing large diameter beam, which is kicked out of the glass amplifiers after four passes. The maximum theoretically achievable gain from these amplifiers allows a beam energy approaching 6 kJ [18].

Z-Beamlet's customizable waveform via the AWG gives a high degree

of versatility to our experimental platform presented in this dissertation. The AWG not only allows the laser to compensate for gain nonlinearities as the gain media desaturate, but it also permits unique pulse trains and customizable powers. This includes the ability to adjust the beam power in time, with ramps, pedestals, temporal foots, or prepulses controllable by the laser operators. For MagLIF experiments and most experiments carried out here, Z-beamlet's customizable waveform capability was used to deliver a double-pulse. The first pulse, or prepulse, is intended to heat the thin film window (LEW) that contains the high pressure target gas. The prepulse was typically in the range of 30 -100 J in our experiments, which is sufficient to heat the window material to a hot, mostly transparent plasma. The idea is for this target plasma to drop well below critical density, such that the subsequent heating pulse can penetrate into the gas with minimal loss. A representative Z-beamlet pulse train with prepulse included in the AWG time sequence is presented in figure 2.1.

In this experimental series, we operated Z-beamlet with energies ranging from 1 to 2 kJ. Typical power for Beamlet is about 1 TW, but we operated around 0.5 TW for most experiments to reduce the overall intensity of the beam at the LEW interface and ostensibly reduce laser-plasma interaction effects. Recently, Beamlet has been optionally co-injectable with a separate laser system beamline from the Z-Petawatt laser. Z-Petawatt was designed to be operable in a temporally-compressed mode for 500 TW peak powers. Jens Schwartz and Patrick Rambo adapted Z-Petawatt to be injected into the same

beam path as Z-beamlet. We have used this co-injection capability to deliver an early pre-pulse for laser heating experiments. It can supply up to several hundred Joules with a time separation from Z-beamlet that is tunable up to or beyond hundreds of nanoseconds [19]. This early prepulse helps to blow away the LEW earlier, such that the main heating beam encounters a lower density and density gradient once it arrives.

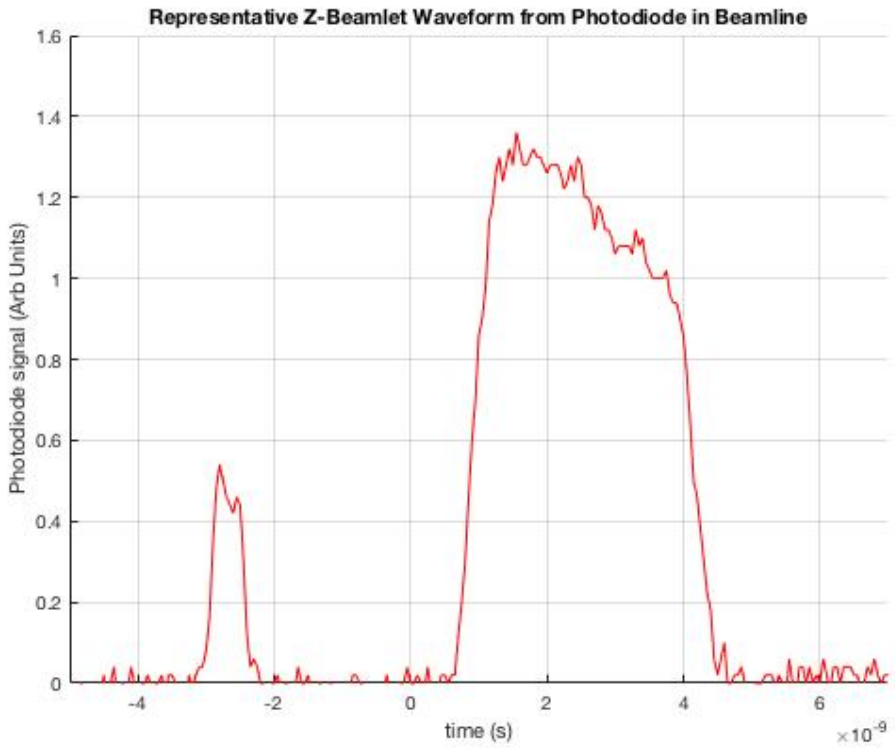

Figure 2.1: This figure shows an example photodiode trace from the Z-beamlet beamline. This is representative of heating pulses delivered to gas cells. The prepulse is included. Overall heating pulses are in the range of 2-4 ns in duration.

Additionally we have employed techniques for spatial beam smooth-

ing. In the absence of any beam smoothing techniques, Beamlet's square spot contains hotspots and intensity gradients that span the entire radial extent of the beam. MagLIF experiments reported by Gomez et. al used this beam profile [2]. Refer to the leftmost unconditioned beam spot image in figure 2.2 for an example of the near-field beam cross section.

Beamlet can also field several different sizes of distributed phase plates (DPP) which are intended to change the focal length of the lens variable, creating a bundle of very narrow speckles. The spread of these speckles is highly uniform, such that the radial intensity profile is flat to within a 10% up to the specified radius. The DPP speckles do not vary in time, but they do vary along the Z axis since they vary in focal length. DPP smoothing works best in the near field; farther from the narrowest beam waist more of the original beam features return and the edges become more smoothly varying; figure 2.3 demonstrates the effect of slight defocusing on the beam cross-sectional shape with a DPP in place.

Figure 2.3 illustrates that the beam is still relatively uniform when defocused. On Z and on the Pecos target chamber, Z-Beamlet passes through a 3.2 m focusing lens at f/10. We operate experiments on the Conchas chamber at f/6.6, and this results in a corresponding change in the spot size with the same size DPP. The -3.5 mm defocal distance shown in figure 2.3 corresponds approximately with a -5 mm defocus that we frequently used. Chapter seven will give a similar beam spot image showing a 690 micron DPP spot defocused by -5 mm. In that configuration, we defocused the beam by 5 mm to give a

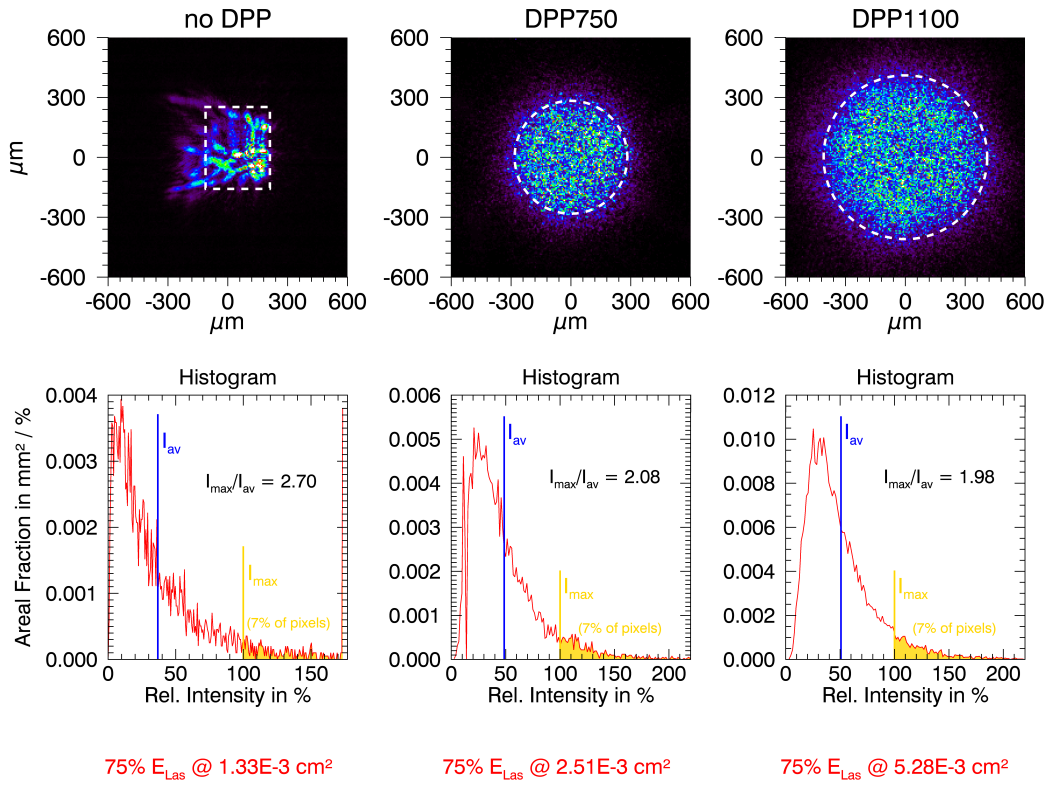

Figure 2.2: This figure from Matthias Geissel's 2018 Physics of Plasmas paper [20] explains what Beamlet's near field focal spots look like both with and without beam conditioning via a distributed phase plate (DPP) [21]. The 95% irradiance circle is also defined by an area, and the spot with in the near field is found to be very close to expected using the radius of that circle. Note that our experiments on the Conchas chamber used a 2 m lens, instead of the 3.2 m lens on Pecos for which these images are valid. We used a phase plate which gives a 690 micron diameter, which will be similar but smaller than the 750 micron shown here. We also later used a 940 micron spot, which again will be similar but smaller than the beam spot on the right with a width of 1100 microns.

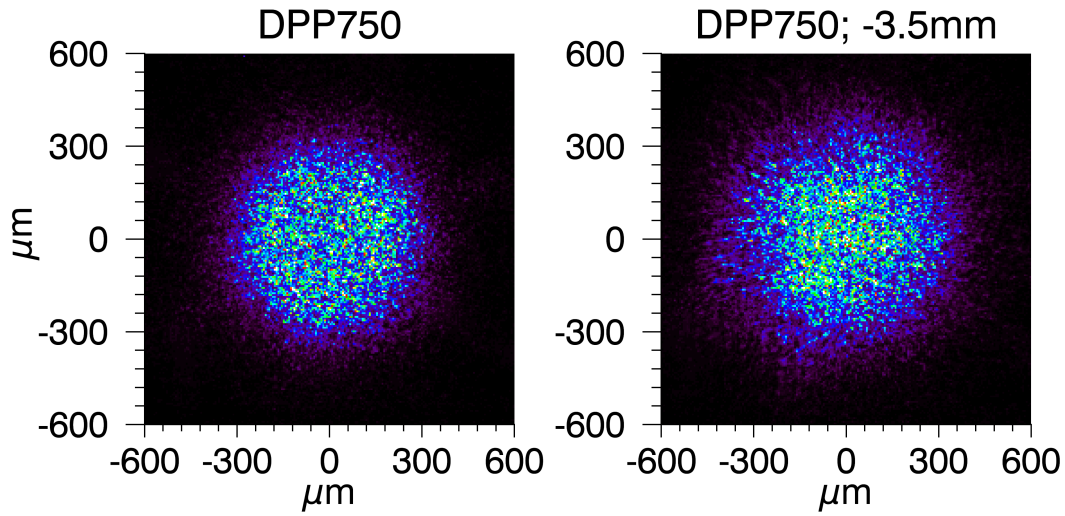

Figure 2.3: This compares the beam spot on Pecos with a 3.2 m lens both with and without defocusing [21]. These images are similar to what might be expected from the 690 DPP we used when defocused by -5 mm, but are obviously slightly larger in scale. For comparison, see figure 7.3. Notice that the beam becomes axially asymmetric as it is defocused.

round spot size of approximately 1 mm, which was asymmetric and measured about 950 microns by 1300 microns FWHM. Also, a series of older experiments were done with a phase plate that would give a 550 micron spot, but we defocused the beam to yield a 1 mm spot that preserved many of the near-field hot spot features and gradients in the beam intensity. These experiments are only represented in this dissertation by the blast wave data in chapter six, and unfortunately we do not have beam spot images for those cases. In all cases, the beam was focused to the smallest diameter in front of the target and was subsequently diverging when arriving at the LEW interface. There will

be significantly more details later about what laser conditions were relevant to specific experiments in future chapters.

2.1.2 Z-Beamlet Target Chambers and the Conchas Chamber

We re-purposed a previously existing target chamber for doing the experiments presented in this dissertation. ZBL currently supports a host of target chambers for conducting experiments in addition to providing support for the Z-facility. Since ZBL is not a user facility, shot opportunities depend on the Z facility schedule, along with availability of a number of other experiments that take priority. The experiments we conducted for this thesis occurred during brief windows of opportunity allotted for experimental capability development occurring on a several-shots-per-month basis.

ZBL supports experiments in three separate hexagonal target chambers called Pecos, Jemez, and Chama. The chambers and the supporting lasers are named after the rivers of New Mexico. The experiments we conducted for this work took place in a the Conchas chamber. This chamber is located very near the pulsed power machine for magnetic field delivery, and is cylindrical in shape. Conchas has a a hemispherical door and original round section for side and rear diagnostic access, as well as a longer-axis cylindrical volume to provide axial diagnostic viewports with 22 degree off-axial diagnostic access to the target. Conchas used to be known as the Calorimeter chamber, and Aaron Edens also used it for his blast wave experiments. Shane Speas moved the chamber to the 1305 laser support lab in May of 2015, and subsequently we

have worked to enable this chamber for B-field system development and gas cell experiments with shadowgraphy probe laser support, x-ray diagnostics, and gas cell target capabilities. Additional work that was required for the chamber included mounting target-beam alignment cameras, installing a PC work station on a moveable arm, and installing supporting electronic hardware such as scopes and delay generators. With safety documentation in place, the first laser shots into the Conchas chamber took place in fall of 2015. Around this time, Mark Kimmel had probe laser support available via the Gila laser system. The B-field system became operational in 2016 and the integrated system is fully operational as of 2017.

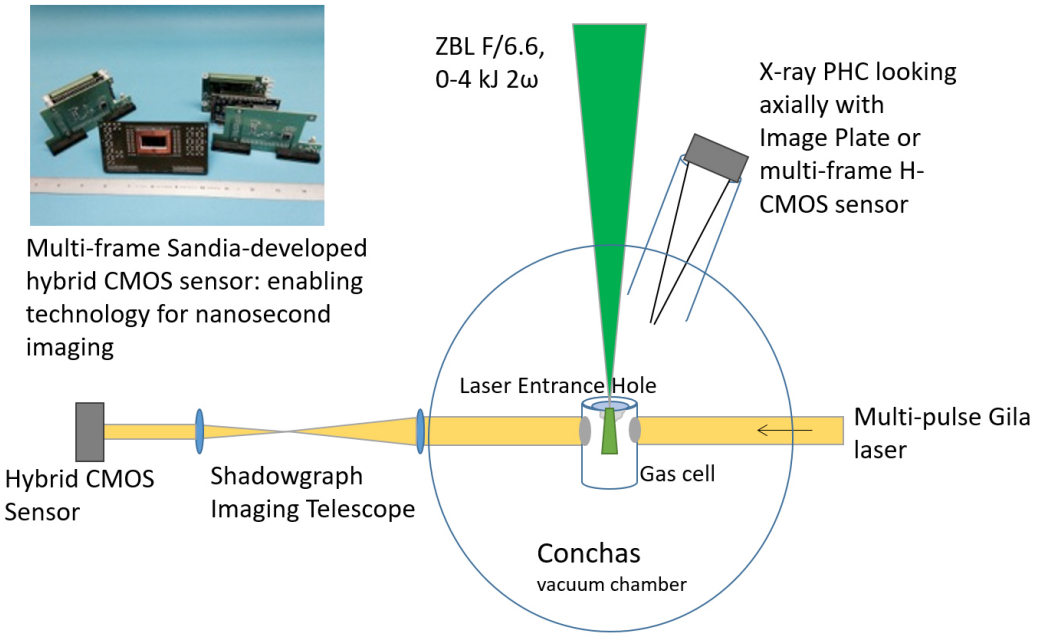

Figure 2.4: The Experimental Layout and Primary Diagnostics. We also field transverse x-ray pinholes which would effectively be looking into the page in this figure.

2.2 Gas Cell Targets and Pressure System

2.3 Gas Cells

We needed a way to store target gas in a surrogate, portable vessel similar to MagLIF. It needed an laser entrance window (LEW) that would be functionally the same as those on MagLIF targets. Like MagLIF the LEW needed to be a thin film at the end of the vessel to hold back the high pressure gas while the target is filled. The LEW needs to be accessible by the laser axially so it can be brought below critical density to permit heating the gas. Also, this gas-filled target, or gas cell, needed to have diagnostic access axially and from the side to image plasma transport after laser heating. We were fortunate to have Nathan Riley's gas cell designs from his work on magnetized blast waves on Texas Petawatt. Nathan created the gas cells to contain the low pressure xenon gas for his experiments and keep the gas away from the magnetic field coils. His original University of Texas gas cell designs had an open end so the gas could flow continuously. He later added an LEW similar to MagLIF. He also increased the scale of the gas cells so we could have diagnostic assess later in time once the laser-heated plasma had expanded further. We revised the gas cell design several times. Jeff Kellogg did most of the recent design work following Nathan's initial prototyping, with design revisions from John Porter, Matthias Geissel, and the author.

Changes included opening the area around the LEW to a 45 degree conical taper so the LEW region can be viewed with an open field of view on beam-target alignment cameras and potential x-ray diagnostics. These

targets have an laser entry hole (LEH) opening that can accommodate a thin polyimide or Mylar window of our choice. We also made the gas cell itself one piece, and added x-ray diagnostic port capabilities. These gas cells are also equipped with a copper field coil, with two turns in parallel. Diagnostic ports are between the turns of the coil.

We also needed a target with similarity to MagLIF in terms of electron density which we could fill with appropriate target gasses. We chose helium instead of deuterium as our surrogate target gas because it is non-flammable and easy to work with.

We had the acrylic gas cell parts fabricated at Backerworks manufacturing. More than half of the targets used in these experiments, and all of the recent ones in 2017, were professionally assembled and tested by Shaffer Manufacturing. Our optical-grade AR coated polycarbonate diagnostic windows were manufactured by Optical Filter Source LLC located in Austin, TX. We started off assembling the gas cells with cyanoacrylate superglue, but transitioned to epoxy for easier construction. We found it difficult to avoid leaks in the gas cell construction early on. Perfecting the process and fixing leakage-prone areas in the designs took some time, but eventually Shaffer Manufacturing in Albuquerque took over construction of the gas cells for Sandia.

2.3.1 Pressure Fill System

We needed a custom pressure fill system for our gas cells that would allow evacuation of the air from them and filling with the appropriate gas or

Figure 2.5: I assembled gas cells from raw parts from 2014 to 2016. 2 micron thick LEW and x-ray windows needed to be glued onto inserts and washers. We then attached these parts to the gas cell. Optical quality polycarbonate 1 inch windows came separately and needed to be glued on also. The hose barb connections for the fill lines are a stock part from McMaster-Carr company and needed to be glued on also. Pictured on the right is a completed gas cell target.

mixtures.

Measuring the gas cell pressure required judicious use of gauges. Since

we are using gasses other than air, we needed pressure gauges that worked with any type of gas. Certain gauges, such as Piranni gauges, will read different pressures for different types of gasses. We used an MKS 902B piezo-based absolute pressure transducer for measuring pressures in Torr less than a maximum of 1300 Torr or about 19.5 psi. All of our pressure measurements needed to be relative to vacuum so they we needed an "absolute" or "compound" scale. During the shot, helium would slowly diffuse out of the volume, possibly through the LEW. This created an error on shots even when the gas cell held pressure in ideal conditions without leaks. To help solve this problem and to make reliable on-shot pressure measurements for higher pressures, Matthias Geisel and I both implemented a pair of ProSense pressure transducers, one reading vacuum pressure ranges and 150 psi. I also implemented a Datachart 1250 data logger which saves a time history of the gas cell pressure on shot based on these transducers.

The filling procedure is relatively simple. Our pressure systems uses the vacuum system of the primary chamber to evacuate the gas cell and fill lines. Typically, the entire fill line and gas cell volume is open to the vacuum chamber until pressures in the gas cell and fill line drop to fractions of one Torr. Then, we close off the valve going to the chamber volume and allow the fill line to reach 10-20 psi of the desired gas. We can accommodate mixtures of two gasses also. Next, we use the needle valve to bleed pressure into the gas cell until it reached the appropriate pressure.

2.3.2 Gas Cell Types

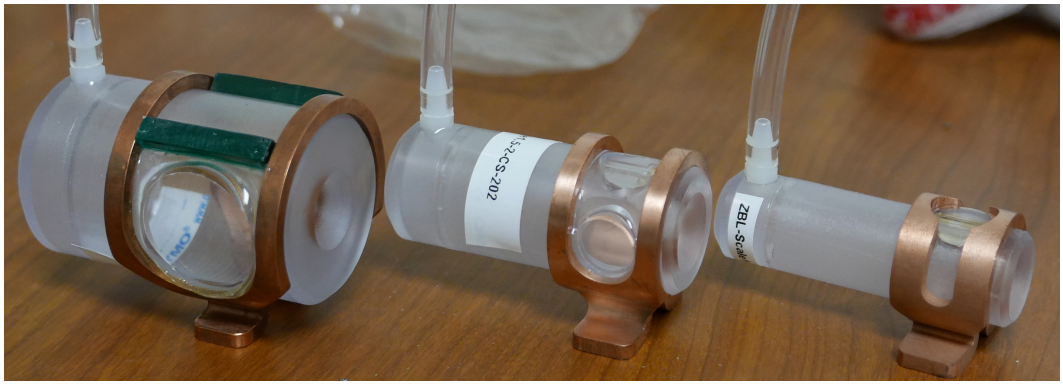

Figure 2.6: Three different gas cells, left to right are scale 2, scale 1.5, and scale 1. Each has different design motivations.

The types of gas cells used in these experiments include mainly three different scales. The original designs by Riley were "Scale 1" with an outer diameter of about 1.9 cm (0.75 inches) and an optical viewport on both sides, each with a visible diameter 1.27 cm (0.5 inches). Nathan used scale 1 gas cells to perform experiments on the Texas Petawatt Laser. For our purposes, the scale 1 gas cells have been heavily modified from his original design. Scale 1 gas cells have the smallest coil of all gas cell options, giving us the strongest magnetic field. However, these gas cells we have built now only have one viewport available. This means that scale 1 gas cells are really only useful with x-ray diagnostics, which are well suited to show the dynamics of the hottest plasma regions which are influenced by the magnetic field.

Nathan later created a design for a "scale 2" gas cell and again it has since evolved significantly with changes to the design made by Jeff Kellogg

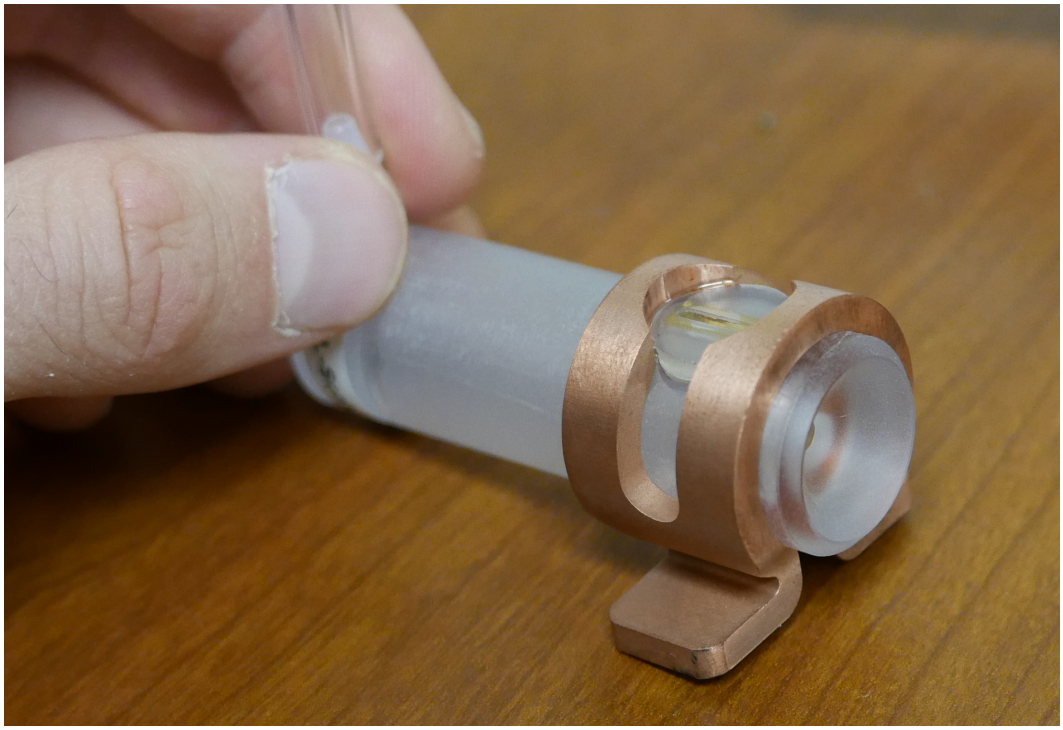

Figure 2.7: Scale 1 gas cell constructed by Shaffer, showing the x-ray side window. The x-ray window consists of a thin sheet of mylar or Kapton, usually 2 microns thick.

with suggestions from Matthias Geisel, John Porter, and I. These scale 2 gas cells have an outer diameter of 3.81 cm (1.5 inches) and accommodate a 2.54 cm (1 inch) optical flat viewport that is approximately 0.5 cm thick. The final and most recent design is a "Scale 1.5" gas cell with both x-ray window on top and a pair of 0.5 inches shadowgraphy viewports on the side, supporting both x-ray and shadowgraphy diagnostics on the same shot. Typically these days all of these coils are made with a supporting magnetic field coil structure, which may or may not be used on shot to generate a field. Originally I constructed

most of the gas cells we used in these experiments, but by 2017 we transitioned to having them professionally made by Shaffer. Major disadvantages of these gas cells are the lack of an x-ray side-view capability in conjunction with shadowgraphy, and also a limited maximum pressure they can hold. The weakest point for pressure containment on these targets was actually the flat faces of the shadowgraph optical windows, which tend to pop outward and develop pinhole leads. To help mitigate this problem, it was found that reinforcing the optical flat windows with thick layers of glue and plastic scaffolding in the coil gap helped to hold the windows in place and prevent leaks.

Each gas cell can either be equipped with a side-view optical flat window for transverse laser probe beams, or it can have a thin slit with 1 or 2 micron mylar x-ray thin windows. The slits are about 2 mm wide and 10-20 mm long, and can be oriented to view x-rays radially or axially. The side-view slits optimizes the data return from the gas cell in one dimension while still permitting us to have a high pressure gas behind the window. This is because the yield strength of a thin window with pressure behind it is determined by the greatest distance between supporting walls.

We may construct the LEW from any material we wish. The neon gas experiments used 1 micron thick mylar. All other experiments used 2 micron LEH windows, allowing us to hold a higher pressure in the gas cells so we could use helium in the range of 20-60 psi. The early gas cells in the helium series in 2016 used mylar LEH windows, while all subsequent experiments used 2 micron Kapton (polyimide). Kapton is also used in MagLIF targets on Z.

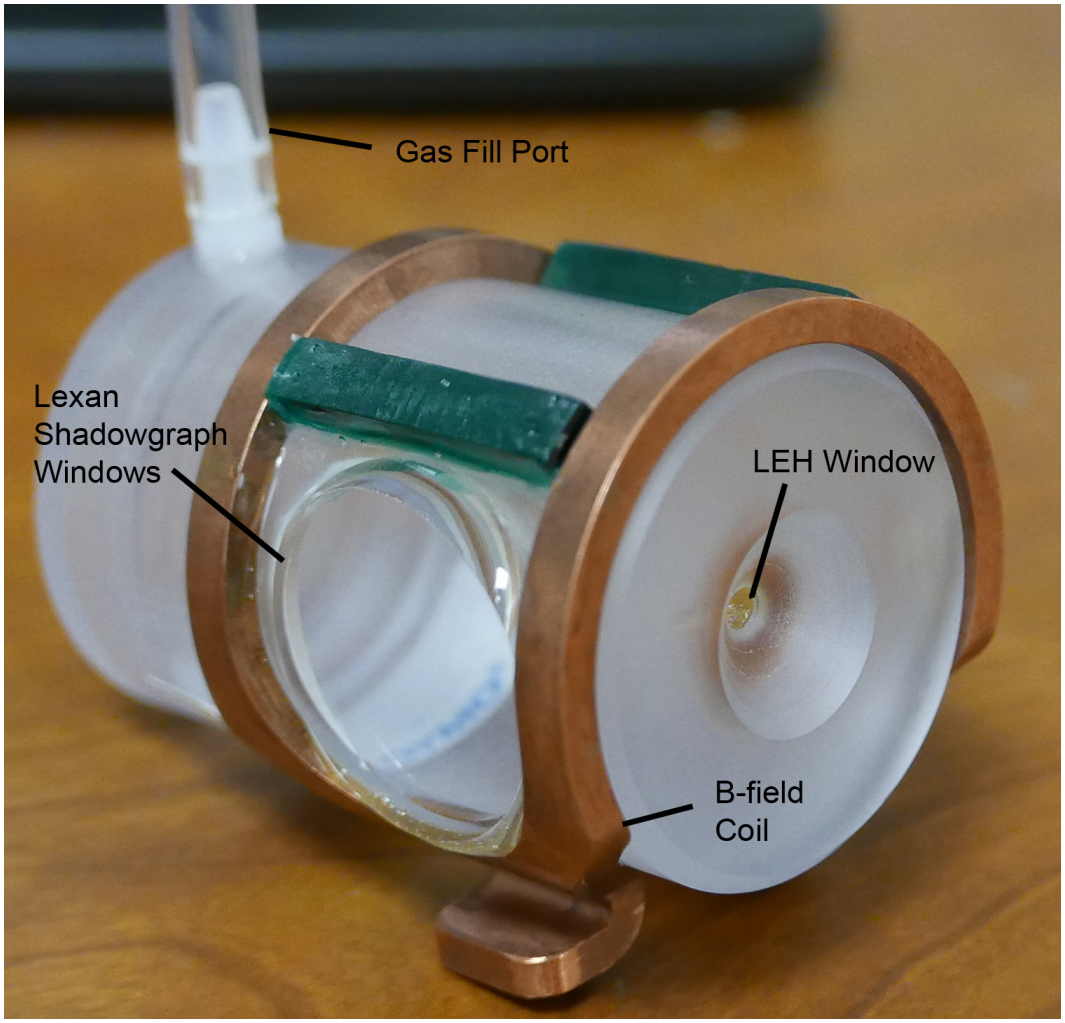

Figure 2.8: Scale 2 gas cells are larger in diameter and allow the greatest visible range for watching later-time blast wave dynamics.

2.4 Diagnostics

Our goal with these diagnostics was understand the plasma's total energy content in axial and radial dimensions. We could measure temperature with a 1D imaging Thompson scattering diagnostic across either the plasma

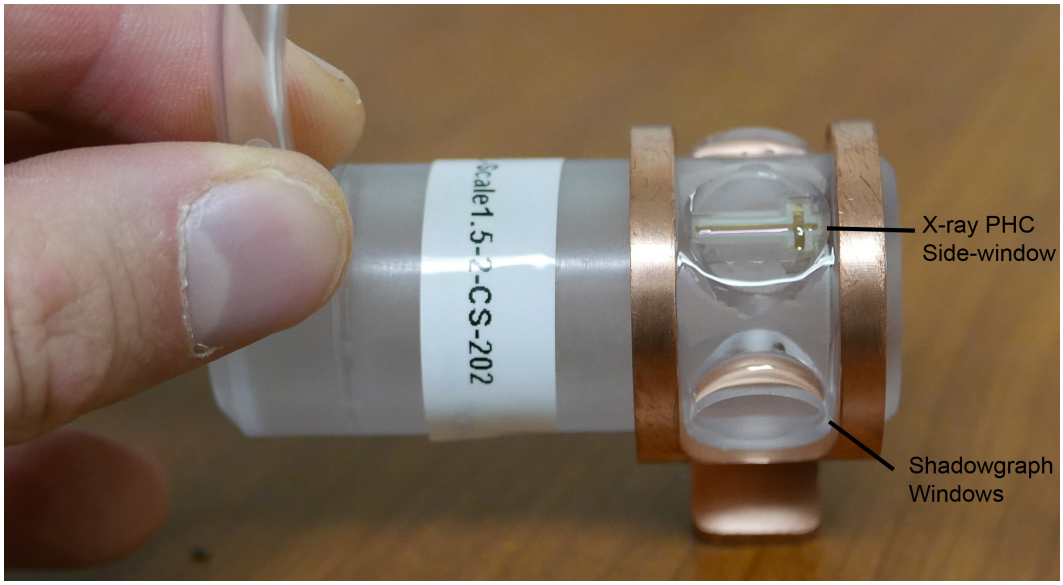

Figure 2.9: Scale 1.5 gas cells provide all the capabilities of both scale 1 and scale 2. However, they have reduced shadowgraph viewport size, which prohibits looking at long-timescale blast waves beyond about 60 ns.

radius, or the axial direction. Or a combination of x-ray spectroscopic techniques could also be used to measure temperature. Such diagnostics are usually limited to 1D imaging in order to capture temporal or spectral information. Instead, we used two primary 2D imaging diagnostics to explore the plasma size, trajectory, and electromagnetic emission. These were laser-backlit shadowgraphs and x-ray pinhole camera imaging. I will discuss the shadowgraph diagnostic in a separate chapter.

Diagnosing plasma transport using 2D imaging at specific time intervals gives a good understanding of the overall energy per unit length across the entire axial depth of the plasma rather than a 1D slice, as would be the case

for a streak camera. We also had photodiodes in place on some experiments to observe the time history of x-ray emission.

For these 2D imaging diagnostic applications and other HED physics diagnostics, John Porter has been overseeing the development a specialized x-ray and visible light sensor that can capture multiple-framed images limited only by the semiconductor switching timescale of a nanosecond [22]. These sensors take advantage of semiconductor hybridization technology to sandwich pixel memory storage components. They can thus store image data on multiple capacitors located within microns of the pixel array, minimizing the electronic transit time required for electronic imaging. This enables rapid read-off and storage of multiple frames of pixel data on the nanosecond timescale, as dictated by transistor switching times [22]. We used this sensor for both x-ray and visible light imaging.

2.4.1 Hybrid CMOS Sensor

For our imaging needs, we used a new semiconductor-based very high time resolution camera sensor that Sandia is developing. It can achieve nanosecond time-gating, which is more than twenty times faster than previous high speed digital cameras. Known generically as the hybrid CMOS sensor or the Ultrafast X-ray Imager (UXI), it was developed for use in high energy density experiments such as on Z and NIF, but it may have many other applications. These sensors are intended to image both x-rays but are also capable of visible light detection without a metal filter in place, and they could also be used for

charged particle radiation such as protons. Development has occurred entirely within SNL, with Sandian and Z-beamlet staff manager John Porter in a lead role in the sensor's development. The camera technology has not yet been published in a journal article to date, and our experiments are some of the first to use the prototype development sensors. So far there is one publication in an SPIE preceding [22].

The cameras combine CMOS photodiode detector arrays with semiconductor hybridization technology. Advances in semiconductor manufacturing have allowed printed semiconductor devices to by sandwiched or hybridized together. Ordinarily, a semiconductor detector array such as a CMOS or CCD sensor would have a large readout time. This is determined by the time it takes for the charge from the device to be switched with transistors and delivered to binary storage on capacitive memory. This time can be shortened significantly be sandwiching the capacitive memory behind the detector array. In this way multiple memory blocks can be stored directly behind the detector. The switching time, or inter-frame time, of the detector is then only limited by the transistors in the device, and can happen on nanosecond timescales.

I will give credit to a number of folks that have been involved in the development of these Hybrid CMOS detectors. John Porter and Larry Ruggles were both conceptual progenitors of the idea, which started as progressively more elaborate photodiode arrays. John Stahoviak has been principle developer of the printed circuit boards for the development models. Both John Stahoviak and Mark Kimmel, along with a masters student named Joel

Long have been the principle developers and testers of the device. The SNL 1700's semiconductor fabrication group including L. Claus, L. Fang, K. Ray, G. Robertson, M. Sanchez, and others.

Our primary H-CMOS cameras for most of these experiments are the Hippogryph models, which have a 1024x448 pixel resolution in 2-frame mode, or 512x448 pixel resolution in interlaced 4-frame mode. Interlaced mode allows neighboring pixels to capture separate timings, enabling up to four frames per camera sensor. The sensors have a pixel size of 25 microns. The Hippogryph models are capable of a minimum of 2 ns exposure times with corresponding 2 ns dead time.

We used two of these sensors combined with the Gila probe laser pulse trains for our 8-frame shadowgraph sequences. The sensor's internal oscillator that controls gate times is either controllable with pre-set digital exposure bins or tunable with an onboard potentiometer. The potentiometer allows custom inter-frame and gate times for such image sequences such as our 27 ns spaced 8-frame experiments. We set delays between the cameras with a Stanford DG535 trigger delay generator, allowing one camera to capture the first set of 4 probe pulses while the second acquires the final sequence, delayed by the appropriate amount.

2.4.2 X-ray Pinhole Camera

In addition to visible diagnostics, we fielded several x-ray pinhole cameras (PHC) looking both at the LEW and in some cases transversely to the

plasma, showing transverse profiles of x-ray emission. The time-resolving x-ray pinhole cameras allow us capture 2D images of the hottest plasma regions from their self-emission. These diagnostics were intended to give us a radial profile of the x-ray emission following laser heating, showing which regions were hot enough to emit x-rays via both bremsstrahlung in helium and neon and also line radiation in the case of neon. In order to see x-ray emission from the side, we needed a special x-ray port on the side of the gas cell that gave us either a transverse slit or an axial slit, showing us the radial x-ray emission profile or axial emission profile. Not all gas cell experiments had side-on x-ray diagnostics because the specific x-ray port on the gas cell was required.

Technical specs for the PHCs are as follows. On the Conchas chamber our PHCs were typically close to 1:1 magnification and about 1 meter away. Initially we used Image Plate (IP) detectors and later transitioned to hybrid CMOS ultrafast x-ray imagers (UXI) on transverse line of sight to the plasma. These x-ray PHCs also have a time-resolving capability with 4 or 8 frames, thanks to hybrid-CMOS sensors. The minimum gating timescale for these frames is about 2 nanoseconds. X-ray images are filtered by the cold helium along the transverse line of sight, as well as 2 microns of polyimide and 2 microns of mylar with 200 nm aluminum coating. We are able to use a pinhole array with different pinhole sizes to characterize different brightnesses. Unfortunately, the transverse PHC is limited by the thin-slit x-ray window in the side of the gas cell to either image a 2 mm wide swath looking radially, or looking axially, or in a T-shaped region transverse to the plasma. On the

Conchas chamber, the axial PHC perspective has a shallow angle of 22 degrees looking at the LEH where Beamlet strikes the thin window. We also had similar detectors looking at an odd angle from the LEH while we did experiments on the Pecos chamber, but that data is not presented here.

Low-Z target gasses such as helium or deuterium do not produce abundant bremsstrahlung x-ray photons for imaging, so we dope the target gas with between 5 and 30 Torr of neon, or about 0.1 to 0.5% by atomic fraction with 60 psi of helium. These neon ions emit significant soft x-ray photons that are visible in the detector through 200 nm aluminum filters. This is due to neon K-shell emission around 850 and 900 eV. These x-ray lines in neon begin to become important when the plasma approaches 100 eV in temperature and increase in strength fairly monotonically to about 400 eV, at which point power emitted in x-rays from neon becomes less temperature dependent. The x-ray emission radial profile was significantly narrower than the corresponding shadowgraphs, suggesting that in the neon plasma most of the heat was concentrated towards the center. We will discuss this in chapter eight. Appendix A describes how an image of x-ray emission at the detector can be inferred from a guessed plasma temperature distribution.

2.4.3 Time Resolving X-ray Diodes

The time history of x-ray emission can be captured on a photodiode with appropriate beam blocks and filters. On some of our experiments early on with neon, we used a photodiode to monitor the time history of x-ray

emission. We set up the photodiode along a line of sight to the LEW, at an angle of approximately 30 degrees from the z-axis along which ZBL propagates. The photodiodes we used are sensitive to soft x-rays and have sub-nanosecond time resolution. We used them to acquire k-shell x-ray emission time histories on neon gas cell experiments. In the data there is a clear overlap between the prepulse and main laser pulse. Following this, the x-ray signal falls off exponentially and rapidly. This may correspond to a drop in temperature of the neon plasma from both radiation and outward heat conduction. The threshold temperatures for k-shell emission in neon is around 300 eV.

2.5 Magnetic Field Driver

MagLIF's background seed field of 10 T (later 30 T) is likely to be important for the physics of laser preheating. To explore the effects of magnetic fields on thermal conductivity and blast wave transport, we needed to develop a magnetic field driver for use with our gas cell targets. Ideally, such a driver would have the capacity to go to higher fields in the future. Ultimately, we adapted a magnetic field driver that was already relatively versatile. It is presently operational to provide a pulsed magnetic field on microsecond timescales from a copper coil, with field intensities in the range of 7-15 T depending on the coil size.

Historically, the B-field system we used was originally constructed with SNL LDRD funding from Kenneth Struve. The LDRD was for a 100+ Tesla portable magnetic field system designed to support cluster fusion experiments

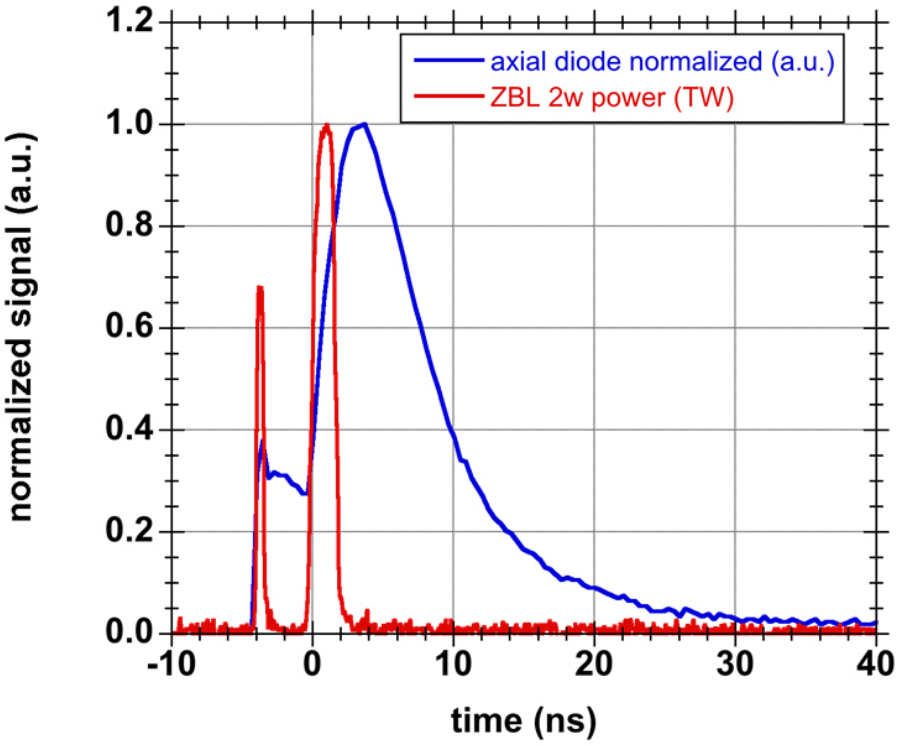

Figure 2.10: The x-ray photodiode traces describe a time history of x-ray emission from a neon gas cell's LEH region, looking at about a 20 degree angle from the z-axis. The gas cell pressure was approximately 300 Torr of neon. Emission likely comes from both the solid target LEH window and neon emission from several millimeters of optical depth of the heated neon in the gas cell.

at the University of Texas at Austin's Petawatt Laser Facility. Original designs were by Ken Struve, Brian Stoltzfus, and others. Matt Wisher, Stoltzfus, Caleb Waugh, and Sean Lewis were responsible for the construction of these

drivers before they were shipped to UT. There were two models developed, including an original development version with 2 capacitors and a later version that could accommodate up to 10 capacitors. Working with UT PIs Todd Ditmire and Roger Bengtson, Wisher and Lewis worked on the system at the University of Texas, demonstrating up to 65 Tesla operation in atmosphere. Nathan Riley and Matt Wisher worked on adapting the target chamber for superior vacuum performance, and ultimately conducted blast wave experiments in a magnetic field on the Texas Petawatt laser.

The B-field system's original construction and design is extensively documented in LDRD reports by Struve. There is also a master's thesis from Wisher on the first prototype version of the machine, and second master's thesis from Lewis describing the second prototype with magnetic field measurements. Wisher's PhD dissertation gives comprehensive detail regarding the engineering of the 10-capacitor version of the device. The full technical details are not relevant here. I will briefly describe the current system's technical capabilities, and the adaptations needed for implementing it on the Conchas chamber.

2.5.1 Description and Capabilities

The B-field system is essentially an RLC circuit. The energy storage comes from multiple 3.1 μF, 100 kV capacitors that operate in parallel. The system has an overall inductance of about 250 nH. Rise times are on the order of 1-2 μs and peak currents are about 100 kA per capacitor module at 50

kV. Each capacitor module is easily inserted and removed from the system by attaching a trigger cable, charging cable, and six discharge cables.

2.5.2 Coil Geometries and Expected fields

The maximum field the system can deliver will depend on the radius of the coil, with the field at the center closely approximated by the formula for the field in the center of a single-turn wire loop and uniform to less than 5%. I will show that here. Both sizes of coils have turns that wrap around the optical side-windows, which are themselves 66% of the diameter of the gas cells. A Helmholtz coil has a coil separation equal to the radius of the coils. In this case, the coil spacing is greater, about 1.6 times the radius of the coils. This means there is a central drop in field intensity between the coils as is the case with a "magnetic mirror" geometry. We will later quantify the size of this central drop in field intensity and hence characterize the uniformity of the field in the gas cells. And, of course, a coil twice as large in radius will give half the field, so our scale 2 coils have half the field at the center compared to scale 1. Outside the radius of the coil the field will fall off like $1/z^3$ along the z-axis.

We can derive the field at the center of the two coils by superposition, starting with the following formula for the field strength at a distance z from the center of a wire loop, originally derived from the Biot-Savart Law:

$$B_z = \frac{\mu_0 n I a^2}{2(a^2 + z^2)^{3/2}} \tag{2.1}$$

Here, z is the axial distance away from the center of the coil, μ_0 is the magnetic permeability of free space in SI units, and n is the number of coil turns. The variable a, like above, is the radius of the coil loops.

When there are two identical coil loops each with n turns, we can add these fields. If we choose the z-axis zero to be the centrally symmetric point between the coils, then the term from each coil has a coordinate offset a distance z_c from the center. The total distance between the coils is $2z_c$. For our single-turn, two parallel loops the total field becomes

$$B_z = \frac{\mu_0 I/2a^2}{2\left(a^2+(z_c-z)^2\right)^{3/2}+2\left(a^2+(z_c+z)^2\right)^{3/2}} \tag{2.2}$$

In the above equation, I is the total current in both loops, that is the sum of both loops in parallel, as is the case on our gas cell coils. Typically we consider total current delivered to the whole coil, so this variable makes more sense as the expected output of our pulsed power system.

For n=1 and z_c equal to about $1.6 * a$ as is the case with scale-2 coil geometry, the we expect that the field dips in the center by approximately 3%. So, to a good approximation, the field between the coils is roughly uniform. With the coil geometry as it is, the field at the peak field at the enter is well approximated by $B = 0.6\frac{\mu_0 I}{2r}$ where I is the total current delivered to both coil turns in parallel. The central drop in the field should be less than 5% for both of our coil geometries. More discussion about the details of current distributions and a measurement of the field as a function of z is included in

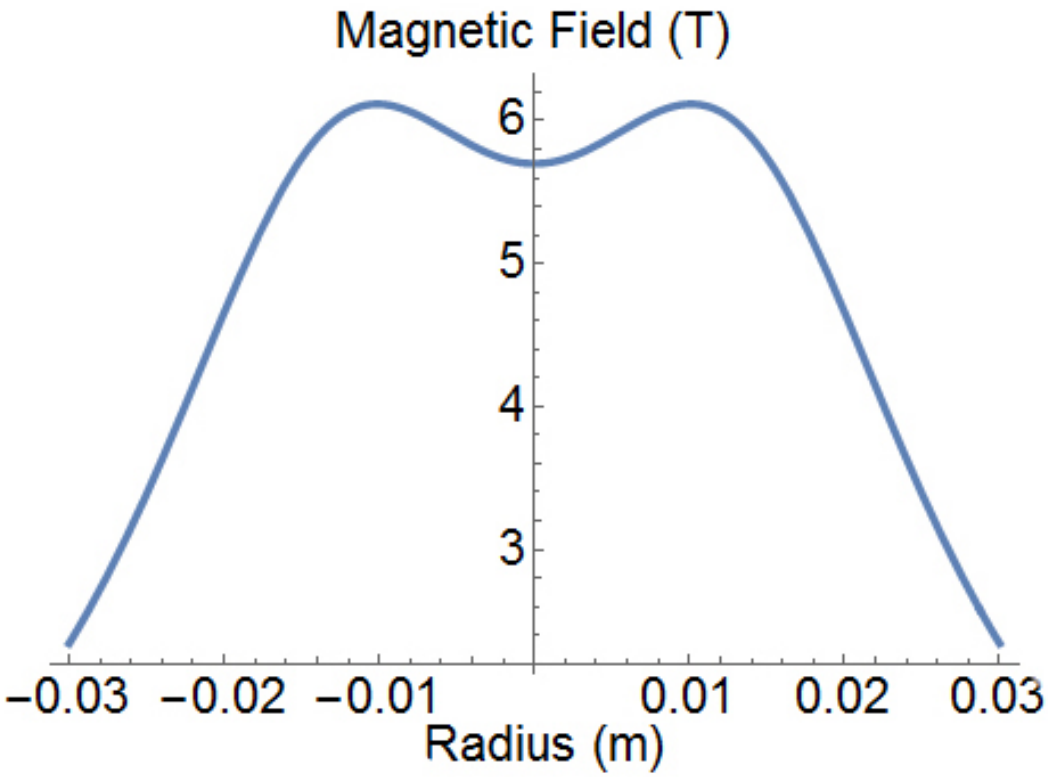

Figure 2.11: This shows a simple analytical model of the expected z-component of magnetic field on axis in a scale 2 coil at 300 kA. The coil spacing is equal to the space between the maxima.

the author's masters thesis. What follows is a plot of the analytical 2-loop coil model above for 300 kA total current. This is the current expected from 3 capacitor modules at around 50 kV and seems to be our present operating limit as of this writing. The same current should achieve about 12 T in our scale 1 geometry.

2.5.3 B-field driver Implementation on Conchas Chamber

We needed to implement several adaptations to the magnetic field driver for gas cell experiments. Primarily, we needed a new way to deliver current to target chamber center, where the gas cells and surrounding field coils would be located. This also necessarily includes a way to adapt the cables from the capacitor modules to a new transmission line. The first version of the design we settled on included a round parallel plate transmission line that cables plugged into. A coaxial transmission line delivers current to target chamber center through a 10 inch Conflat vacuum port available in both Conchas and Pecos chambers. A schematic diagram is included.

We ultimately built a version of the feedthrough transmission line that includes cable attachments for up to 6 capacitor modules. If it had worked as intended, we could be able to reach peak currents at the coils in excess of 600 kA at 50 kV. This would have been sufficient for 24 T fields in scale 1 coils and 12 T in scale 2.

B-field driver development work continued into and beyond fall of 2016. We have had trouble triggering the system synchronously. This prompted as re-design of the trigger system in early summer of 2016. The redesigned trigger system uses a new master switch capacitor that stores more charge than the cables themselves did in the previous trigger system. This adds significant current to the spark that triggers the primary capacitor switches. The new system also doubles the trigger voltage swing. This solved the problems with asynchronous and low-reliability triggering, but once this was resolved several

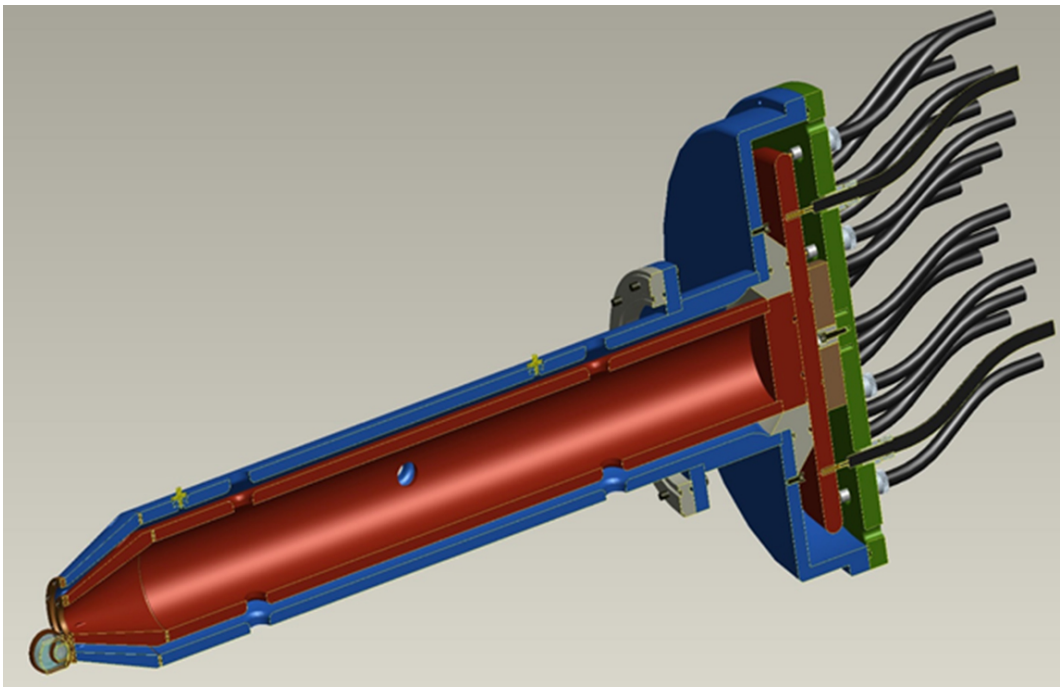

Figure 2.12: This is the pulse power feedthrough currently operational on the Conchas Chamber. 3D rendering from design by Jeffery Kellogg.

issues arose with arcing in the coaxial chamber pulsed power feed. Unfortunately, due to this arcing issues, our peak current is about 300 kA to the coil, which delivers about 6-7 T to scale 2 and 12 T to scale 1 coils.

2.6 MagLIF Similarities and Differences with Experimental Setup

This thesis is focused on plasma heating and and dynamics in the fuel conditioning phase of MagLIF, prior to implosion and following laser heating. We will attempt to understand 2ω laser heating of a helium plasma column in a system that is similar to MagLIF. Our experiments were carried out in

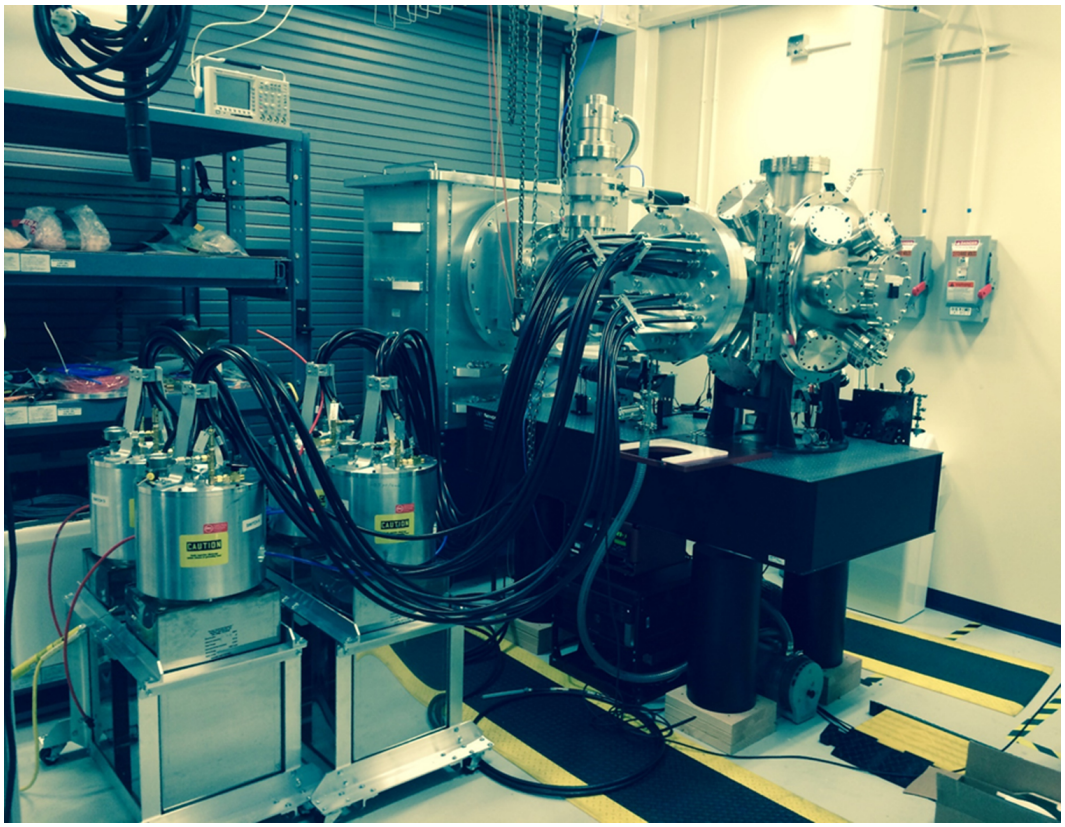

Figure 2.13: This picture shows the Conchas chamber with attached pulsed power feed and pulsed power capacitor modules.

a background gas with electron densities from 10^{20} cm^{-3} to $3 * 10^{21}$ cm^{-3}, where the 2ω critical density is about $4 * 10^{21}$ cm^{-3}. This corresponds to an initial room temperature pressure of 30 to 90 psi for helium and deuterium, assuming helium is fully stripped. For both gasses this is a mass density of 0.67 mg cm^{-3} at 60 psi initial pressure and electron densities of $2 * 10^{20}$ cm^{-3}. This will be our standard operating point for this paper, and it corresponds to an operating density of 5% of critical density at 527 nm.

Functionally, one big difference between the experiments presented here and those of MagLIF is the use of helium rather than deuterium gas. Although we mentioned before that the regime of electron density is the same, the higher Z=2 contributes to a more strongly radiative behavior.

In our experiments we were able to apply an external magnetic field of up to about 15 T, which mimicked the seed field used in MagLIF. Notably, our experiments were carried out in a plastic gas cell which of course has no metal liner wall for the expanding plasma's magnetic field to interact with. The field shape is also different from MagLIF since the coils are smaller and not in a Helmholtz configuration, as will be discussed in chapter two. The coils are far enough away so that we do not expect any change in dynamics from flux compression between the expanding heated plasma and the coils themselves. Despite these differences, we are able to explore the influence that a magnetic field has on plasma heating during the main heating pulse, and conclude that its affect is measurable and significant. In particular, we will see that the plasma column becomes narrower and longer, as well as hotter

and more axially uniform.

Chapter 3

The Shadowgraphy Diagnostic

This chapter describes this work's most frequently used diagnostic, which captures images of the expanding plasma with visible light during and after laser heating. The shadowgraph diagnostic images the plasma using a 532 nm visible light laser pulse passing through the cylindrical plasma from the side. This laser backlighting imaging system captures 2D images of plasma dynamic evolution with sub-nanosecond resolution on 10's of nanosecond timescales.There is an imaging telescope, and it is imaged onto the hybrid CMOS sensors described in chapter two. The combination of time-gated imaging and sub-nanosecond probe laser pulses allows imaging these laser plasmas as they expand at 100 km/s speeds. Here we will describe the laser which produces the temporal picket-fence pulse train, called Gila. We will also describe the optical setup of the diagnostic.

The bulk of the chapter is about the physics of the diagnostic. The shadowgram images show the outer periphery of the ionized plasma. X-ray pinhole cameras image the entire plasma via self-emission. The x-ray images tell us where the highest temperature and density x-ray emitting plasmas are, but the shadowgraphs are very sensitive to small amounts of ionization

even at low temperatures. So, shadowgrams will show us exactly where the cold gas begins to become ionized. This chapter will include calculations on what geometries will cause the probe beam to be scattered, and under what conditions the laser-heated plasmas will be transparent or opaque to the probe beam, for example via collisional laser absorption. Further understanding of why the hot, x-ray emitting regions of the plasma are narrower than the edge seen in shadowgraphs will have to wait for chapter four, which describes thermal conduction and transport.

3.1 Shadowgraphy Optical Setup

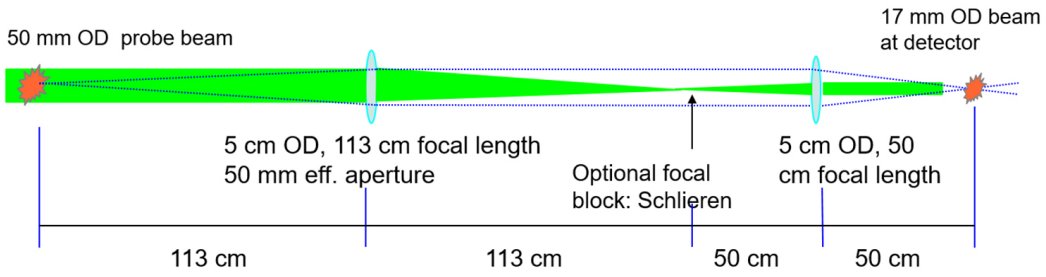

Figure 3.1: A Schematic diagram of our shadowgraphy imaging telescope, showing geometries and focal lengths.

The shadowgraphy diagnostic uses a multi-pulse 532 nm probe laser (described in then next section) that passes transversely through the plasma. It images the plasma with a telescope. Imaging lenses are positioned to image the plasma to a focal plane on the Hybrid CMOS sensors. We use a primary objective lens with a 1.13 m focal length and 5 cm diameter located such that the target plasma is 1.13 m from the optic. This gives us a high f/# of

$113/5 = 23$. The high f/# gives high sensitivity to small changes in refractive index, since it does not take much of a change in angle to scatter the probe beam out of the objective lens. The high f/# also delivers a good focal depth of field for sharp imaging. The telescope's secondary second lens has a 50 cm focal length and 5 cm diameter. So, our telescope has a demagnification of $50/113 = 0.442$, which is ideal for capturing our 2.54 cm diameter gas cell diagnostic windows on our 1.12 cm wide H-CMOS camera sensor. We imaged a spatial resolution of 60 microns on the target, with this imaging setup, which is limited by the 25 micron pixel size of H-CMOS sensor. The theoretical resolution of the imaging telescope would be 15 microns. By changing the lenses we might go to a magnification closer to 1:1, which would make the image on the sensor larger and bring the smallest visible resolution of the target plasma from 60 microns to 30 microns, or close to the sensor's limit of 25 microns per pixel. This is a possible improvement for the future.

Shadowgraph imaging is similar to Schleiren imaging, in the sense that both methods are very sensitive to changes in refractive index. Schlieren imaging uses a physical obstruction such as a thin wire or sharp edge to block the zeroth order Fourier component in the near field of the imaging telescope. Including only higher order changes in the image enhances edges and removes backgrounds, so it improves the image contrast by emphasizing changes in refractive index and darkening flat backgrounds. The shadowgraph setup converts to "Schlieren mode" by inserting very thin beam block at the focal point of the telescope. However, we have found that our shadowgraphs are already

quite sensitive without subtracting uniform backgrounds so we generally do not operate in Schleiren mode.

3.2 Multi-Frame Techniques

Several innovations were required to capture multiple 2D time-gated images per shot. SNL's Z-Beamlet group has been developing these techniques for several years, and I can take very little credit for them. Some of the inspiration came from Aaron Edens' work in blast waves. Aaron wanted to be able to capture multiple frames of expanding blast waves per shot, but the capability did not exist at that time. Over time, John Porter led a campaign in Sandia's semiconductor fabrication group to develop a highly sophisticated multiple-frame CMOS detector with nanosecond gate times. Simultaneously, Mark Kimmel developed an Nd:YAG laser front-end architecture that allowed us to deliver transverse probe pulse trains with 300 ps duration and up to 8 pulses with adjustable spacing. The time-gating of the H-CMOS sensor by itself is in the range of 2 ns, so by itself this technology would show some plasma motion blur. The short-duration probe laser ensures that the images are sharp, and the sensor's time-gating ensures that only a single probe pulse is captured per image frame.

3.2.1 Chaco and Gila Probe Lasers

Mark Kimmel constructed the probe lasers that we used. The laser systems called Gila and Chaco are two separate systems which supply shad-

owgraphy probe beams. We primarily used the Gila laser delivered to the Conchas chamber for the experiments described in this document. Chaco includes additional glass amplifiers for delivering higher beam powers, while Gila is essentially a regenerative amplifier loop with a maximum energy per pulse of about a millijoule. Even a millijoule is plenty for the H-CMOS sensors, and usually several neutral density filters are stacked for an attenuation factor of about 50. Physically, Gila is oriented on a separate table from the Conchas target chamber. We periscope the beam overhead and send it down vertically through Conchas, and the shadowgraphy diagnostic ports are oriented vertically [19].

We run our Gila probe pulses with frequency-doubled second harmonic green light at 532 nm following a KDP crystal right outside the regenerative amplifier. In order to distinguish between the stray light from Z-beamlet and the probe beam light, we stack two 532 nm interference filters with 6 nm bandwidth. This gives a factor of 10^6 attenuation of the 527 nm ZBL light.

Timing of Gila's first pulse has to be synchronized with the experiment. So, Gila includes a master oscillator that is synchronized with Z-beamlet through a 0.2 Hz clock signal and appropriate delays. This ensures that our probe pulses arrive at the correct times relative to Z-beamlet, which creates the plasma we are probing. However, additional trigger timing steps were required which essentially involves removing an inhibit for triggering sensors and other important experimental hardware when Beamlet actually fires. These timings are controlled with a series of Stanford Research Systems DG535 and DG645

units, which are also optionally controllable via NI Labview software. This determines the relative timing of the first pulse in the multi-pulse sequence.

The pulse train's timing is also customizable. Mark's design includes an AWG (arbitrary waveform generator) on Gila, which allows customizable pulse trains inside a 10 ns window. This allows us to send out up to 4 pulses with a spacing of 2.5 nanoseconds maximum. Following seeding with the AWG and master oscillator, Gila's architecture is mostly just a regenerative amplifier cavity, with an optical travel time of about 13 ns. The 1064 nm ND:YAG rod is multi-passed until a Pockels cell allows the light out. Careful timing of the Pockels cell gating permits kicking out two successive pulses whose spacing is set by the regenerative amplifier's round-trip time of about 13 ns. Mark can also program the Pockels cell opening times to send out more than one pulse with a delay of four times the round trip time, giving an inter-pulse timing of 52 ns nanoseconds.

We can effectively double the number of pulses from Gila by using a polarization-based optical delay leg. Mark has set up a waveplate to rotate the polarization of the beam, and following this is a polarized beam-splitter. A properly rotated linearly polarized beam is evenly split into component polarizations. One beamline goes through an arbitrary optical delay that is set by bounces between mirrors. The beams are then recombined into the same beam path, with separate optical travel times.

Combining these delay methods allows us to create pulse trains in many different modes. Originally there were three configurations for timing between

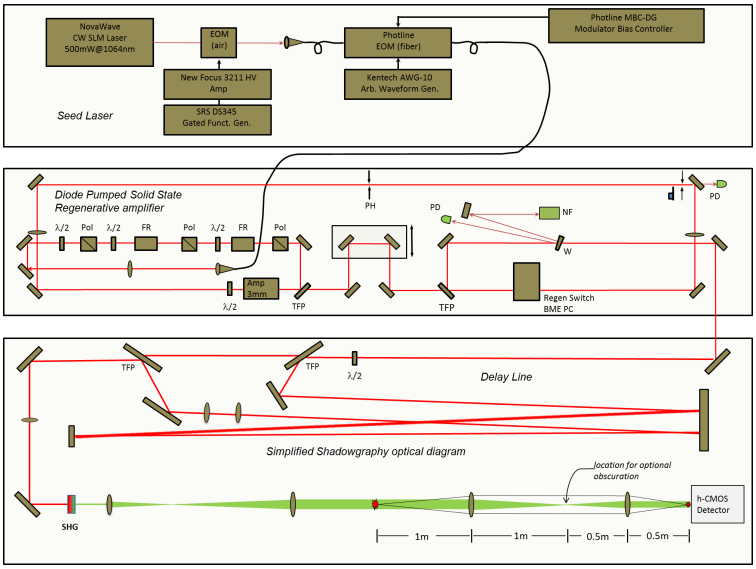

Figure 3.2: The shadowgraphy probe beam is generated by the Gila laser system, with regenerative amplifier, time-of-flight optical delay leg, and shadowgraphy telescope optics imaging the plasma. Original diagram courtesy of Mark Kimmel at Sandia National Laboratories [23].

pulses. The 13 ns regenerative amplifier timing originally allowed us to send 4 pulses with a 13 ns spacing, but we found only four pulses to be less useful. We can also send up to 4 pulses with a 2 ns spacing from the AWG, then optical delays of 8 ns allow us to send another for pulses for 8 total pulses with 2 ns spacing over 16 ns. To get 8 pulses spaced 26 ns apart, we can use an optical delay of 26 nanoseconds with polarization and a delay leg. This is combined with four-pulse output from the regenerative amplifier spaced 52 nanoseconds apart. These outputs from the regenerative amplifier must be carefully controlled via adjusting time-dependent voltage on a Pockels Cell to equilibrate pulse amplitudes.

Later, during fall of 2017, Mark implemented a new AWG an with increased time duration for up to 40 ns of waveform control. He also doubled the cycle time of the regenerative amplifier cycle to about 27 ns. This allows flexibility to generate arbitrary multi-pulse probes within this time window. With the optical delay segment, this AWG time sequence can be doubled. Once Mark implemented these changes, we were not limited to the three above timing sequences. So, afterward we frequently did experiments with 3, 6, and 6 ns spacing between probe pulses.

3.3 Shadowgraphy Example Results

3.3.1 Shadowgraphy in Helium

The time spacing between image frames in our experiments came in two regimes: long time-scale and short time-scale. We used a shadowgram

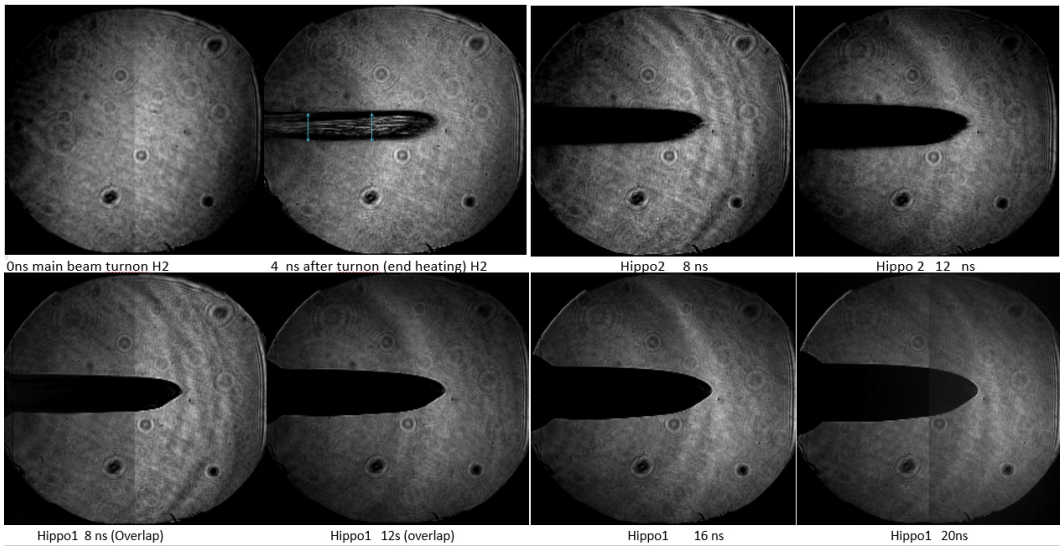

Figure 3.3: Shadowgraph image sequence from two Hippogryph cameras with 2 nanosecond separation between frames. The entire sequence spans 16 ns. We use this timescale to explore short time sound speed expansion and infer a temperature and energy density.

frame time spacing of 27 ns covering almost 200 ns to understand the plasma in a blast wave transport phase once the classical adiabatic blast wave regime came into effect. Short-timescale plasmas informed us about the sound speed expansion of the plasma, with inter-frame times between 2 and 6 ns. Each of these regimes will be described in future chapters concerning blast waves and sound speed transport, respectively. Figures 3.3 and 3.4 are example shadowgrams from both timescale regimes, showing what the sound wave and blast wave image sequences look like.

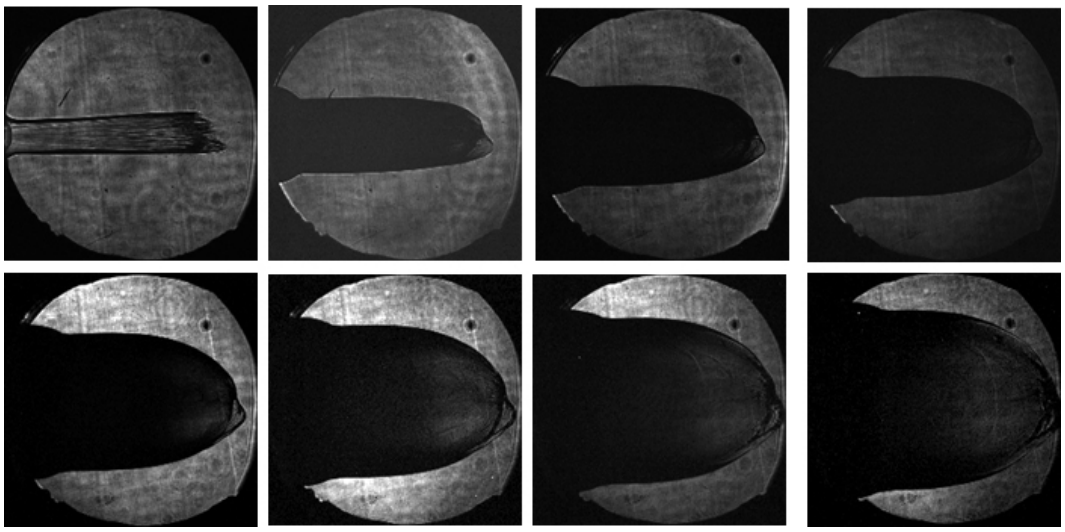

Figure 3.4: Shadowgraph image sequence from two Hippogryph cameras with 27 nanosecond separation between frames. The entire sequence spans 189 ns. We use this timescale to explore blast wave dynamics and from that extract energy per unit length.

3.4 Physical Meaning of Shadowgrams

This section describes two physical meanings of the dark regions representing the plasma in the shadowgrams. The shadowgraph diagnostic works somewhat differently from conventional imaging via backlight, which is concerned with imaging the dark shadows of opaque objects. That is because our diagnostic is sensitive not only to light absorption from plasma opacity, but also to refraction of the probe beam out of the collection optic. However, probe beam absorption via inverse bremsstrahlung does play an important role, particularly at higher densities.

3.4.1 Probe Beam Absorption in Shadowgraphy

The most dominant absorption mechanism that increases opacity to the probe beam in shadowgrams is probably collisional absorption, also called inverse bremmstrahlung. However, other absorption mechanisms may also play a less dominant roll in causing the "shadow" that we see. These could be stimulated Brillouin scattering (SBS), stimulated Raman scattering (SRS), and possibly other nonlinear scattering processes. The probe beam photon energy and the laser intensity is insufficient to ionize the surrounding cold helium gas, and this laser wavelength does not fall on any major helium spectral lines. The laser is not interacting with the plasma or cold gas bound-free or bound-bound radiative atomic absorption processes. The multi-photon absorption cross section is also quite small.

We are left with a fairly high collisional absorption cross section, particularly if the plasma is less than about 30 eV in electron temperature. Using formulas and calculations that we will describe in a future chapter, we see the collisional absorption mean free path is relatively short for green light. The mean free path is much smaller than the plasma width above some threshold density and below a plasma temperature around 600 eV. Figure 3.5 illustrates that our plasmas will be opaque to the transverse probe beam for all but the lower density ranges corresponding to initial helium pressure less than 20 psi, except when temperatures are very uniformly high in the plasma.

High-temperature transparency should only persist while the plasma is extremely hot. We can use partially transparent shadowgraphs to put a lower

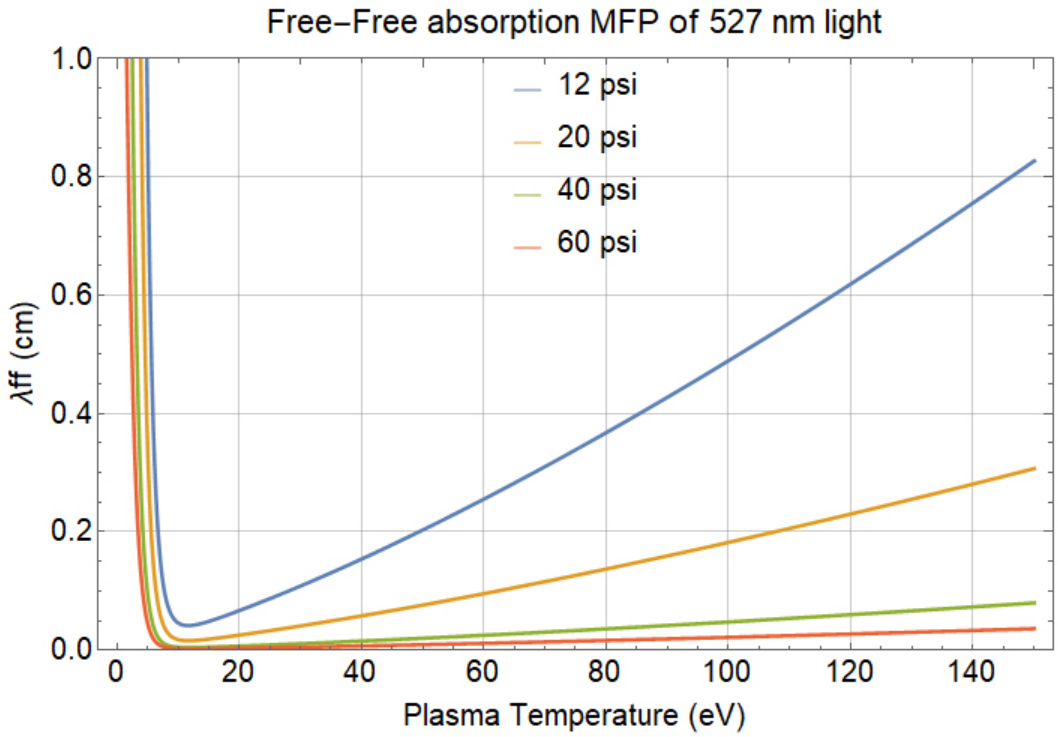

Figure 3.5: Calculations on the free-free (inverse bremsstrahlung of collisional absorption) photon absorption or mean free path in our plasma, which take into account a temperature-dependent ionization state, show that our plasmas are opaque at 527 nm for all but the hottest plasmas and lowest densities in our experimental range. The long mean free path at very low temperatures is from finite ionization, which I included in the model because it affects electron density. Other radiative absorption processes become important at those temperatures, such as line radiation and photoionization, but these are not relevant to this figure.

bound on the plasma temperature. A higher-density plasma that is transparent to the probe beam will provide a higher lower bound on the temperature. In the case of our 12 psi fill pressure helium experiments, we can say the plasma is at least 70 eV. The shadowgram from that experiment is shown in figure 3.6.

We have also observed plasma with 20 psi fill that is transparent to the probe laser within a nanosecond of the main heating beam turnoff. Higher pressure gives a stronger constraint and this tells us this helium plasma formed from 20 psi helium must be above 140 eV to have a free-free absorption mean free path that is longer than the plasma dimensions. Finally, some shadowgrams on gas cell experiments with 60 psi helium fill pressure showed partial transparency of the probe beam through the central half of the cylindrical plasma. In order for this plasma with an electron density of $2 * 10^{20}\ cm^{-3}$ to be transparent to collisional absorption of 532 nm light over its 3 mm depth, it must have a temperature greater than 600 eV! This experiment was done with a magnetic field and the implications will be described in chapter nine.

The helium plasma shadowgrams generally show a sharp edge, defined by the boundary where the cold background gas begins to become ionized. A thermal wave precursor with diffusive radiative heat conduction that is strongly nonlinear with temperature will cause the narrow ionization front at the end of the plasma. Once hydrodynamics are relevant after the plasma radius has doubled, we might expect this diffusive thermal wave to lead out in front of the developing hydrodynamic shock. Once the blast wave dynamics dominate, we can expect a factor of four increase in electron density at the shock front of a blast wave, as we shall prove in the chapter concerning blast waves. Once the plasma has expanded to form a blast wave there will have been a substantial temperature drop, which guarantees the plasma will be opaque via collisional absorption. This guarantees that later-time plasmas are

going to appear dark in shadowgrams. Also, in plasmas of higher Z such as neon, the plasma edge is much more poorly defined due to radiative ionization from long mean free path radiation, which ionizes cold gas beyond the edge of thermal waves and blast waves.

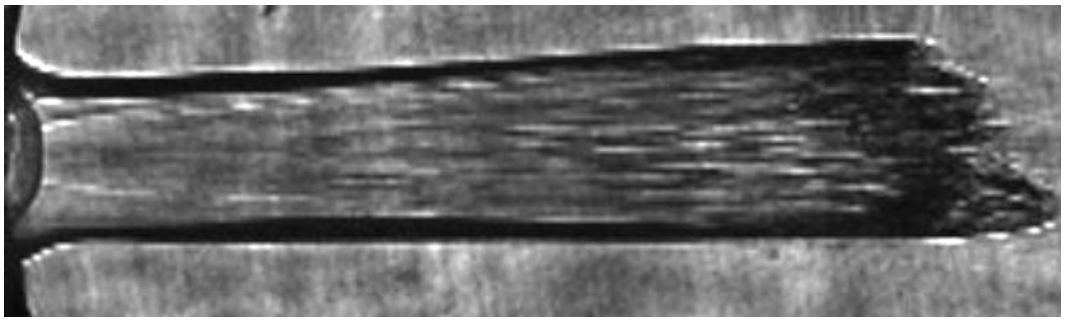

Figure 3.6: This is the first frame of a shadowgram sequence showing a laser heated helium plasma during laser heating. The fill pressure was 12 psi. The image is captured near the very end of the 3.5 ns laser heating pulse. Internal structure is visible in the image which may be filamentation, as well as a limb-darkening effect from refraction. A blast wave is also forming in the laser entry region on the left. The plasma is transparent because of the lower electron density, which allows the probe beam's collisional absorption mean free path to be longer than the plasma length scale.

3.4.2 Probe Beam Refraction and Scattering in Shadowgraphs

In this section, we will quantify the strength of the refractive properties of the plasmas we will encounter. In our data, this becomes important when we have plasmas that are partially transparent, which only occurs in certain circumstances. By quantifying the scattering angle we expect in our diagnostic, we can describe the regimes in which these different effects are important for inferring physical behavior of our plasmas. The shadowgraph diagnostic is

extremely sensitive to small variations in plasma refractive index because of the high f/# of the collection lens, so we can also use it to place weak bounds on the density variations in the plasma in the cases in which the plasma is partially transparent, such as in figure 3.6.

The refractive index scales like the square root of electron density up to an index of unity at the plasma critical density. Plasma refractive index is given by:

$$n_1 = \sqrt{1 - \frac{n_e}{n_c}} = \sqrt{1 - \left(\frac{\omega_{laser}}{\omega_p}\right)^2} \tag{3.1}$$

Thus the shadowgraphy diagnostic is sensitive to a very slight small increases in electron density due to ionization, and is likely sensitive to partial ionization even around 2 eV in helium. The plasma edge in shadowgrams is a sharp ionization boundary at the front of a precursor thermal wave. Thermal waves created by nonlinearly temperature-dependent conductivity produce very sharp temperature gradients at their boundaries, as we shall see in chapter four.

The plasma is shaped like a cylindrical lens along the transverse line of sight of the laser. Unlike conventional materials like glass which would focus light as a cylindrical lens, plasmas acts like diverging lenses because the plasma has a refractive index lower than one. This diverging lens can be strong enough scatter the incident probe beam laser out of the collective area of the objective lens if the electron density is high enough and the geometry

of glancing angles is correct. The primary objective's collection angle for light is a cone with a 1.27 degree half-angle. This angle in degrees is given by $\frac{180}{\pi} ArcTan(0.025/1.13)$ where the laser aperture diameter is in the numerator and the objective lens focal length is in the denominator. This means that if the plasma refracts the probe beam outward by more than 1.3 degrees it will not be visible to the diagnostic.

We can calculate the drop in refractive index that would refract the

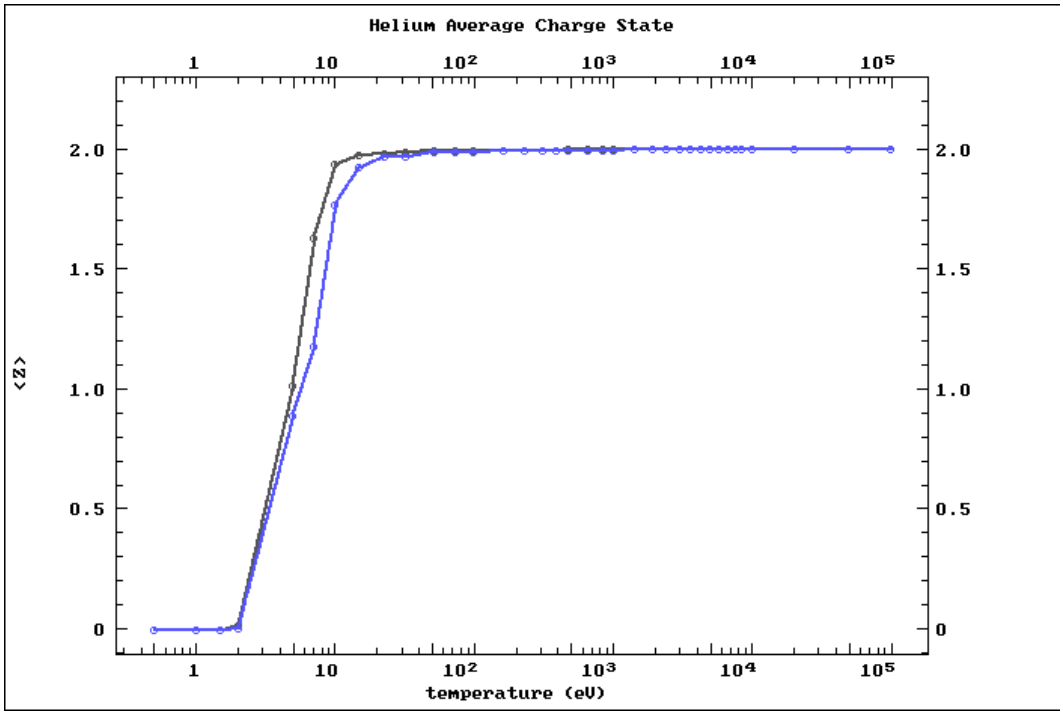

Figure 3.7: This illustration, which is an interpolated plot from experimental data, shows the ionization state of helium as a function of the plasma's electron temperature. The two plots are for ion number densities of 10^{19} and 10^{20} cm^{-3}, showing that there is not a significant difference. There is a sharp rise in helium ionization from 2 to 10 eV [24].

beam and generate the sharp edge in the shadowgraph images. However mathematically this is a little tricky because of the geometry of glancing angles. We cannot use the thin lens approximation formulas which make use of a first order linear approximation of sine. The steeper angles on the periphery of the cylindrical plasma cause more substantial beam refraction. It is notable that at lower densities, light still passes through the center of the plasma in shadowgraph images, but with significant distortion as visible in figure 3.6. So, we expect a much stronger effect in the edges of the plasma, where the probe laser's incident angle relative to the plasma surface's normal vector is larger.

We can calculate the refracted angle using Snell's Law and geometry. For our first calculation, we will assume a uniform electron density within the

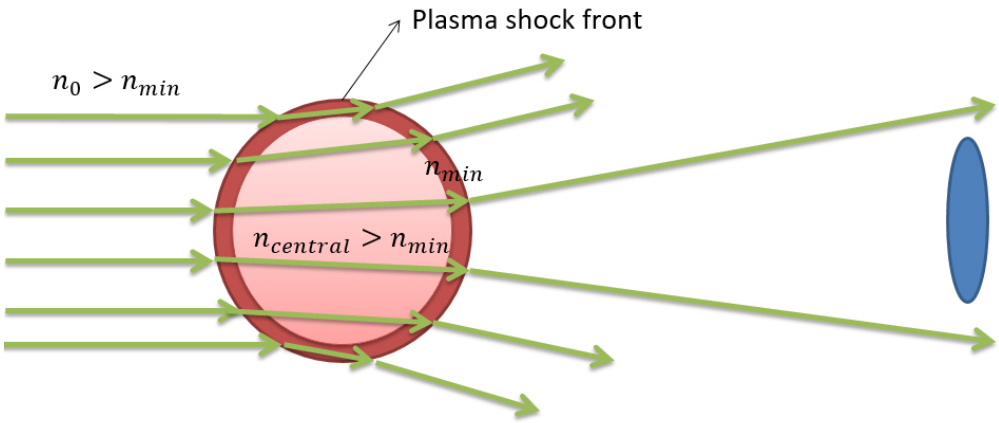

Figure 3.8: Schematic illustration of the way that the plasma refracts the green probe laser light out of the primary objective lens (shown on the right). Various refractive indices are shown, and in this case we have a plasma with a dense shock front, but mainly it is important to show that $n_{plasma} < n_{background}$. This causes the plasma to act like a diverging lens for the probe beam.

cylinder. This is a good approximation if the plasma temperature is higher than about 10 eV, producing fully stripped helium. It will be a function of the beam's offset from the plasma center line as it passes through a chord in the plasma. We can define the Z-axis as the plasma's axis of symmetry, the x-axis as the probe beam propagation direction, and the y-axis as the axis measured from the plasma's center line transverse to both the probe beam propagation direction and the plasma z-axis. If the probe beam rays incident on the plasma are collimated, then the angle of incidence θ_0 on the outer surface of a plasma with radius r_p is given by $sin\theta_0 = y/r_p$. By Snell's law, the angle of refraction is then given by:

$$sin\theta_1 = \frac{n_0}{n_1}\frac{y}{r_p} \tag{3.2}$$

where n_0 is the neutral gas index of refraction equal to one, and n_1 is the plasma index of refraction, which is less than one.

Next we will get into the geometry of the scattering, using a series of incident angles as the probe beam passes through a chord of the plasma. We will attempt to find the scattering angle away from the x-axis, with the figure 3.9 diagram to guide us.

We can argue by symmetry that the angle of incidence into the plasma should be the same as the outbound angle of refraction as the ray leaves the plasma. This symmetry argument is easily understood because we can rotate the coordinate system so that the chord ray formed by the probe beam through

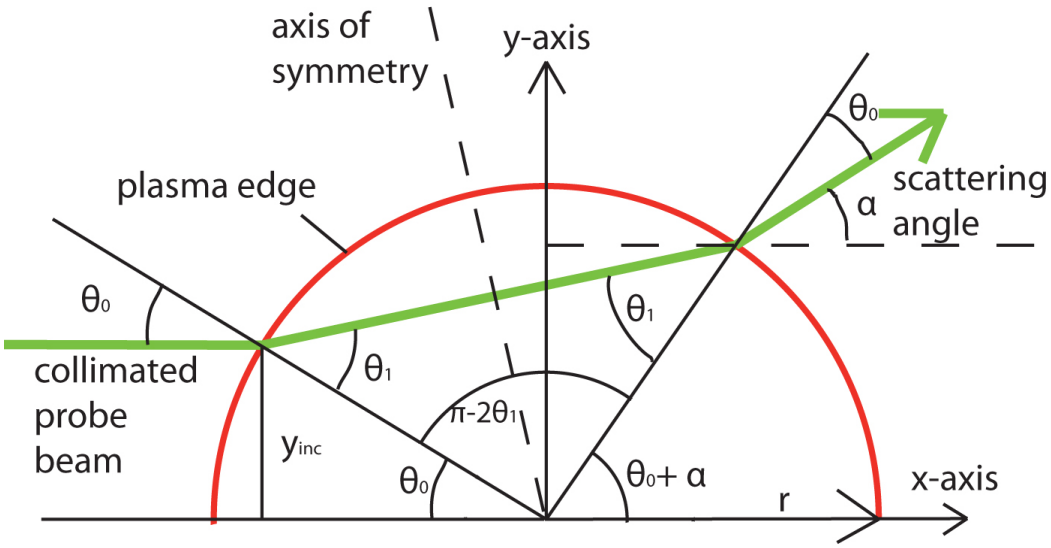

Figure 3.9: Diagram showing the relevant angles we need to do a calculation of the scattering angle in a uniform-electron-density plasma. The probe beam follows the green path, and the plasma periphery is in red.

the plasma is parallel with the x-axis. If we do this we see that the system is symmetric about the new y-axis after the transformation, so inbound and outbound incident angles the same.

Now we just need to do a little more geometry to find the scattering angle, because it is not the same as the angle of refraction out of the plasma θ_0. This is clear from the diagram since the axis of symmetry is tilted from the y-axis. We can find the scattering angle by using the fact that the half-circle angles must add up to π radians, along with the interior triangle formed by two radii to the chord. The following must be true, where angles are given in radians and the angles are as described in figure 3.9:

$$\pi = \alpha + \theta_0 + (\pi - 2\theta_1) + \theta_0 \tag{3.3}$$

Again, this equation was found by arguing that the sum of angles in the interior triangle and the semicircle must be π radians. This equation simplifies to

$$\alpha = 2(\theta_1 - \theta_0) \tag{3.4}$$

and substituting the above equations from Snell's law and the incident ray geometry we arrive at the final equation for the scattering angle alpha, given by:

$$\alpha = 2\left[Arcsin\left(\frac{n_0}{n_1}\frac{y}{r}\right) - Arcsin\left(\frac{y}{r_p}\right)\right] \tag{3.5}$$

The geometrical dependencies in this equation are only the plasma radius and the incident height of the probe beam ray with respect to the center of the plasma, given by y. The scattering angle also depends on the plasma index of refraction, which of course depends on the electron density. Figure 3.10 plots the above equation for scattering angle in degrees with the ray height as the independent variable normalized to the cylindrical plasma's radius.

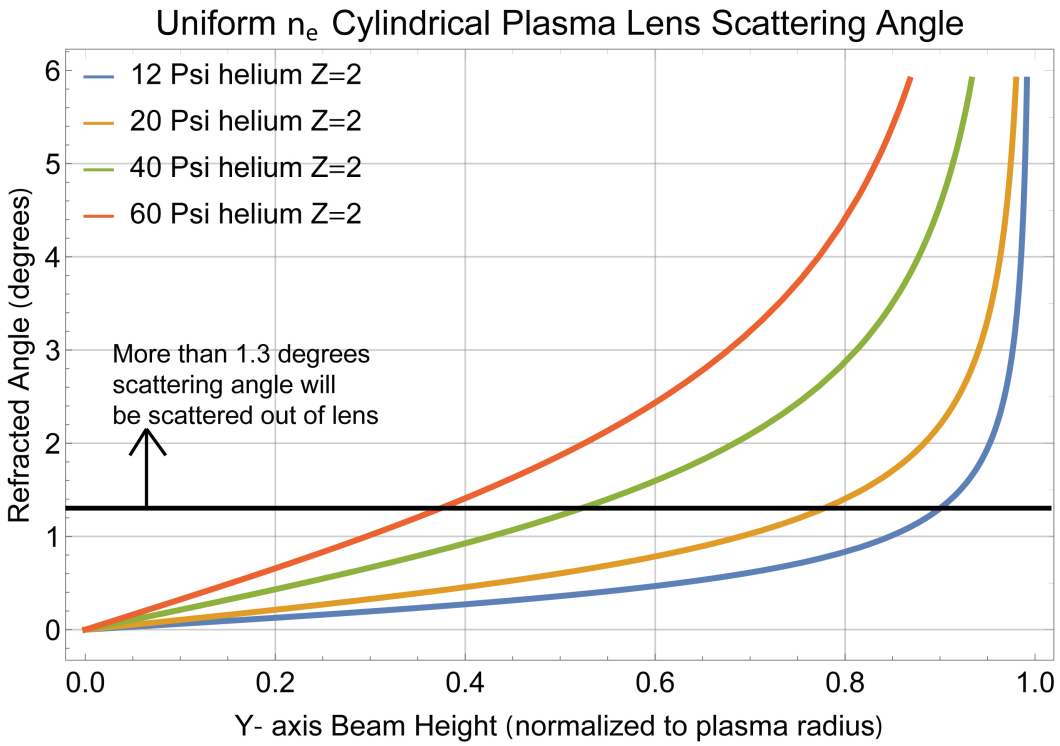

Figure 3.10: This plot shows the scattering angle for a collimated beam created by a cylindrical plasma diverging lens. The plot is for fully ionized helium of equal ion density to the background gas at various pressures. The strongest refraction effect should be visible when the height of the beam approaches the plasma radius, at which point there should be a strong limb-darkening effect caused by the geometry of the steep incident angle. Notice that the limb darkening in the 12 psi semi-transparent shadowgram (figure 6) roughly match the y-axis threshold crossings we would expect from scattering angles. This means that the plasma is still close to its original uniform ion density.

3.4.3 Shadowgraph Scattering by a Double-Layer Plasma

We can actually go a step further and describe the scattering angle for plasma with a shock-compressed shell of higher density gas of thickness Δr, as would be the case for a blast wave. This solution becomes important later

in the plasma's evolution. The whole plasma has radius r as before, but we will call the shocked-shell refractive index n_2 and the interior region refractive index n_3. Again we can argue by symmetry that the incident and outbound angles with respect to a plasma-surface-normals will be the same. However, the geometry gets more complicated because there are now 4 different interfaces where we must apply Snell's Law.

Let's work through the equations needed to constrain the denser-shell refraction problem. Again, as before, Snell's Law with the higher density plasma refractive index equal to n_2 gives

$$sin\theta_0 = Arcsin\left(\frac{y}{r_p}\right) sin\theta_1 = \frac{n_0}{n_2}\frac{y}{r_p} \tag{3.6}$$

Snell's law will give us the middle angle θ_3.

$$sin\theta_3 = \frac{n_3}{n_2} sin(\Delta\phi + \theta_1) \tag{3.7}$$

We will also define the angle $\Delta\phi$ which is the angle between the radii of the 1^{st} and 2^{nd} interfaces. It is given by the following, in which dR is the thickness of the denser outer shell of gas and r is the overall plasma radius.

$$\Delta\phi = 2Arcsin\left(tan\left(\theta_1 \frac{dR}{2(r - dR)}\right)\right) \tag{3.8}$$

We can constrain the problem with the angles formed around the plasma center by the various radii. Because the inbound beam is coherent,

the first angle is identical to θ_0. The goal of this argument is to find the values of sufficient angles in the 180 degree diagram to constrain the scattering angle α. We find α using the right hand angle around the half-circle called ϕ_1, and using symmetry again to say that $\phi_1 = \theta_0 + \alpha$.

We can write the full summation of all angles around center of the plasma as the following (in radians):

$$\pi = \theta_0 + 2\Delta\phi + (\pi - 2\theta_3) + \theta_0 + \alpha \tag{3.9}$$

This simplifies to the following

$$\alpha = 2(\theta_3 - \Delta\phi - \theta_0) \tag{3.10}$$

which is close to the final, fully constrained solution for the scattering angle. We just need an expression for $\Delta\phi$. It can be found by drawing a triangle with one side equal to the thickness of the higher density region and the hypotenuse length equal to the probe beam ray segment through the higher density region. z is the third side of that triangle.

$$tan\theta_1 = \frac{z}{\Delta r} \tag{3.11}$$

And using z to find half of the angle $\Delta\phi$ that we are looking for we get the following:

$$sin\left(\frac{\Delta\phi}{2}\right) = \frac{z}{2(r - \Delta r)} \tag{3.12}$$

And combining these we get

$$\Delta\phi = 2sin^{-1}\left(\frac{\Delta r tan\theta_1}{2(r-\Delta r)}\right) \tag{3.13}$$

Using the equation for α and plugging in the equations for θ_1, $\Delta\phi$, and θ_3 we have now fully solved the problem. You could actually generalize these arguments to arbitrarily many interfaces via mathematical induction, or just implement a ray tracing code. I will not go to this effort; it does not seem to be worth it.

Here is what this shocked-shell cylindrical plasma refraction solution looks like when the thin shell of higher density has a thickness equal to 12.5% of the entire plasma radius. This is the thickness that the shell would have late in time, based on rules from thermodynamics and gasdynamics as described in the chapter covering blast waves. As before, we are looking at the scattering angle as a function of the initial incident height of the beam in the y direction. The following figures 3.11 and 3.12 are for higher density shell regions of density 1.5 and 1.3 times the background plasma gas density. A stronger refraction effect compared to the uniform-uniform density case away from the limb is obvious. Note that once the shocked shell region approaches the thermodynamic limit of four times the background gas density, the refraction is so strong as to scatter the beam in nearly all conceivable parameter ranges.

The shadowgrams in lower density helium show the plasma is still largely transparent out to about 90% of the radius in the case of 12 psi helium,

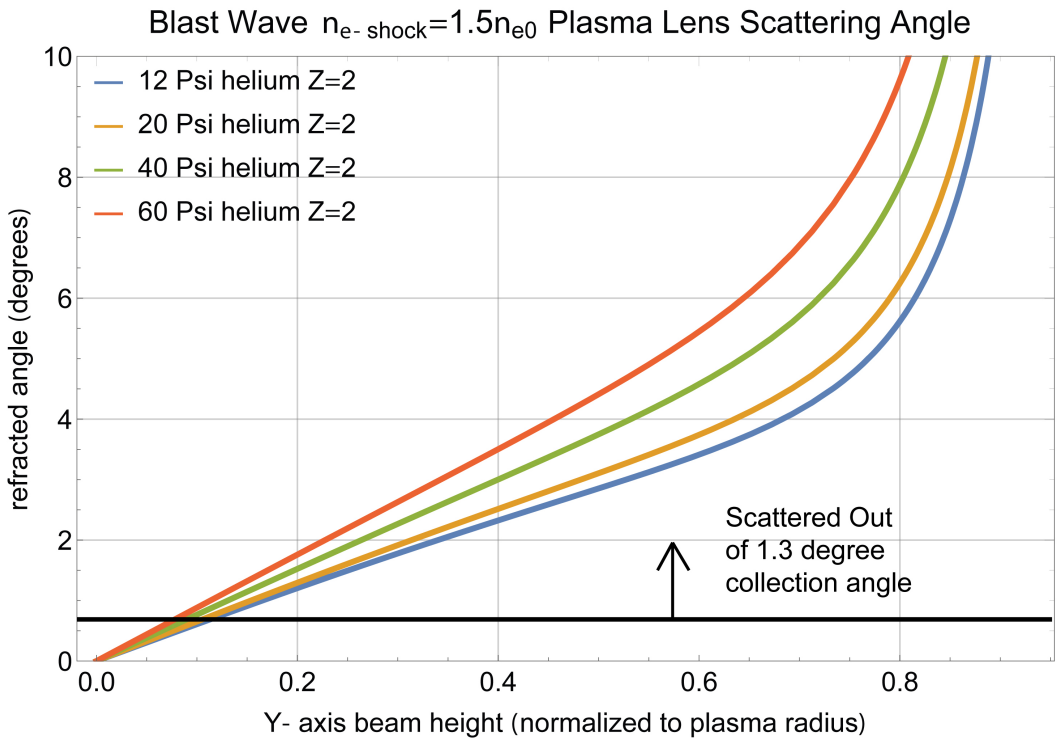

Figure 3.11: The probe beam scattered angle is more significant in the case of a shock-compressed plasma with higher density on the periphery than the it is for the uniform density plasma in figure ten. This is the beam divergence angle for a collimated beam passing through a cylindrical plasma with a finite-thickness shell when electron density is 1.5 times the central density.

which indicates that the shock compression on the boundary is probably less than a factor of 1.3, unless the compression is very thin.

3.5 A Diffusive Radiative Thermal Wave Precurser is the Early-Time Ionization Edge in Shadowgraphy

We observe that the x-ray emitting regions of these plasmas are typically much narrower than the ionized regions that occlude and scatter the

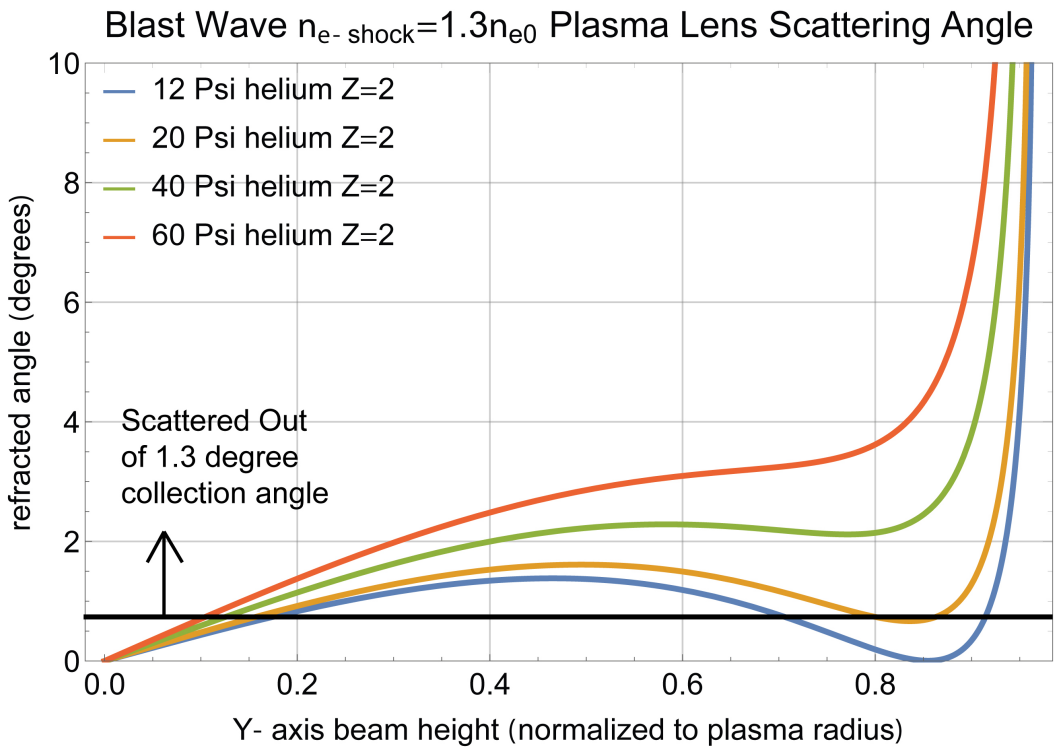

Figure 3.12: This is the beam divergence angle for a collimated beam passing through a cylindrical plasma with a finite-thickness shell when electron density is 1.3 times the central density.

transverse probe beam. The laser-heated plasmas visible in x-ray pinhole images show a self-emission region that varies in width depending on shot parameters, but is typically in the range of 1 to 1.5 mm FWHM during the several nanoseconds of laser heating. This size is which is about 1.2 to 2 times larger than the heating beam diameter. In contrast, the shadowgrams show an ionization front in helium that is typically in the range of 3-4 mm in diameter while the laser is heating. This means that the hottest regions of the plasma has a volume that is only about 20% as large as the full volume of ionized

plasma.

The best explanation for this behavior is that the hottest regions of the plasma remain approximately as wide as the heating beam. However, a diffusive thermal wave likely mediated by photons in the UV range most likely propagates outward from the heated core. Such a scenario is described in Zel'dovich and Raizer's chapter ten concerning thermal waves [25]. The radiative precursor plasma has a temperature that is around the ionization threshold for the plasma. Photons with an energy higher than the ionization threshold will have a longer mean free path in the plasma and likely escape, but the photons with an energy below the ionization threshold energy are readily absorbed and emitted. In helium, the high ionization threshold energy of about 25 eV is likely to be the temperature of the thermal precursor. Photon absorption in this spectral region is very efficient in the cold gas, and the strongly non-linear aspect of radiative thermal conduction ensures that there is hard edge visible in the shadowgraphs. We will discuss this precursor thermal wave in more detail in the next chapter.

Phenomenologically, we are concerned with whether the thermal precursor with an initial thickness of about 1-2 mm will dominate the dynamics of the expanding ionization edge as it that continues to grow. The alternative scenario is that the thermal precursor will develop a well-defined thickness and its dynamics will be controlled by the internal hydrodynamics of the expanding plasma. What we see from imaging the plasma expansion with x-rays and shadowgraphy simultaneously is that the thermal wave ionization front visible

on the shadowgrams are typically following several hundred microns outside the x-ray regions. This behavior sets up after laser heating is concluded.

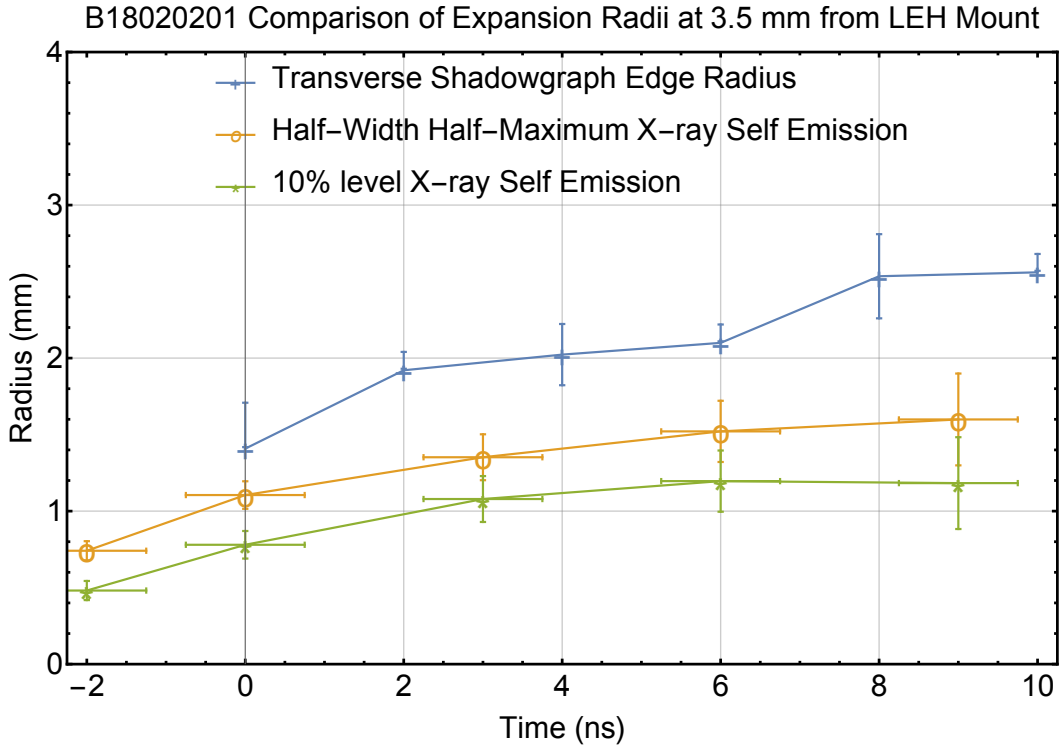

Figure 3.13: This is a comparison of the plasma edges as seen by different diagnostics at different times on the same shot and at the same axial depth. We extracted both the half-width half-max as well as the 10% of maximum of the x-ray self-emission profile. This is shown compared to the larger radius edge that we see in the shadowgraph diagnostic. This is from shot B18020201, which features 5 Torr of neon dopant in 60 psi of helium as well as a 20 ns co-injected prepulse and a 4.8 ns long 1/2 TW heating pulse.

The expansion sequence from these different diagnostics is evidence that there is a common expansion speed visible in both x-rays and shadowgraph edges after the first few nanoseconds. The shadowgraphs follow outside the

range of the expanding x-ray emitting region for about the first six nanoseconds. Refer to data in figure 1.13. After six nanoseconds, the x-ray emission is too dim to track the hydrodynamics of the internal hot core of the plasma, and the effective radius of the x-ray emission region no longer follows the same expansion trajectory as the thermal precursor edge visible in shadowgram. This is because the plasma is cooling fairly rapidly as the plasma has radiated away much of its energy and cooled while expanding, so the half-maximum and 10% levels are no longer representative of the plasma's hot regions. The important point is that the internal hydrodynamics at a constant sound-speed expansion dominates the transport, and a lower-temperature thermal precursor is probably responsible for for the shadowgraph edge we see outside of the hottest core region. Doping the target with neon for x-ray emission causes rapid cooling the plasma during expansion, making it necessary to image plasma transport as early as possible before significant energy loss occurs. Without neon the shadowgraph expansion follow a constant sound speed trajectory. In the absence of neon dopant, the initial radiative thermal wave precursor is likely heated by electron thermal conduction and the plasma comes to a relatively uniform temperature within a few nanoseconds, and the sound speed expansion proceeds from there.

Significantly more detail on thermal waves, sound waves, and blast waves will occupy the next three chapters, explaining the three different stages of plasma evolution that we see in shadowgrams.

3.6 Conclusions from Physics of Shadowgraphy

The shadowgraphy imaging system shows dark regions without probe beam light because the probe beam is both absorbed and refracted away from the objective lens. We can used the images to measure the size of the plasma at the time of the image frame, since have both measured and calculated a calibrating resolution in pixels per micron at the target. In most cases, the probe beam is totally absorbed by the plasma through collisional absorption. There is a minority of experiments in which the plasma appears partially transparent, with a limb-darkening effect visible on the top and bottom edges of the cylinder. The limb darkening effect is due to the large refractive effect of a glancing incidence geometry.

In general, the dark regions of the shadowgrams are plasmas that are cool enough to absorb the probe beam via collisional absorption. From the collisional absorption opacity for 12 and 20 psi helium fills we can infer these plasmas must be at least 140 eV in temperature during laser heating. We can also infer that some experiments at 60 psi must have been hotter than 600 eV.

In the experiments that appear partially transparent, we can use the analysis of scattered angle presented in this chapter. We learn that these plasmas not have begun significant shock-compression during laser heating. We can place a bound on a density change to be less than a factor of 1.3. This tells us that hydrodynamic motion has not set in significantly and density has not changed by more than 30% while the laser is heating.

Chapter 4

Thermal Transport and Heat Wave Theory

In this chapter we focus on thermal transport via diffusion. We'll cover solutions to the heat diffusion equation in the form of propagating heat waves. Next we will explain applications of the heat equation by describing important types of heat conduction and diffusion in plasmas, and the conditions under which these conduction modes are valid. Thermal wave behavior will depend on the temperature scaling in the dominant form of heat conduction. Electron thermal conduction will be important for the hot parts of the plasma, but helium also supports diffusive radiative transport at low temperatures and photon energies. This causes a low temperature radiative precursor to propagate away from the hottest plasma regions. In this case, a radiative precursor is a low-temperature ionizing front that extends out of the hotter plasma regions, in which radiation behaves diffusively. This would explains why the shadowgrams show larger diameter plasmas than hottest x-ray emitting regions. This region probably contains at least on the order of 100 J of energy in the case of helium plasmas.

When we apply a magnetic field, the diffusion coefficient is effectively clamped to a maximum value and no longer scales with a simple power law

of temperature. This is because longer mean free path electrons associated with higher temperatures have their movement restricted in two dimensions to the length scale of the gyro-orbit. For this reason, a nonlinear thermal wave description of diffusive heat transport is no longer accurate. In this case, we could take a zeroth-order approximation and solve the heat equation with a constant diffusion coefficient. We will work through these possibilities, and provide examples of radial heat distributions showing thermal waves and Gaussian heat solutions with variously dominant forms of heat conduction. This will tie into work later in the dissertation, when we can provide approximate temperature distributions via transverse x-ray emission diagnostics.

In reality, thermal transport not only includes electron collisional diffusion, but also the bulk hydrodynamic motion of heat-carrying particles. For this reason, bulk plasma expansion plays a role in thermal energy transport which we will not address yet. Once hydrodynamics become important, ion acoustic waves are launched. We will discuss sound speed transport in the next chapter: chapter five. The bulk transport of density at the sound speed is often comparable to or dominant over simple collisional diffusive heat transport on the basis of the speed of energy transport. We might expect the thermal diffusion solution to be important on very early timescales, before significant sound speed motion has occurred [25]. While thermal waves propagate faster than the ion sound speed they will tend to smooth out any mass accumulation due to pressure gradients, but once thermal waves slow to about a factor of two of the ion sound speed then an ion sound wave will become the dominant

form of energy transport. Using the time derivative of the heat front solution, we will find a formula for the transition time at which a nonlinear thermal wave slows to the plasma sound speed. We will see that this transition time is usually about a nanosecond, which is well within the laser heating time frame. So, in fact, heat transport is occurring via both diffusion and bulk particle motion, but thermal diffusion is important for establishing temperature distributions on the sub-nanosecond timescales during laser heating. It will also be important for transporting heat away from a hydrodynamic front, such as in an ionizing precursor.

Heat conduction in a plasma obeys the heat equation is most circumstances relevant to us, but to get a full picture of the plasma transport we need to find a new, self-consistent description using methods outlined in Braginskii's 1965 paper [26]. The fluid equations of collisional plasmas were worked out in detail by Braginksii in his classic theory of plasma transport. This description is often discretized and used for plasma simulations. A complete description would include the bulk plasma sound speed motion mentioned above, but it would also include effects which we will not be able to cover here, including electric fields and currents in the plasma. The original form of these solutions in Braginskii's paper would not work, since we have such a rapidly expanding plasma that is not in thermodynamic or hydrostatic equilibrium. Applying a magnetic field complicates the picture even further, for example via the plasma diamagnetic effect and the complicated modification to collisional diffusion, but these effects should still be present in a full fluid model [27]. All of

these phenomenon are also likely to be included in various appropriate plasma computational models, but it would be important to know which are important a priori. But, there are some high-thermal-gradient behaviors that might not be easy to model, including the plasma diamagnetic effect in high thermal gradients, plasma end current effects, and failures of diffusion models due to non-local transport. Such descriptions would ultimately be the best way to model our heat conduction. Of course our goal here in this chapter is gaining an understanding and background in the underlying physics and motivating future models that might be more accurate.

4.1 Thermal Waves

All systems out of thermal equilibrium in which thermal gradients are not extreme will exhibit diffusive heat flow via the heat equation. The heat or diffusion equation is a partial differential equation for which we have solutions for both linear and non-linear thermal diffusion coefficients. In general these solutions are diminishing traveling waves. When heat conduction depends on temperature nonlinearly, the solution to the heat equation can be described as a spreading thermal wave. Thermal waves are rapidly propagating heated regions with sharp heat front boundary. Their trajectories can be expressed with self-similar solutions, like a blast wave, although they evolve on faster timescales. The stronger the temperature dependence, the sharper the heat front and more uniform the temperature inside the wave.

We will present an original derivation for a solution to the heat equation

in cylindrical geometry based on work in Zel'dovich and Raizer [25]. The solution provides insight into the time at which thermal waves approach the ion sound speed, which is an important transition for the transport processes we observe. We can find the general linear energy density (energy per unit length) of these distributions in cylindrical geometry. It will also give us the temperature at the plasma core following an initial heating distribution, via an evolving temperature distribution solution.

How valid is this thermal wave solution? Mainly, it makes assumptions on initial values and the lack of driving heat sources. Ordinarily, a self-similar solution requires that there are no characteristic length scales. However, all of our experiments begin by launching a heat wave from a finite sized plasma. Barenblatt argues that such initial finite-radius heat waves will rapidly approach a self-similar asymptotic solution [28]. While the temperature profile may not be initially self-similar due to the finite extent of the laser heating profile, we can guess that it very quickly might evolve to a self-similar thermal wave. This is because electrons transmit heat very rapidly via diffusion. The timescale for this is on the order of the free-streaming plasma length scale over the thermal velocity of the electrons. With electron thermal velocities of about 5 mm/ns, for us this value is on the order of a hundreds of picoseconds, which is shorter than the laser heating time. So outside of the laser heating region we might expect the temperature distribution to evolve to a self-similar thermal wave very rapidly, in timescales we can't see on the diagnostics.

Another inadequacy is that this thermal wave full solution we find is for

an initial value problem with a thin heat source and no subsequent heating as a function of time. For most of the rest of this treatment I will ignore the source term in the heat equation, although it is required for a complete description. Unfortunately for us an accurate description including the laser heat source would be complex, because collisional absorption is a nonlinear function of time, laser intensity, and temperature, so it couples with heat transport! We could do further work to find the full solution to find the solution of a more general, driven heat source problem.

Finally, our thermal wave solution is no longer valid if the dominant heat transport depends on temperature in some way other than $\chi\ T^n$. If the thermal diffusivity is a weak function of temperature then we might solve the linear heat equation. This leads to the so-called fundamental Gaussian heat kernel solution. Finally, there are other non-linear solutions to the heat equation which also support propagating wave solutions that are quite different from the self-similar thermal wave solution. These might be important for cross-field diffusion, but we will not attempt to solve them here.

4.1.1 The Heat Equation

Thermal transport via particle collisions in plasmas without bulk motion is described by the heat equation, a partial differential equation. The general form for the heat equation is a partial differential equation in which the change in temperature with time is proportional to the spatial change in gradient of temperature. It is:

$$\frac{dT}{dt} = \chi \nabla^2 T + q \tag{4.1}$$

where T is temperature, q is a thermal source field, and χ is the coefficient of thermal diffusivity. Thermal diffusivity is proportional to mean free path and mean thermal velocity. The temperature dependence in the diffusion coefficient χ will turn out to be very important.

The heat equation in cylindrically symmetric geometry has the following form as a PDE for $T(r,t)$ where we assume there is no angular θ dependence:

$$\frac{dT}{\partial t} = \frac{1}{r}\frac{\partial}{\partial r}\left(\chi r \frac{\partial T}{\partial r}\right) \tag{4.2}$$

Zel'dovich and Raizer outline a method for solving the heat equation for nonlinear heat conduction where the thermal diffusivity has a dependence on temperature like $\chi\ T^n$, with $n > 0$ using a self-similar solution. It is important to note that with a nonlinear heat conduction exponent greater than one we will see a sharp, finite boundary in the thermal wave front, but a thermal diffusivity that is independent of temperature would produce a nonphysical, instantaneously nonzero heat at arbitrary distance away. Even if the thermal diffusivity is a weak function of temperature, the heat equation is only an approximation of the physical reality of colliding particles and in that situation the heat flow is limited by the speed of propagation and by the finite mean

free path. There are other situations in which the heat equation fails for large thermal gradients, which we will discuss later.

4.1.2 Nonlinear Heat Conduction in Thermal Waves

Zel'dovich and Raizer give solutions to the heat equation using a self-similar thermal wave in planar geometry and spherical geometry [25]. The solutions have initial heat sources originating from an infinite sheet and a point, respectively. They mention that a cylindrical solution also exists. I will not repeat their results for those geometries of thermal waves here, but I did follow their methods closely to find the analytical self-similar solution to the nonlinear heat equation for cylindrical geometry that is applicable to a laser-heated channel.

4.1.3 Thermal Waves in Cylindrical Geometry

One can use dimensional analysis starting from the heat equation to get the general form of the solution. From there, we search for a combination of variables that gives a unitless self-similarity variable and associated analytical heat wave solution. Then, the derivation will use conservation of energy to find the time-dependence of the full solution.

For the general form of the thermal wave solution, recall the heat equation 4.2 with the Laplacian in cylindrical-polar coordinates. First we postulate that the coefficient of thermal diffusivity χ can be written in the self-similar form aT^n. This works for several simple models, including Spitzer conductiv-

ity in which $n = 5/2$. The coefficient a is the ratio of thermal conductivity to the product of mass density and specific heat at constant pressure. So, $a = \sigma/(\rho_m c_p)$. We have our heat equation as:

$$\frac{\partial T}{\partial t} = \frac{a}{r}\frac{\partial}{\partial r}\left(T^n r \frac{\partial T}{\partial r}\right) \tag{4.3}$$

Based on this equation's left hand side units, "a" should have units of $\frac{Length^2}{Time(Deg)^n}$. Zel'dovich and Raizer use degrees for temperature units, although we could just as easily use Joules or eV. I will use degrees to illustrate. So, the units in the cylindrical form of the heat equation are the following:

$$\frac{deg}{time} = \frac{length^2}{deg^n * time}\frac{1}{length^2}\left(deg^n * length\frac{deg}{length}\right) \tag{4.4}$$

Note that this combination gives $deg/time$ on both sides, so we have found the right units for the coefficient.

Now we can use the form of thermal diffusivity χ we postulated a combination of parameters aQ^n that only has units of length and time, where a is the same coefficient in $\chi = aT^n$. aQ^n is the logical choice because Q will be an unchanging quantity with units of temperature times area. This quantity will be preserved during thermal wave expansion due to energy conservation, so it serves as the similarity variable for a similarity transform. In cylindrical geometry Q is the areal integral over the circular differential disk of the temperature distribution, and thus it should have units of $deg * length^2$. Q is an important value to the rest of the dissertation because when Q is multiplied by

particle number density, it gives the extremely important quantity of energy per unit length in units such as $Joules/cm^2$. The combination aQ^n has units of $\frac{Length^{2n+2}}{Time}$. From this we can construct a unitless self-similarity variable.

$$\xi = \frac{r}{(aQ^n t)^{1/(2n+2)}} \tag{4.5}$$

Each thermal wave trajectory will have a unique similarity variable. From this we can argue that the radius of the edge of the heat wave front r_f should have the following time-dependent scaling:

$$r_f \propto (aQ^n t)^{1/2n+2} \tag{4.6}$$

This dependence will be very important for us. We can find the full solution for the trajectory of the thermal wave later.

So, since we can guess that the thermal wave will become self-similar quickly, we can write an equation for the heat wave's radius using initial data. Since the radius of the heat front scales with the time to a known exponent, we can determine the constant in front and thus find all future radii with the simple relation:

$$r_f(t) = r_0 \frac{t^{1/2n+2}}{t_0^{1/2n+2}} \tag{4.7}$$

This approach has given us the solution for the trajectory up to a constant, and gives a useful result if we begin with an initial radius.

4.1.4 Full Solution to Thermal Wave Trajectory with Cylindrical Symmetry

In this section I will use Zel'dovich and Raizer's methods to find the full solution for the trajectory of a thermal wave expanding from an infinite heated line at a finite initial temperature.

The solution involves doing a change of variables on the heat equation to the similarity variable. Once we have performed the change of variables, the heat equation will become an ordinary differential equation for ξ. We know from the above that we are looking for a full solution of the following form:

$$T = \left(\frac{Q}{at}\right)^{2/(2n+2)} f(\xi) \tag{4.8}$$

We will proceed first by inserting the form of the temperature solution in 4.8 into the left hand side of the heat equation, which is $\frac{dT}{dt}$. The left hand side becomes:

$$\frac{d}{dt}\left[f(\xi)\left(\frac{Q}{at}\right)^{2/(2n+2)}\right] \tag{4.9}$$

And with the product rule:

$$\frac{d\xi}{dt}\frac{df}{d\xi}\left(\frac{Q}{at}\right)^{1/n+1} + f(\xi)\left[-\frac{1}{t}\frac{1}{n+1}\left(\frac{Q}{at}\right)^{1/n+1}\right] \tag{4.10}$$

There are two derivatives in 4.10 that we will need to expand. Note that we can use the chain rule to find the derivatives of the function of the

similarity variable.

$$\frac{df}{d\xi} = \frac{\partial f}{\partial t}\frac{\partial t}{\partial \xi} \tag{4.11}$$

Also we will need the time derivative of the similarity variable ξ.

$$\frac{d\xi}{dt} = -\frac{aQ^n r\left(aQ^n t\right)^{-\frac{1}{2n+2}-1}}{2n+2} = -\frac{r}{t}\frac{1}{2n+2}\left(\frac{1}{aQ^n t}\right)^{1/2n+2} \tag{4.12}$$

Inserting 4.12 into 4.10, we get the LHS equal to:

$$-\frac{r}{t}\frac{1}{2n+2}\left(\frac{1}{aQ^n t}\right)^{1/2n+2}\frac{df}{d\xi}\left(\frac{Q}{at}\right)^{1/n+1} + f(\xi)\left[-\frac{1}{t}\frac{1}{n+1}\left(\frac{Q}{at}\right)^{1/n+1}\right] \tag{4.13}$$

After noting that $r = \xi\left(aQ^n t\right)^{1/2n+2}$, we can simplify to:

$$-\frac{1}{t}\frac{1}{n+1}\left(\frac{Q}{at}\right)^{1/2n+2}\left[\frac{\xi}{2}\frac{df}{d\xi} + f\right] \tag{4.14}$$

Before attempting to simplify further, we will work on the similarity variable transform on the RHS of the heat equation. The RHS of the heat equation is the following:

$$\frac{a}{r}\frac{d}{dr}\left[r\left(\frac{Q}{at}\right)^{n/n+1} f^n \frac{d\xi}{dr}\frac{d}{d\xi}\left[\left(\frac{Q}{at}\right)^{1/n+1} f\right]\right] \tag{4.15}$$

Taking the derivative w.r.t. the similarity variable:

$$\frac{a}{r}\frac{d}{dr}\left[r\left(\frac{Q}{at}\right)^{n/n+1} f^n \left(\frac{1}{aQ^n t}\right)^{1/2n+2}\left(\frac{Q}{at}\right)^{1/n+1}\frac{df}{d\xi}\right] \tag{4.16}$$

As an intermediate step, note that the following portion of the above equation can be greatly simplified (noting equation 4.5 for the similarity variable):

$$\frac{r}{(aQ^n t)^{1/2n+2}} = \xi \left(\frac{Q}{at}\right)^{n/n+1} \left(\frac{Q}{at}\right)^{1/n+1} = \frac{Q}{at} \tag{4.17}$$

the RHS becomes:

$$\frac{1}{r}\frac{d}{dr}\left(\xi \frac{Q}{t} f^n \frac{dt}{d\xi}\right) = \frac{Q}{rt}\left(\frac{1}{aQ^n t}\right)^{1/2n+2} \frac{d}{d\xi}\left(\xi f^n \frac{df}{d\xi}\right) \tag{4.18}$$

Next, we will simplify the above using $r = \xi(aQ^n t)^{1/n+1}$,

$$\frac{Q}{rt}\left(\frac{1}{aQ^n t}\right)^{1/2n+2} = \frac{Q}{\xi t\,(aQ^n t)^{1/n+1}} = \frac{1}{\xi t}\frac{Q}{(at)^{1/n+1}\,Q^{n/n+1}} \tag{4.19}$$

Which simplifies to

$$\frac{1}{\xi t}\left(\frac{Q}{at}\right)^{1/n+1} \tag{4.20}$$

Let us now put the whole equation together following the similarity transform, although there will be much to simplify:

$$-\frac{1}{t}\frac{1}{n+1}\left(\frac{Q}{at}\right)^{1/2n+2}\left[\frac{\xi}{2}\frac{df}{d\xi} + f\right] = \frac{1}{\xi t}\left(\frac{Q}{at}\right)^{1/n+1} \frac{d}{d\xi}\left(\xi f^n \frac{df}{d\xi}\right) \tag{4.21}$$

After cancellation we arrive at the final ODE that we need to solve:

$$\frac{1}{n+1}\left[\frac{\xi}{2}\frac{df}{d\xi}+f\right]+\frac{1}{\xi}\frac{d}{d\xi}\left(\xi f^n\frac{df}{d\xi}\right)=0 \tag{4.22}$$

The next step is to solve this ODE. We can expand it with the product rule. Afterward, the solution is indeed of the form given by equation 4.8. The full solution to the temperature distribution turns out to be the following:

$$T=\left(\frac{Q}{at}\right)^{1/n+1}\left[\frac{n}{2(2n+2)}\xi_0^2\right]^{1/n}\left[1-\left(\frac{\xi}{\xi_0}\right)^2\right]^{1/n} \tag{4.23}$$

The above solution is not particularly useful yet because it is in terms of the similarity variable ξ. Also there is an unknown quantity in the form of ξ_0. We will need to transform back to variables we are familiar with, such as radius and time. We will do this in a moment. Note that the function $f(\xi)$ appears on the left. This solution is valid while $\xi < \xi_0$ and will be 0 otherwise. $f(\xi)$ from 4.8 is given by:

$$f(\xi)=\left(\frac{n}{2(2n+2)}(\xi_0^2-\xi^2)\right)^{1/n} \tag{4.24}$$

We can apply an additional constraint on the solution, which will allow us to find the value of ξ_0 based on the fact that the integral of the temperature distribution must remain constant as the thermal wave expands. This is just a consequence of conservation of energy. We get the following for all radii:

$$k_b 2\pi\int_0^{r_f} f(\xi)r\,dr=1 \tag{4.25}$$

where r_f is the radius of the thermal wave front and k_b is the Boltzmann constant. Let's plug in the form of $f(\xi)$ given in 4.24, and we get a slightly different integral:

$$\left(\frac{n}{2(2n+2)}\right)^{1/n} 2\pi \int_0^{\xi_0} \left(\xi_0^2 - \xi^2\right)^{1/n} \xi d\xi = 1 \tag{4.26}$$

Unlike in spherical and planar coordinates, this integral has a nice solution that does not require beta or gamma functions or other cumbersome functions:

$$\left(\frac{n}{2(2n+2)}\right)^{1/n} \frac{2\pi n \xi_0^{2/n+2n/n}}{2+2n} = 1 \tag{4.27}$$

After solving for ξ_0, we get:

$$\xi_0 = \left(\frac{2+2n}{2n\pi}\right)^{n/2n+2} \left(\frac{2(2n+2)}{n}\right)^{1/2n+2} \tag{4.28}$$

Now that we have ξ_0 we can plug it into $r_f = \xi_0 \left(aQ^n t\right)^{1/2n+2}$ to get the full solution for the edge of the thermal wave front, which will be the following:

$$r_f = \left(\frac{2+2n}{2n\pi}\right)^{n/2n+2} \left(\frac{2(2n+2)}{n}\right)^{1/2n+2} \left(aQ^n t\right)^{1/2n+2} \tag{4.29}$$

Now that we have the full form of the solution for r_f, let's continue to unravel the similarity variable out of the temperature solution. If we use our function for ξ_0 from 4.28, T simplifies to the following function of only Q, a, t, and r_f...

$$T(r,t) = T_c \left(1 - \left(\frac{r}{r_f}\right)^2\right)^{1/n} = \left(\frac{Q}{4\pi a t}\right)^{1/n+1} \left(1 - \left(\frac{r}{r_f}\right)^2\right)^{1/n} \tag{4.30}$$

In the above, T_c is the temperature at the center of the distribution, which is a value that falls with time like $t^{-1/n+1}$. The forms for r_f and ξ_0 in r_f given as before. We can eliminate the dependence on r_f if we wish, and obtain the following:

$$T = \left(\frac{1+n}{\pi n}\left(Q/at\right)^{n/n+1} - \frac{r^2 n}{(4n+4)at}\right)^{1/n} \tag{4.31}$$

We have now solved our nonlinear heat equation in cylindrical coordinates; we have found the full solution for temperature as a function of time and radius.

We can also find a solution to the temperature distribution at arbitrary times, assuming we know the outer radius of the heat front as a function of time and an initial radius r_0 and central temperature T_{c0}. We will have to guess at initial central temperature which is the central maximum temperature at the initial time at which the plasma has the radius r_0.

$$T(r,t) = T_{c0} \frac{r_0^2}{r(t)_f^2} \left(1 - \frac{R^2}{r(t)_f^2}\right)^{1/n} \tag{4.32}$$

4.1.5 Cylindrical Thermal Wave Energy Per Unit Length

In this section we will explore the meaning of the energy per unit length and the variable Q in the temperature solution in cylindrical geometry. We will find that there is a simple relation between the radius of the heat front, the central temperature, and the energy per unit length. We can say that the energy per unit length in the plasma at a particular time with the temperature distribution given in equation 4.30 is as follows:

$$E_{th} = N2\pi k_b T_c \int_0^{r_f} \left(1 - \frac{r^2}{r_f^2}\right)^{1/n} r dr \tag{4.33}$$

Here, N is the plasma particle number density (capitalized to distinguish it from the exponent of temperature in thermal conductivity). The integral is in cylindrical-polar coordinates so we have integrated out a factor of 2π for cylindrical symmetry. The solution to this integral evaluated at the endpoints is actually pretty simple:

$$\int_0^{r_f} \left(1 - \frac{r^2}{r_f^2}\right)^{1/n} r dr = \frac{n(1-(r/r_f)^2)((r/r_f)^2-1)r_f^2}{2n+2}\Bigg|_0^{r_f} = \frac{nr_f^2}{2n+2} \tag{4.34}$$

so the energy per unit length becomes:

$$E = \frac{NkT_c n\pi r_f^2}{n+1} \tag{4.35}$$

This is a very nice, simple result that relates the energy content to the central temperature and the radius for any particular thermal conductivity

dependence. This will be a very important result for us later! We can use it to argue that we can make a good guess about the total energy per unit length in the plasma based only on the radius of the plasma, the central temperature, and the thermal conductivity.

Now let us use the form of T_c and see if we can simplify further. Recall $T_c = (Q/4\pi at)^{1/n+1}$ and that $r_f = \xi_0 \left(aQ^n t\right)^{1/2n+2}$. Plugging these in for T_c in the expression for E, we get much cancellation and the energy per unit length becomes:

$$E = Nk_b Q \tag{4.36}$$

Which is exactly a validation of the definition of Q, the integral of the temperature distribution over the differential disk. This is a good check.

If we wish to write the final form of the temperature as a function of radius, time, and energy per unit length, we can now eliminate the functions for r_f, ξ_0, and Q. We get the following final result:

$$T = \left(\frac{1+n}{\pi n} \left(E/atNk_b\right)^{n/n+1} - \frac{r^2 n}{(4n+4)at} \right)^{1/n} \tag{4.37}$$

4.1.6 Transition to Ion Sound Transport Regime

Next I will present an original derivation for the time it takes for a thermal wave to slow down to nearly the ion sound speed in a plasma, or

around Mach 1-2. This time represents the duration of time over which diffusive thermal transport is faster than hydrodynamic transport via ion acoustic expansion in the plasma. After the thermal wave is slower than the sound speed, ion density waves can begin to accumulate. Of course is important to note that this is not a blast wave yet, just an ion sound wave which builds density as it forms a shock later.

The derivation for this transition timescale uses the time derivative of the thermal wave front position r_f. This is a worthwhile result to present anyway: it is the speed of the thermal wave front as a function of time!

$$\frac{dr_f}{dt} = \frac{d}{dt}\left[\left(\xi_0 a Q^n t\right)^{1/2n+2}\right) = \frac{\xi_0 \left(aQ^n t\right)^{1/2n+2}}{(2n+2)t} \tag{4.38}$$

which simplifies using the definition of r_f to just

$$v_f = \frac{r_f}{(2n+2)t} \tag{4.39}$$

If we know an initial radius and time for the blast wave, this could also be written as:

$$v_f = \frac{r_0}{t_0^{1/2n+2}} \frac{t^{1/2n+2}}{(2n+2)t} \tag{4.40}$$

This speed can now be equated to the ion sound speed, and we can solve for the transition time at which they are both equal. In a non-thermalized plasma the ion sound speed is:

$$v_{cs} = \sqrt{\frac{\gamma_e Z k_b T_e + \gamma_i k T_i}{M_i}} \tag{4.41}$$

Where M_i is the ion mass, γ is the adiabatic index, and Z is the charge state of the plasma. Equating these gives:

$$\frac{\xi_0 \left(aQ^n t\right)^{1/2n+2}}{(2n+2)t} = \sqrt{\frac{\gamma_e Z k_b T_e + \gamma_i k T_i}{M_i}} \tag{4.42}$$

If we solve for for the transition time t_x at which those two equations are equal, we get:

$$t_x = (aQ^n)^{1/2n+1} \left(\frac{\xi_0}{2n+2}\right)^{\frac{2n+2}{2n+1}} \left(\frac{M_i}{\gamma k(ZT_e + T_i)}\right)^{\frac{n+1}{2n+1}} \tag{4.43}$$

This is the solution to the transition time from thermal waves to sound waves. Notice that the transition time depends on temperature. Since the thermal wave has a nonuniform temperature, the transition will happen at different places at different times in the thermal wave. The temperature dependence is a negative power, so higher temperature will give an earlier transition time.

Also, unfortunately this transition time still depends on Q and on the form of ξ_0 given in 4.28, so it is not yet particularly useful. We can also find a valid form of the transition time from equation 4.32. That transition time is:

$$t_x = (t_0)^{-1/2n+1} \left(\frac{r_0}{2n+2}\right)^{\frac{2n+2}{2n+1}} \left(\frac{M_i}{\gamma k(ZT_e + T_i)}\right)^{\frac{n+1}{2n+1}} \tag{4.44}$$

We can simplify the result by making some strong assumptions. We can assume that we are concerned with the electron temperature, and that it is well thermalized, although this is not necessarily a good assumption! For a highly nonlinear thermal wave, the central temperature will be close to the same temperature through much of the heat front. This allows us to insert the formula for the central temperature T_c of a thermal wave in place of the ion and electron temperature. This may be a valid approximation because the regions with the highest temperature will have the earliest transition to sound speed regimes, and the transition will propagate outward from there. With the formula for the central temperature inserted, there is much cancellation. We get the following simple result:

$$t_x = \frac{r_0}{2n+2}\sqrt{\frac{M_i}{\gamma Z k_b T_c}} \tag{4.45}$$

This is a very nice, simple formula and it actually lets us estimate the transition time. For helium ion density and temperatures in the range of 100-500 eV, and an initial radius in the range of 500 microns to 1 mm, this equation gives a narrow range of results. We find a transition time on the order of 1 nanosecond for nearly all experimental configurations we might expect. This is one of the major results of this chapter's work.

This formula 4.45 has several major shortcomings. First, the central temperature is actually a function of time. So although we can make a guess about what it might be, we would do better to eliminate it from the equation. Let's start from equation 4.45 and insert the $T_c = (Q/4\pi at)^{1/n+1}$. We get:

$$t_x = (4\pi)^{1/2n+1} Q^{n-1/2n+1} a^{2/2n+1} \left(\frac{\xi_0}{2n+2}\right)^{\frac{2n+2}{2n+1}} \left(\frac{M_i}{\gamma Z k}\right)^{\frac{n+1}{2n+1}} \tag{4.46}$$

We could insert the equation $E = NkQ$ and find the transition time in terms of the energy density also. This is the final, rather complex result that would let us make a calculation of the transition time based on only the energy per unit length and dominant type of thermal conductivity. It is probably less useful than equation 4.45 because it assumes an initiation from an infinitely thin heated line.

4.2 Intro to Various Thermal Conductivity Models

This section covers different types of thermal conductivity. We will give the associated diffusion coefficients of those that are important. First, we will introduce the electron collisional diffusivity in the absence of a magnetic field, called the Spitzer thermal conductivity.

Next, we will describe radiation-based diffusive heat flow. In general, radiation will dominate over electron thermal conductivity when the density and temperature are extremely high and when the average atomic number is higher, for example in the solid density regimes with higher Z ion species. Radiative thermal conduction can be diffusive and behave similarly to particle collisional diffusion. This applies to plasmas with high opacity to the thermal photons exchanged via transitions such as line radiation for high Z ions or for bremsstrahlung emission in low Z ion species [25]. For our purposes, we

have dominantly free-free radiation transitions via bremsstrahlung and inverse bremsstrahlung. This likely supports diffusive radiation transport only for low energy photons and leads to a thermal wave precursor outside of the plasma's hottest regions.

The diffusion equation fails for extremely large thermal gradients where heat flow is limited by the population of electrons that can flow across the gradient. The diffusion equation also fails for situations in which there may be a population of super-thermal electrons, which can carry substantial energy in plasmas and do not obey conventional rules of collisions and diffusion. These phenomenon are difficult to model with simulations. However, we do not see strong evidence that they are needed to explain anything in our plasmas. We will mention them for completeness.

4.2.1 Spitzer Conductivity

Thermal conductivity where electron collisions dominate is the most important thermal conduction for our plasmas. This is because at relevant electron densities of about 10^{20} cm^{-3}, electrons are highly collisional. Electrons collision time is typically on the order of picoseconds for the densities we are concerned with. Although collisional absorption does produce a non-Maxwellian velocity distribution, the electrons will thermalize to a Maxwellian on picosecond time scales, which is short compared to laser heating and thermal expansion.

Electron diffusive thermal conductivity is called Spitzer thermal con-

ductivity in honor of initial theoretical work [29]. I will not cover a derivation of the Spitzer conductivity here. It comes from a collisional Fokker-Planck fluid description with a Maxwellian velocity distribution. A modern expression for the Spitzer electron thermal diffusion coefficient following several subsequent theoretical papers with correction factors is given by:

$$\chi_s = \left(\frac{8}{\pi}\right)^{3/2} G(Z) \frac{(k_b T)^{5/2} k_b}{Z e^4 m_e^{1/2} ln\Lambda} \tag{4.47}$$

Where m_e is the electron mass, $ln\Lambda$ is the Coulumb Log, and Z is the charge state. Also, G(Z) is the Gaunt factor which corrects electron-electron collisions and reduces conductivity. It is given approximately by $(1+3.3/Z)^{-1}$ [4]. Importantly, the conductivity depends on temperature to the 5/2 power. We could use this expression to produce a thermal wave trajectory and temperature distribution using the machinery earlier in the chapter. Both figures 4.3 and 4.8 include an example of thermal waves with radial temperature distributions derived from dominant electron collisional diffusion.

4.2.2 Radiative Thermal Transport

For our typical helium plasma column with electron density in the range of 10^{20} cm^{-3} and temperatures up to 1 keV, radiation is not as important as electron thermal transport. Both the plasma itself and the surrounding cold gas are largely optically thin, and will not absorb most of the spectrum beyond about 30 eV photon energy. Diffusive thermal transport can only occur with the photon mean free path is small compared to the plasma length

scale. When this happens, the degrees of freedom in the photon population can carry a substantial fraction of the plasma's energy and will reach local thermal equilibrium (LTE) with the plasma. Our hotter plasma regions, with temperatures above 100 eV or so, are not in LTE with radiation and have long mean free paths for photons, so there will be no diffusive radiative thermal conduction.

We can see that the plasma should be optically thin over most photon energies by looking at the photon mean free paths for various radiative processes. First, during the first 10's of nanoseconds the main part of the plasma has high temperatures and should be fully ionized. Thus we might expect photon exchange involving bound electrons to be less important, so free-free transitions via collisional absorption should be the dominant exchange mechanism for photons. The surrounding cold gas has a very long mean free path for most of the spectrum, because the photo-ionization (bound-free) cross section is quite low. Figure 4.1 shows the mean free path for photon energies above the first ionization threshold in helium. These length scales are much, much longer than the plasma or gas cells. Thus x-rays and UV should escape without significant ionization or photon attenuation, which is important to know for x-ray diagnostics.

However, in helium plasmas there is likely a low-temperature ionizing precursor thermal wave in which diffusive radiative conduction is important. To see that this might be the case, consider the mean free path of the most dominant radiative transport mechanism, via free-free transitions, also called

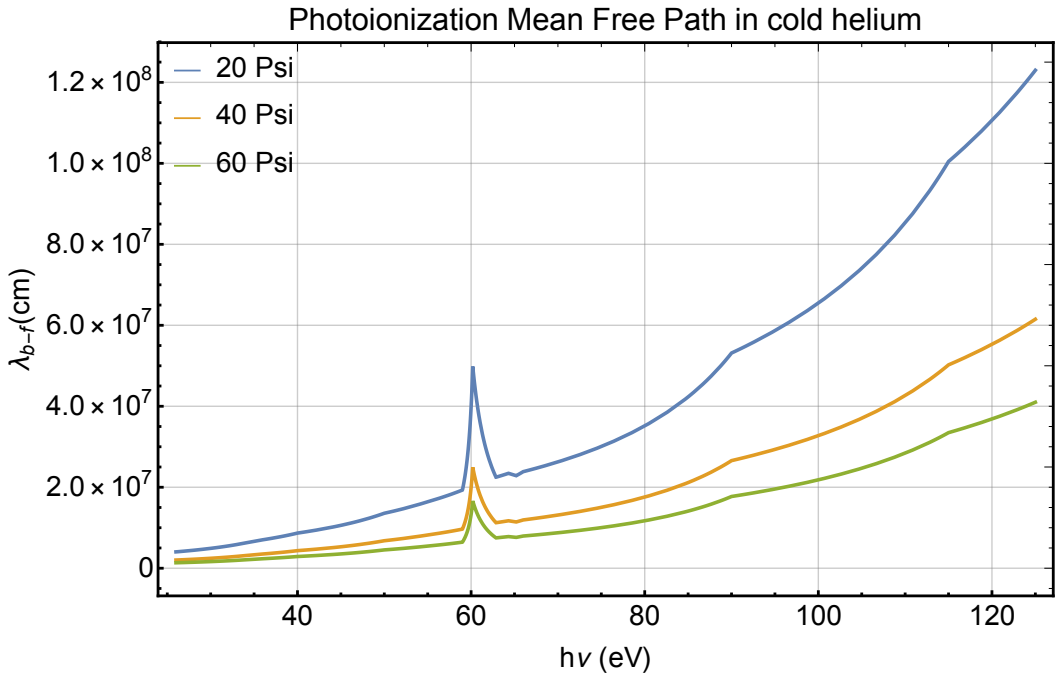

Figure 4.1: In cold helium gas the mean free path for bound-free absorption of photons with energies above the 25 eV ionization threshold in helium is quite long; it is much longer than the plasma or gas cell lengths. This figure uses data from Samson and Stolte [30]

.

collisional absorption. We are looking to see if the mean free path is shorter than the plasma length scale. The formula for this mean free path is given by:

$$\lambda_{free-free} = \left(\frac{\nu_{ee}}{c} \frac{n_e}{n_{crit}} \left(1 - \frac{n_e}{n_{crit}} \right)^{-1/2} \right)^{-1} \tag{4.48}$$

The 3D plot in figure 4.2 shows the mean free path of photons through collisional absorption after taking into account an average Z model for the ionization state as a function of temperature. A relatively short mean free

path of free-free transitions for photons of energy below about 20 eV in energy is obvious. While the mean free path gets shorter up to a certain point, in fact we might expect this curve to continue via other radiation processes such as bound-free and free-bound interactions at very low temperatures, as the plasma may only be partially ionized.

We conclude that in the range of photon energies below about 20 eV, the mean free path is short enough for diffusive transport and thus a low temperature radiative thermal wave in which the plasma is in LTE with these photons in the range of 1-20 eV. So, the temperature of this radiative precursor is likely on the order of 10-20 eV or just above the range in which helium becomes fully ionized. This scenario is also mentioned in chapter three because it likely forms the outer edge of the ionized region visible in shadowgrams. Zel'dovich and Raizer's chapter ten also mentions this scenario, in which a hot plasma core drives a radiative thermal wave outward, similar to figure 4.3 [25]. Figure 4.3 shows a low-temperature radiative thermal wave surrounding on a hot core region mediated by electron conductivity. The dimensions in this figure roughly match those expected in our experiments.

The formula for the diffusion coefficient of radiative thermal conduction is given by the following [25]:

$$\chi_R = \frac{16\sigma_{sb}T_e^3\lambda_R}{3} \tag{4.49}$$

in which σ_{sb} is the Stefan-Boltzmann Constant, T is the electron tem-

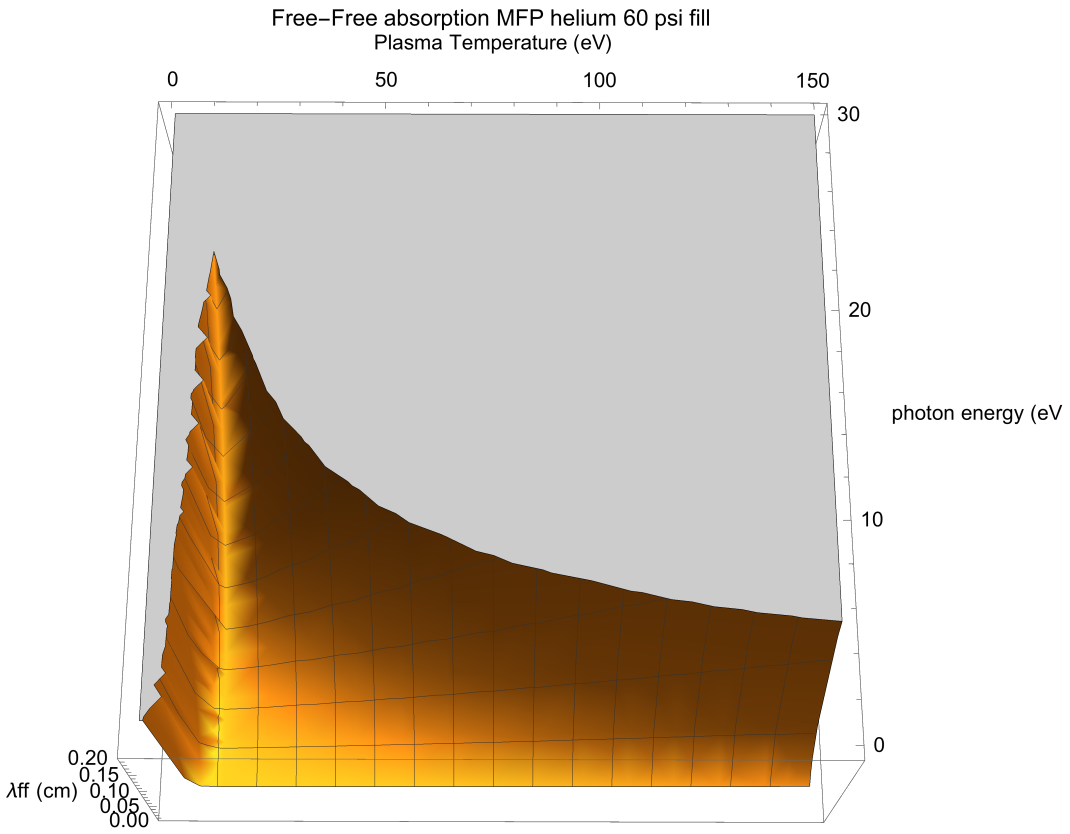

Figure 4.2: In our helium plasma, the collisional absorption mean free path is significantly smaller the plasma length scales in a narrow range of photon energies and corresponding plasma temperatures. This likely supports a low-temperature radiative thermal wave that propagates out of the hotter plasma regions. In this 3D plot, all regions with mean free path longer than the plasma length scale of about 2 mm are cut off (grey) while visible contours show the photon energies and plasma temperatures that might be acting diffusively.
.

perature, λ_r is the relevant mean free path, and c is the speed of light. Ordinary, for very large or very dense plasmas in which the plasma is optically thick across most of the spectrum, the mean free path would be taken as the Rosseland Mean Free Path. However, in our case, it might be more appropriate to

just use an averaged collisional absorption mean free path, which also happens to be a function of temperature. The negative power law dependence of the collisional absorption mean free path on temperature weakens the temperature dependence of this radiative diffusion coefficient. So, the overall temperature dependence of this radiative diffusion might be close to $T^{3/2}$. This is substantially weaker than the usual temperature dependence of radiative conductivity, and would produce a thermal wave temperature distribution that is almost a parabolic function of radius.

In experiments with laser heating of hydrogen the laser heated column appears to be narrower in shadowgrams, perhaps in the range 1-2 mm diameter rather than 3-4 mm. So, a radiative precursor is not as obvious [21]. This is likely because hydrogen is less radiative than helium and will not have the radiative precursor that can ionize the plasma outside of its hottest regions.

We can estimate the energy content of these radiative precursors, and find that it is significant. The overall temperature of such a thermal wave is most likely small, but photons and ionization potentials must also be counted. Initially, our plasma edge in shadowgrams is about 3-4 mm in diameter. If we roughly balance photon energy, ionization energy, and thermal degrees of freedom, at a fill pressure of 60 psi, this equates to about 200 J/cm consumed by this thermal wave. This is likely a nontrivial fraction of the deposited laser energy, particularly when deposited energies are likely in the sub kilojoule range.

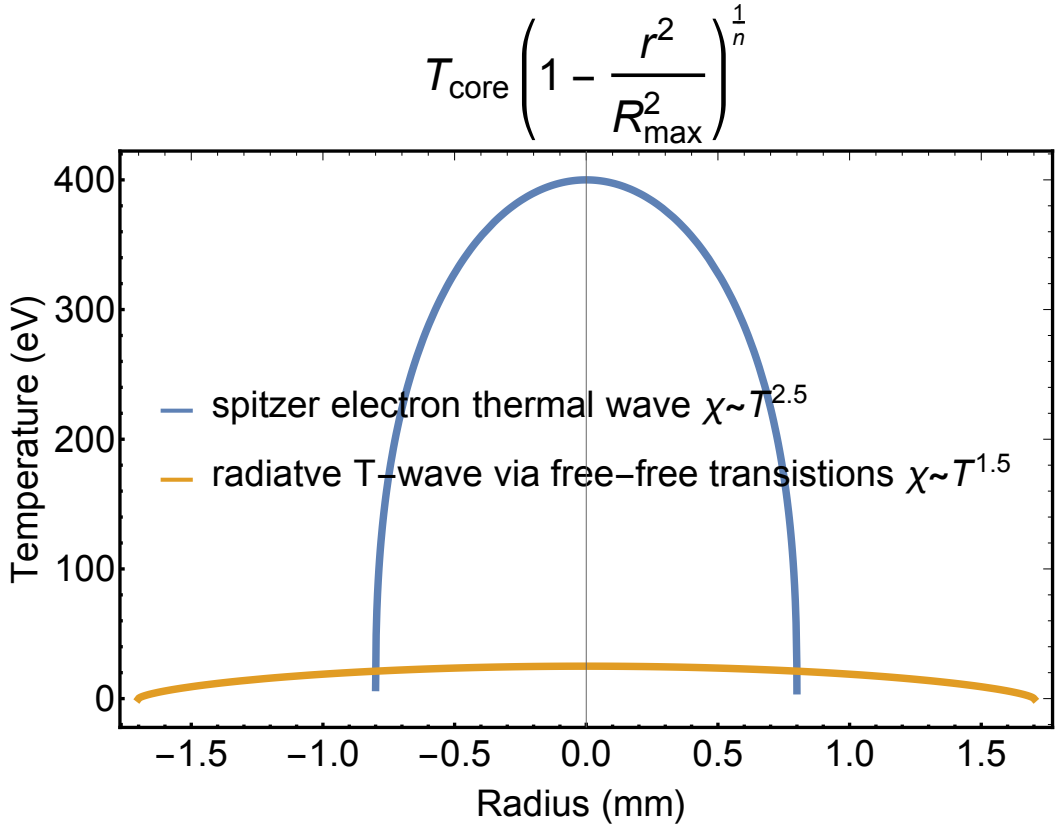

Figure 4.3: Here we plot the temperature distributions of thermal waves whose shape is determined by the dominant mode of thermal conductivity. The radiative precursor likely explains the large plasma diameters we see in shadowgrams. The energies densities and temperatures chose here are arbitrary.

4.2.3 Flux-Limited Free-Streaming Model

When thermal gradients are very high, as is often the case in high energy density plasmas, Spitzer conductivity fails to describe electron heat conductivity. In this case, heat flux is limited by the number of particles available to transport heat across the high-gradient region. This may only be important for us while the laser is heating the gas, when temperatures are

highest and length scales are smallest. In general, free-streaming heat flux will only occur in a narrow region in which the gradient length scale is smaller than about 50 times the electron mean free path λ_e [4]. Thermal gradient length scales are $L = T/\nabla T$.

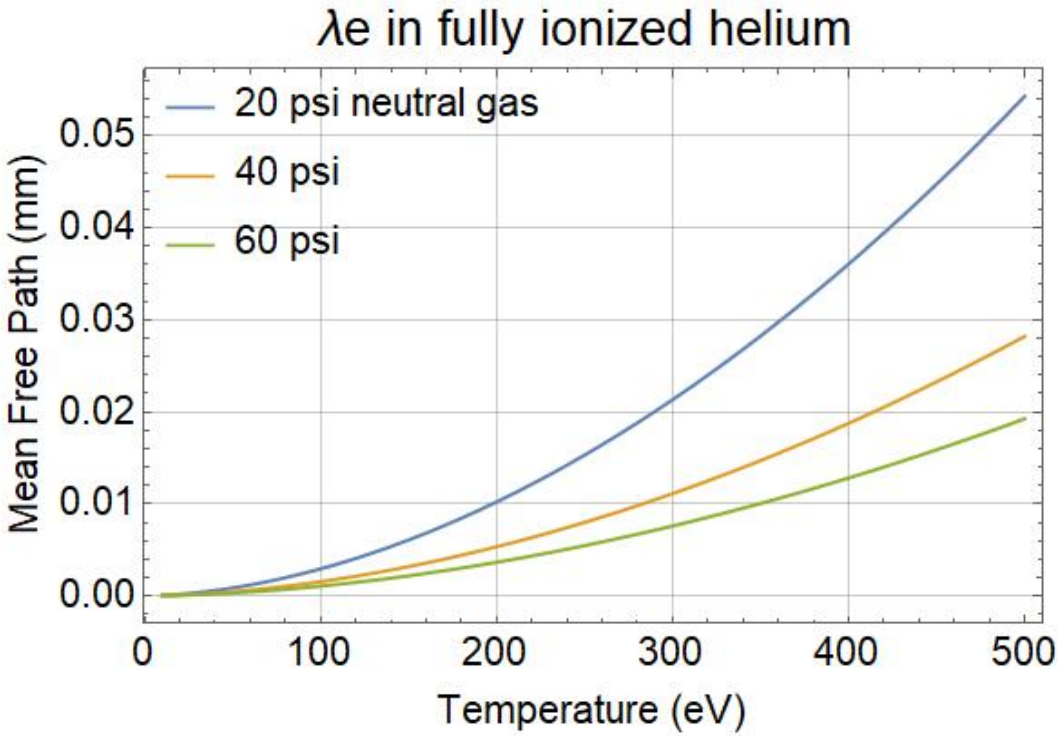

Figure 4.4: Electron mean free path varies with temperature and the initial helium fill pressures in our experiments. The calculations assume helium becomes fully ionized.

The thermal gradients we might expect are difficult to estimate. They might depend on the beam smoothing dynamics, and so could be empirically expected to be about a few hundred microns. For an electron thermal heat front with Spitzer conductivity, we expect a sharp boundary of the temperature

distribution, over which the gradient is high and the diffusive approximation might break down. So in reality, at that location we might expect the free-streaming limit to be reached and the heat flux to be reduced. The electron mean free path is typically on the order of 10's of microns, as shown in figure 4.4. So, as long as the temperature gradient length scales are less than 500 microns, the free-streaming heat flux limit may be important.

In some of models for laser absorption developed later in this dissertation we approximated radial thermal transport away from the laser heated regions by using a free-streaming electron transport model. This is a good way to estimate the maximum rate that heat is carried away from the laser channel regions, and the real behavior will be somewhere in between this limit and zero heat transport. So free-streaming limit sets a practical maximum to the diffusion rate and is useful to bound the effects of heat transport on plasma phenomenology.

In free-streaming heat conduction, the dominant mechanism of heat conduction comes from the bulk thermal motion of the plasma species flowing down the thermal gradient. An individual particle will transport an energy equal to $k_b T$ outward at a rate proportional to the thermal velocity $v_t h$. The maximum thermal energy density transport would occur when all of the plasma particles expand outward, carrying energy $k_b T$ at velocity v_{th}. But all electrons cannot go down-gradient simultaneously. Based simply on having well-distributed velocity vectors, in a strong thermal gradient one might expect a total flux of hot plasma species proportional to perhaps 20% of the

overall density. There is also a population of colder electrons flowing backward to balance the charge. In total, the reduction factor for particles contributing to free-streaming heat flux is generally considered to be about 8% to 10% of the overall density. This determines the number f in the free-streaming limit [4]. This limit has been known since the seventies and was originally the ad-hoc "flux-limiter". Much literature has been produced attempting to explain both the exact value of the flux limiter and its theoretical origins. The free-streaming limited thermal flux is given by the following:

$$F_{fs} = f n v_{th} k_b T \tag{4.50}$$

Also in this equation, v_{th} is the thermal velocity, usually taken as the mean thermal velocity. Using the equation for mean thermal velocity $v_{th} = \sqrt{\frac{2k_bT}{\pi m_e}}$ where T is again the electron temperature, the flux-limited heat flux of electrons becomes:

$$F_{fs} = 0.08 \left(\frac{2}{\pi m_e}\right)^{0.5} n_e \left(k_b T\right)^{1.5} \tag{4.51}$$

The equation usually refers to electron temperature and electron thermal velocity [4].

Practically speaking, this effect will tend to smooth out the steep boundary of a temperature distribution of a thermal wave, as well as clamp the overall maximum thermal conductivity which makes the thermal wave slower to grow initially and increases the central maximum temperature.

4.2.4 Nonlocal Transport and Super-Thermal Electrons

Nonlocal thermal transport is non-diffusive heat transport that does not depend only on local parameters, such as the local temperature or the temperature gradient. Thus the heat diffusion equation is not applicable. In fact there are generally thought to be no general analytical solutions for describing nonlocal transport effects and typically they must be modeled numerically with a kinetic model. Typically this thermal transport is carried out by non-thermal fast electrons at the tail of the velocity distribution, whose mean free path is long enough to render them unaffected by local parameters.

The edge visible in shadowgrams, which represents the outer boundary of ionization, is significantly larger than the laser diameter on sub-nanosecond timescales, which is at first surprising. It is also larger than the hottest, x-ray emitting regions. One possible explanation is non-local transport. Ditmire et. al. describe a non-local transport in plasmas in a 1998 paper. This was a plasma produced with high intensity laser interaction with atomic clusters of argon rather than slow heating over nanosecond time scales, but this plasma is heated to a similar energy density, with electron density of 10^{20} cm^{-3} and temperatures of 1 keV [31]. Subsequent work by McCormick and Arefiev et. al published in 2014 indicate that the cluster plasmas generate an ionization wave that propagates outward, with a strong electric field driven by hot electrons in the tail of the distribution that are in the 100's of keV range [32]. However, we do not expect electrons this hot in our plasmas. The radiative thermal wave precursor already mentioned provides a more compelling explanation for the

large ionized plasma diameters we see in the first nanoseconds following laser heating.

4.3 Thermal Transport in a Magnetic Field

4.3.1 Classical Cross-Field Diffusion

The diffusion of plasma species in a magnetic field can be reduced and heat conduction is slowed down because particles are confined to gyro orbits. The plasma species will deviate from their guiding centers only following collisions or in the presence of electric fields. The particle diffusion along field lines is uninhibited, but across field lines the conventional Spitzer conductivity for electron diffusion is modified to the following [5].

$$\chi_{\perp} = \frac{\chi_e}{1 + \omega_c^2 \tau_{ee}^2} \tag{4.52}$$

A simple theoretical model of collisions causing a random-walk in the guiding center of gyro orbits leads to this formula for classical diffusion, in which ω_c is the electron gyrofrequency, τ_{ee} is the electron collision time, and χ_e is the diffusion coefficient in the absence of a magnetic field, ie. the Spitzer electron conductivity. The diffusion coefficient has units of $length^2/time$. In the absence of a field the diffusion coefficient is $\chi = kT/m\nu$ where ν is the collision frequency, m is the species mass, and T is temperature. When the magnetic field is very strong and has a strong impact on diffusion, then $\omega_c \tau_{ee}$ is much greater than one. In that case we can re-write the diffusion formula

as the classical cross-field diffusion given by [5]:

$$\chi_{\perp} = \frac{kT\nu}{m\omega_c^2} = \frac{ckT\nu}{e^2B^2} \tag{4.53}$$

In which e is the fundamental charge, B is the magnetic field, kT is the temperature, c is the speed of light, and ν is the collision frequency. The scaling with $1/B^2$ is apparently favorable for magnetic confinement.

There are other types of diffusion in the presence of a magnetic field. Early research showed that many plasmas have much more rapid diffusion B-field diffusion than the classical diffusion, which led to the group to postulate a different diffusion coefficient. This Bohm diffusion is faster cross-field diffusion that scales like $1/B$, and has been shown to be related to various anomalous transport phenomenon such as emergent electric fields, convection, and instabilities [5]. Bohm diffusion is given by:

$$\chi_{\perp} = \frac{1}{16}\frac{kTe}{eB} \tag{4.54}$$

In practice, the diffusion rates typically fall within a range between classical diffusion and Bohm diffusion. The plasmas in our experiments are higher density and more collisional than typical MFE plasmas, and the classical cross-field diffusion is probably a better model. The usual MFE plasma instabilities and anomalous transport mechanisms which lead to Bohm diffusion likely do not have time to form in the face of extreme outward electron pressure.

4.3.2 Criteria for Modified Diffusion in a Magnetic Field

Electron collisional diffusion will be slowed only in some cases. If the magnetic field produces a gyro orbits are smaller than the mean free path at a given temperature, then diffusion across field lines will be altered, but in a weaker magnetic field there is no change. This can be quantified using the parameter $\omega_c\tau$, which is the product of the product of the gyro frequency in radians per second and the collision time in seconds. If electrons satisfy $\omega_c^2\tau^2 > 1$ then their collisional heat transport should be inhibited. This parameter depends on the magnetic field, density, and temperature. Since we have conducted experiments primarily at 60 psi and 20 psi fill pressures in helium, figures 4.5 and 4.6 give $\omega_c^2\tau^2$ for various magnetic fields and temperatures.

For our plasmas and for MagLIF preheat plasmas prior to magnetic flux compression, ion diffusion will not be inhibited in the magnetic field. This is because their gyro radii are larger than the plasma lengths.

4.3.3 Radial Electric Fields and the Plasma Diamagnetic Effect

When we create the hot plasma with a laser inside an applied magnetic field, it is not clear how strongly magnetized the electrons remain. As soon as laser heating occurs, the hot electrons will generate an outward pressure and try to leave the ions. This generates a radial electric field within the plasma which is present on the periphery of the heated regions, or likely near the front of the electron thermal wave. The thickness of this electric field region

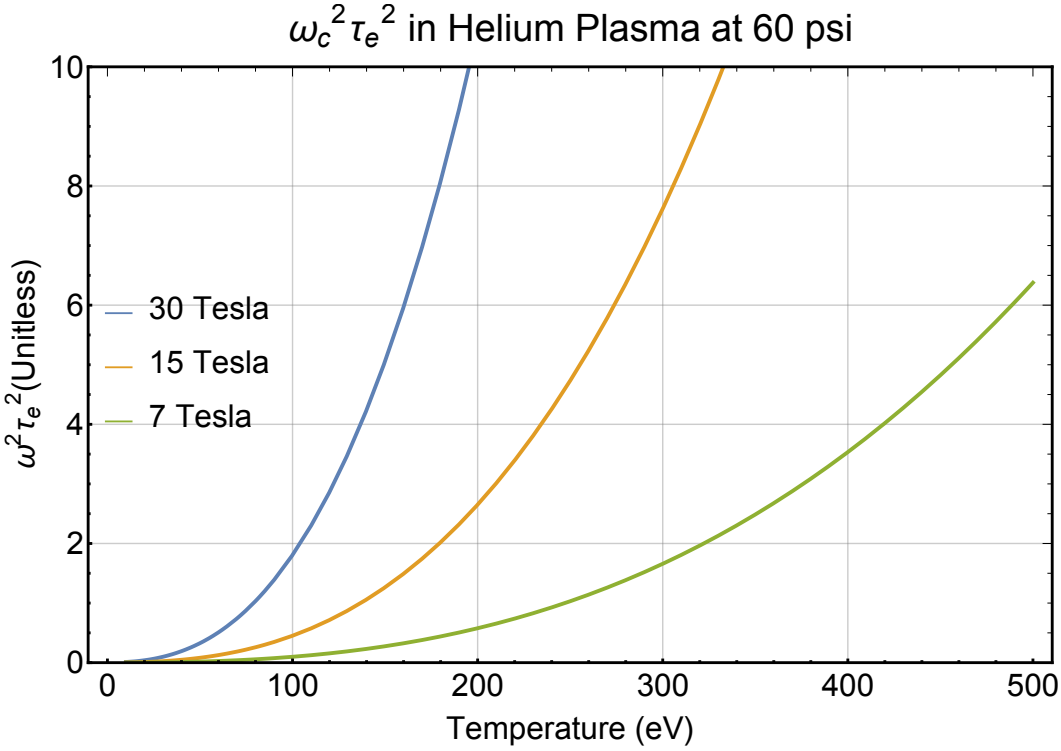

Figure 4.5: The square of the quantity $\omega_c\tau$ should be much greater than one for magnetic fields to inhibit diffusion across field lines. This parameter gives the parameters in which we can expect electron thermal conduction to be reduced. The effect is stronger for species in higher temperature plasmas because their mean free path is comparatively larger. At this density, electron thermal conduction inhibition becomes important at temperatures around 300-400 eV in plasmas in the range of magnetic fields in our experiments and in the MagLIF seed field. Conductivity in hotter plasmas will scale more slowly with temperature than the Spitzer conductivity.

is only on the order of the 10 micron Debye length, but it has important consequences [27] [25]. Given a thermal gradient on the boundary of about 100 eV over 10 to 100 μm, we have a corresponding electric field on the order of 10^6 to 10^7 V/m. If there is an applied axial magnetic field in the system,

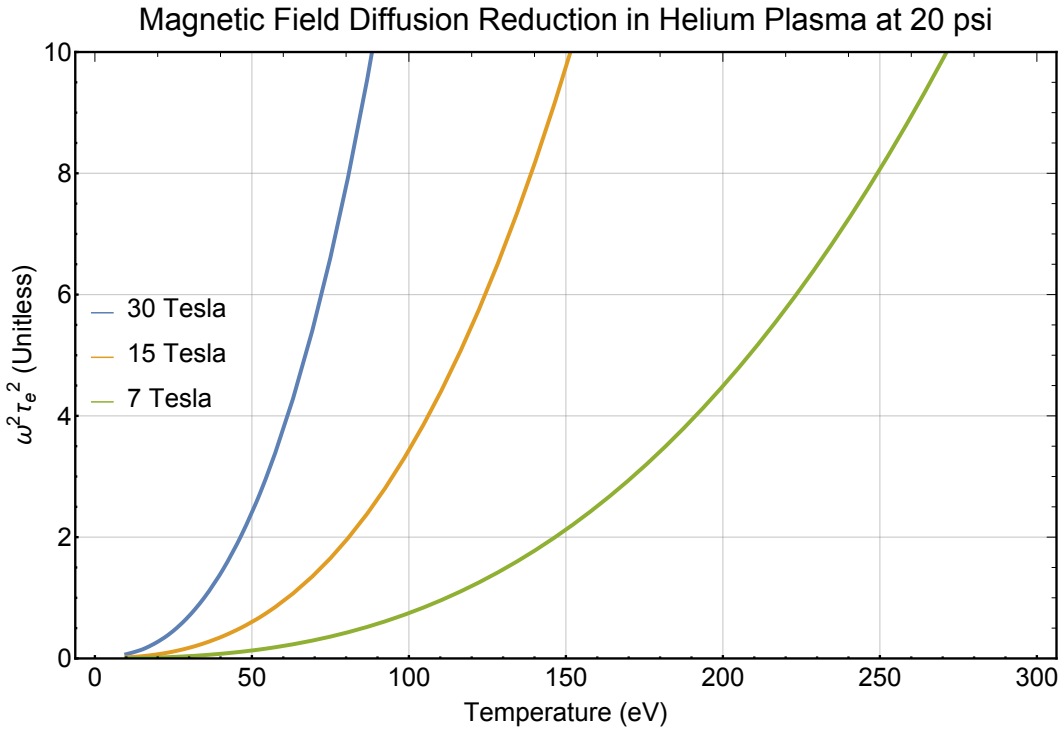

Figure 4.6: In lower density plasmas the $\omega_c\tau$ parameter is higher for the same temperatures and fields. So, it is easier to inhibit diffusion at lower density. For the range of 5-15 T, cross-field diffusion should be reduced above temperatures of about 150 eV.

the E and B fields will create an azimuthal ExB drift for electrons, which are much more mobile than the ions. Ordinarily, the ions would be affected too and travel in the same direction, causing a bulk rotation of the plasma, but the ions are much heavier and their gyroradius is large enough that the ExB drift will not affect them [27]. This azimuthal electron current generates an magnetic field that will tend to oppose the externally applied magnetic field. This is the plasma diamagnetic effect. Back of the envelope estimates are that the total azimuthal current may be significant, which means the plasma's

internal magnetic field may be strongly weakened by this diamagnetic effect. We would need to account for this when developing models for cross-field diffusion.

The radial electric fields can be short-circuited by electric current through the plasma that travels axially to regions without strong thermal gradients or radial electric fields [5]. In our case this might occur if the ends of the plasma near the LED and at the end of the laser heated region possess small radial temperature gradients. This will tend to counteract the plasma diamagnetic effect.

Temperature gradients by themselves can also generate an azimuthal plasma current even in the absence of the external magnetic field. As a radial electric field develops due to radial pressure, currents may develop in opposition to this field. One way to do this is to reduce the outward thermal pressure, and this can occur through magnetic pressure generated by azimuthal currents. So even in the absence of a magnetic field there may be azimuthal currents and an azimuthal or helical magnetic field. This is the Nernst effect in plasmas.

All of these factors should be captured in the appropriate simulations or in a full reworking of the Braginskii approach, but we would need to be careful to build the appropriate two-fluid model and finite size effects [27]. The important point is that using the external magnetic field's vacuum value is only an approximation and the real field is likely weaker because of diamagnetism and Nernst effects.

4.3.4 Phenomenology of Cross-Field Diffusion

We cannot use a thermal wave approach to model heat diffusion across magnetic field lines. Ignoring other forms of heat transport such as bulk plasma motion, the electron diffusion will again follow the heat equation, but the functional dependence of the diffusion coefficient on temperature is now much more complex. To make matters more complicated, we have seen that the magnetic fields we apply are not strong enough to quench transport at all temperature ranges, and so we cannot use the limit formula for cross field diffusion either. In cylindrical geometry, we would need to solve the following nonlinear partial differential equation:

$$\frac{dT}{\partial t} = \frac{1}{r}\frac{\partial}{\partial r}\left(\frac{kT/m\nu}{1+\omega_c^2\tau_{ee}^2} r \frac{\partial T}{\partial r}\right) \tag{4.55}$$

Obviously this is a difficult equation to solve, although perhaps not impossible. And again, if one is going to this effort, a better self-consistent description of this plasma would be given by a solution to the plasma fluid equations as was worked out by Braginksii because it would include bulk transport, electron currents, and fields in addition to heat diffusion [26]. One might attempt to simplify the problem if our the magnetic field was very strong ($\omega_c^2\tau_{ee}^2 >> 1$) since in that case cross-field diffusion scales more simply like $T^{-1/2}$. Note that this situation does not really apply to us since our magnetic fields are effectively still "weak" over a range of temperatures. Even this simpler temperature scaling does not support the same type of traveling

nonlinear thermal wave we derived earlier, which applied for positive powers of temperature in the coefficient of diffusivity. But there is indeed a traveling wave solution to this easier PDE with $\chi\ kT^{-1/2}$, which was found by T.K. Amerov (1990) and J.R. King (1992). One might attempt to implement it, but we have not done so.

We might make a guess at the simplest approximation we might make to the solution of the heat equation with cross-field diffusion. Let us look at the behavior of the diffusion coefficient at various fields, using the full form of the modified cross-field diffusion coefficient given in equation 4.52.

Figure 4.7 shows that, effectively, a magnetic field clamps the diffusion coefficient at a maximum value, and from there the dependence on temperature is weak. In the low-temperature range, the diffusion coefficient still depends on temperature in the same way as Spitzer Conductivity. But, with this observation, we can postulate an extremely rough approximation, which just takes the diffusion coefficient to be constant. This is a zeroth-order approximation. The fundamental solution to the heat equation with a constant coefficient of diffusivity is well known as the Gaussian heat kernel. In cylindrical-polar geometry this solution is given by the following, with a normalizing factor included:

$$T(r,t) = \frac{E}{4\pi\chi t} e^{-r^2/4\chi t} \tag{4.56}$$

χ is the supposedly constant coefficient of diffusion that shows up in the heat equation, with units of $length^2/time$. The factor Q is the total amount

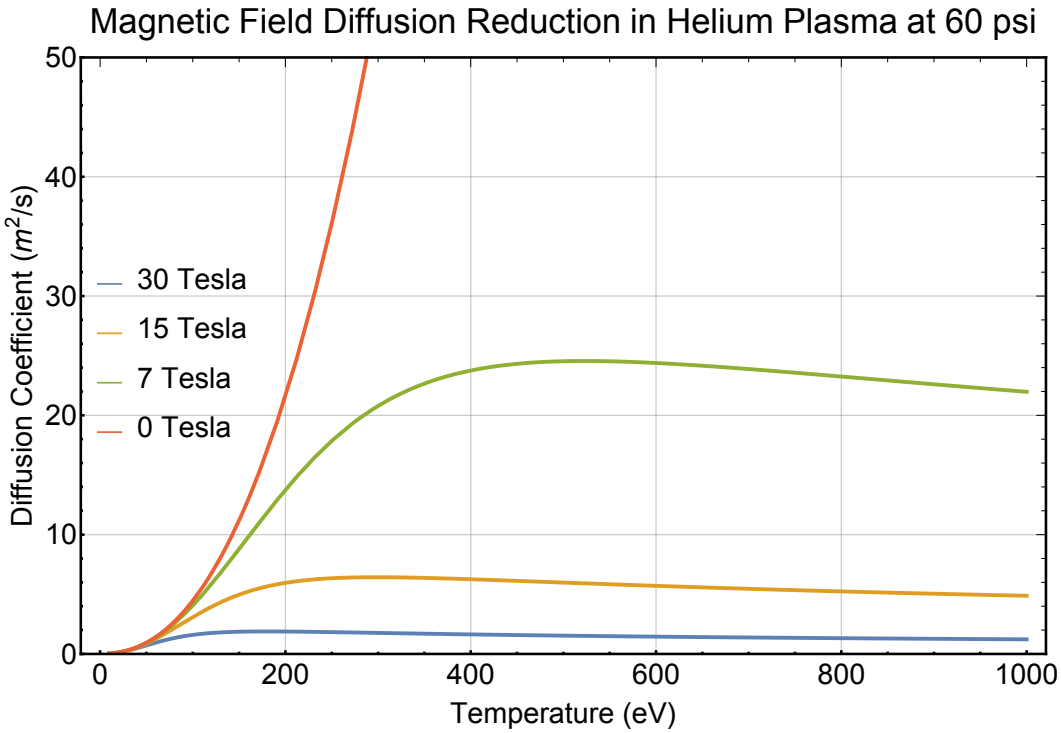

Figure 4.7: The diffusion coefficient as it would appear in the heat equation for cross-field diffusion. Notice that in the absence of a field, the diffusion coefficient scales as a power of temperature continuously. Once a field is applied, there is a maximum diffusion coefficient that is not exceeded. Diffusion will be fastest at that temperature.

of heat in the problem, so it is added to give the equation the right units. It should have units of temperature times area, eg. $eV * cm^2$. This ensures that the heat kernel will have units of temperature, and when integrated it will have the same units as Q of temperature times area. We then multiply by the particle density to get the total amount of energy per unit length in the problem, similarly to the heat wave scenario.

It is worth noting that if we take this approach to approximating the

solution to the heat equation, we will find it very inadequate in the regions of low temperature. This is because our constant diffusion coefficient approximation does not capture the fact that the diffusion coefficient indeed falls to zero at zero temperature. This means that the low-temperature tails of the Gaussian distribution will not be present, and the radial temperature distribution will still have a strong, sharp edge. Of course, radiative processes may take over at lower temperatures.

Figure 4.8 shows the general types of thermal waves which we might expect, with radiative and electron-thermal waves in general being less centrally peaked. Generally speaking, regardless of what methods of approximation we might consider, the magnetic field is going to decrease thermal conduction. This will cause the radial temperature distribution to be narrower than it would be otherwise. Perhaps the radial temperature distribution will be closer to a Gaussian or a parabola. Regardless, the central temperature is expected to be higher with an applied field.

It is important to note that this approach ignores a source term from an initial spatial distribution of laser heating. Z-Beamlet heating beams with a distributed phase plate and a diverging beam would likely heat a relatively uniform, round area. In the absence of self-focusing effects the beam should have a waist of about 0.8 mm. Nonlinear laser-plasma interactions and focusing due to passage through the plasma may cause the ordinarily flat-top profile to evolve to more of a Gaussian-like radial profile. Thermal transport concurrent with beam transport is a complex feedback process, since the hottest regions

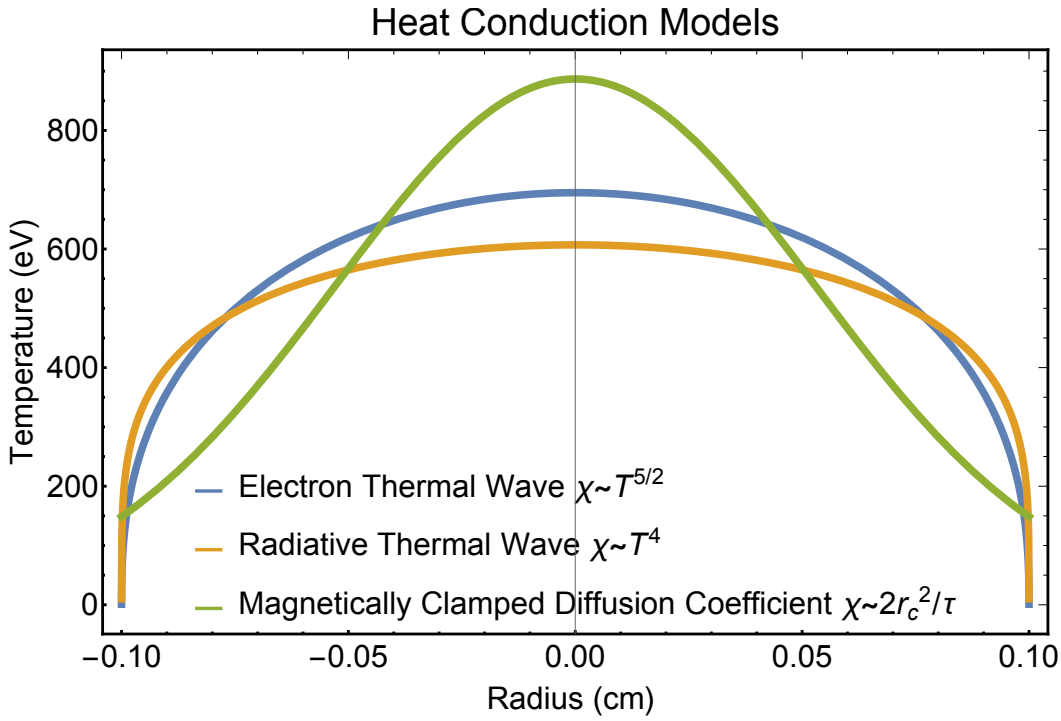

Figure 4.8: Various models of solutions to the heat equation. In general, as the temperature dependence in the thermal diffusion coefficient weakens, the temperature distribution will become narrower, more centrally peaked, and less sharply defined on the edges. Cross-field diffusion that scales like temperature would produce a parabolic heat wave. For our zeroth-order approximation of a diffusion coefficient that is constant with temperature, we have the Gaussian heat kernel solution which in this case is shown without its wide, low temperature tails. Of course, cross-field diffusion is not truly a constant, but perhaps if we add low-temperature radiative diffusion and cross-field diffusion together an approximately gaussian shape might be appropriate. Note that in all cases depicted here, the energy density is 500 J/cm, and the central peak temperature has been correspondingly scaled. This energy density is representative of that which we might expect from our experimental data.

are more transparent while the regions that are cooled can absorb more energy.

It is difficult to say what shape the heating beam will take, but intuitively

we might expect these two behaviors to balance each other and produce a relatively uniform heating region with a width around 0.7 mm. The laser will cause heating over time and this probably makes thermal waves propagate further outward while maintaining the central temperature at a relatively high and spatially uniform value within the beam waist. All heat distributions we wish to compare with x-ray profile measurements would need to be corrected for this.

There are many other failings of the zeroth-order approximate Gaussian model. For example, the magnetic field is likely to be reduced inside the plasma by nernst and diamagnetic effect. This causes pileup of the field lines outside the plasma and reduces thermal conductivity only at the periphery, which steepens the temperature gradient while leaving the interior regions virtually unchanged. This would cause the profile to resemble a more conventional thermal wave. And, of course, the diffusive model ignores hydrodynamic transport. In the presence of a magnetic field, hydrodynamic transport very likely dominates energy transport over electron diffusion. For this reason, nonlinear self-focusing due to plasma density variations may be stronger with a magnetic field.

4.4 Conclusion

Electron thermal transport dominates the hottest regions of the plasma, which will transport heat away from the laser heated regions. A thermal wave with a well understood shape will spread from the laser heated region on sub-

nanosecond timescales, roughly doubling the size of the hottest part of the plasma. The highest thermal gradients are limited by free-streaming particle currents and will have thermal conduction reduce. Thermal conductivity at low temperatures is relatively high compared to electron conduction, due to radiative free-free transitions, which supports a low-temperature ionizing precursor that propagates further out of the hot plasma core. Effectively, radiation dominates the low temperature conductivity and means that the low-temperature diffusion coefficient of electron thermal conductivity is less important. After about a nanosecond, thermal waves will stop controlling the temperature distribution and ion density will begin to transport faster than heat diffusion. A magnetic field will clamp thermal conductivity and cause the radial temperature distribution to appear narrower, perhaps similar to a Gaussian profile. In future chapters, we will be able to compare models of temperature distributions to x-ray emission profiles and temperatures convolved from them.

Chapter 5

Plasma Sound Speed Theory and a Method for Estimating Energy Density

This chapter discusses the phase of plasma expansion in which it is expanding at an approximately constant speed equal to the ion acoustic speed. This is the phase during which hydrodynamics begins to be relevant, as prior to this during laser heating and thermal wave dynamics the ion density does not change by more than perhaps 20%. This expansion phase corresponds with a time when the tremendous electron thermal pressure of the plasma interior begins push the ions outward. The electrons are bound to the ions electrostatically, so the electron thermal pressure drives the ions outward at a speed that is determined by the ion's inertial mass. This expansion phase lasts between the time the laser is on and about 15-30 nanoseconds later, or whatever time the plasma's hot regions have doubled in radius. Because the sound speed depends only on the electron temperature, we can use this phase as a diagnostic of the electron temperature in the early part of the plasma's evolution.

It is worth noting that this analysis is less applicable if the plasma is cooling via radiation, which it will do if it contains more radiative ion species

like neon. This causes the plasma's electron thermal pressure to drop more rapidly, and couples less kinetic energy to the ions. It also couples the ion temperature to the electrons and photons through free-free transitions, which reduces their outward kinetic energy.

The sound speed expansion will persist while the bulk of the plasma's energy remains in the thermal pressure of electrons. But, meanwhile the expansion at the boundary is sweeping up new, cold ions and piling them up at the plasma boundary where the thermal gradient is high. A region of increasing ion density begins to form at the boundary of the thermal region. The fraction of the plasma's total energy in the form of the kinetic energy of these ions grows comparable to the electron thermal pressure. Once this happens the plasma has transitioned to a blast wave transport regime.

We will look at the effect of an external magnetic field on the plasma transport during the plasma expansion at the sound speed and early in the blast wave evolution. Chiefly, we will look at a comparison of thermal to magnetic pressure which is characterized by the plasma beta parameter.

Finally, and most importantly, In this chapter we will develop a method for finding the energy per unit length in a cylindrical plasma. The method is independent of blast wave trajectory analysis, since it relies on the early phase of plasma expansion prior to the transition to a blast wave. We will later use it to make inferences about the energy density distributions in the plasma, as well as the overall total energy density.

5.1 Hydrodynamics of Ion Acoustic Waves and Blast Wave Transition

5.1.1 Ion Acoustic Waves

The ion sound speed, or simply the sound speed, is the natural speed for free-expansion of a plasma. There are multiple ways of thinking about it. For us it will be most relevant to think of it as the speed limited by the inertia of the ions which are driven outward by electron thermal pressure. One can derive the speed of these waves by equating the ion kinetic energy with the electron thermal energy through a pressure. However, one can also derive the speed by using the equations of hydrodynamics to derive a wave equation, with the ion acoustic speed as the speed of small perturbations in density with an electrostatic restoring force. We will work through a quick derivation using the electron pressure.

The electron pressure or energy density is given by $\gamma n k_b T_e$, where γ is the adiabatic index, n is the number density, and kT is the thermal kinetic energy as usual. This exerts an electrostatic force per unit area on the massive ions, which will move with kinetic energy density given by $(1/2)m_i n_i c_s^2$. Equating these two energy densities, we get the following mostly correct form for the sound speed:

$$c_s = \sqrt{\frac{\gamma_e Z k T_e}{2 m_i}} \tag{5.1}$$

You can also carry out the same derivation by considering the energy in each ion and electron and equating them. Note that for very high pressures

and electron temperatures, γ_e is frequently taken to unity because thermal conductivity is great enough to keep them isothermal on long time scales. The ion sound speed is dispersionless and independent of the density, and is thus a robust method of establishing the electron temperature if γ and the ionization state of the ions Z are well known.

Note that the full version of the ion sound speed includes the thermal energy of the ions also:

$$c_s = \sqrt{\frac{\gamma Z_i k T_e + \gamma_i k T_i}{m_i}} \tag{5.2}$$

However, in the case of laser-heated plasmas the electrons are usually much hotter than the ions so we can ignore the ion temperature term on timescales smaller than ion-electron collisions. In our helium plasmas, inverse bremsstrahlung should strongly preferentially heat the electrons. So a realistic form of the sound speed in helium with Z=2 becomes the very simple expression:

$$c_s = \sqrt{Z k T_e / m_i} \tag{5.3}$$

How long does this version of the equation remain valid? The following is the equation for the ion-electron collision frequency, which roughly determines the timescale for energy transfer from electrons to ions:

$$\nu_{ie} = \frac{4\sqrt{2\pi} m_i Z^2 e^4 ln\Lambda_e}{3\left(4\pi\epsilon_0\right)^2 m_e^{1/2} \left(kT_e\right)^{3/2}} \tag{5.4}$$

where e is the fundamental charge, kT_e is the temperature of electrons, m_i is the ion mass, n_i is the ion density, m_e is electron mass, and $ln\Lambda_e$ is the Coulomb Log [5]. From this equation we find collision times on in the range of about a nanosecond to many tens of nanoseconds, depending on the temperature and other factors; see figure 5.1. Lower temperatures will equilibrate temperature faster. These timescales are slower than the laser heating timescale and often slower than the sound speed expansion regime, so using the electron temperature for the sound speed is sufficient.

5.1.2 Approximate Solution of Gas Dynamic Equations During Transition to Sound Speed Expansion

I found a somewhat new expression for the sound speed during the time that mass is accumulating, between the time when sound speed is approximately constant and when a blast wave self-similar solution applies. This approach goes one step beyond equating energies of electron pressure and ion kinetic motion with all mass at the boundary since it allows for density changes. This approximation method is superficially similar to the Chernyi approximation for a blast wave which will be given in chapter six which I found described in Zeldovich and Raizer's text [25]. This approach is is slightly more general because it does not assume that all of the mass has been transported to the shock shell as the Chernyi approximation does.

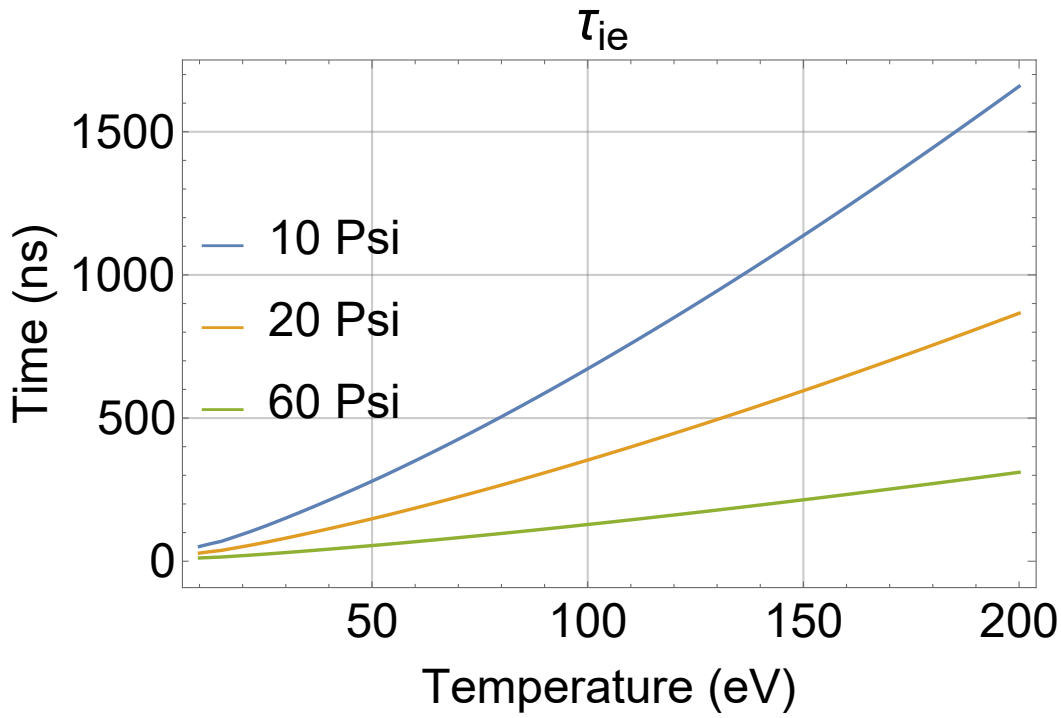

Figure 5.1: The electron-ion collision timescale is long compared to our plasma heating and sound-speed expansion, which usually happens in less than 30 ns.

There are several fundamental assumptions, which are approximations, that I make to derive this result. We will divide our cylindrical plasma into two regions. The central region inside r_1 is defined by approximating a uniform pressure with no pressure gradient. In that region we define the central pressure as p_c out to the radius r_1, so $\nabla p_c = 0$ throughout that region. Outside the region of constant internal pressure is a peripheral shell region of accumulating mass between r_1 and r_2, with thickness $r_2 - r_1 = \Delta r$.

Next we assume uniform densities inside the plasma, with a discontinuous jump at r_1. These densities are ρ_c and ρ_2. Consequently, since pressure

is assumed to be constant in the central region, constant mass density also implies a constant temperature there. Also, the external density ρ_0 outside the plasma is constant. Intuitively, $\rho_c < \rho_0 < \rho_2$.

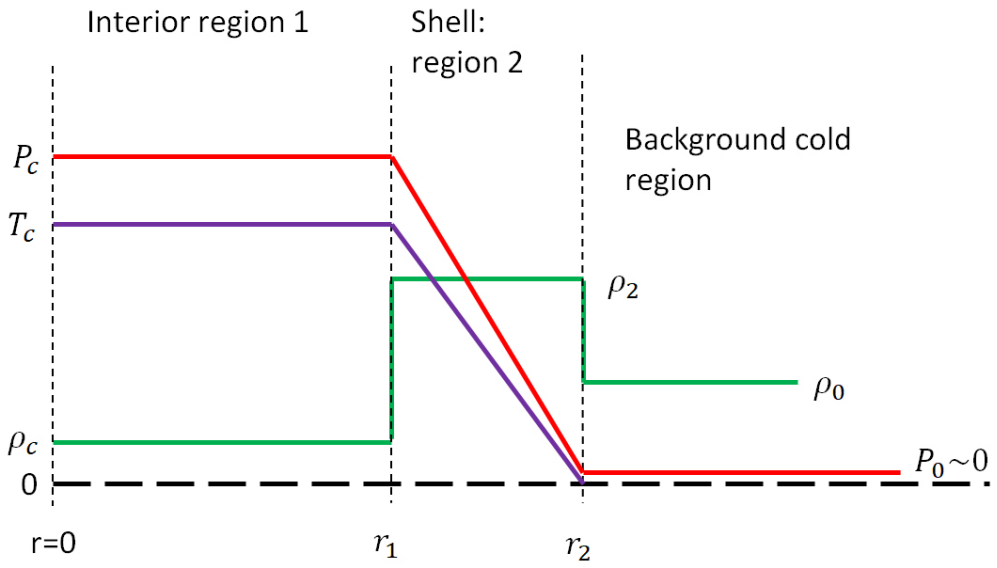

Figure 5.2: This diagram shows the variables we use in the approximate solution to the gas dynamic equations which we will use to get a density-ratio dependent sound speed.

The last major physics approximation involves the pressure in region 2, which is the region accumulating a higher density. We assume this pressure ramps down linearly from p_c to p_0, the external pressure. So in the shell region $\nabla p = (p_c - p_0)/\Delta r$. If later we could assume p_0 is small compared to p_c to get a further simplification, but we will wait to do this.

Now, using energy conservation, we will find an expression for the total energy per unit length. This is given by the radial integral of the pressure,

as well as the kinetic energy of the outer shell region. The energy balance is initially almost entirely in electron pressure, but once the radius has doubled the kinetic energy in the thickening high-density shell is comparable and the transition to blast wave dynamics occurs. We are interested in the intermediate regime in which both thermal pressure and kinetic energy are important. Since the pressure in the shell region is linearly ramping, we approximate by integrating the average. The kinetic energy term can be found using the mass density of that region and the speed v_2 at which it is expanding.

$$\frac{E_{total}}{2\pi} = \int_0^{r_1} p_c r dr + \int_{r_1}^{r_2} \frac{1}{2}\left(p_c - p_0\right) r dr + \int_{r_1}^{r_2} \frac{1}{2}\rho_2 v_2^2 r dr \tag{5.5}$$

Next, we can write the equation for the force acting on the mass, based on the gas dynamic equations and including the advective term. This equation of motion for a gas has the following form:

$$\frac{dv}{dt} + v\frac{dv}{dr} + \frac{1}{\rho}\frac{dp}{dr} \tag{5.6}$$

We are concerned about the motion of the shell region, so this is the region for which we want to find the speed v_2.

$$0 = \rho_2 \frac{dv}{dt} + v_2 \rho_2 \frac{-v_2}{\Delta r} + \frac{p_c - p_0}{\Delta r} \tag{5.7}$$

Now we can assume that p_0 is small compared to p_c. Rearranging the terms, we find:

$$v_2^2 \rho_2 = \rho_2 \Delta r \frac{dv}{dt} + p_c \tag{5.8}$$

Now that we have this force expression, we can combine it with the equation for energy density. Conveniently, the LHS appears inside some of the integrals in the energy equation. The goal will be to evaluate the integrals and solve for $\frac{dv_2}{dt}$. We will also approximate p_0 to be 0. The energy equation becomes:

$$E_{total}/2\pi = \frac{1}{2}\int_0^{r_1} p_c r dr + \frac{1}{2}\int_{r_1}^{r_2} \left(\rho_2 \Delta r \frac{dv_2}{dt} + p_c\right) r dr + \frac{1}{2}\int_{r_1}^{r_2} (p_c - p_0) r dr \tag{5.9}$$

Next, by grouping terms and consolidating integral ranges as well as ignoring the background pressure p_0, we find:

$$E_{total}/2\pi = \int_0^{r_2} p_c r dr + \frac{1}{2}\int_{r_1}^{r_2} \left(\rho_2 \Delta r \frac{dv_2}{dt} + p_c\right) r dr \tag{5.10}$$

On the path toward solving for $\frac{dv_2}{dt}$ there is one more relation that we can bring in, which has to do with mass conservation. Since the total mass is conserved within the plasma volume defined by the outer radius r_2, we know that the volumetric sum of the two densities over their respective regions must equal the background density over the whole volume. The densities ρ_2 and ρ_c are changing, as well as the thickness of the shell region Δr, so our solution will actually be unconstrained with the above equations and the mass conservation alone. However, let's go forward with finding the solution.

Mass conservation goes like the following, in which we have made an approximation for the volume of the shell:

$$\pi\rho_c\left(r_2-\Delta r\right)^2+2\pi\rho_2 r_2\Delta r=\pi\rho_0 r_2^2 \tag{5.11}$$

This can be solved for a term that already appears in the consolidated energy equation above, which allows us to eliminate all ρ_2 dependence.

$$\rho_2 r_2\Delta r=\frac{1}{2}\left(\rho_0 r_2^2-\rho_c\left(r_2-\Delta r\right)^2\right) \tag{5.12}$$

The left hand side can be substituted into the energy equation now. Solving for $\frac{dv}{dt}$ we arrive at the following:

$$\frac{dv}{dt}=\frac{E_{total}/(2\pi)-p_c r_2^2}{\frac{\Delta r}{4}\left(\rho_0 r_2^2-\rho_c\left(r_2-\Delta r\right)^2\right)} \tag{5.13}$$

Since ρ_c, r_2, and Δr are all functions of time, this differential equation is not well determined. We know the asymptotic limits on this equation, which come from thermodynamics. In the early time, the solution will be the sound speed propagation of the plasma edge. Late in time, the ratio of Δr to the outer radius r_2 becomes fixed by the thermodynamic limit of density accumulation, which for a monoatomic gas or plasma is a factor of four times the background gas density. We will see this in the chapter about blast waves based on $\rho_1=\rho_0(\gamma+1)/(\gamma-1)$ with $\gamma=5/3$. This fixes the ratio $\Delta r/r_2$ to be 1/8 in the asymptotic limit of the Sedov blast wave (see chapter six). However, in the intermediate regime the density ρ_c is gradually depleting.

One approach to finding an approximate solution to this equation would be to relate the central density ρ_c to the inner radius $r_1 = r_2 - \Delta r$ and the central pressure. Since the pressure is constant in the center, we could approximate the shell to be thin and assume the pressure is falling roughly according to the energy density decreasing with r^{-2} for cylindrical geometry. But that's basically what Chernyi does. To solve the differential equation 5.12 ultimately we'd need to have some expression relating the rate of density buildup to the radius somehow, possibly by using the initial and final densities we expect and smoothly interpolating. I will not do that but one could do it.

Ultimately, we can make one last approximation- we can find an expression for the sound speed in the earlier phase of expansion, when $\frac{dv}{dt}$ is small. Let's say that the gradient in pressure is a constant in this region. From the force equation, $\nabla p/\rho + v_2 \frac{dv}{dt} = -\frac{dv}{dt}$. When the change in velocity is small at early time, the sound speed regime dominates. We have:

$$\nabla p_2 \simeq \frac{p_1 = p_0}{\Delta r} = -\rho_2 v_2^2 \frac{\Delta v}{\Delta r} \tag{5.14}$$

Based on our assumptions of constantly ramping variables in the shell, Δv_2 here could just be $-v_2$, since v goes from 0 to v_2 in backward order. If we ignore p_0 again and cancel Δr, we can further simplify. Also, we know that $p_c = \rho_c k T_c / m_i$, so we find that

$$v_2 \approx \pm \sqrt{\frac{\rho_c}{\rho_2} \frac{kT_c}{m_i}} \tag{5.15}$$

Which is an interesting result. This is the sound speed, but the sound speed is modified by a fractional ratio of the density in the center to the density in the shock shell. As the density in the shell increases, the sound speed will fall. Based on what we will see in the next section, this proceeds until around the time the radius has roughly doubled in the case of a cylindrical plasma. A somewhat more complete version of this result would provide expression for this density change as a function of radius.

5.1.3 Sound Speed Transition to Blast Waves

Sound speed expansion will slow to a self-similar Sedov blast wave trajectory around the time the radius has roughly doubled, and we will show that here. This is the plasma length scale for the energy balance to transition from primarily thermal energy to half thermal and half kinetic, with the shocked shell region at the thermodynamic limit of density. We wish to find the final radius r_2 at which the total thermal energy per unit length of a cylindrical plasma with initial radius r_0 will be split equally between thermal and kinetic energy of expansion. We can find this energy-balancing radius as a function of the initial radius. It characterizes the length scale at which the sound speed expansion at a constant rate can no longer be valid.

Let us begin by looking at expressions for energy. If we assume a uniform energy density to start with, then initially the energy in the plasma will be characterized approximately by $\rho_0 k T_0 \pi r_0^2 / m_i$. The plasma will initially expand at the sound speed, given by $\sqrt{\gamma k T_0 / m_i}$. The kinetic energy of the

shocked shell will be given by $(1/2)\,2\pi\Delta r(r_2-\Delta r)\rho_2 v^2$, where v_2 will initially be the sound speed.

Equating the initial thermal energy per unit length to half of the kinetic energy of the shell gives us the following:

$$\rho_0 k T_0 \pi r_0^2/m_i = \frac{1}{2}\pi\Delta r\,(r_2-\Delta r)\,\rho_2\,(kT_0/m_i) \tag{5.16}$$

Using the sound speed results in some cancellation. As the plasma expands initially close to the sound speed, the density in the denser shell will be increasing as we saw in the previous section. In the blast wave chapter, we saw that geometry and thermodynamics dictate that the asymptotic limit for late time blast waves in plasmas is that the shell density is four times the background density and the dense region thickness is about 1/8th of the outer radius. Using these relationships for Δr and ρ_2 we find that:

$$r_0^2\rho_0 = \frac{1}{2}\frac{r_2}{8}\frac{7r_2}{8}\rho_0 \tag{5.17}$$

After cancelling and solving, and pretending that $7/8 = 1$, we find $r_2 = 2r_0$. So, once the plasma has roughly doubled in radius, we can expect the sound speed to no longer be a valid approximation of the plasma expansion rate and the blast wave regime is beginning to become relevant.

5.2 Hydrodynamics and Sound Waves in a Magnetic Field

In our experiments, external magnetic fields will have a minimal influence on density transport during the initial stages of sound speed expansion, as is the case with the MagLIF preheated plasma. However, as the blast wave evolves after the radius more than doubles, thermal driving pressure will drop sharply. This is because the plasma gains more matter from the surrounding cold gas so it will drop rapidly in temperature, while greatly increasing in volume. The magnetic field exerts its own pressure and we will learn how to compare it with plasma pressure. We expect a time during blast wave expansion in which the magnetic field is important.

Also, not only does the plasma pressure drop, but the magnetic field strength can be increased outside the shock boundary of the plasma. This shock-driven magnetic flux compression will be significantly stronger if the plasma is surrounded by a conducting metal cylinder, as is the case for MagLIF but not in our case. In that case magnetic field lines are slow to diffuse into the electrically conducting plasma and liner from their induced opposing currents. However, once the plasma's thermal pressure approaches the magnetic pressure from the magnetic flux compression between the liner wall and the shock boundary, we have achieved a unity-beta condition and the sound wave or shock wave may slow or reflect. These behaviors will not be observed in our gas cell experiments because our field coils are too large in radius to influence the plasma behavior significantly through magnetic flux compression, but on

long time scales we might expect the blast wave to slow down more rapidly than the Sedov solution would indicate. We have not observed this behavior in experiments, but there have not been any successful to date. If we could get a trajectory of blast waves on long time scales it would help place constraints on the background field and may provide an interesting test bed for plasma diamagnetism and Nernst effects in the future, but this is beyond the scope of our work here.

5.2.1 Beta Parameter and Duration of High beta Conductions

The earlier discussion does not describe bulk plasma transport in magnetic field. The sound speed transport of plasma density assumes that the outward thermal pressure is the only important pressure driving expansion of the plasma. In fact, if there is an applied magnetic field, it exerts a pressure that tends to oppose outward thermal pressure. We can measure the ratio of these pressures with the beta parameter. Plasma β has thermal pressure in the numerator. In SI β is given by the following equation, in which B is the magnetic field, n is the particle number density, and μ_0 is the permittivity of free space.

$$\beta = \frac{nkT}{B^2/2\mu_0} \tag{5.18}$$

Initially, our plasma is very hot and the thermal pressure is hundreds of times greater than magnetic pressure. Figure 5.3 gives the plasma beta for a range of temperatures with the three initial helium fill pressures. The

sound speed transport will not be affected because beta is so high, although technically we must look at the magnetosonic wave rather than the ion sound wave as we shall see eventually.

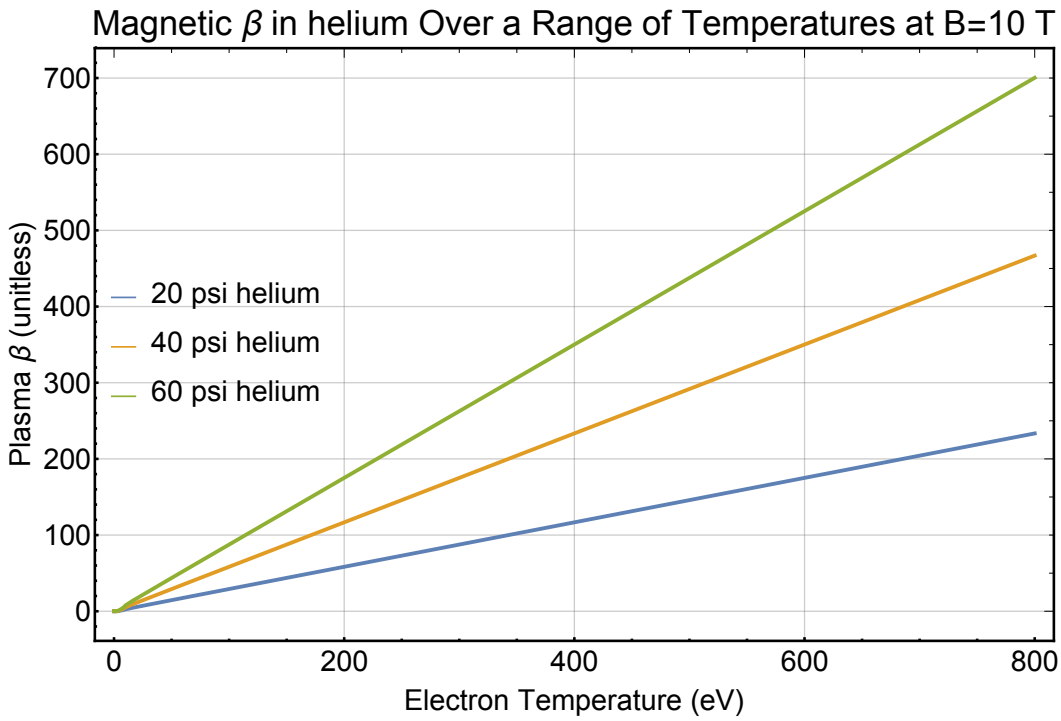

Figure 5.3: With initial high temperature and the external applied field of 10 T, the beta parameter is in the range 100 to 500 for nearly all densities and most temperatures applicable to laser heating conditions during experiments with helium.

If we wish to see the magnetic field pressure affecting the plasma expansion trajectory, we need only look later in time. The plasma pressure is dropping rapidly as it expands and becomes a blast wave. The volume is increasing like r^2, so if linear energy density remains constant then based on this alone the temperature should decrease like r^-2. However, the plasma is also

accumulating more cold material which must be ionized and heated, the quantity of which will scale like r^2 also. So depending on the equation of state, the thermal energy is spread over more particles. So we might expect the plasma temperature to scale like r_0/r^4 [27]. This gives β as a function of r:

$$\beta = \frac{r_0^4}{r^4} \frac{nkT_0}{B^2/2\mu_0} \tag{5.19}$$

In the absence of other effects that change the magnetic field, such as shock-driven flux compression, the Nernst effect, and the diamagnetic effect, we expect beta to approach the unity condition fairly quickly. It will most likely occur once the blast wave radius has increased by a factor of four from the initial plasma diameter. Shock boundary flux compression, Nernst, and diamagnetic effects will tend to exclude the magnetic field within the plasma and push it to the boundary which further reduces the time required for unity beta conditions. Figure 5.4 presents beta as a function of radius, assuming the magnetic field strength does not change. We expect the hottest regions to initially be about 0.7-1 mm in radius. So this transition to magnetic pressure dominance might occur at plasma blast wave radius of about 3-4 mm.

Indeed, in MagLIF, the hope is that the expanding plasma will achieve unity beta prior to shock impact on the liner wall [1]. This would require unity beta conditions being achieved before the bulk plasma transport at the sound speed causes the hottest plasma region to grow by a factor of three, since initial MagLIF liners are initially about 3 mm in radius and beam widths are

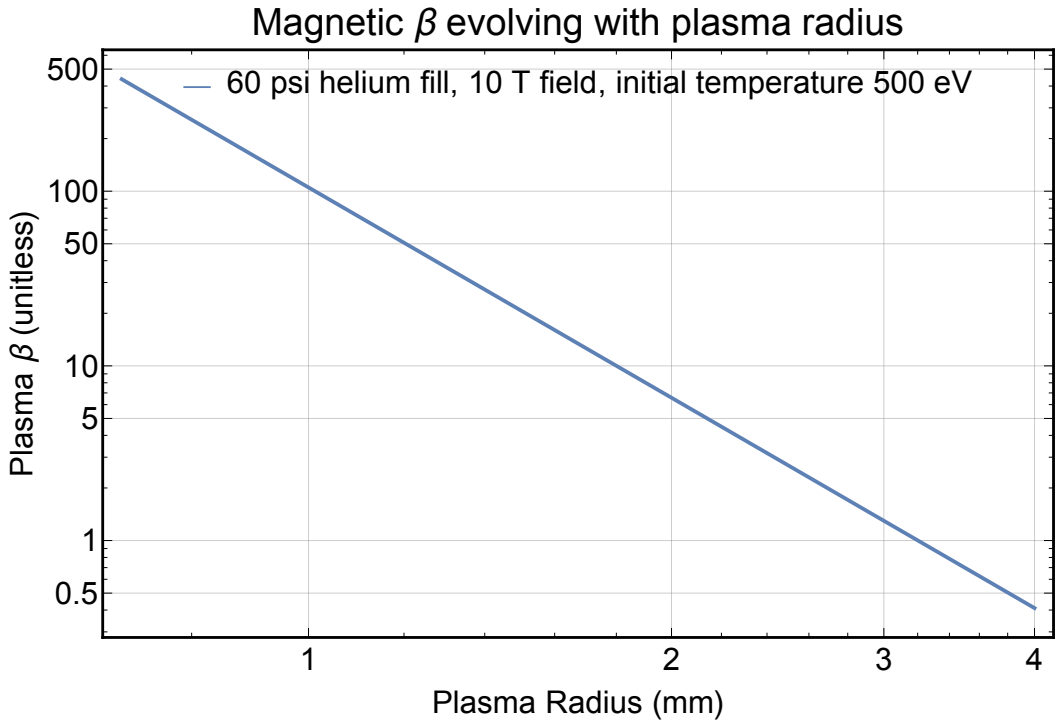

Figure 5.4: We depict β as the plasma radius grows in a fictitious, fixed magnetic field. Approach to unity conditions would occur after radius tripling, during the blast wave phase. This scenario uses only the drop in plasma temperature to calculate β and ignores changes to magnetic fields.

typically sub-millimeter scale. Figure 5.5 gives the beta factor as a function of plasma radius as it approaches a hypothetical conducting wall such as the MagLIF liner. To model this, we use the following estimate:

$$\beta = \frac{r_0^4}{r^4} \frac{2\mu_0 nkT_0}{\frac{r_{liner}^2 - r_0^2}{r_{liner}^2 - r^2} B^2} \tag{5.20}$$

Figure 5.4 explains why it is important to keep the initial heated region of the plasma at around half of the liner diameter or less, so that the initial

volume of magnetic field that gets compressed is greater. Our experiments cannot address the increase in B-field in this scenario because there is no conductor around the plasma, and the field coils are significantly farther out, so there will be no flux compression. Parameters are highly idealized in figure 5.5, because it assumes the region between the hot parts of the plasma and the liner are non-conductive. In reality they may be electrically conducting as a result of radiative precursors. This would weaken the flux compression effect, and perhaps allow direct contact of the blast wave with the liner inner wall. This might allow temperatures to thermalize more rapidly to the liner wall and would be non-ideal for MagLIF energy content.

5.2.2 Ion Sound Waves Become Magnetosonic Waves

In the absence of a magnetic field, the plasma expansion is driven by hot electron pressure constrained by ion inertia and will travel outward at the ion sound speed; this is an ion acoustic wave. However with a magnetic field present this wave becomes the magnetosonic wave. The phase velocity of the magnetosonic wave is given by the following:

$$\frac{\omega^2}{k^2} = c^2 \frac{c_s^2 + v_a^2}{c^2 + v_a^2} \tag{5.21}$$

Where c is the speed of light, c_s is the ion sound speed, and v_a is the Alfvén Speed. The Alfvén speed in SI is $B\left(\mu_0 \rho_m\right)^{-0.5}$ where ρ_m is the mass density and μ_0 is the SI magnetic permeability of free space [5]. The Alfvén speed at 5 T with a 20 and 40 psi helium fill should be around 5 km/s. By

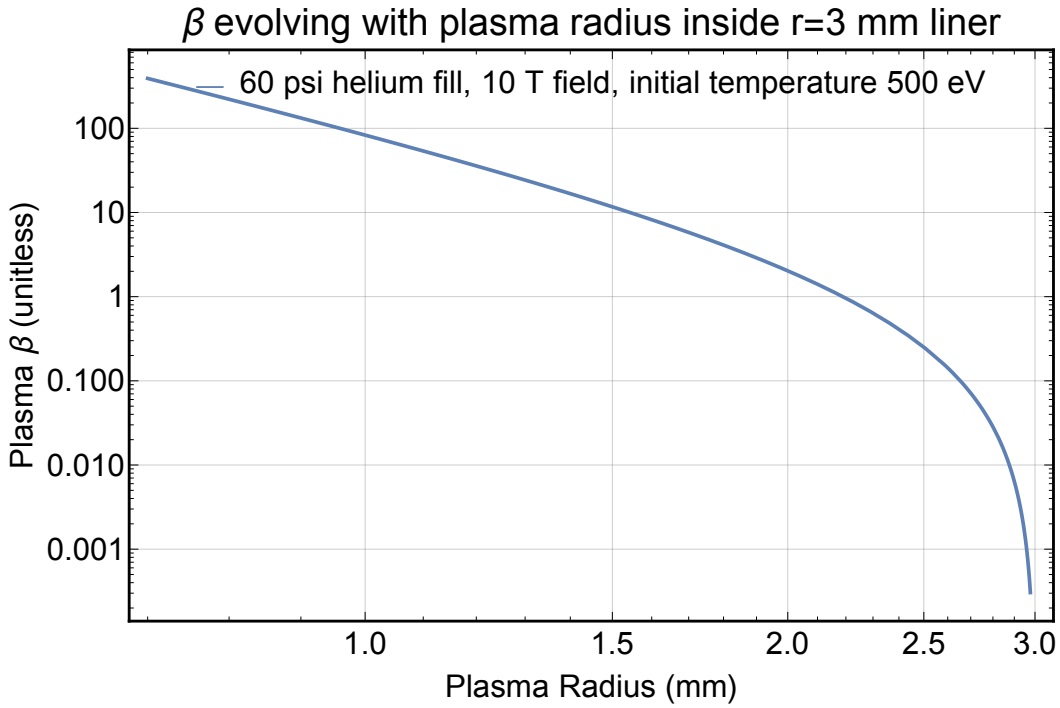

Figure 5.5: This figure is for a hypothetical expanding hot plasma within a 3 mm radius conducting liner, eg in MagLIF. The initial plasma radius in this case is about 0.7 mm. We see that, even with an initial field of only 10 T, β approaches 1 as the expanding plasma front approaches to less than 1 mm of the liner wall. We assume no flux loss into the liner, but in this case we consider that the plasma is excluding the field lines, eg. by the Nernst and diamagnetic Effects.

contrast, the ion sound speed ranges from 10's to about 100 km/s, which is much faster. The magnetosonic wave propagation speed will be very close to the ion sound speed for weak B-fields, and in this case the effect on a 100 km/s ion sound speed is about 0.1 km/s, which is unmeasurable. We do not expect to see a difference in the speed of the initial expansion speed of the plasma during the initial launch of an ion sound wave from a magnetic field.

Even for a 10 psi helium fill plasma, with an ion density around $2 * 10^{19} cm^{-3}$, with a 20 T B-field, can expect an Alfvén speed around 50 km/s. This could increase the speed of all slower expansion to the order of 50 km/s for regions of the plasma that are at a low temperature, notably the end of the plasma. This would be hard to measure because the region with such low expansion velocity is small or non-existent. The bulk majority of the plasma does not get strongly affected, as the expansion speed would increase from the ion sound speed by at most 5%.

The benefit, though, is that we can still use the expansion speed of the plasma as a diagnostic of temperature except at low densities in the regions where temperature is the lowest, as it would be on the ends for an experiment with more than 10 T and less than 40 psi helium density. For 10 T and 60 psi helium, we do not expect an observable affect of the B-field on early-time expansion because the Alfvén speed is only about 7 km/s.

However, once the plasma has more than doubled in radius and blast wave dynamics become important, plasma beta is approaching unity as we saw in the previous section. In that case, the B-field will increase as the blast wave expansion speed is decreasing, and so we might expect the blast wave to slow more rapidly than a Sedov solution. At this point the distinction between a magnetosonic wave and a blast wave with external magnetic field pressure is not so clear.

5.3 Interpreting Sound Speed Expansion to find Temperature and Energy Density

The main reason for discussing sound speed plasma expansion in such detail is that we will use it as an indirect diagnostic of temperature and energy density. Since the expansion speed in given by the simple expression in equation 5.3, this gives us a straight-forward way of inferring electron temperature from the sound speed. If we know the plasma radius, we can also estimate the overall energy density. This section will outline the method for analyzing shadowgrams to get both temperature and energy per unit length as a function of axial length in the plasma.

5.3.1 Algorithm for Image Analysis to find Sound Speed at each Axial Depth

This section explains the basic algorithm that we used to interpret the shadowgraphy diagnostic images to obtain a sound speed expansion between frames. In order to extract the sound speed from 2D image data, we used MATLAB to extract the edge of the plasma for each axial pixel column.

The first step in image analysis after the raw data was available from the sensors was background subtraction and contrast enhancement if necessary. In many cases in which two cameras were used for image sequences, the images from one camera needed to be offset to match the other camera, as well as flipped vertically. Sometimes the contrast would need to be enhanced. Next, we applied the Canny edge detection algorithm in ImageJ. This usually

produced lines at the edge of the plasma while filtering backgrounds, but it could miss portions of the plasma edge where contrast was low. In those cases we drew lines at plasma edges with pixel-editing drawing tools in ImageJ. After edge detection, we manually erased extraneous edges caused by optical blemishes, gas cell window edges, or other image features. The end product was an image with empty pixels except at the plasma's sharp edge. Figure 5.6 gives an example of a shadowgram image after we applied the edge detection process. Such images are ready to be imported to MATLAB and read as a matrix of pixel values.

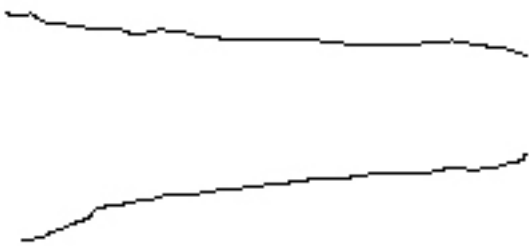

Figure 5.6: An example of a shadowgram image which has been run through an edge-detection algorithm and cleaned up to show only the plasma boundary. The radial axis is vertical in the image and Z runs left to right.

Using the edge-detected image data, the MATLAB script extracts the vertical difference in the image matrix's outer nonzero pixels. When multiplied

by the image scale this gives the plasma diameter. This generates a vector of radii at each axial depth. This script does this for each of the eight image frames in the image sequence. We can now subtract between the radii vectors in subsequent frames to find the change in radius between frames. Dividing by the shadowgraph probe laser's timing interval gives the expansion speed between frames. We have local sound speed at each axial depth which comes from the initial and final radius over the shadowgraph frame interval. This sound speed is given by the following equation, where t_{shad} is the shadowgraph probe interval:

$$c_s = \frac{R_2 - R_1}{t_{shad}} \tag{5.22}$$

Figure 5.7 is an example result for sound speed between two shadowgram images.

The sound speeds are on the order of 50 to 200 km/s for nearly all cases.

The main sources of uncertainty are as follows. We have a systematic uncertainty in timing between the laser pulses relative to ZBL's heating pulse which is on the order of 0.2 ns. This which affects probe laser timing with respect to heating, but not the differences in frame times which is used to calculate the sound speed. Typically the uncertainty on the inter-frame timing is systematically accurate to within 50 ps, and is the same on every shot. The fundamental resolution limit from the finite size of pixels on the sensor

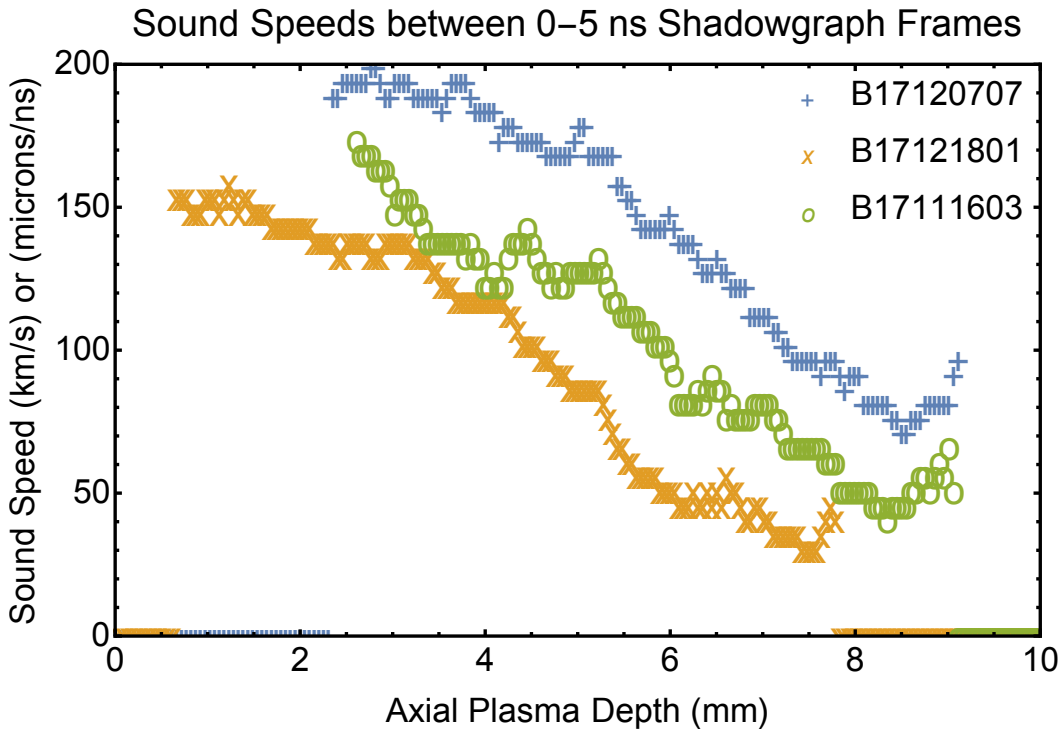

Figure 5.7: An example of a sound speed distributions for three different shots calculated between two radii from 0 to 5 ns.

accounts for the majority of uncertainty in the sound speed. The data is limited to about 60 microns per pixel resolution. We might conservatively double that resolution by doubling the optical magnification. This would bring the scale from 40 pixels per millimeter to about 19.6 pixels per millimeter. Unfortunately, this would also make it harder to align the image to the sensor, and would potentially cut off the image of portions of the viewing window which are important for showing transport later in the plasma's evolution. Regardless, with the current resolution and since the temperature depends on the square of the sound speed, if we rely on the difference between only two

images the temperature error is about 30 eV just from pixel resolution.

We can make firm statements about how long the sound speed interpretation will remain valid. As we have seen from estimates with the important equations of energy and thermodynamics, the plasma should expand at the sound speed until the radius roughly doubles. In practice, we've seen the plasma transport at a constant speed for up to about 30 ns in some cases (figure 5.8), but usually 15 ns is a better cutoff time for sound speed interpretation. These numbers are approximate, since laser heating usually takes place over several nanoseconds. However, when a neon dopant is added, the constant sound speed expansion is not constant because the plasma pressure is dropping rapidly. So, when dopants are causing radiative cooling the sound speed needs to be measured as early as possible. Characterizing the radiative energy loss could be done in the future and might be a useful check on radiative power.

There are practical limitations of inferring a temperature from sound speed motion close to the laser entry region. Our shadowgraph viewing windows on these gas cells restrict observation of the region within several millimeters of the LEH. This region is obscured relatively early on as the plasma expands because the viewport curves away. However, during sound speed transport, this only causes perhaps 1 millimeter to be obscured. Future designs for gas cells mitigated this problem, but it does not solve two other, separate problem that make it difficult to measure sound speed transport close to the LEH. One issue is that we often observe a blast wave originating from

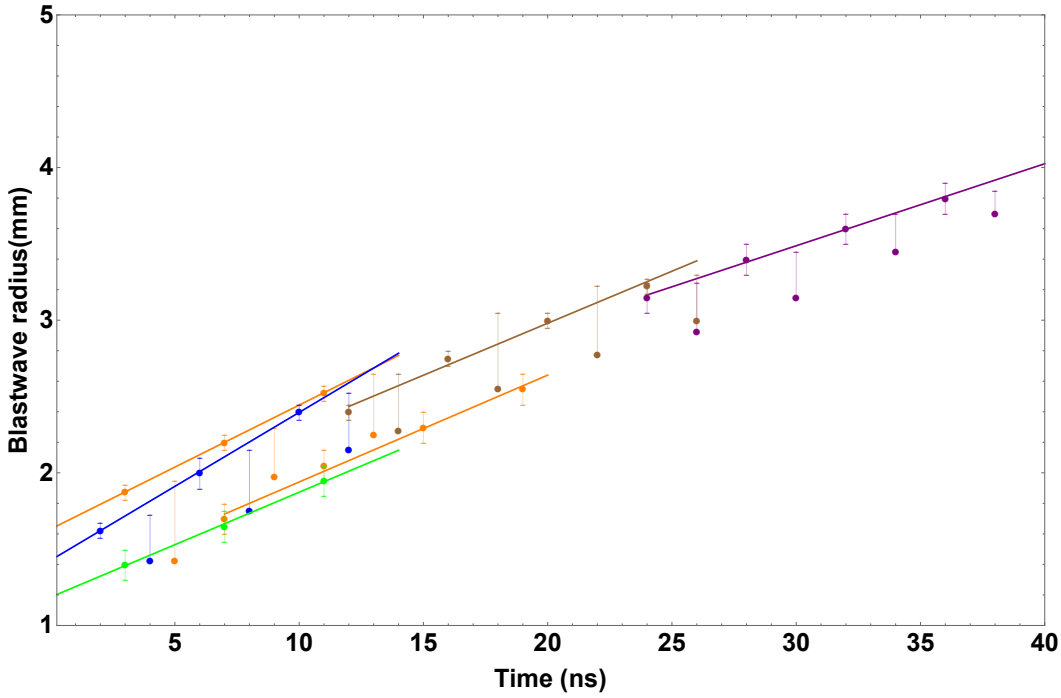

Figure 5.8: Experiments with a shadowgraphy time separation of 2 ns indicate that the ion acoustic wave deceleration is not measurable on 16 ns durations intervals and the speed of expansion remains approximately constant over that time, up to about 35 ns. In this figure, different colors correspond to different datasets. The sound speed does appear to do drop around 15 ns, but it is unclear from this figure if this is shot-to-shot variation in the sound speed or if it is a consistent effect. We later found that the sound speed is more reliably constant up to about 15 ns based on shadowgram trajectories.

the region of the LEH. This is a spherical blast wave that originates from the laser interaction with the LEW, but it is usually small on the time scales during sound speed transport. Entirely separate from this, phenomenologically we observe unusual plasma opacity outside of the usual hydrodynamic fronts with thermal wave precursors. This strange opacity region exists in the first several millimeters of the plasma's axial depth, rendering the sound speed

analysis highly inconclusive in that region. This behavior will be discussed in more detail later, but it is the most severe problem with interpreting the sound speed motion in the first millimeters of the plasma. All of these difficulties restrict the region which we can diagnose with sound speed methods to an axial range starting at 3-4 mm and going to the end of the plasma.

Another important point is that the choice of plasma species affects the sound speed. MagLIF uses deuterium. The greater ion mass of helium means that the sound speed will be 30% less in helium versus deuterium with the same driving pressure. This decrease means that radial mass transport in MagLIF will be 30% faster than what we observe.

5.3.2 Axial Electron Temperature Distribution

Once we know the sound speed we can get the electron temperature. The ion mass is the mass of the helium nucleus in our experiments and we typically ignored dopant species to do the calculation. Since we are working with helium, we used a charge state Z=2, which is a good approximation above about 10 eV. The factor of two cancels in the numerator and denominator.

$$kT_e = \frac{c_s^2 m_i}{\gamma Z} \tag{5.23}$$

This equation is applied locally to each axial depth to give an temperature associated with the electron pressure wave driving inertial expansion of the ions. From the same shots shown before, we can get the temperature, as in figure 5.9 for example.

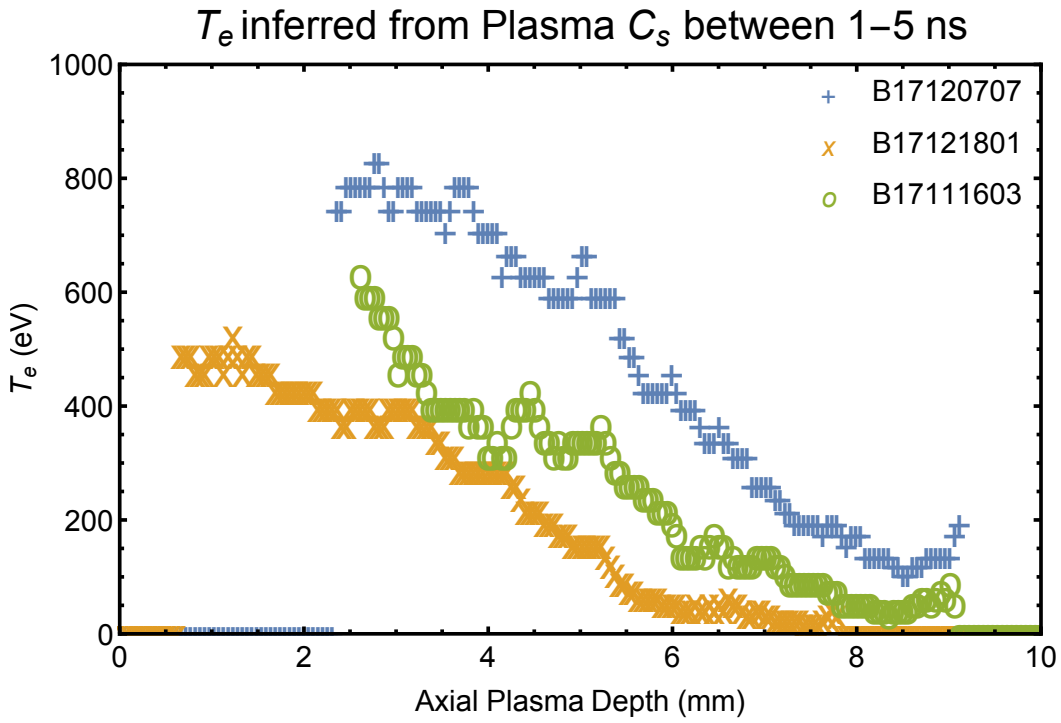

Figure 5.9: Here are example electron temperature axial distributions calculated from the sound speed expansion between 0 and 5 ns frames. The spread in temperatures provides a good characterization of pixel uncertainties.

The temperatures we observe are typically in the range of 100 eV to 700 eV and usually decrease monotonically throughout the axial depth of the plasma. In some cases the temperature axial distribution is more uniform, as in the case of a plasma with an applied magnetic field.

5.3.3 Method for Estimating Energy Densities

Now that we have a temperature from the sound speed expansion, we can make an estimate of the local energy content in the plasma at each axial

position. We will need not only the temperature, but also the plasma density and the volume over which we should apply that energy density.

We need to make several assumptions. To get the energy density, we will need to assume some temperature distribution. We will also need to either calculate or ignore the kinetic energy of the expanding plasma. For now, let's assume the temperature is uniform. Then, if we have the temperature at a given axial position in Z, all we need to find the thermal energy is the density of the gas and the radius of that region at a given time. We neglect energy present in ionization at first, which may or may not be a good assumption. Once these plasmas have doubled in radius to 2-3 mm, the amount of energy required to fully ionize helium can be hundreds of Joules. Finally, we will need to assign an experimentally relevant radius for the plasma in order to make an estimate the total energy.

This is the equation we used to find the energy present in the electron thermal motion. The equation uses the volume calculated from the average radius between frames. We use the ion density and charge state from Zn_i to get the electron number density.

$$E_{t,z} = Zn_i kT_{e,z}\pi \left((R1_{0ns,z} + R_{5ns,z})/2\right)^2 \tag{5.24}$$

where $R_{t,z}$ is a vector list of radii of the plasma across z at the given time in the subscript. $T_{e,z}$ is the temperature at that position, which we found from the sound speed. We take the charge state Z=2 for helium.

For all of the following calculations and figures which will follow in chapter seven, we used the averaged radius between the two shadowgraph frames to estimate the volume of the plasma during the time over which this sound speed is relevant. This may cause us to over-estimate the energy density, because it is possible that a better radius for estimating the energy density would be the radius of the hot plasma in the first of the two frames.

5.3.4 Validity of Uniform Temperature Assumption in Energy Density Estimates

Next we will discuss whether assuming a uniform temperature across the plasma radius interpreted from shadowgrams is a good assumption. There are two expected systematic uncertainties with this approach.

The first difficulty arises with using the volumetric choice of the averaged radius from the shadowgram radii. We have see that there is a substantial ionizing radiative precursor, which seems to remain on the order of 600 microns thick and tracks the hottest plasma regions for at least 6 ns (see figure 3.13). This precursor becomes clear in the shadowgrams when they are compared to x-ray images. So, the shadowgraph radii are larger than the hottest regions of the plasma by several hundred microns. The explanation of this larger width as a radiative thermal wave precursor would suggest that it should have relatively uniform and constant thickness that will not change as the plasma hydrodynamics evolve. The sound speed measured from shadowgrams is valid since the edge tracks the hotter interior, but the plasma volume is an over-

estimate of the hot regions. For this reason, we expect to over-estimate the energy per unit length. Our estimates should still provide a useful relative comparison between axial positions on the same show, and between different shots.

The second problem is the fundamental assumption of a uniform temperature within the plasma, which obviously might not be accurate. We can guess that it might be approximately valid because of the strong electron thermal conductivity, which causes the temperature to be relatively uniform throughout the plasma up to within a few hundred microns of the edge. The more strongly nonlinear thermal conductivity is with temperature, the more uniform the internal temperature within the plasma. Chapter four discusses this thermal conductivity in detail. The radial distribution of electron temperature near the edge of the plasma is probably closely approximated by a diffusive self-similar thermal wave, while the interior could be considered to be almost uniform. Certainly equilibration of pressure will likely drive the energy density to be roughly uniform within the plasma. The temperature distribution of thermal precursors as a function of radius should be approximately given by the distributions in chapter four, for example from equation 4.30. Fortunately, if the dominant form of thermal conductivity remains unchanged, then the energy density will be a constant factor that depends linearly on the temperature, multiplied by the square of the radius. See equation 4.35. This means that the energy density we estimate using our methods will be off systematically by roughly the same factor in all cases.

Based on the physics of sound speed expansion, the best volume and density conditions would come from the initial x-ray distribution during laser heating. These initial plasmas are probably very close to the background gas density, and their radii and temperature distributions are solvable from x-ray emission distributions. We could also infer overall energy under the self-similar thermal wave that best matches the x-ray data. And, these initial plasmas would best match the sound speed regime in which relatively little of the plasma's energy is tied up in kinetic energy of a denser shock front. Unfortunately, on many shots where we have shadowgram expansion rate, we do not have transverse x-ray emission images.

The most important point here is that determining the exact energy content of the plasma depends on the radial distribution of temperature and density. So, while we can make a fairly good estimate of the total energy content, it is not going to be exact. Importantly, however, our energy density in units of energy per unit length should scale appropriately such that we can use it to diagnose relative energy content, and to make strong statements about energy uniformity and relative improvements between shots in absorption fractions in the regions of the plasma visible to diagnostics. This analysis will be the bulk of chapter seven.

5.4 Conclusions on Sound Speed Methods for Energy Density Comparison

We have seen that the plasma sound speed is explained by the initial thermal pressure of the electrons driving outward, which are held back by the inertia of the ions. Since we have taken multiple frames showing the plasma evolution separated by fixed time intervals, we can find the speed of expansion between intervals and get the sound speed. This will give us an electron temperature. We can go one step further and infer a local energy per unit length if we know the heated area. Since the method for energy density depends on assumptions about the temperature distribution and extent, it is not exact. However, it can provide comparisons between experiments, but not necessarily absolute numbers. The method likely over-estimates the total energy density, and thus places upper bounds on the total energy content of the plasma in the cylindrical portion of the plasma past the first few millimeters of axial depth.

Chapter 6

Blast Wave Theory and Method for Energy Diagnosis

6.1 Introduction

This chapter explains the behavior of blast waves that is needed to use them as a diagnostic for energy density. Intense explosions in gases and plasmas drive shock waves that are called blast waves if the energy release is sufficient. Blast waves are supersonic shock disturbances that propagate away from small areas of very high temperature and energy release. Blast waves are characterized by the buildup of a higher-density layer at the shock boundary and the rarefaction of density in the interior region. This feature distinguishes them from a sound wave. Their intensity, high mach number, strong density and pressure ramp, and origin from a single point distinguishes a blast wave from a weak shock wave. Since they are not driven, and originate from an initial strong explosion, blast waves often decelerate in a predictable way that can follow a self-similar power law trajectory if energy is conserved or lost continuously [25].

First there will be a explanation of the three regimes of plasma transport. Next I will give the relevant theory behind blast wave dynamics and tra-

jectories, using the an approximate solution for the Sedov-Taylor blast wave. Finally, we will show how to use blast wave trajectories to extract an energy per unit length distributions from our laser-heated plasma columns that are similar to those in MagLIF. After image analysis we have energy density distributions available at three different densities in helium. Energy content is an important diagnostic of the success of laser heating, and depositing a large amount of energy is important for the success of MagLIF as we saw in chapter one. The energy densities evolve from low but uniform energy density at 12 and 20 psi helium fills, to a steeply ramping energy density distribution at 40 and 60 psi helium fills. These steeply ramping trends are also present in analysis via the plasma sound speed, and will be discussed in future chapters.

6.1.1 Summary Chronology of Plasma Transport Evolution

During the time that the laser is heating the plasma, rapid heat transport occurs through radiative diffusion and primarily through electron thermal transport. Thermal transport continues outward in the form of a thermal wave, escaping from the laser heated region on the same timescales that the laser is further heating the gas. The thermal wave will continue to propagate with a rapidly decelerating edge until the speed of the front approaches within a factor of 2 of the plasma sound speed, at which point ion motion begins to play a role and the thermal wave no longer dominates energy transport. This transition occurs within about a nanosecond of the plasma's direct heating.

Next, between laser turnoff and about 30 ns later, the plasma is ex-

panding at a roughly constant plasma sound speed. Sound speed transport was discussed in chapter five. A region of increasing ion density begins to form at the boundary of the thermal region, but while that region is still relatively comparable in density the sound speed regime persists.

Eventually the sound speed expansion transitions to a blast wave, as described in chapter five. As ion density transport proceeds, more and more energy in the plasma transfers from thermal energy in the interior to the kinetic energy of the massive shock shell. This shell is becoming more massive, but there is a thermodynamic limit to the density that hydrodynamic mass transport can accumulate at the high-pressure-gradient region on the plasma shock front. This depends on the plasma and neutral gas's adiabatic index. We will find this limit in this chapter. This limit is reached at a specific radius, which for us is about double the initial radius of the electron thermal wave as we saw in chapter five. Once this energy and mass transfer is complete, the sound speed expansion begins to decelerate as the plasma sweeps up more mass on the shock front. The blast wave phase lasts the longest compared to the other phases. It will continue to propagate until the internal pressure approaches the pressure of the background, at which point it will transition to a sound wave traveling at Mach one in the background gas conditions. This end of blast wave evolution cannot be observed in our experiments since it would occur much later, outside the gas cell volume.

6.2 Blast Wave Background Theory

A blast wave's energy consists of both the kinetic energy of the dense shock region and the thermal pressure driving it outward. The classical blast wave that conserves energy as it expands is called a Sedov-Taylor-Von Neumann blast wave (STBW). These individuals found solutions to the trajectory of the shock front of the blast wave. The exact trajectory of the blast wave depends on the geometry and whether it is losing energy via such processes as radiation or ionization. In general, it will be a power-law trajectory in which the radius scales like time to a fractional power. In our case, with no energy loss in cylindrical symmetry we have $R \propto t^{1/2}$ [33] [25]. These trajectories are self similar, which means that the length and time scales can be proportionally scaled by changing a single variable based only on the initial energy content and density. Radiative blast waves and other scenarios in which the blast wave is losing energy will have different power law behaviors that are between the adiabatic limit and other solutions, called the pressure or momentum driven snowplow solutions [25]. These solutions have constant radiative heat loss at the boundary or have already lost all of their internal thermal pressure, respectively.

In this theory section, we will qualitatively describe blast waves in a plasma. Next will be the Hugoniot relations and the thermodynamic limits on a blast wave's shock jump conditions. Afterward we will derive a solution for the adiabatic blast wave trajectory in the relevant cylindrical geometry via an approximation method attributed to Chernyi and presented in Zel'dovich

and Raizer's text [25]. We will very briefly look at radiative blast waves and qualitatively describe the pressure driven snowplow and momentum driven solutions without deriving them.

6.2.1 Blast Waves in Plasmas

There are specific differences between a classical blast wave and a blast wave in a hot plasma. First, we expect that the high-density region at the shock boundary will consist of increased ion density. However, there will be also be a thermal precursor which extends outside of this region. The spatial extent of the precursor is determined by the radiative and electron thermal conductivity as a function of the temperature of the shock. The plasma temperature drops as the fourth power of the radius, so the precursor may lessen as the shock expands [25]. It is not easy to find an analytical behavior of this driven thermal wave precursor, but we can say that it will have a sharp boundary similar to a blast wave because the coefficient of thermal conductivity is nonlinear with temperature. Empirically, we know that the precursors can extend several hundred microns outside of the plasma within the first 10 ns. Importantly, however, these precursors do not significantly modify the energy content of the blast wave or its trajectory behavior. There is also a minor charge separation as the ions will build up at the shock boundary but the electrons will be hot outside the boundary. This charge separation leads to an electric field which is usually about the width of the Debye radius in spatial extent [25]. All of these behaviors are described in more detail in chapter seven of Zel'dovich's

text [25].

6.2.2 Thermodynamic Limits on Shock Jump Conditions

I will describe the thermodynamic-limited shock ramp functions, also called the Rakine-Hugoniot relations. These describe the transition in thermodynamic state variables such as density and pressure across the shock boundary. This set of relations will help us describe how dense the shock-compressed region is in our blast waves, as well as provide necessary relationships for finding an approximate solution to the trajectory of a blast wave. These derivation is widely available, for example in Zel'dovich and Raizer's text [25]. Since these can be found in many other places, I will neglect a lot of details and only give a rough outline.

This derivation begins by using the conservation equations for mass, momentum, and energy respectively. The conservation of mass can be given as the following:

$$\rho_1 u_1 = \rho_0 u_0 \tag{6.1}$$

where ρ is the density and u is the velocity. Subscripts refer to outside and inside the shock for 0 and 1, respectively. For momentum we have:

$$p_1 + \rho_1 u^2 = p_0 + \rho_0 u_0^2 \tag{6.2}$$

and energy conservation, where ϵ is the energy:

$$\epsilon_1 + \frac{p_1}{\rho_1} + \frac{u_1^2}{2} = \epsilon_0 + \frac{p_0}{\rho_0} + \frac{u_0^2}{2} \tag{6.3}$$

The goal is to use these equations to find a relation for the jump behavior of the thermodynamic variables across the shock boundary, and we will also use methods of thermodynamics. Each of the Rankine-Hugoniot shock equation of state as a jump relations can take the form $P_i = H(P_0, \rho_1, \rho_0)$, for example for density, temperature, and volume. To get there, we first introduce the specific volume V which is the inverse of the density. Using momentum conservation, $V_0/V_1 = u_0/u_1$. Combining with the energy equation we find equations for the velocity squared which can be used to eliminate velocity.

$$u_0^2 = V_0^2 \frac{p_1 - p_0}{V_0 - V_1} \tag{6.4}$$

$$u_1^2 = V_1^2 \frac{p_1 - p_0}{V_0 - V_1} \tag{6.5}$$

Substitution into the energy equation gives:

$$\epsilon\left(p_1, V_1\right) - \epsilon\left(p_0, V_0\right) = \frac{1}{2}\left(p_1 + p_0\right)\left(V_0 - V_1\right) \tag{6.6}$$

The specific internal energy ϵ can also be replaced by $h = \epsilon + pV$, the specific enthalpy. Using definitions of free energy and enthalpy, $\epsilon = c_v T = \frac{1}{\gamma - 1} pV$ and $h = \frac{\gamma}{\gamma - 1} pV$. These leads to the final form of the Hugoniot relations for pressure, specific volume, and temperature given by:

$$\frac{p_1}{p_0} = \frac{(\gamma+1)V_0 - (\gamma-1)V_1}{(\gamma+1)V_1 - (\gamma-1)V_0} \tag{6.7}$$

Which relates the pressure on the front and back side of the shock. The specific volume ratio, and hence density ratio, is given by:

$$\frac{V_1}{V_0} = \frac{(\gamma-1)p_1 - (\gamma+1)p_0}{(\gamma+1)p_1 - (\gamma-1)p_0} \tag{6.8}$$

There are also relations for velocities, u_1 and u_0. Limiting cases when the pressure or energy density are very high lead to the following equations. The ratio of density for a strong shock will be particularly useful for us later.

$$\rho_1 = \rho_0 \frac{\gamma+1}{\gamma-1} \tag{6.9}$$

$$P_1 = \frac{2}{\gamma+1}\rho_0 D^2 \tag{6.10}$$

$$u_1 = \frac{2}{\gamma+1} D \tag{6.11}$$

These equations are limiting cases of the Hugoniot relations, but they're determined by thermodynamics and the gas dynamic relations and should hold in all geometries [25].

6.2.3 Density and Thickness of Shock-Compressed region

The Hugoniot relation for the specific density at the shock-compressed region leads the maximum thermodynamically allowable shock-compressed density for helium as well as the thickness of this region. Using $\rho_1 = \rho_0(\gamma + 1)/(\gamma - 1)$ with $\gamma = 5/3$ as applies to a relatively low temperature plasma and to a monoatomic gas, we see that the mass density of the shock-compressed region ρ_1 equals 4 times the background gas density. This mass density corresponds with the ion and electron density of a plasma for length scales much larger than a Debye length.

We can use the argument to get the approximate thickness of the shock-compressed region. We will make a strong assumption, which is that in a strong shock which has had time to build up density, the central region is mostly depleted of ion density and most of the mass has transported to the shock-compressed region. We'll assume a cylindrical plasma of radius R_p. The mass per unit length contained within the plasma will then be given by $M_p = \rho_0 \pi R_p^2$. The high-density region has a density of $4\rho_0$ and a volume that can be approximately given by $2\pi R_p \Delta r$ where Δr is the thickness of the shock-compressed region. Now we can set the mass contained within these volumes as equal:

$$\rho_0 \pi R_p^2 = 4\rho_0 2\pi R_p \Delta r \tag{6.12}$$

After cancellation and simplifying, we find:

$$\Delta r = R_p/8 \tag{6.13}$$

for $\gamma = 5/3$, which is the case for us with helium and a non-radiative plasma. So we see that the thickness of the shock region is about 1/8th of the blast wave radius in cylindrical geometry.

6.2.4 Sedov-Taylor Adiabatic Blast Waves

If the energy lost to expansion and radiation is insignificant compared to overall energy then the blast wave expansion can be considered adiabatic. Its trajectory as a function of time is precisely solvable analytically and we may consider it a STBW. The solution is a self-similar trajectory, meaning there is no characteristic length scale. This type of blast wave occurs in plasmas and gasses in which the amount of energy lost to radiation and ionization is small compared with the total energy. What is particularly useful about this behavior is that the trajectory is only dependent on the initial energy, adiabatic index, and the mass density of the medium. Since the other two quantities are known, the energy can be determined from the trajectory.

6.2.5 Chernyi Approximation for the Adiabatic Blast Wave in Cylindrical Geometry

Using the gas dynamic equations and a set of approximations for the blast wave, one can arrive at an approximate trajectory solution for a Sedov-Taylor adiabatic blast wave. The method is outlined in Zel'dovich and Raizer

in both planar geometry and for a point-origin spherical-polar geometry. Our problem is in cylindrical-polar geometry, since the laser deposits energy in a relatively uniform long, thin plasma. This method will give us a very powerful result, because the final trajectory depends on the mass density of the background gas and the initial energy per unit length. Thus we can use the trajectory as a measure of the energy per unit length present in the blast wave's thermal pressure and kinetic energy.

An good approximate solution in cylindrical geometry is given in Keilty and Liang's paper following the method of Zel'dovich and Raizer attributed to Chernyi [33] [25]. This solution assumes the blast wave is launched from an infinite line. The trajectory for the radius as a function of time is given by the following:

$$R(t) = \left(\frac{4(\gamma-1)(\gamma+1)^2}{\pi(3\gamma-1)}\right)^{1/4} \left(\frac{E_0}{\rho}\right)^{1/4} t^{1/2} \tag{6.14}$$

in which linear energy density, which would be given in Joules per meter in SI units, is the variable E_0. The uniform background gas mass density is ρ, and this is known. The factor in front is roughly equal to 1.1 for γ of 5/3, which is applicable for a plasma and for a monoatomic gas in which radiative degrees of freedom are not important.

The derivation for this trajectory assumes that all of the pressure driving the blast wave is internal, while all of the mass in the expanding cylindrical volume of the blast wave is concentrated on the outside. The pressure

and energy will be given in units of pressure and energy per unit length in all subsequent equations. The central pressure will be given by P_c and is assumed to be relatively uniform in the interior region of the blast wave. We will say that $P_c = \alpha P_1$ where P_1 is the pressure behind the shock front. The force equation becomes:

$$\frac{d}{dt} M u_1 = 2\pi R P_c = 2\pi R \alpha P_1 \tag{6.15}$$

where M is the total mass per unit length of the blast wave plasma contained within outer radius R, and u_1 is the velocity behind the shock front. The mass M can be found using the volume of the shock plasma and the initial gas density ρ_0, since all the mass in the interior volume must be conserved, $M = \pi R^2 \rho_0$.

The force equation will then become:

$$D \frac{d}{dr} \left(\pi R^2 \rho_0 u_1 \right) = 2\pi R \alpha P_1 \tag{6.16}$$

where I used the chain rule and the definition of the velocity of the outer radius of the plasma $D = \frac{dR}{dt}$ to take a derivative with respect to r instead of t according to

$$\frac{d}{dr} = \frac{dR}{dt} \frac{d}{dR} = D \frac{d}{dR} \tag{6.17}$$

The next step in the force equation is to use the thermodynamic shock jump conditions given in Zel'dovich and Raizer: equations 6.9 through 6.11.

These equations are independent of the geometry and depend only on the thermodynamics of the gas or plasma. We'll plug in the expressions for u_1 and P_1:

$$D\frac{d}{dr}\left(\pi R^2\rho_0\frac{2}{\gamma+1}D\right) = 2\pi R\alpha\frac{2}{\gamma+1}\rho_0 D^2 \tag{6.18}$$

After cancellations, the force equation on the massive thin shock shell is now relatively simple:

$$\frac{d}{dr}\left(R^2 D\right) = 2R\alpha D \tag{6.19}$$

Next we apply the product rule to the left side to simplify the differential equation for D.

$$\frac{d}{dr}\left(R^2 D\right) = 2RD + R^2\frac{dD}{dR} \tag{6.20}$$

Now the final differential equation is:

$$\frac{dD}{dR} = \frac{2R\alpha D - 2RD}{R^2} = 2(\alpha-1)D/R \tag{6.21}$$

The general solution of the differential equation for D is:

$$D = aR^{2(\alpha-1)} \tag{6.22}$$

where the constants α and a must be found from boundary conditions and the energy conservation equation. This is as far as we can go with the force

equation alone, but it has given us a first order differential equation for the radius as a function of time, since $D = \frac{dR}{dt}$.

So, let's examine the integral form of the energy conservation equation from gas dynamics. The energy in the plasma is in two forms. There is kinetic energy present in the motion of the massive shell, and there is the internal thermal energy represented by the pressure of the plasma's central region. Kinetic energy will be given by $\frac{1}{2}Mu_1^2$ and the thermal pressure by $\frac{1}{\gamma-1}\pi R^2 P_c$.

$$E_{total} = \frac{1}{\gamma-1}\pi R^2 P_c + \frac{1}{2}Mu_1^2 \tag{6.23}$$

Again, we assume that all of the mass in the outer radius R is contained in the outer shell such that $M = \pi R^2 \rho_0$. We'll also use $P_c = \alpha P_1$ and the thermodynamic shock-jump conditions again.

$$E_{total} = \frac{1}{\gamma-1}\pi R^2 \alpha \frac{2}{\gamma+1}\rho_0 D^2 + \frac{\pi R^2 \rho_0}{2}\left(\frac{2}{\gamma+1}D\right)^2 \tag{6.24}$$

We'll also insert $D = aR^{2(\alpha-1)}$ from the solution to the differential equation for the force on the massive shock shell.

$$E_{total} = \frac{1}{\gamma-1}\pi R^2 \alpha \frac{2}{\gamma+1}\rho_0 a^2 R^{4(\alpha-1)} + \frac{\pi R^2 \rho_0}{2}\left(\frac{2}{\gamma+1}\right)^2 a^2 R^{4(\alpha-1)} \tag{6.25}$$

This simplifies to the following, where the dependence on R has been simplified:

$$E_{total} = \pi \rho_0 a^2 \frac{2}{\gamma + 1} \left(\frac{\alpha}{\gamma - 1} - \frac{1}{\gamma + 1} \right) R^{4\alpha - 2} \tag{6.26}$$

The crucial assumption is that energy is conserved, and cannot depend on the radius of the plasma R. Therefore the exponent of R must vanish, giving $0 = 4\alpha - 2$ which means $\alpha = 1/2$. This gives us the exponent in the trajectory equation, which is the differential equation for the velocity.

$$D = \frac{dR}{dt} = aR^{2(\frac{1}{2} - 1)} = aR^{-1} \tag{6.27}$$

Finally, we can find the trajectory $R(t)$ by solving this ODE. The result is:

$$R(t) = (2(at + C_1))^{1/2} \tag{6.28}$$

Most solutions take the constant C_1 to be zero, corresponding to the initial condition of zero radius at $t = 0$. However, other solutions are possible. If C_1 is nonzero then the solution is no longer self-similar.

We can also use the energy conservation equation to give us the constant a. The coefficient in front can be found with the following, taking $E_{total} = E_0$ and using $R^0 = 1$:

$$E_0 = \frac{2\pi a^2 \rho_0}{\gamma + 1} \left[\frac{1/2}{\gamma - 1} + \frac{1}{\gamma + 1} \right] = \frac{\pi a^2 \rho_0}{\gamma + 1} \left[\frac{(\gamma + 1)(\gamma - 1)}{(\gamma - 1)(\gamma + 1)} \right] \tag{6.29}$$

The terms involving the adiabatic index γ can be simplified to the following:

$$\frac{3\gamma - 1}{(\gamma - 1)(\gamma + 1)^2} \tag{6.30}$$

Recall that a is the coefficient of R in the trajectory and it appears buried in the above equation. Solving for a one arrives at the following:

$$a = \left(\frac{E_0}{\rho_0}\right)^{1/2} \left[\frac{(\gamma - 1)(\gamma + 1)^2}{\pi(3\gamma - 1)}\right]^{1/2} \tag{6.31}$$

This a is the coefficient in the equation $D = aR^{-1}$. Recall the solution to this differential equation was the full trajectory $R(t) = (2(at + C_1))^{1/2}$. Since we have the full form of a now, we can plug it into this trajectory equation and arrive at the following:

$$R(t) = \left(\frac{4(\gamma - 1)(\gamma + 1)^2}{\pi(3\gamma - 1)}\right)^{1/4} \left(\frac{E_0}{\rho}\right)^{1/4} t^{1/2} \tag{6.32}$$

This is the trajectory solution given in Liang and Keilty's paper for a cylindrical blast wave [33].

6.3 Radiative Blast Waves

Radiative blast waves are important in astrophysics, but will be less important to us. These are blast waves in which the internal energy contained

within the shock front is being lost due to long-mean-free-path photons escaping the shock boundary without being re-absorbed. We see this in experiments where the fraction of higher Z species is high, for example when we did experiments with neon. It is worth mentioning them because radiative behavior precludes being able to use blast waves for diagnosing energy content.

6.3.1 Radiative Blast Wave Trajectories

These two regimes are the only analytically solvable blast wave solutions besides a the adiabatic case. They apply to blast waves in which radiative transport of energy away from the shock front is important. I will only mention them here briefly, because they apply to late-time trajectories for neon blast wave experiments we carried out. A momentum-driven snowplow solution is a blast wave in which the thermal pressure driving the blast wave is no longer significant as a result of extensive radiative cooling. Yet the shock continues to coast with its own momentum as it accretes matter from the surrounding medium [34]. The radius in cylindrical geometry for a momentum-driven snowplow trajectory scales like $t^{3/8}$. A pressure-driven snowplow solution involves a blast wave that is actively radiating energy at the shock boundary at a constant rate. In cylindrical geometry, the radius in the pressure driven snowplow trajectory scales like $t^{1/3}$ [34]. Partially radiative trajectories also exist, in which radiation is still important but energy loss is not simple or a limiting case. These typically have a power law exponent in their trajectory which is between the adiabatic case and the pressure-driven snowplow solution.

For helium blast waves, we have seen trajectories which slow down faster than the adiabatic solution when neon is added to the gas. We can't use the trajectory of these blast waves to extract energy content when significant radiative cooling has occurred, because the radiative loss cannot be accounted for.

6.4 Blast Waves Trajectory Analysis as a Method for Diagnosis of Energy Density

Now that we have the machinery for adiabatic blast waves in cylindrical geometry, we can interpret data from shadowgraphy to obtain a blast wave trajectory. This will inform us about the overall energy content of the plasma, and how uniformly the energy is distributed.

6.4.1 Method of Image Analysis

The data from shadowgram edges shows these blast waves expand very closely following a classical adiabatic trajectory with $t^{1/2}$. The expanding plasma radii data in figures 6.1 and 6.2 were measured manually by looking at the blast wave edges in a region that seemed to be in a region of cylindrical symmetry. In figure 6.1 we see a 20 psi helium fill experiment in which the blast wave behavior evolves from the sound speed behavior smoothly. The transition to a blast wave occurs sometime before the 27 ns image frame. Figure 6.1 gives a best fit for a sound speed expansion between the first two shadowgraphy frames. The sound speed was $69 km/s$ which is representative

of the sound speed over the length of the plasma at this fill pressure. The log-log plot makes a linear equation appear curving upward. The later-time behavior from frames two through eight fits well to a STBW trajectory with the form given in 6.33, so we are justified in doing a non-linear best fit.

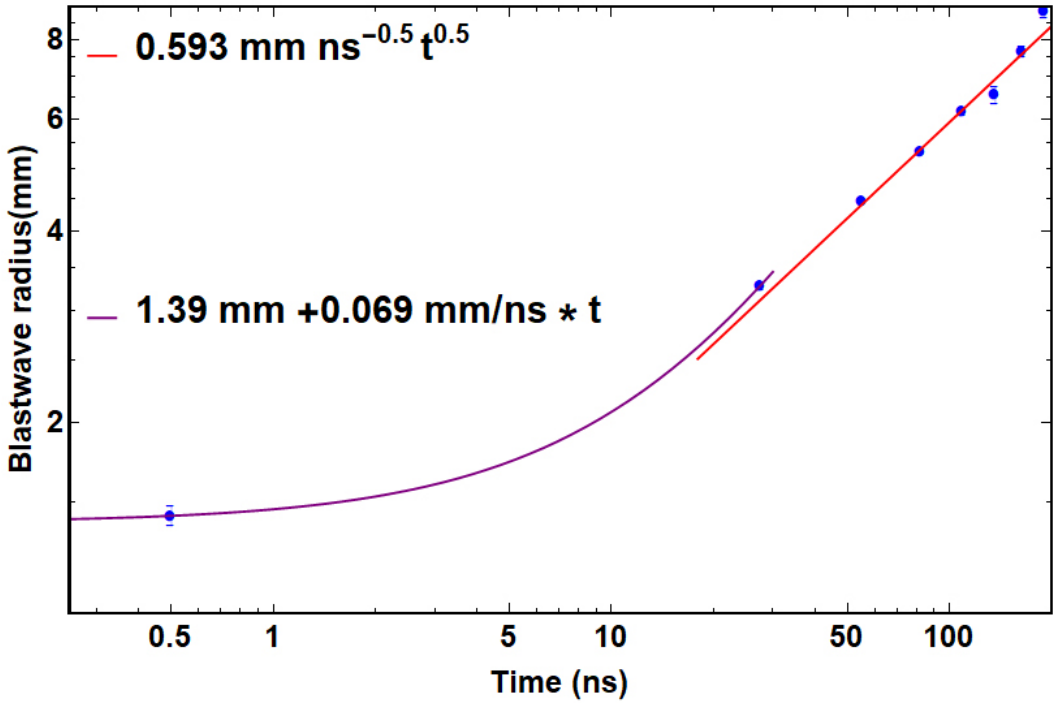

Figure 6.1: Blast waves evolve from the sound speed. Here, a best fit for a linear sound speed expansion early in time followed by a STBW expansion in the final 7 frames seems to match data well. Occasionally, poor image quality and blemishes increase the error in the radial position of the plasma edge and decrease the quality of the power law fit.

We can see the energy density associated with these STBW trajectories. Figure 6.2 shows contours for energy per unit length. We can use the coefficient of the fit for a STBW, if the fit parameters are in the right units, to give the

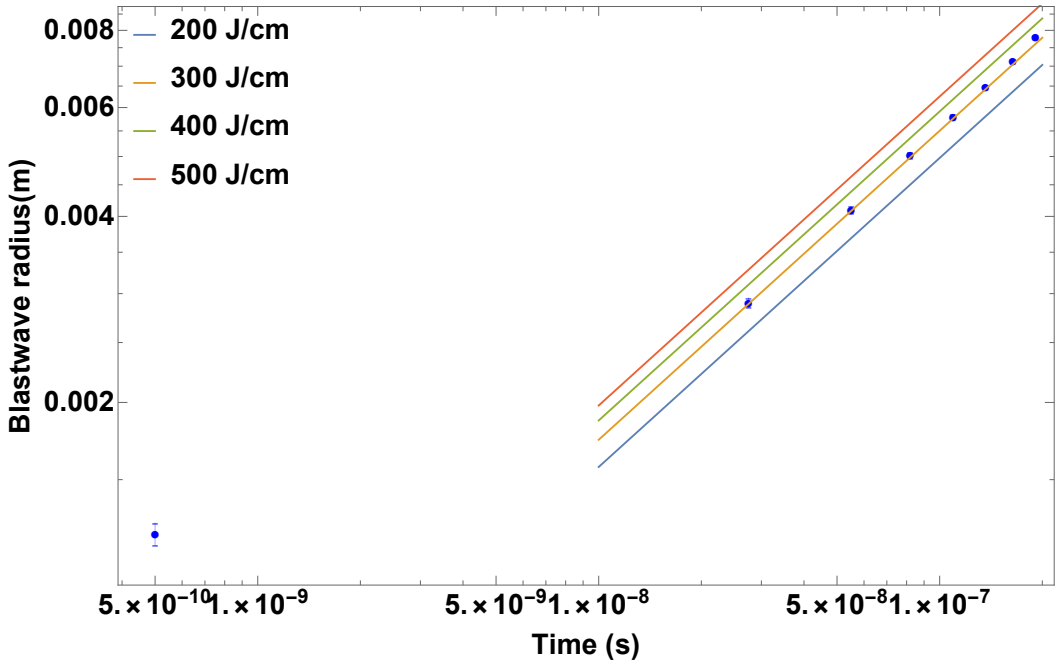

Figure 6.2: We can understand how the blast wave trajectory determines the initial energy density by looking at contours of different initial energy densities. The trajectory data fallows closely to a STBW $t^{1/2}$ behavior in most of our experiments, and thus should give a clear energy density from the trajectory. Here, radii are measured at a central location about 6 mm from the LEW. This experiment used helium at a fill pressure of 43.6 psi. Energy density falls slightly above 300 J/cm in this instance.

initial energy per unit length or compare to contours expected from STBW's with a range of energies, as shown in figure 6.2. The behavior strongly validates the approach of using this data to determine the initial energy density.

We used MATLAB to extract radii data from edge-processed image data in a similar way to that described in chapter five. The algorithm begins in the same way, with edge detection described in chapter five. The results of extracted radius data from an eight-frame sequence of images show restrictions

on the viewing area from looking through a circular viewport, as shown in figure 6.3.

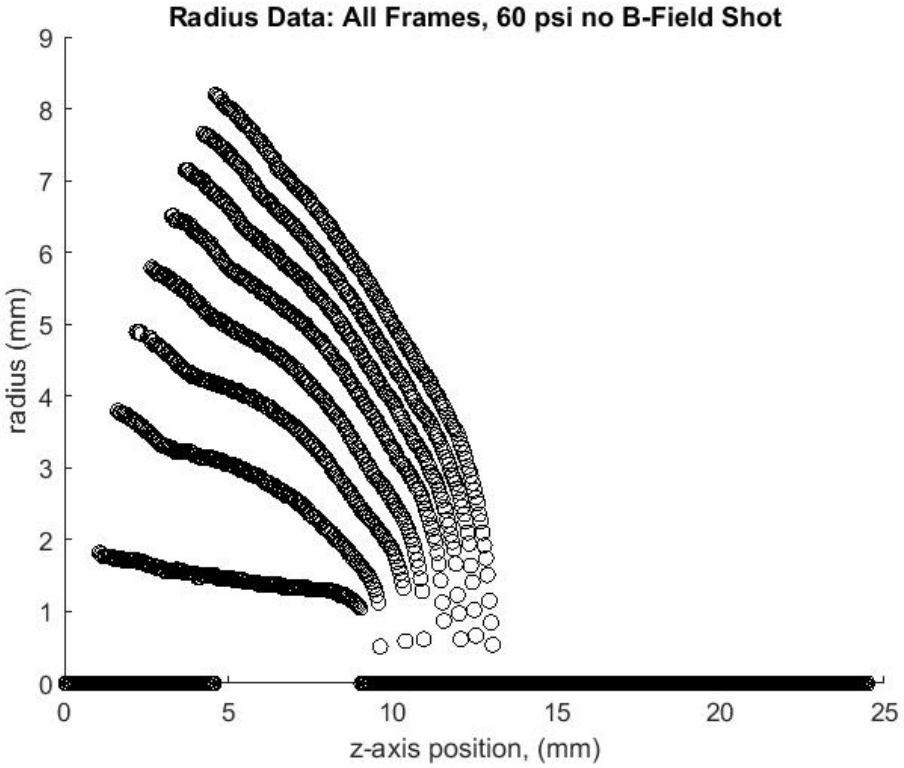

Figure 6.3: Once the data is imported into MATLAB from an edge-detected image, the radii can be plotted superimposed on each other. Time separation from this shot is 27 ns. Notice the slight inflection in each radius contour caused by a spherical blast wave originating at the laser entrance window.

We are able to use MATLAB to do a non-linear best fit for the trajectory using radii from the blast wave trajectories for every pixel row of the image. We are able to do this for each pixel in the axial direction with the final 6 or 7 of 8 shadowgraph image frames. Using the first set of radii gives misleading results, since the plasma is still in the sound-speed expansion regime.

We will later explore energy densities obtained using a best fit for a STBW trajectory with the time exponent forced to 0.5. We can explore the validity of forcing the exponent to 0.5 using a separate nonlinear best fit in which the exponent is allowed to vary. Examples of the best fit exponent at each axial depth for blast wave experiments at three different fill pressures are shown in figure 6.4.

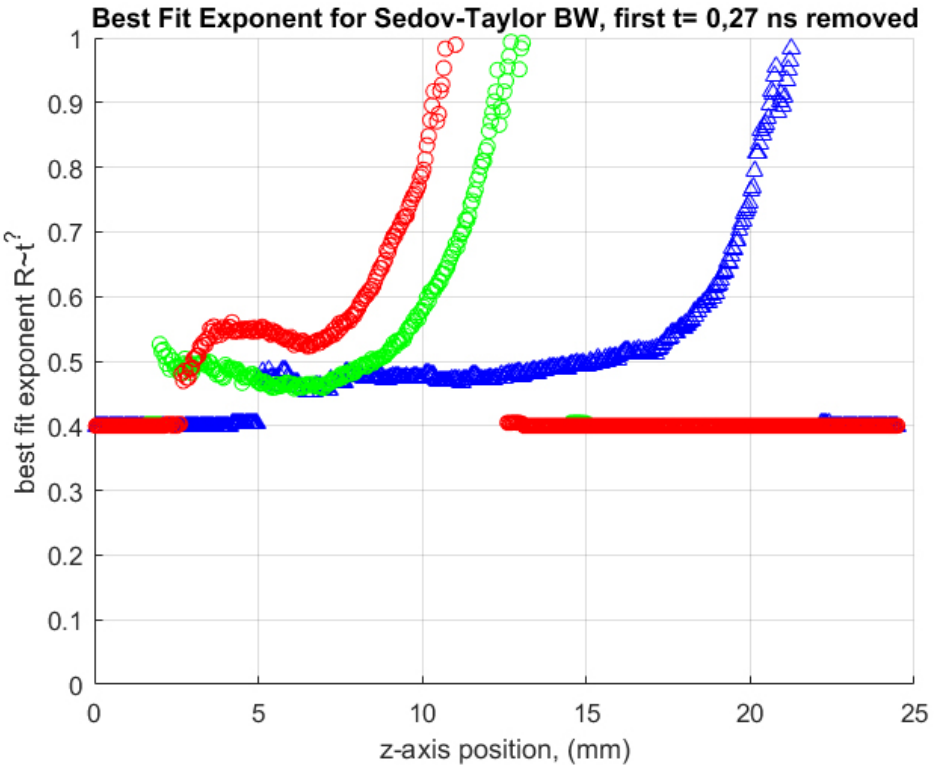

Figure 6.4: A non-linear best fit with the exponent of time allowed to vary shows the axial regions in which the blast wave trajectory analysis is valid. In particular, the STBW behavior of $t^{1/2}$ is not a good fit on the ends of the plasma, where expansion is free to take place both radially and axially. The three colors are for blast waves at different pressures of 12, 40, and 60 psi.

For later time after approximately 30 ns, we find that if the exponent of time is allowed to vary, the best fit power law has an exponent of 0.5 to 0.55 for most of the plasma's axial depth. This is close to the STBW behavior we expect. However, in the last several millimeters the best fit exponent increased gradually to about 0.8 or even 1. This is the in the region where we can no longer apply a cylindrically symmetric trajectory, because there was no initially deposited energy at that axial position. So, in those places, at the ends of the laser plasma, the blast wave would be better modeled with a spherically expansion trajectory.

The regions closer to the laser entry are also problematic. Scale two gas cells (see chapter two) are the preferred gas cell type for viewing blast wave transport, because of the larger viewing window. The viewing window curves away from the LEH and prevents blast waves from being imaged there. It turns out that this is not a limiting problem, because we see modifications of the blast wave behavior from a spherical blast wave generated where the laser strikes the LEW. These regions usually slow a slightly lower best fit exponent in figure 6.4 as a result of the offset spherical blast wave, from which we measured a chord. The blast wave from the LEW interaction was a more severe limitation for blast wave energy interpretation in the first few millimeters of the plasma that the restricted gas cell viewport. Although we can see the affected area clearly in the shadowgrams, it is sometimes subtle and the transition from a cylindrical behavior to the large energy deposition at the LEW is usually almost continuous. Regardless, the difficulties in the region near the LEH leave

a narrow region in which the STBW trajectory techniques allow an accurate diagnosis of the energy density in the plasma. Both effects propagate forward axially with time, so if the more shadowgram frames are captured prior to 100 ns this effect would be reduced. Effectively these issues restrict useful blast wave measurements from about 4 mm axial depth up to the end of the plasma column. In low fill pressures near 20 psi or below, the plasmas are longer and permit a longer diagnosis of energy density. For fill pressures above 40 psi, however, this method only allows the energy density to be diagnosed in a region several millimeters long in the axial direction.

6.4.2 Results of Energy Distributions from STBW Blast Wave Trajectories

Here we will present three energy density distributions which originate from the coefficients of the best fit of a STBW trajectory. These datasets were collected in 2016 and early 2017, during a time in which most of our experiments took place at lower densities corresponding to 20 and 40 psi helium fills.

These blast waves are only approximately cylindrical. The Z-beamlet laser heats a long channel on the order of one centimeter or more in length. However, as mentioned previously, near the ends of the plasma the cylindrical solution would not apply. Also, as the blast wave evolves to a length scale approaching the initial length of the plasma, it will also tend toward the spherical solution as the initial spatial distribution of energy deposition matters less and

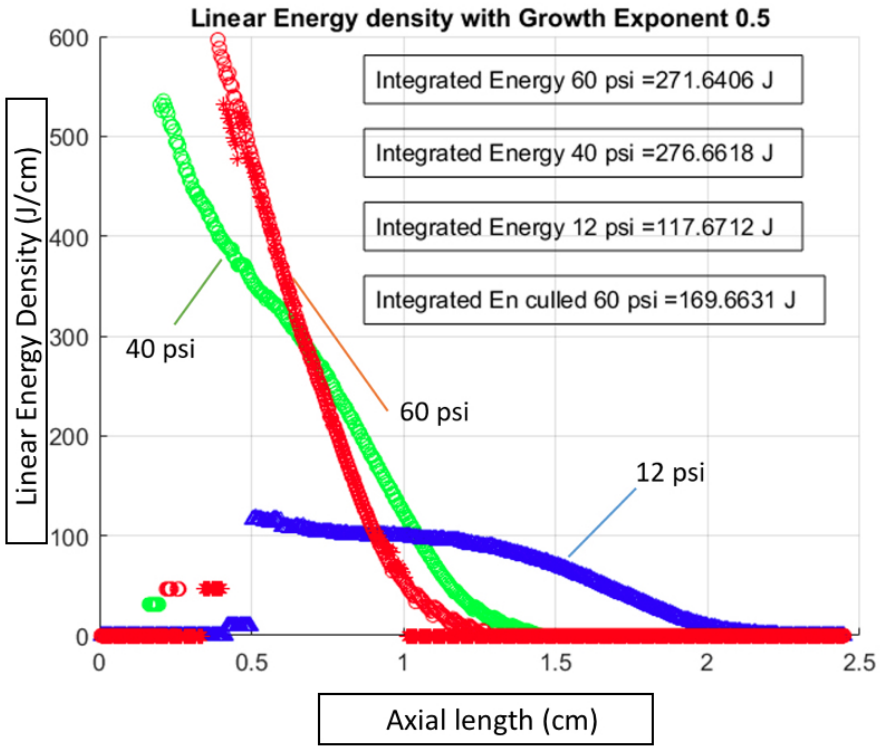

Figure 6.5: Energy per unit length inferred from a best fit of the blast wave trajectory at three different pressures. These distributions are representative of the 10 shots in helium with longer time scale separations of 27 ns between frames. The total energy from a summation of the energy density is shown in the boxes in the top left. Note that the "culled" energy density refers to a total energy content counted after removing the portions of the cylindrical blast wave that are obviously influenced by a spherical blast wave originating at the laser entry region. The overall energy content is low compared to the laser energy in all cases, indicating that the bulk of the energy is lost or deposited in the laser entry region at all densities.

less at such a large radius.

It is worth noting that we initially looked for a difference between trajectories from a 7 T applied magnetic field, and although none was observed,

we did not check carefully. The data may need to be re-examined, since we expect the plasma β to approach unity during the expansion.

6.4.3 Comparison between Energy Density Distributions from Sound Speed and Blast Wave Methods

We can verify that our interpretation of energy densities from ion acoustic transport is valid by comparing it with an energy per unit length that we find from a late-time blast wave trajectory.

Unfortunately on most shots with 60 psi of helium, we did not look late enough in time to see blast wave trajectories. However on one shot we had 27 ns separation between shadowgraph frames, which allowed us to compare the energy per unit length obtained from sound speed analysis with blast wave analysis on the same shot.

Fortunately, the energy densities obtained from the blast wave trajectory seem to follow closely with that of the sound speed. The axial profiles for energies obtained via two different methods seem to follow within 20% for most of the length. Near the end of the plasma, the cylindrical geometry blast wave trajectory we used is less valid. Here, the blast wave can also expand axially, so the trajectory more closely matches a spherical blast wave and forcing the exponent of time to be 0.5 causes an overestimate of energy. We expect that the energy from the sound speed calculate is less overall because the ion acoustic wave has begun to slow down. 27 ns is beyond the blast wave transition in which mass accumulation at the shock boundary is building while

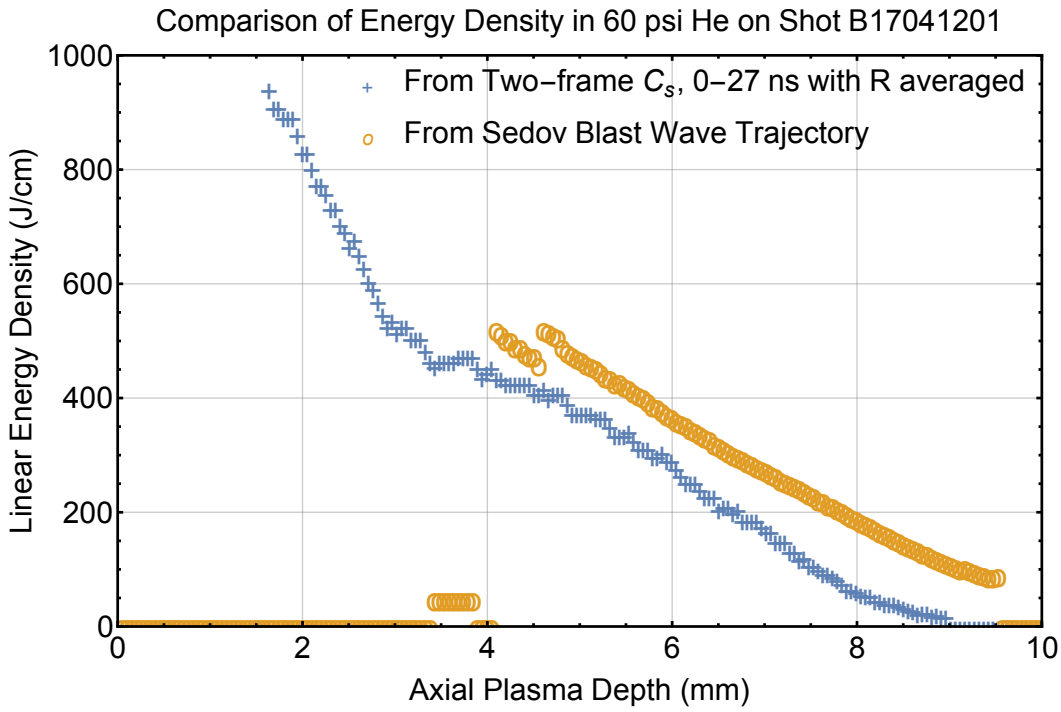

Figure 6.6: Energy per unit length inferred from the sound-speed temperature and plasma radius from the same 60 psi helium fill pressure shot B17041201. In order to calculate the volume at the calculated temperature from the sound speed, the methods in chapter five were used. The energy density that we calculate from the sound speed uses the calculated temperature and assumes the initial gas density and a uniform temperature over the average radius between the frames.

internal pressure is dropping. Regardless, the approach seems to validate that we can use either method and get an energy density distribution that will be useful for relative comparison of different laser parameters. The same methods should give corresponding comparisons between shots.

Ultimately the interpretation of energy density using the sound speed of the plasma may be more useful, because it allows a large region of interest

to be diagnosed without interference from the late-time spherical blast wave originating from the LEW. We will explore what we learn from this approach in chapter seven.

6.5 Conclusions from Blast Wave Analysis

We have shown that the cylindrical blast wave behavior is a good model for helium plasma expansion in the range of time from 30 to 200 ns. This behavior allows us to extract an energy per unit length of the plasma using only the best fit of the STBW trajectory and the initial helium fill density. In general, the results are in the range of 100 to 400 J/cm and reflect a lower overall energy content in the laser-plasma than is ideal for MagLIF. The results also seem to show that at lower densities the energy per unit length is highly uniform, which is very unexpected from solutions of collisional absorption and heating beam transport. At higher densities of 40 psi helium fill pressure and above, corresponding to electron densities of 10^{20} cm^{-3} and above, the energy per unit length begins to steeply ramp down with axial length. This is similar to the behavior for energy density distributions expected from a simple model of collisional absorption deposition as presented in Slutz's initial MagLIF paper [1], but there maybe differences that we cannot resolve. This suggests some other undesired behavior such as self-focusing may be occurring, at least at lower densities. We will explore these energy densities at higher fill pressures further in chapter seven, next.

Chapter 7

Energy Density Distribution Results

This chapter will use the methods from chapter five using sound speed transport to compare energy density distributions. We compared different laser parameters to see which would produce better overall energy density distributions at the same density. Parameters that were explored are laser beam spot size, the time delay for the prepulse, the main pulse duration at the same power and intensity, and the magnetic field. These shots were largely used for diagnostic and experimental capability development, so a substantial fraction had non-ideal diagnostic returns. Also, in several cases we were not able to make direct comparisons between two shots because more than one parameter varied. Experiments including a range of laser parameters still revealed several trends that we can describe here.

All of these experiments are motivated by MagLIF. Recall from chapter one that MagLIF's yield is strongly affected by the preheat energy. Also, the initial preheat energy should be uniformly high through the one centimeter length of the MagLIF target. Yet there have been few measurements of the quantity or distribution of the initial preheat energy in the plasma. So these measurements are valuable as a comparison for simulations and to optimize

experimental parameters for maximum delivered energy. We found that the preheat energy was relatively low across a range of initial parameters that had been used for some initial MagLIF experiments, so this work will inform the program about preheat in the most recent MagLIF experiments versus older experiments.

In many cases, we will find that the energy density is a steeply descending function of axial depth. This is not dissimilar from what we expect from collisional absorption, although the profile is slightly different. Simple collisional absorption, with no other effects such as radial transport, produces a temperature distribution given by the following relation relation:

$$T(z) = T_0 \left(1 - z/z_f\right)^{2/3} \tag{7.1}$$

where T_0 is the temperature at the laser entry area, and z_f is the final axial length [1]. This equation is the solution to the differential equation for the plasma temperature as nonlinear heating bleaches out the plasma opacity. This temperature distribution is plotted in figure 7.1, obtained from Slutz's paper.

In practice, as we will see, the temperature and energy per unit length seem to be an approximately linear function of z with a negative slope when a magnetic field is not present. This is similar to the above solutions, but generally higher in energy and temperature closer to the LEW. Although axial thermal conductivity should tend to homogenize the axial energy distribution,

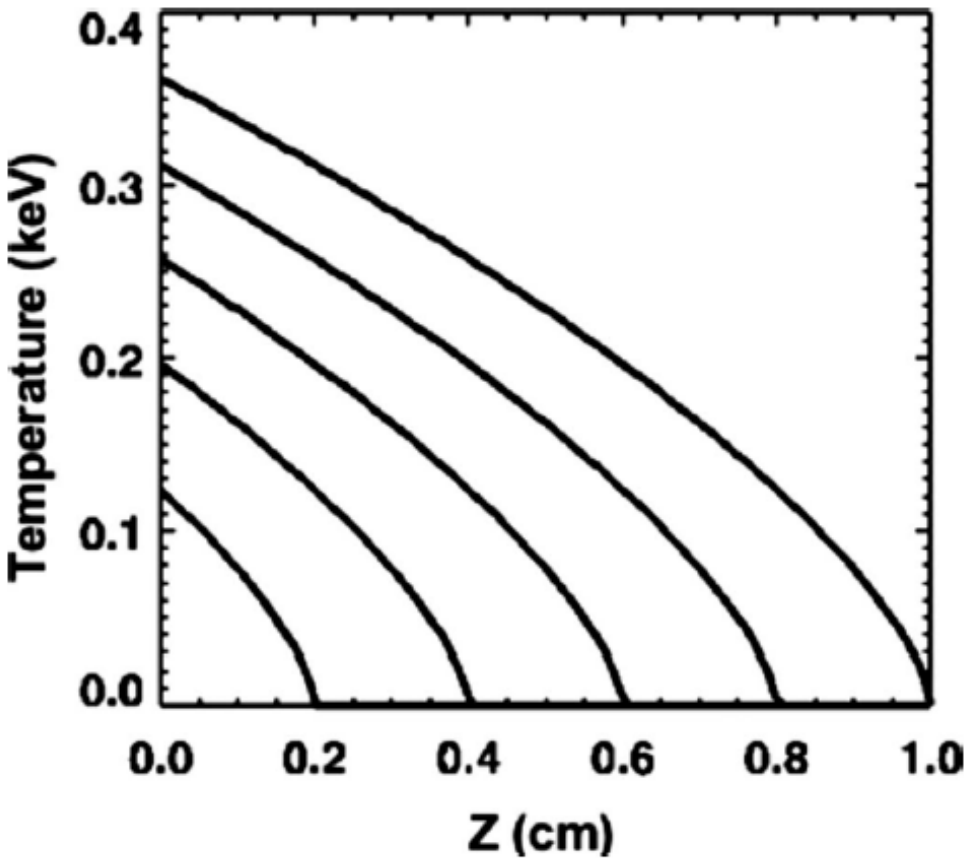

Figure 7.1: This figure from Slutz's paper gives the general shape of a temperature distribution in which collisional absorption is the only effect important for determining the plasma heating profile. This theoretical solution ignores radial transport and energy lost to radiation [1].

we did not see evidence for that in the time scale of sound speed expansion in about 10 ns. Generally, MagLIF benefits from uniform energy density distributions so such a descending function would not be ideal. However, the energy density distributions in this chapter will not be directly applicable to MagLIF because the magnetic field was not present. The energy density and

temperature profiles in chapter eight might be more valuable to designers and simulators of MagLIF, while the profiles here in this chapter will be useful for understanding transport processes and collisional absorption without a field.

This downward-ramping energy density behavior might be explained if the cross sectional area of the heated plasma is decreasing with axial length, or if radiative loss processes near the laser entry are depriving the beam of intensity and sapping away energy faster than collisional absorption. Self-focusing in the plasma could explain a drop in the cross section of heated plasma, but so could radial thermal transport bias toward the laser entry. A driven electron thermal wave replenished by continuous laser heating at its core would expand outward radially as a nearly linear function of time, possibly explaining the linear downward-ramp with axial length. This is corroborated by transverse x-ray images that we will see in chapter eight. The uniformity of the energy density profile as a function of axial depth is improved with the addition of a 17 Tesla magnetic field, as we will see in chapter eight.

We can compare energies delivered between shots, but absolute quantities for energies inferred from the sound speed have a large uncertainty. This is because they assume a constant temperature over an unrealistically large cross-sectional area of the plasma which we measure from shadowgrams. However, the sound speed methods can place an upper bound on the energy per unit length in the plasma. This could be compared to the total delivered laser energy. This provides a simple absorption fraction with a large error bar, which we can compare on different shots to understand general trends. While

our measured total energies from the sound speed methods are likely an upper bound, we observed coupling efficiencies change by 50% to 500% as laser parameters such as prepulse delay time were varied. This informs us about the relative importance of changing laser parameters.

Throughout this chapter and the next chapter, shot numbers will be mentioned so the reader may refer to Appendix B for a shot table. This table will describe the important parameters of each shot, along with important measurements, such as energy delivered. Raw shadowgram data from selected shots can also be found in Appendix B.

7.1 Affect of Laser Parameters on Energy Density Distributions

With the initial laser and target configurations we explored, we found energy deposition to be low in the diagnosable regions of the plasma. In general, a class of laser parameters used in many prior MagLIF experiments only produced on the order of 100's of Joules in the mid-regions of the plasma's axial depth. Decreasing the laser intensity from about $2 * 10^{14}$ W/cm^2 to mid 10^{13} W/cm^2 range by increasing the spot size had a measurable but small effect by itself. However, we see a substantial improvement in centimeter length-scale energy coupling efficiency and overall energies (perhaps exceeding 1 kJ) by implementing a combination of a longer delay in a prepulse (20 ns time gap) and a longer duration heating pulse (4.8 ns) with a correspondingly higher energy heating pulse (about 1800 J total) while operating in the mid

10^{13} W/cm^2 intensity range.

We can make relative comparisons of total energy integrating the energy per unit length over the diagnostic-visible length. Since some shots were only measurable beyond about 3 or 4 mm, we chose 4 mm as the common point at which energy comparisons would take place. Since we know the energy that Z-beamlet delivered to the target, we can get an absorption fraction. Absorption fractions permit rapid comparison between laser parameters. At the lower end, we saw deposited thermal energies on the order of 100's of Joules. Improvements across all four experimental parameters that we varied generated overall deposition energies well above 1 kJ, or at least a factor of 10 improvement in the absorption fraction beyond 4 mm.

7.1.1 Influence of Beam Intensity

Controlling heating beam intensity is important for mitigating laser-plasma interactions (LPIs). If beam power is fixed we can control intensity with the beam spot size. Typically, lower intensities help avoid thresholds for LPI losses, so a lower intensity beam over a larger spot size should be better for energy deposition. This is the case up to a point where the heated region is too wide for practical implosion in MagLIF, which is perhaps about 1.25 mm in radius. Figure 1.4 in chapter one gives the ideal beam width scalings for MagLIF yield. This figure indicates that if the beam is narrower than 1 mm, preheat temperature needs to be very high, above 2 keV, to achieve significant yield. However, our experiments used a beam radius of 0.5 mm or less, which

is in the far left of the range in figure 1.4 and requires very high temperatures to deliver sufficient significant preheating energy. Both this figure and the necessity to mitigate LPI would suggest that a larger beam width is favorable.

We used a DPP to improve beam uniformity in our experiments. The DPPs are described in detail in chapter two, including beam profile images and histogram characterizations. For most of the shots discussed in this work, we used a DPP designed to produce a 95% energy contained within a circle of width 1.1 mm on a 3.2 m focal length lens. For our 2 m lens, the corresponding circle has a width of about 690 microns in the near field. This small spot size with a 1/2 TW heating pulse produces an irradiance at the LEW of 10^{14} W/cm^2. In some of the most recent experiments of 2018, a phase plate that gives a 1.5 mm spot with a 3.2 m lens was used. This phase plate gives a 940 micron width circle of 95% irradiance when used on our 2 m lens, and a pedestal irradiance of mid 10^{13} W/cm^2.

We defocused the 690 micron DPP to increase beam width and reduce irradiance on initial experiments. For two shots, namely B17111401 and B17111505, we used the narrowest waist of this DPP on the target laser entry window (LEW). We used the defocal distances of 0, 2.5, and 5 mm. Figure 7.2 gives the beam profile lineouts at three defocal ranges. These measurements are based on beam images such as the 5 mm defocused 690 DPP image in figure 7.3. The data from figure 7.2 gives full-width half-maxima which are about 720, 800 to 1000, and 1000 to 1200 microns, as measured from images such as figure 7.3. This figure illustrates that the beam width varies differently along

different axes. The beam also becomes more square in shape as a consequence of the square beam transport in the far field. While subsequently defocusing to control spot width, we configured the beam to be diverging as it approaches the LEW, with narrowest beam waist in front of the LEW. Figure 7.10 gives an explanation of the defocusing setup, with three different blue LEW locations showing the defocus positions while we used the 690 micron phase plate. We also explored a DPP that gives a 1 mm spot later in the experimental program with some shots in 2018. Figure 7.10 also shows a different DPP that we used much earlier in the program, in 2016, which had a much narrower beam width and was not used for any shots in this chapter, only for those presented in chapter six.

The energy density results for a variation in width via defocusing distance with a the 690 micron DPP are in figure 7.5, with corresponding temperatures in figure 7.4. Changes in beam width with defocal distance are seen in the radial lineouts After exploring these variations in spot size, all subsequent experiments with the 690 micron DPP used a 5 mm defocus distance for the largest spot size of around 1 mm in the width dimension viewed by the shadowgraphy diagnostic. It is worth noting that, by operating away from the near-field of the DPP, we are allowing some native non-uniformities of the beam to reach the target, including larger-scale radial intensity gradients and a partially rounded square shape. Also, the beam width is greater in the y-axis along the line of sight of the shadowgraphy probe beam, and the beam is about 1.4 mm wide in that dimension.

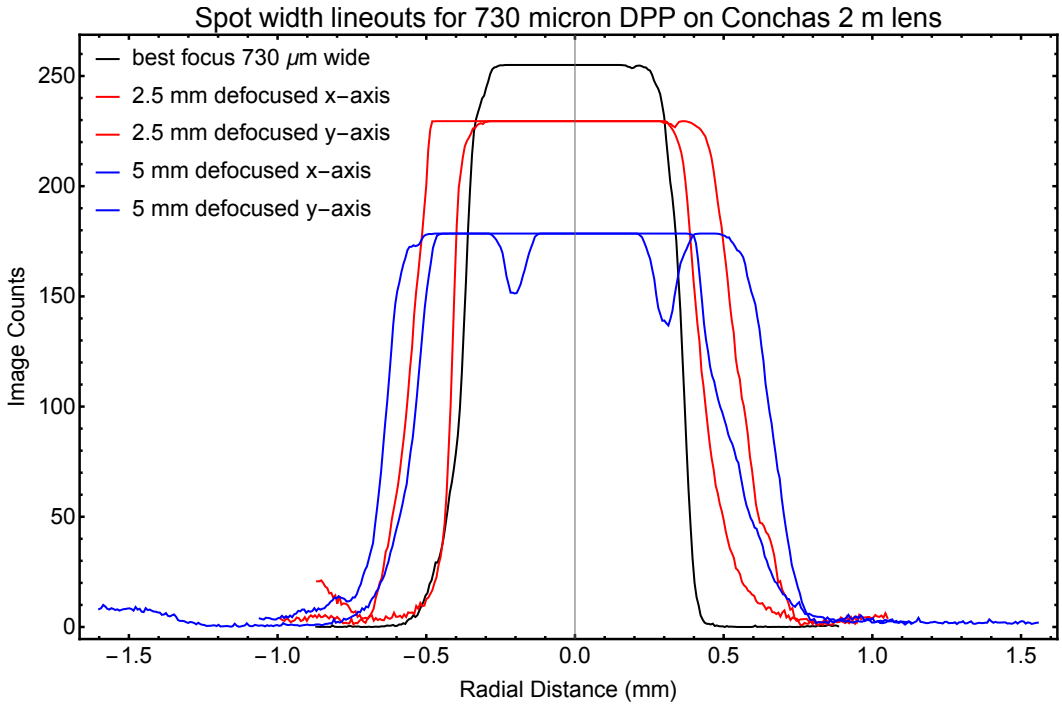

Figure 7.2: These images are lineouts from images of the beam at various defocal distances, as the beam is projected on a viewing card and imaged via scattered light. An example beam image used for this measurement is given in figure 7.3. They were taken in December, 2017 with the distributed phase plate (DPP) that was used on the majority of these shots. This DPP gives 1.1 mm spot on best focus with a 3.2 m lens, but with the 2 m lens on Conchas it produces a 690 micron best focal width. As it is defocused, the width of the beam in x and y vary differently by more than 35%. The x-axis, which has less width expansion with defocal distance, is the axis we viewed transversely with shadowgrams. The FWHM as measured from this data may be over-estimates, since the images usually saturated the pixel-count.

We varied the the spot size while other laser parameters were less in a less favorable range, with a 2 ns prepulse delay and a 3.5 ns heating pulse duration at 1/2 TW. Increasing the spot size produced small increases in the total energy within the diagnosable region and reduced the overall size

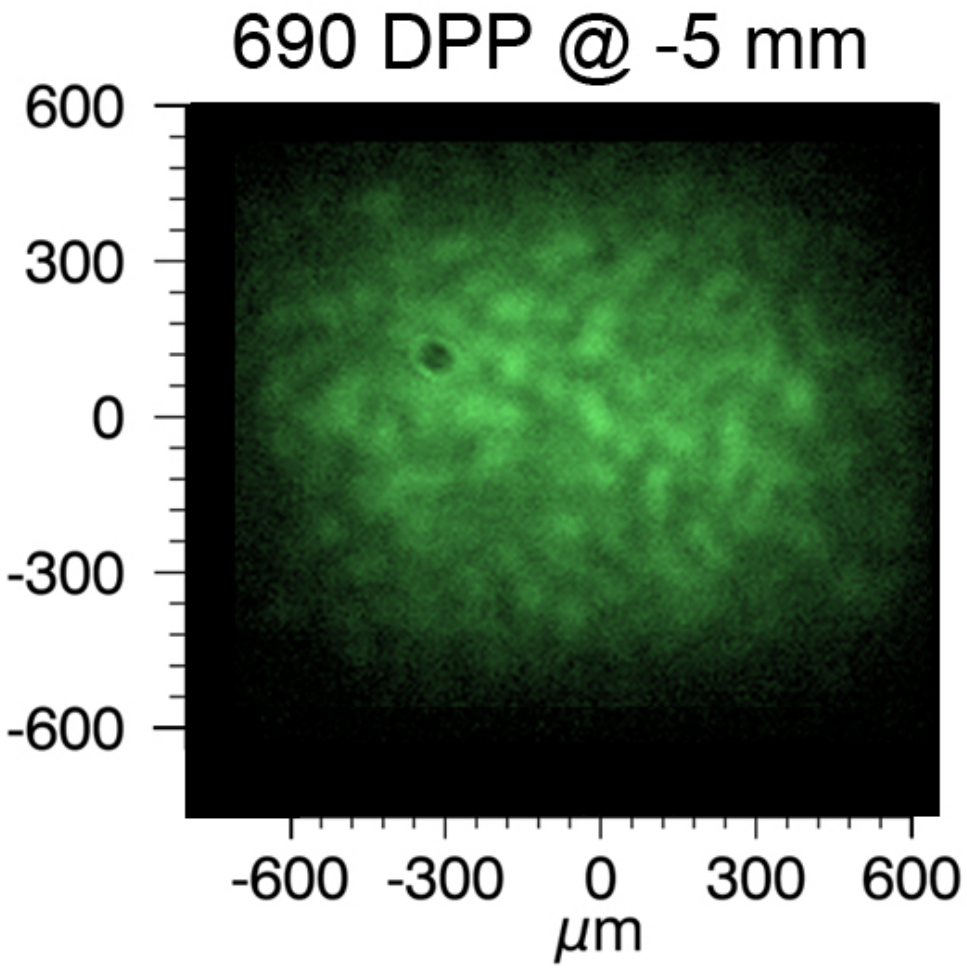

Figure 7.3: This is a photo of the beam using scattered light from a viewing card, with the imaging camera at about 20 degrees from the beamline such that trigonometric corrections to the image aspect ration are minimal. This photo is the nominal beam image for the beam as it would strike the LEW on most of the shots presented in this chapter.

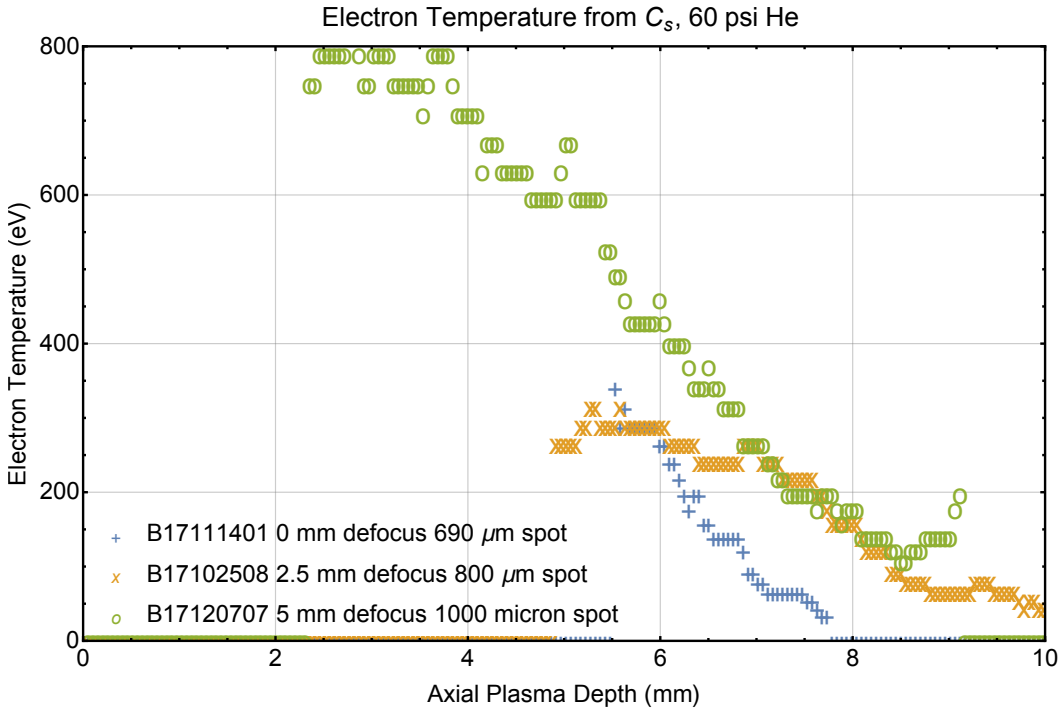

Figure 7.4: Here we compare temperatures from three shots that were performed early in the campaign with a range of three laser spot sizes, as controlled by the axial defocusing distance from the narrowest beam at the near field of the DPP. The lineouts of beam widths at the LEW for these three shots are in figure 7.3. Large regions of anomalous opacity associated with higher irradiance at the LEW prevent accurate measurement of the energy density via the sound speed close the the LEW, out to about 5 mm on shot B17111401.

of anomalous opacity regions, as exemplified in figure 7.6. These anomalous areas are interpreted as ionized regions of fairly cold plasma of surrounding the first few millimeters of the plasma's axial depth, in the region close to the LEW. They extend outward by about 2-3 mm in an oblong shape beyond the plasma radius. The simplest explanation for these anomalous opacity features is ionization caused by either hot electrons or strong UV and soft

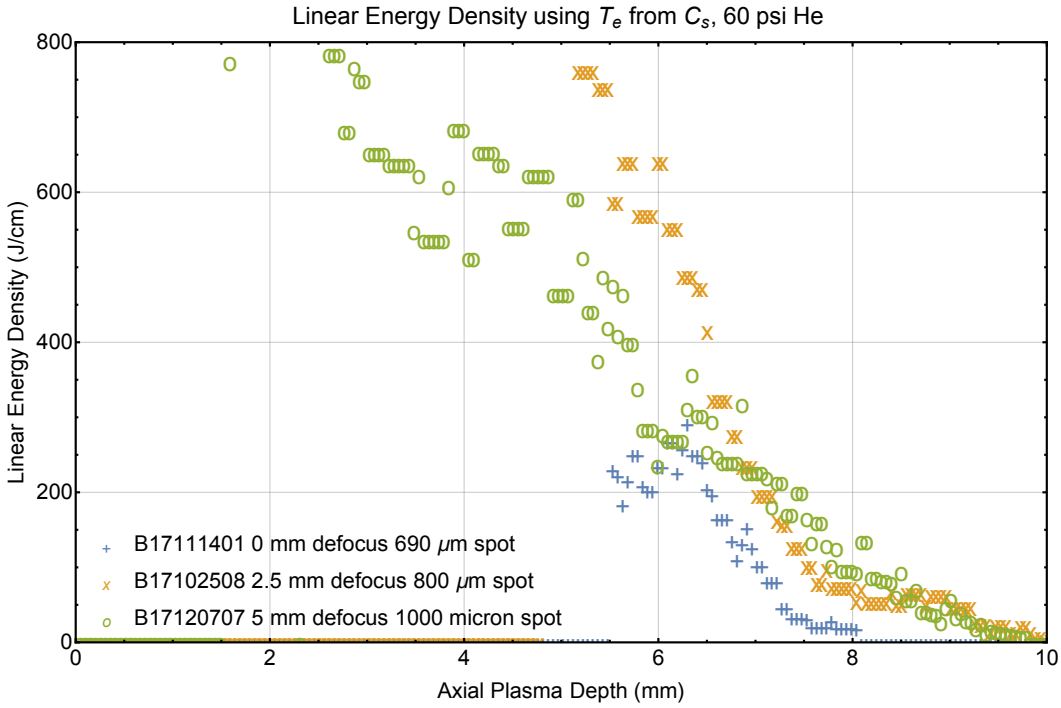

Figure 7.5: Here we compare energy densities from three shots that were performed early in the campaign with a range of three laser spot sizes, with the same shots compared in figure 7.4.

x-ray radiation emerging from the LEW region. Phenomenologically, on some shots these regions correlate with shots at higher laser irradiance and shorter heating pulse duration, including some of the shots in figure 7.4 and 7.5. These shots have an energy energy content beyond about 4 mm is generally less than 100 J. Geissel et. al. observed these anomalous opacity features in experiments in the Pecos chamber also [35] [20]. These regions are too large and grow too quickly to be a sound speed or blast wave hydrodynamic front at this time scale. Unfortunately these regions preclude effective sound speed analysis, so on these shots we could only diagnose the region from about 4 mm to 8 mm

axial length.

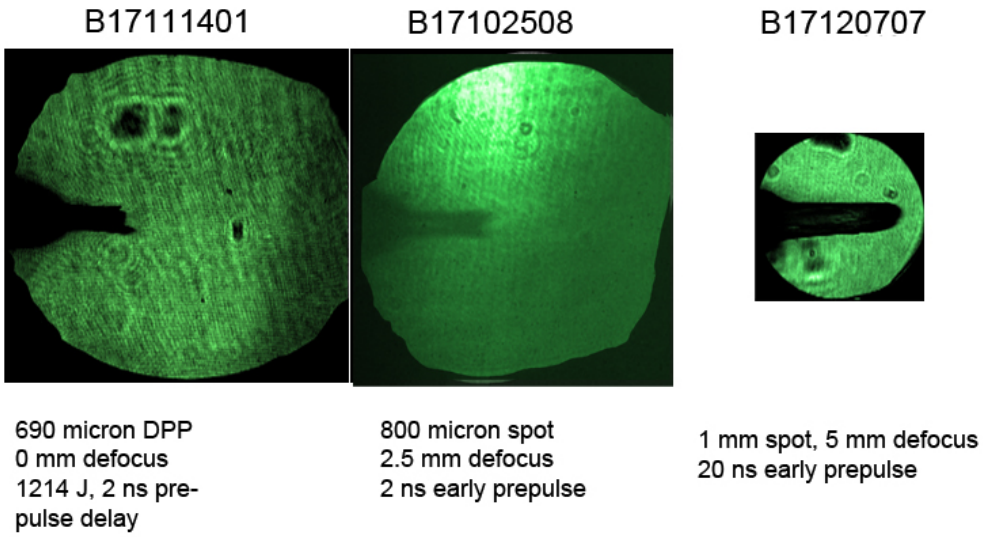

Figure 7.6: These are the same three shots with energy densities compared in figure 7.5. These shadowgrams are captured just after laser heating is over. All of these shots used a 3.5 ns main heating pulse with a laser power in the range of 1/2 to 1/3 TW. B17120707 used a 20 ns early prepulse while the others used a 2 ns early prepulse, so that may account for some of the difference. All shots have the anomalous region of opacity surrounding the LEW, followed by a narrow heated plasma, but the region is greatly reduced in B17120707.

We also observed these regions of anomalous opacity later in the campaign. They are typical of the first 2 ns of heating in some experiments. We carried out an experiment with 5 mm defocus that used a longer prepulse delay gap, and a longer heating pulse. On shot B18020201, the shadowgraph frame midway through the 4.8 ns heating pulse reveals a plasma with anomalous opacity that is qualitatively very similar to earlier experiments, as compared in figures 7.15. This includes the plasma having roughly the same length and

width. However, after 2 ns of additional heating the shadowgraph plasma has grown to the full length of the viewing window and doubled in width. This suggests that there may be an energy and/or laser duration threshold that must be overcome in order to deliver substantial energy into the plasma, and these early experiments did not sufficiently exceed that threshold. The threshold is apparently exceeded midway through a 5 ns long main pulse.

7.1.2 Variation of Prepulse Delay Time

We also varied the pre-pulse delay time gap. This had a significant positive effect on the overall energy density in the plasma except on a pair of shots. Most early experiments used a 2 ns early, 100 J prepulse that was part of the six nanosecond Z-Bemlet AWG timing window. The AWG window thus limited the main pulse to 3.5 nanoseconds in duration. A representative waveform for this configuration is shown in chapter two in figure 2.1. We also had the option of increasing the delay time between the prepulse and the main heating pulse using a separate laser system, co-injected along the same beam line. This allows a custom time delay between the prepulse and the main heating pulse. 20 ns was chosen as a reasonably early prepulse duration to give the LEW time to drop in density. Recall that the prepulse is intended to rapidly heat the LEW so that it can be reduced below critical density and allow the main heating beam to pass through. A longer prepulse delay should improve laser transmission by giving the LEW plasma more time to disassemble at the sound speed. A longer delay should also help mitigate

unfavorable laser interactions with the LEW. The sound speed in a carbon ion plasma resulting from the LEW expansion is around 30 microns per ns. Ideally this C, N, and O plasma would drop to less than 1/40th critical density and be sufficiently dissipated to absorb and re-radiate relatively little of the main laser pulse energy. These higher-Z atoms may be the origin of radiation or electrons that ionize the bulbous region of anomalous opacity that we see in the LEH window region on some shots; for examples see figures 7.6, 7.7, and 7.15. Long mean free path radiation or hot electrons from the laser interaction with the LEW material may be ionizing the cold gas sufficiently to obscure the probe beam via collisional absorption in these cases. However, at this time we cannot make definitive statements about the origin of these regions.

Increasing the prepulse delay seems to have a very strong effect on the overall energy and the steepness of the energy profile, although not on all shots. All shots with a two nanosecond prepulse delay had absorption fractions in the less than a couple hundred Joules total in the mid-regions of the plasma. The energy delivered beyond 4 mm is usually on the order of 100 J for those experiments. The only shots for which the 20 ns early co-injected prepulse did not have a dramatic improvement were two (B17111505 and B17111603) one of which was close to best focus of a 690 micron phase plate. Since B17111505 had a a higher intensity at the LEW, interactions with the LEW such as through LPI likely created significant losses there. B17111603 also had a large region of opacity around the LEW. Qualitatively, when an dramatically increased absorption fraction from co-injected early prepulses, this was accompanied by

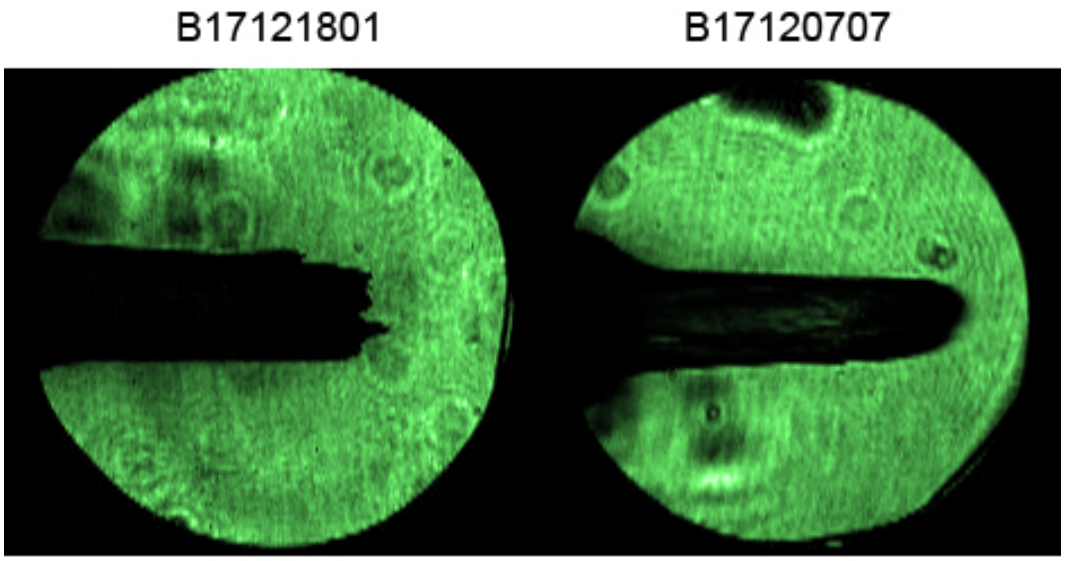

Figure 7.7: This figure shows the post-heating shadowgram images from two of the three shots compared in figures 7.8 and 7.9, demonstrating a qualitatively different character. B17121801 is wider, and the end of the plasma suggests a set of parallel filaments. B17120707 has a weak region of opacity around the LEW, but it is not as strong as the shots with a higher irradiance such as B17111505, which also had co-injected early-prepulse.

reduction or lack of the anomalous high-opacity bulbous feature surrounding the LEH region on most shots. Those anomalous features are indicative of strong energy losses in the LEW region.

Experiments in 2018, all with co-injected 20 ns early prepulse, had mid to high ranges of energy densities. Energies beyond 4 mm were in the range of 400-600 J. Longer pulse durations combined with a co-injected prepulse seem to have a better overall impact, as we shall see. Regardless, the concluding statement is that a 20 ns early prepulse increases the energy delivered beyond 4 mm increases by a factor of 4 to 6, depending on the pulse duration and

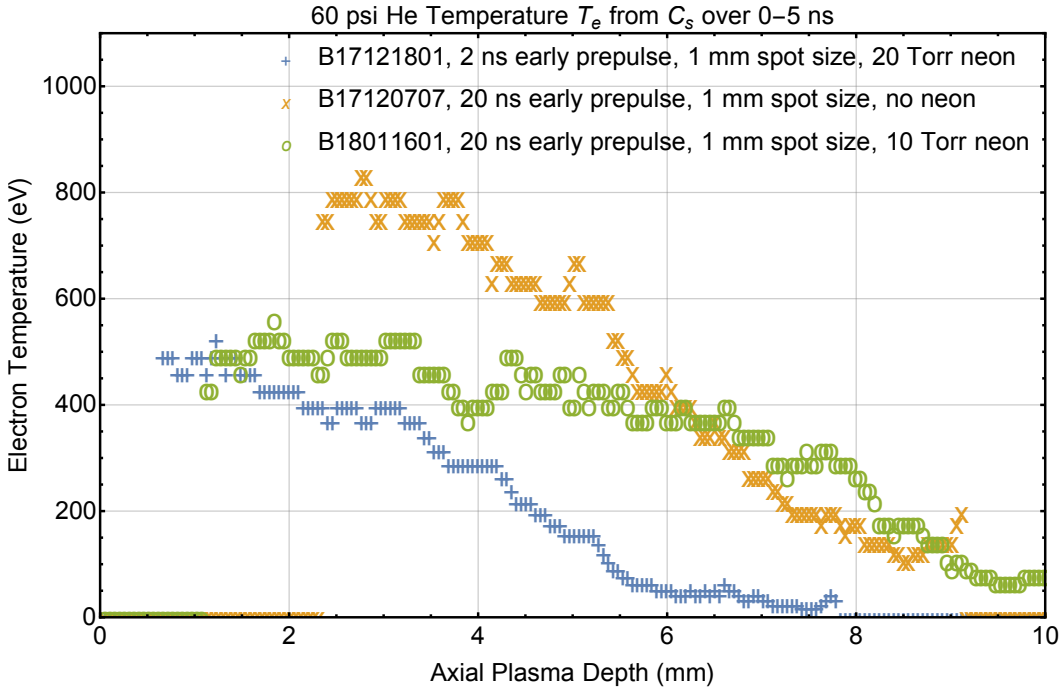

Figure 7.8: We compare temperatures between one shot with a 2 ns early prepulse (B17121801) and two shots with a 20 ns early prepulse (B17120707 and B18011601). The increase in overall temperature with the earlier prepulse is apparent. Also, the differences in neon dopant density do not seem to cool the plasma sufficiently to overcome this significant increase in temperature from the earlier prepulse.

other factors.

In the experiments with a co-injected prepulse and a defocused beam, the prepulse beam spot size is smaller than the heating beam. This is because the co-injected prepulse beam is a separate, sub-aperture beam. The co-injected beam is smaller in the far field as it transports through beamlines. Nominally it would be the same size in the near field at the best focus of the DPP. However, when a defocused beam strikes the target, the beam width and

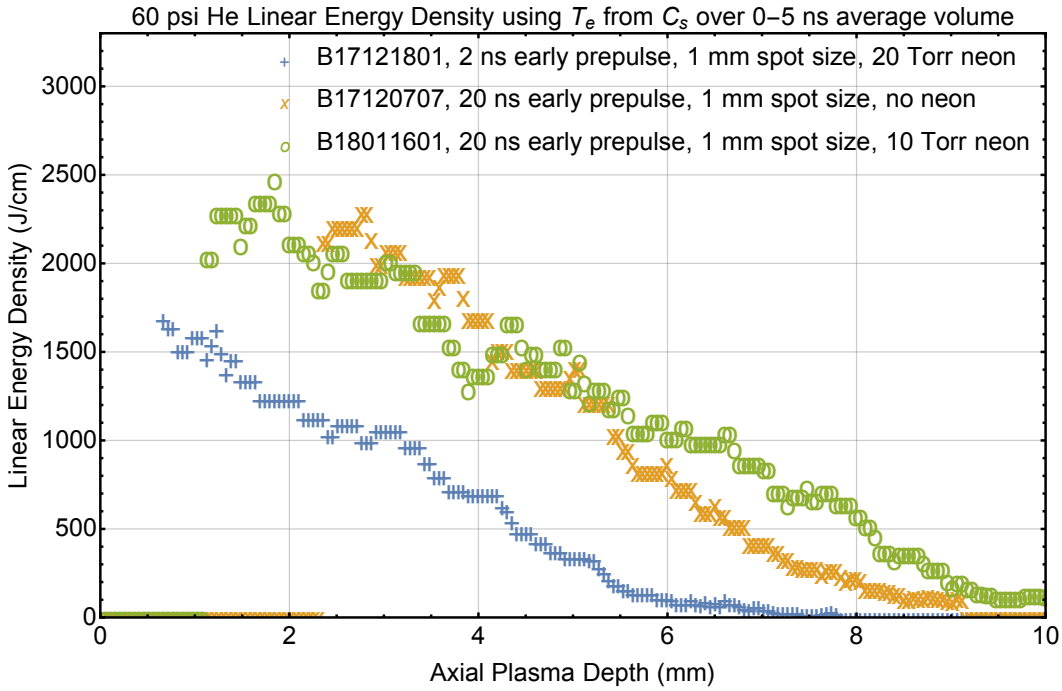

Figure 7.9: Energy densities compared between one shot with a 2 ns early prepulse (B17121801) and two other shots with a 20 ns early prepulse (B17120707 and B18011601).

features of the beam in the far field matter. So, the prepulse beam will produce a smaller spot size than the Z-beamlet's heating beam if the DPP's best focus is not right at the LEW. This means that when the main heating pulse arrives, it could encounter an annular region surrounding the prepulse beam spot that was never directly heated by the prepulse. Only thermal transport away from the prepulse beam width can heat the surrounding LEW, which may not be as effective in bringing it below critical density when the main heating pulse arrives. This complicates the improvements which may come from using co-injection. To resolve this question, we present comparisons between two shots

with con-injected 20 ns early prepulses and in which we changed between the two types of DPP next. The results essentially show that improvements from co-injected early prepulses are still extremely significant.

7.1.3 Influence of Focal Convergence

We did experiments with three types of distributed phase plates (DPPs). The physical configuration of these beams is explained in figure 7.10. Most recently we used the 690 micron DPP at a defocal distance of 5 mm, and another which produces a nominally 940 micron spot in the near field with our two meter focal length lens. Historically, in 2016 and early 2017 we also used a phase plate with a 550 micron spot, which required the greatest defocal distance to approach a 1 mm spot. With smaller beam-waist DPPs, the heating beam is diverging at approximately the focal ratio of the lens as it approaches the LEW. However, with the 1 mm DPP, the narrowest beam spot is right at the LEW and it would continue at that width for a few millimeters in vacuum. In the absence of any plasma optical effects the beam would diverge from there more slowly, since the empirical Rayleigh length is about 5 mm. If self-focusing is occurring, a beam that is already diverging might be less susceptible.

As mentioned previously, a co-injected prepulse should have a smaller spot size on the LEW than the main heating pulse. This leaves open the possibility that there might be some peripheral regions of the LEW at close to solid density. This would be highly detrimental to beam transport through

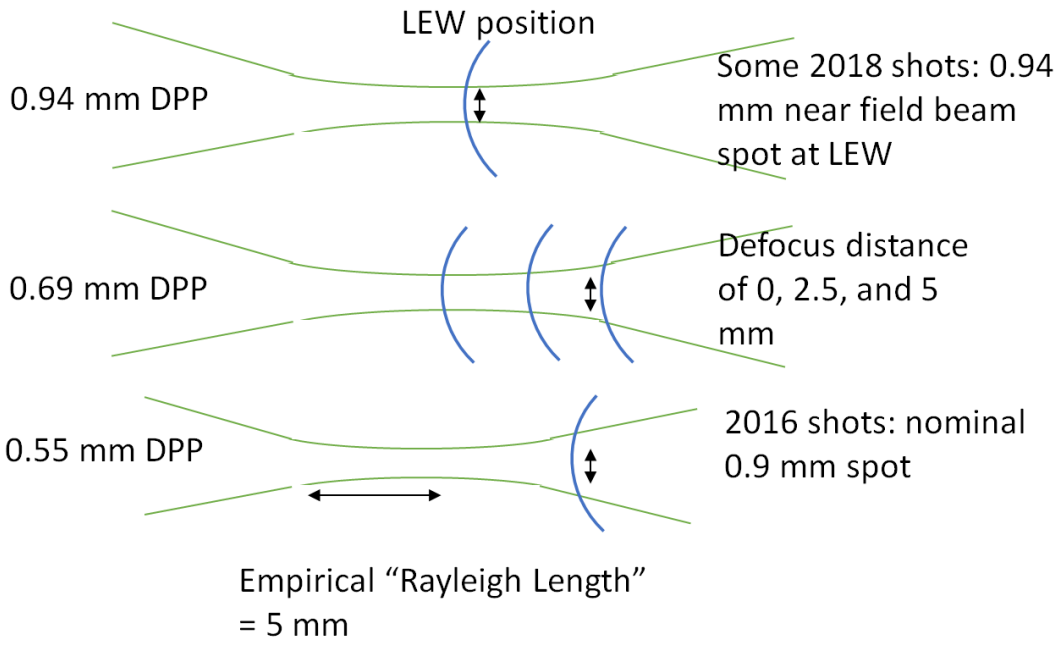

Figure 7.10: The beam spot at the laser entry (LEW) ranged from about 0.8 to 1 mm in width. Here, we show various schemes for producing a beam at the LEW with that width. In the absence of other effects, the beam would diverge going into the gas at an angle determined by the f/# of 2 of the Conchas lens. However, within the approximate length of about 3 mm, the beam is relatively uniform in width. See figure 7.2 for lineouts at various defocal distances.

the LEW region. Since both the smaller co-injected beam and the main ZBL heating beam would have the same size in the near field, using the 1 mm DPP with the near field at the LEW should mitigate this effect. This change in phase plate size did not change the energy density outcome, as shown in figure 7.11.

We compared energy densities from two shots with a 0.94 mm DPP and a 0.69 mm DPP defocused by 5 mm in figure 7.11. These two experiments

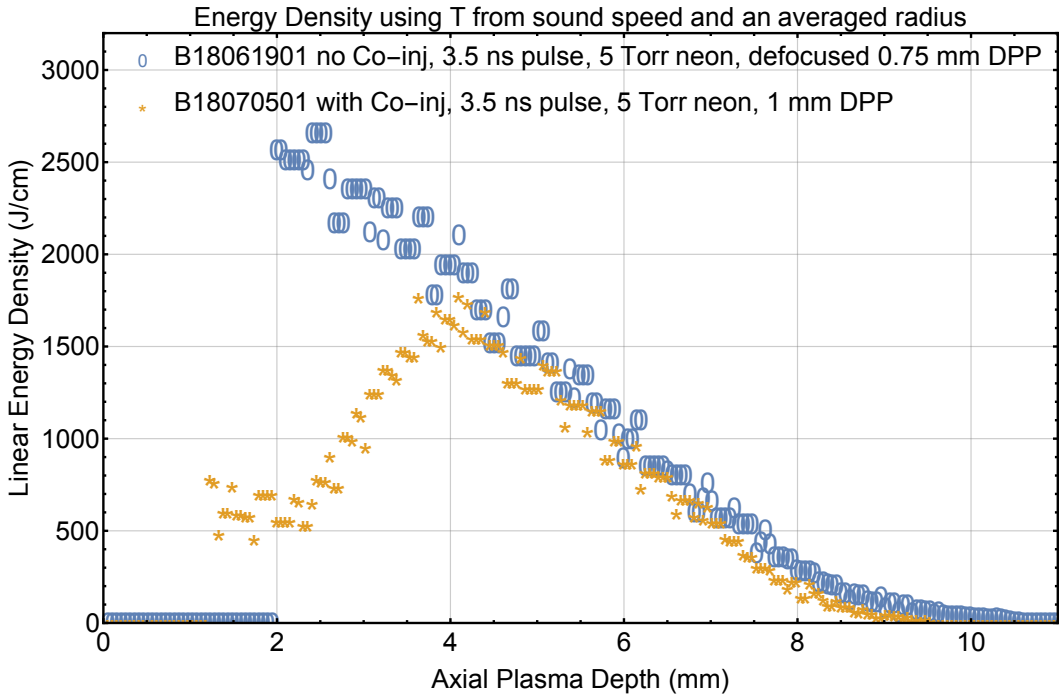

Figure 7.11: Two shots had 5 Torr neon, a 20 ns early prepulse, approximately 1300 J delivered to the target with a 1/3 TW power and 1 mm beam size. There was no magnetic field. The only difference is the DPP, and whether the beam was diverging or converging. The energy densities are very similar, except that the 1 mm DPP case produced a region of anomalous opacity that interfered with the shadowgraph sound speed measurement, as can be seen by the nonphysical drop in energy density from 0-4 mm that the analysis method interpreted.This is illustrated here for completeness; all other shots with this region have been edited to remove data from this region, where an energy density cannot be inferred.

controlled all other parameters, including a 20 ns prepulse made possible by a co-injected beam and a beam energy within 100 Joules. The results indicate that energy densities produced by this change in the DPP were essentially identical beyond about 4 mm. The major difference was that the plasma

produced by the diverging beam at the LEW did not produce a region of anomalous opacity in the first few millimeters of the LEH, while the 1 mm DPP experiment did. The defocusing also tends to reduce the intensity gradient at the beam profile's boundary, which may also be important. Since the cause of these regions of anomalous opacity is unknown, it is unclear at this time why a diverging beam versus a converging beam would affect it.

7.1.4 Influence of Pulse Duration

Intuitively, increasing the pulse duration and corresponding beam energy should add more length of heated plasma and increase the overall energy delivered. Since we maintained the laser power and intensity as the pulse length is increased, the overall energy delivered also increased, so it would be surprising if increasing the pulse duration did not generally increase the deposited energy. With a 2 ns early prepulse, the longest pulse duration of the main pulse is approximately 3.5 ns. However, with co-injection, a main heating pulse duration of as long as 5.5 nanoseconds is available. We did a series of shots with 4.8 and 3.5 ns main heating pulse durations. Figure 7.12 illustrates the temporal profiles of these heating beams. For shots with a 2 ns early heating pulse, figure 2.1 is representative of the temporal history which includes the prepulse, but on shots with a 20 ns early prepulse the time history for both beams is not available.

And indeed, increasing the pulse duration produced an increase in the total energy systematically. It also generally increased the axial energy pen-

etration length. Based on the total energy diagnosable with sound speed methods, the absorption fractions increased by approximately a factor of two. This is despite the fact that many of these shots had neon dopant which cools the plasma and decreases the observed sound speed. This immediately causes us to speculate that the radius used to calculate overall energy density is too large, leading us to systematically over-estimate delivered energy. Indeed, on B18020201, by the usual method for calculating energy per unit length from sound speed temperature and an averaged radius, we find a total energy greater than the delivered laser energy.

As an example comparing shots with different heating pulse duration, consider figures 7.13 and 7.14. The prepulse time gap remained at 20 ns for this comparison. The variable parameter was the heating pulse duration, with 3.5 ns to 4.8 ns pulsed available with laser intensity from 5 to $7*10^{13}$ W/cm^2. This modification necessarily requires the 20 ns early prepulse, because otherwise the a longer laser pulse configuration than 3.5 ns would not fit within the 6 ns AWG window of Z-Beamlet along with a 2 ns early prepulse. There was also a difference in the neon dopant density, which cools the plasma and may introduce an error in the sound speed results. The change from 0 to 5 Torr in this case did not dramatically change the energy density distribution on the two shots with 3.5 ns pulse duration, so we expect this to be a small effect. As a comparison between many shots with longer pulses and co-injection versus a few with shorter pulses and no co-injection, figure 7.16 plots energy densities from many shots. This shows a general improvement from both parameters.

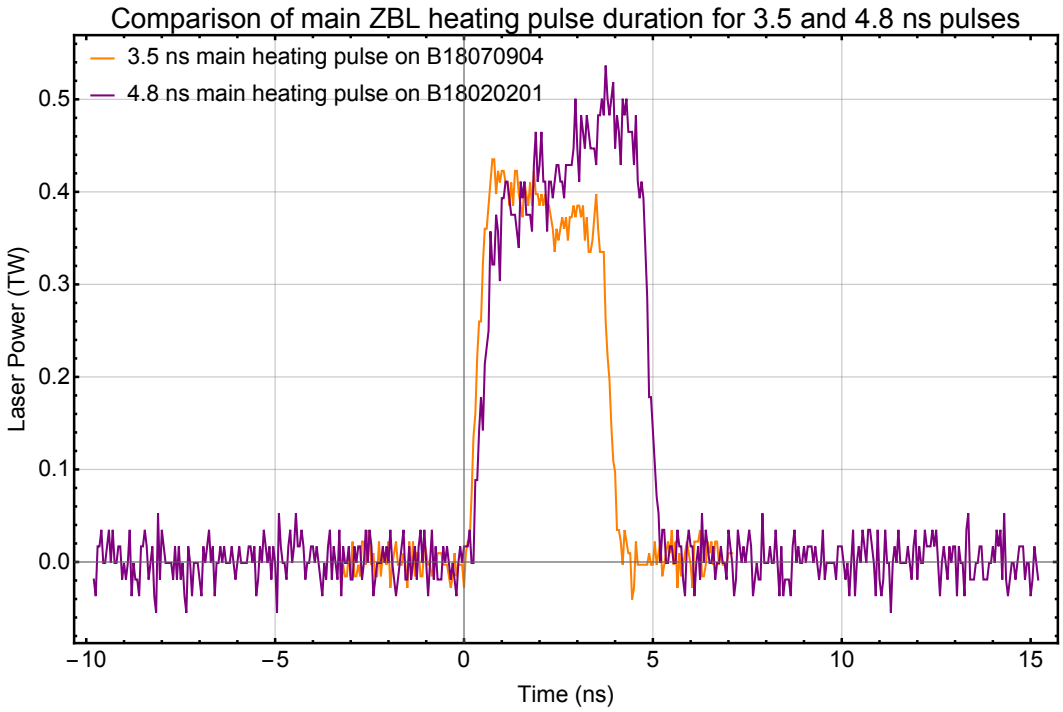

Figure 7.12: These laser temporal profiles show representative examples of two main pulse durations used in experiments, including the 3.5 ns and 4.8 ns main heating pulse of Z-beamlet. They both have similar powers of approximately 0.4 TW. These data are obtained using photodiode measurements on-shot, which are calibrated using time-sensitive full aperture calorimeters by Ian Smith. The data is courtesy of Ian Smith and the Z-Beamlet group [36].

The fraction of the delivered laser energy inferred from shadowgrams delivered beyond 4 mm axial depth went from about 0.3 in the two shots with 3.5 ns heating pulses in figure 7.14, to 0.45 on the shot with a 4.8 ns heating pulse. This is a 50% improvement in coupled energy beyond 4 mm. This implies that nearly all of the energy delivered in the last 1.5 ns likely coupled to the gas beyond 4 mm in axial length. Coupled energies on the longer pulse beyond 4 mm totaled 780 J on the shot with the longer pulse duration.

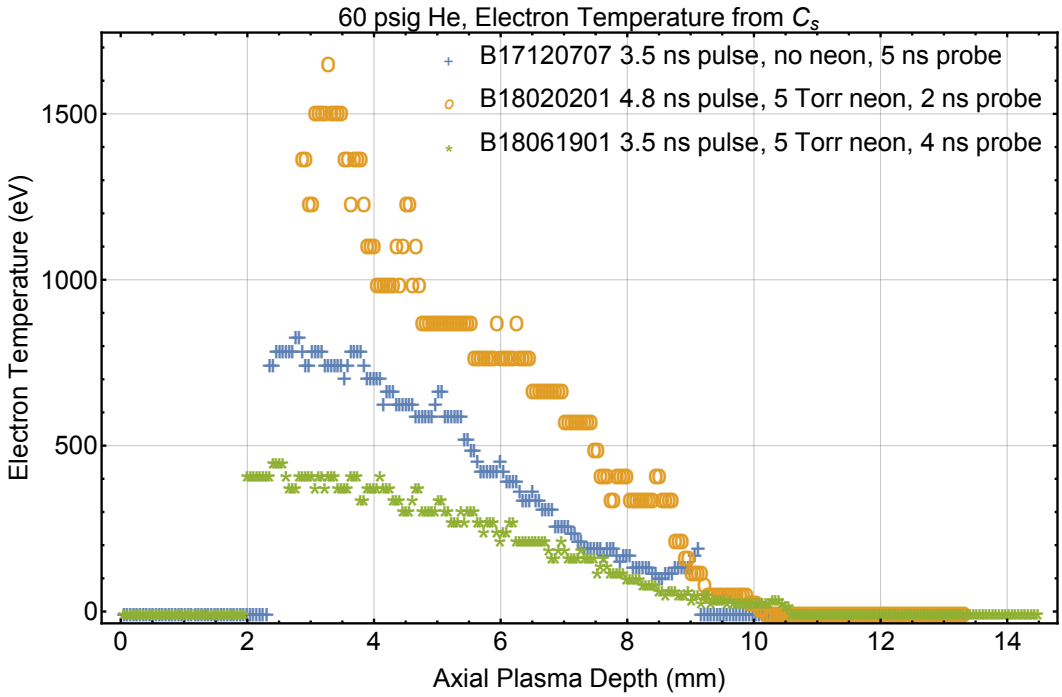

Figure 7.13: Plasma temperature axial distributions for three different shots, two of which had a longer pulse. These are representative of a general trend of higher temperatures further along axially when a longer pulse is used.

The strongly nonlinear improvement of energy penetration with pulse duration is suggestive of a threshold energy and/or time that must be overcome in order to improve energy coupling efficiency into the plasma. That threshold may be related to radiative losses in the LEH region, as mentioned earlier. The absorption fraction is strongly nonlinear with energy and pulse duration. This is obvious because as we moved from delivering on the order of 1200 J to about 1800 J laser energy and pulse durations from 3.5 to 4.8 ns at the same laser power, we saw a twofold to threefold increase in deposited energy efficiency beyond 3 mm in z. This behavior is well-supported by experiments done on

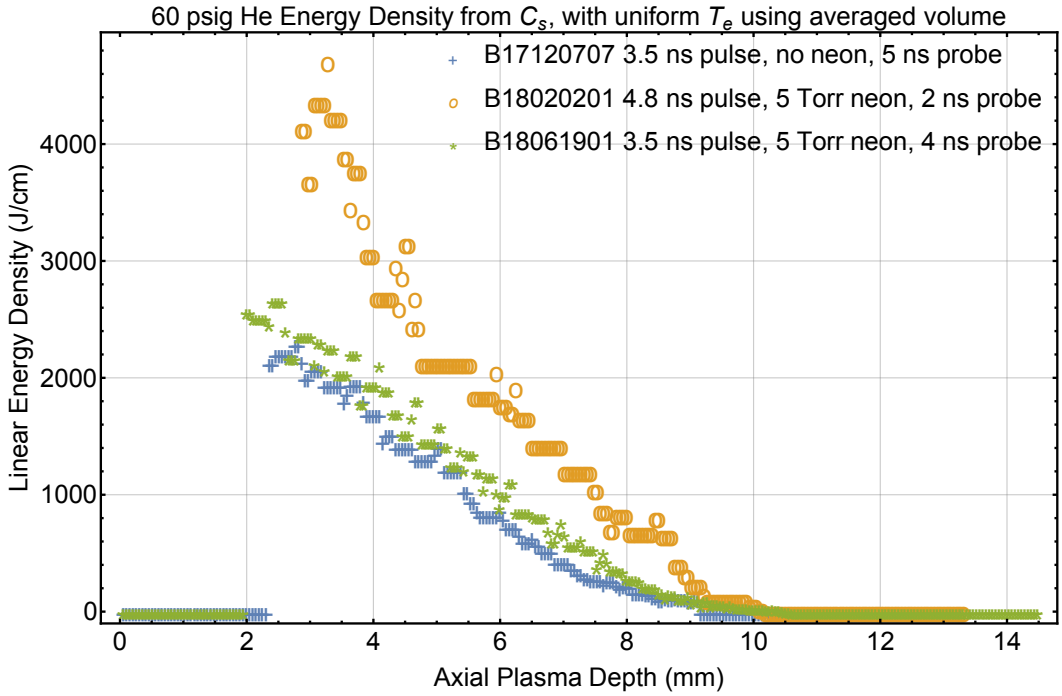

Figure 7.14: Here we see an improvement between three very similar shots. The main differences, besides pulse duration, are the neon dopant level and the probe interval. The pulse duration seems to have the effect of increasing the energy penetration by about 1-2 mm. The sound speed is decreasing as a result of the pressure drop from neon radiative energy loss, so the shorter shadowgraph probe interval of 2 ns on the longer pulse length shot introduces some error.

Omega-ep by Harvey-Thompson et. al., in which they saw laser coupling efficiency climb significantly to almost 0.82 for pulse durations exceeding 3 ns [16].

7.2 Laser Energy Loss Sources

Here we briefly mention Some sources of energy loss in the system.

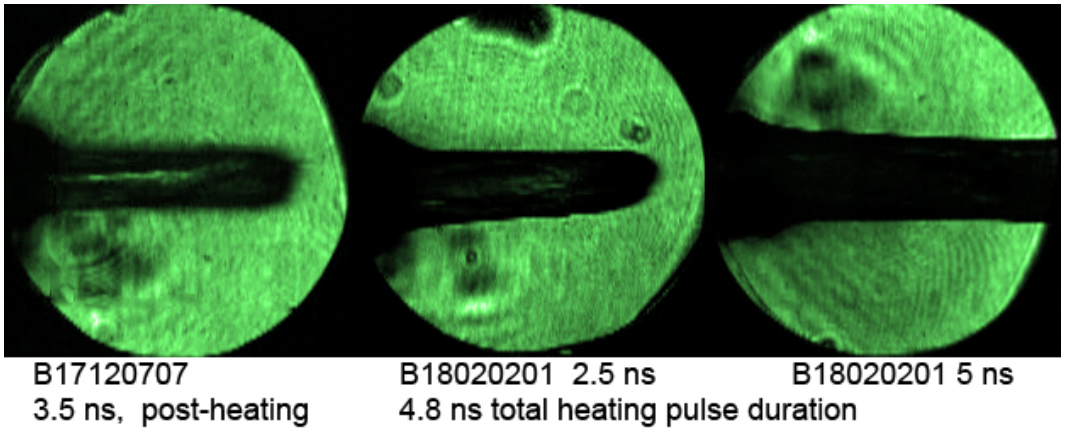

Figure 7.15: This figure compares shadowgram images on two shots. On the left this frame was taken within 200 ps of the end of the 3.5 ns heating beam B17120707. In the middle and on the right we have frames from a 4.8 ns long heating pulse on shot B18020201. The middle frame is from 2.5 ns into the heating pulse, and the right frame is the end of laser heating. Qualitative similarity between the left and middle frames is obvious, including the region of anomalous opacity surrounding to the LEW which we attribute to radiative energy loss in that region. Shots with this shorter pulse duration show energy penetration is less than 200 J beyond about 4 mm. Another 2.3 ns of heating on B18020201 produced the plasma with a striking increase in length and width shown in the frame on the right. This suggests that a threshold had been exceeded with a longer pulse.

First there is window material heating, which as mentioned previously is particularly vulnerable to radiative losses due to the higher Z materials in the plastic LEH window. These higher-Z emitters can produce radiation which transports out of the region through the LEH, and may also be responsible for the anomalous regions of opacity we see on some shots. These regions are usually strongest early in the history of heating, and are associated with experiments in which little energy makes it past the first few millimeters of

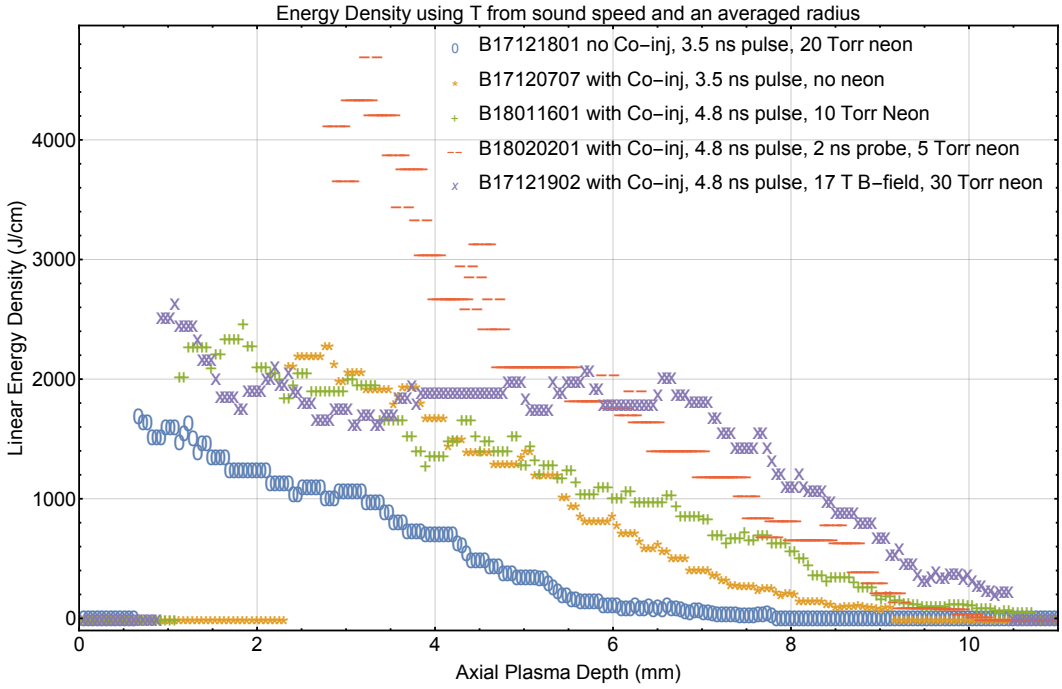

Figure 7.16: Here we see an improvement across a variety of shots in the overall energy which stems from an increased main pulse duration and the use of a co-injected prepulse. The shot with the highest energy density in the 4-5 mm region also had a 2 ns shadowgraph probe rather than a 5 ns shadowgraph probe, so we likely see less time for radiative loss from the neon dopant on that shot.

axial length.

There is also backscatter due to SBS and Raman which are addressed in detail in Geissel et. al. 2018 [20].

There are ionization energy costs, which for helium are particularly high. Most importantly, the use of helium versus hydrogen as the target gas creates a fivefold increase in energy cost to fully strip each atom. With a helium plasma, the energy cost of fully stripped ions is 80 eV. The energy cost

to fully strip a cylinder of 60 psi fill pressure helium 1 mm in radius and one cm long is 40 J at the minimum, and probably closer to 100 J once radiation populations are accounted for. Helium photon exchange in the spectral region around the ionization energy is expected to be nearly diffusive. This likely contributes to a radiative thermal wave which causes the shadowgraph plasma to appear larger in diameter than the hot plasma regions that are emitting x-rays. This also explains why deuterium plasmas in experiments on the Pecos chamber at Sandia do not appear as wide, and are typically much closer to the diameter of the heating beam. The region inside the shadowgraph boundary has a plasma ionization energy proportional to r^2. Once the shadowgraph plasma is has expanded to 3 mm radius, the ionization energy cost is 350 J in helium, but would still only be 60 J in deuterium. In a shadowgram with a 2 mm radius, we expect the energy to create a 600 micron thick radiative thermal wave precursor to be on the order of 150 J, including ionization cost, warm electrons, and photons. This value will scale approximately linearly with radius as the plasma expands, since the radiative precursor remains approximately the same thickness. But, as a fraction of absorbed laser energy, we expect the precursor to be about 10-15%.

Radiative losses due to the dopant gas are important. We need to better characterize the rate of radiative losses due to neon dopant in the gas, and the effect that this might have on the sound speed diagnostic methods. This may lead to a re-interpretation of some of these results. In general, however, the shots in which we used neon dopant were coincidentally the same shots in

which we saw substantial improvement in overall deposited energy from longer pulse durations an co-injection, so it is difficult to de-convolve these effects. Removing the neon is expected to only help couple more energy into the gas, since the amount of energy radiated before a sound speed can be measured is expected to be on the order of a 100 Joules.

7.3 Summary

We began to address the challenge of measuring and optimizing a laser-heated plasma column with an energy density and energy uniformity that is as high as possible. We studied sound speeds in the helium plasmas created by collisional absorption using the several-nanosecond pulse duration Z-beamlet laser. Novel time-resolving diagnostics imaged ion acoustic waves in 2D. From the transport trajectories, we inferred temperatures and energy density distributions as well as total energy deposited beyond a certain of axial depth. This allowed us to infer a temperature and a relative energy per unit length.

Generally speaking the energy distributions suggest that the plasma's axial energy density is strongly biased towards the first few millimeters of length except on the later shots in the series, with an applied magnetic field, which we will discuss in the next chapter. Without a magnetic field, the energy per unit length decreases approximately linearly as a function of axial length of the plasma. This is not at all what is expected from solutions of collisional absorption equations. These unfavorably steep profiles would be detrimental to MagLIF yields because a more uniform distribution is more

ideal. However, without a magnetic field, the energy density profiles are not particularly relevant to MagLIF, since MagLIF requires a seed magnetic field of at least 10 T. The energy density profiles without a magnetic field may only be useful to compare the total delivered energy beyond a certain benchmark axial length, thus enabling comparisons between laser parameters.

One explanation for rapidly declining energy density with length is that radiative losses dissipate energy away from the heating beam rapidly, leaving most energy dissipated before the laser heating via collisional absorption can penetrate very far into the plasma. Another possible explanation is that strong radial thermal transport is heating the surroundings of the heating beam at a relatively constant function of time, which would be consistent with a driven electron thermal wave. This thermal wave heats a widening cone around the plasma, and cools the regions that the laser passes through. Once this region is cooled, the collisional absorption efficiency increases and more energy is delivered for radial transport. Heated regions close to the LEW have more time for radial thermal transport and should produce wider temperature distributions. Filamentation or thermal self-focusing can also lead to a narrowing of the heating beam, which would cause a steeply declining heated volume.

We will summarize the results of varying laser parameters next, as presented in figure 7.17. Although practical issues prevented comparison of energy densities between z=0 and z=4 mm, we can use the range of shots we have to compare deposited energy beyond 4 mm. Further work needs to be done, with more shots, to compare the general trends of energy absorption

fractions, as well as quantify energy losses and absolute energy present in the plasma. However, with the shots we have, we can compare general trends from absorption fractions and energy penetration. Figure 7.17 gives the coupled fraction of the total laser energy inferred from sound speed measurements beyond 4 mm, and also shows the length of the plasma over which the energy per unit length is higher than 1 kJ/cm.

The energy densities and absorption fractions indicate that laser parameters used on a number of MagLIF shots early in the history of MagLIF may have only delivered a few hundred Joules beyond a few millimeters of axial length. This is consistent with the possibility suggested by Sefkow et. al that early MagLIF experiments may have coupled only a few hundred joules into the gas [3]. The laser parameters with low energies that we observed include delivered laser energies of about 1500 J at the target, heating pulse durations of about 2 to 3 ns, intensities of about $2*10^{14}\ W/cm^2$, a 2 μm thick LEW, and a 2 ns early pre-pulse. Beam conditioning with a DPP and without a DPP had little effect, possibly because we were bringing the beam to the LEW in the far field anyway.

Increasing the spot size and correspondingly decreasing the laser intensity produced a minor improvement in energy depth and overall energy but did not greatly improve profile steepness in this regime. These heating laser intensity reductions by themselves were not sufficient to see an improvement, but were likely necessary for improvements later. That is because when an early prepulse was applied at these higher heating beam intensities, it did not

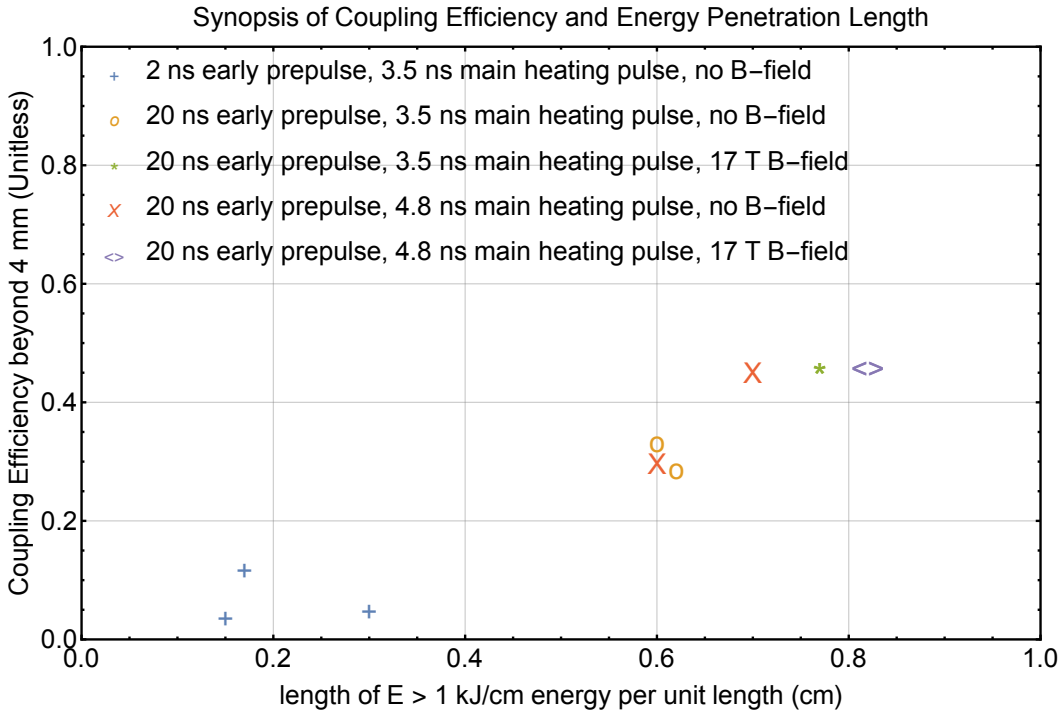

Figure 7.17: The energy per unit length distributions that we obtained from shadowgraph measurements can be interpreted with several metrics and compared. Here, we compare the total fraction of laser energy coupled beyond 4 mm of axial depth. We also compare the length of the plasma that has a reasonably high energy density on the x-axis. Ideally, the entire 1 cm length of the plasma would have an energy per unit length of well over 1 kJ/cm. The absorption fraction would likely be substantially higher on some shots if the energy coupled to the first 4 mm were also accounted for in this figure. Two shots with a magnetic field are also shown here; those shots have the best performance for energy coupling to a greater axial length. All of these experiments had roughly the same laser power of about 1/3 TW, and a beam spot width of about 900 microns, for an intensity of about $5 * 10^{13}$ W/cm^2. One of the two red X's does not match the trend; this shot had neon dopant so it would radiatively cool, but it had only a 2 ns shadowgraphy probe interval versus 4 ns.

produce an improvement in delivered energy.

The largest improvement in energy deposition and overall plasma length came from co-injecting a separate laser prepulse 20 ns early, which should remove the LEW material earlier. A early prepulse increased the absorption fraction for energy delivered beyond 4 mm by a factor of three when the pulse length was 3.5 ns. The dramatic jump in absorption fraction was often accompanied by the disappearance of a region of anomalous opacity near the LEW. Circumstantial evidence connects these features with poor absorption efficiency. We have also observed this feature about 2 ns after heating begins during a 4.8 ns heating pulse. It may be caused by radiation or long mean free path electrons originating from the LEW blowoff plasma.

We also saw significant improvements in overall energy and depth of the energy profile from the combination of a longer pre-pulse delay and a longer heating pulse with correspondingly more energy. The longer pulse by itself produced a factor of about 50% increase in the absorption fraction beyond 4 mm in the plasma's axial depth. With both an longer prepulse delay and a longer pulse, we saw an improvement of perhaps a factor of four to six in the overall absorption over a shot with a short pulse and 2 ns early prepulse. Besides simply making the heating pulse longer, other recent work has shown that a pedestal or foot prepulse of about 1 ns in duration added prior to the main heating pulse is highly beneficial to energy deposition [21]. Dramatic coupling efficiency improvements in were seen at 3ω for pulse durations from 2 to 10 ns in Harvey-Thompson et. al's work when heating with pulses longer

than 3 ns [16].

In general, the coupling efficiency is a strongly non-linear function of pulse duration beyond a threshold energy of about 1 kJ and/or a threshold main pulse duration of about 2.5 ns. This threshold behavior is supported by shadowgrams midway through a 5 ns heating pulse demonstrating only minimal penetration into the cold gas axially during the first 2.5 ns of heating. This threshold may be the cost of losses to interaction with the LEW material. Once this threshold is overcome, coupling to the target gas becomes much more efficient. The threshold loss in the LEW region may be greatly reduced with an earlier prepulse.

Chapter 8

Magnetic Field Effects

We observed a number of effects which point toward an applied magnetic field causing more energy to be delivered beyond three millimeters of axial depth. Transverse x-ray emission images also show that the plasma is narrower with an applied magnetic field.

Previous literature strongly suggests that the magnetic field will narrow the laser-heated plasma's temperature distribution as a result of reduced cross-field radial thermal conductivity [37] [38] [1]. Temperature increases and conductivity reduction from laser heating in a magnetic field were seen by Montgomery et. al. [37] and Froula el. al. [38]. Transverse Thompson scattering measurements by Froula et. al .showed a temperature profile that followed with what they claimed was a Braginskii transport model, in which the magnetic field suppresses radial thermal conduction by what they claim is factor of 15. Simulations by Slutz et al. show that the MagLIF seed field should inhibit radial thermal conduction which maintains a relatively high central temperature in the MagLIF preheat column after laser heating and prior to implosion [1]. We include some rough explanations for magnetic field thermal conduction, including a constant coefficient of thermal diffusion ap-

proximation in chapter four of this dissertation. Our theoretical work makes the approximate guess that, in the presence of a magnetic field, a thermal wave might take the form of a narrow Gaussian radial distribution, although the low-temperature boundaries of such a distribution are nonphysical.

The results also suggested that the laser-heated column becomes significantly narrower with an applied magnetic field. There may be two reasons for this. The simplest is that the applied axial magnetic field reduces electron thermal conduction in the radial direction. This would nominally prevent a thermal wave from spreading out the laser-heated regions, and would likely lead to a more narrowly peaked temperature distribution. In chapter four we saw that a pseudo-Gaussian temperature distribution might be approximately applicable when a magnetic field suppresses thermal conduction at higher temperatures.

There is a more subtle possible explanation for why the temperature distribution might be more narrow with an applied magnetic field: the field enhances laser self-focusing. Likely both effects are occurring and re-enforcing each other. The radial inhibition of electron thermal conduction maintains a hotter and narrower region within the laser heating beam. This increases the local electron pressure and consequently increases the sound speed transport of ion mass, which is uninhibited at these field levels. The sound speed would also be 30% higher in deuterium because of the smaller deuteron mass. As the electron and ion density drops, the refractive index also drops, which creates a plasma waveguide. This is thermal self-focusing. It may be occurring for

small-scale filaments , or it may be take place over the entire width of the beam at the LEW region when the laser first interacts with a plasma. Gradients in electron pressure can lead to self-focusing. But, in the presence of a magnetic field, these gradients become even steeper.

There is evidence for self-focusing with an applied magnetic field on the two shots with a 1 mm DPP. The evidence includes possible filament features visible in transverse shadowgraphs, as exemplified in figure 8.1. Evidence also includes a visible tapering of x-ray emitting regions with axial length, although this effect is subtle and explicable with other effects. Tapering in the absence of a magnetic field may be a result of radial thermal transport to regions surrounding the laser beam, bringing them up to the x-ray emitting temperature. Regions closer to the LEW have more time to propagate heat radially. So, with a magnetic field, thermal conduction suppression alone may be enough to account for the narrower beam profile. However, some degree of self-focusing must be occurring because the highest-temperature regions that emit x-rays beyond about 4 mm axial length are about 40% narrower than the heating beam at the LEW. X-ray evidence points toward intense heating, with > 1.5 keV temperatures in a region narrower than the laser would be in vacuum at this focal distance.

A narrower plasma with the same overall energy density will be longer axially. We saw a general increase in the overall length of the plasma on the shots with a shorter pulse duration, which fits with the heated regions being narrower with an applied field. The energy density seemed to be higher beyond

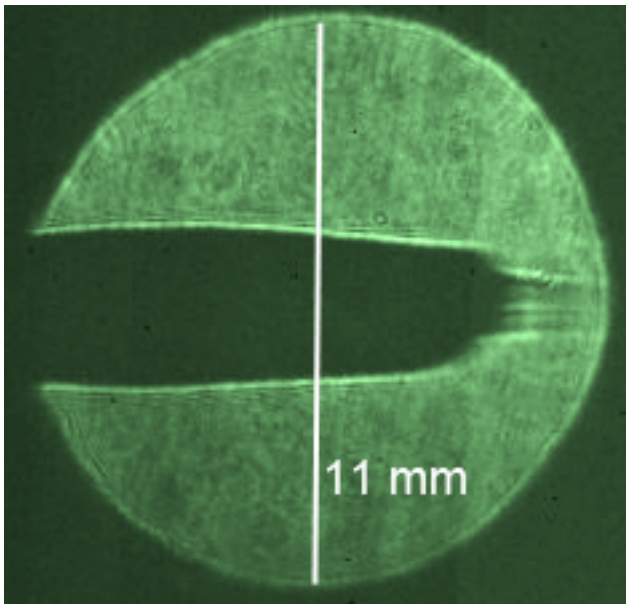

Figure 8.1: This shadowgram from 2.5 ns into a 3.5 ns heating pulse on shot B18070904 shows a filament emerging from the axial end of the plasma, which is the part that is being most actively heated. The central filament structure has never been present on corresponding shadowgram images without a B-field.

4 mm with a magnetic field, with increases ranging from a factor of 50% to a factor of 2 depending the pulse duration. Longer pulses showed a stronger effect of the magnetic field for energy penetration, up to a factor of two for a 5 ns heating pulse.

The information here about radial and axial energy density profiles may be valuable to MagLIF modelers, and inform the program about better ways to improve the total deposited energy in the plasma. In principle, an applied B-field might be detrimental to the sum energy content in a 1 cm long plasma if it contributes to self-focusing too much and narrows the heated region beyond what is ideal. Recall from figure 1.4 in chapter one that the optimum MagLIF

yield is achieved with a specific correspondence between preheat temperature and heated width. At 1.5 keV temperatures the optimum heated width is more than 2 mm. Once temperatures approach the range of about 1 keV, the collisional absorption coupling efficiency is comparatively much lower and heating will proceed only at greater axial length. For this reason it becomes difficult to add more energy to the plasma in the 1 cm available without increasing the heating width.

8.1 Energy Density and Temperature Distributions from Sound Speed

We used a sound-speed interpretation to infer the temperature and energy per unit length of experiments with and without a magnetic field. These provide insight into the overall axial distribution of energy, and demonstrate that these distributions become more axially uniform with an applied magnetic field. This is especially the case with a longer pulse duration and more delivered energy.

We may be confident that hydrodynamic transport is not altered by the magnetic field, since at these field levels β is of order 100 or more. The mass transport driven by electron pressure will become a magnetosonic wave, but this wave's speed will be identical to an ion acoustic wave. So, we may be fairly confident that our sound speed interpretation methods in chapter five are still valid.

8.1.1 First Comparison with and without Applied Magnetic Fields

We applied a magnetic field in the range of 15-17 T to a range of experiments which produced reasonably high energy density initially, but still demonstrated an axially downward-ramping energy density. The experiment consists of three shots, two with an applied magnetic field and another as a control without a magnetic field. A similar shot, B18061901 had a different DPP and focal configuration and no magnetic field, and demonstrated similar energy density and temperature beyond 4 mm to B18070501 with the 1 mm DPP, despite changes in the anomalous opacity. The total shot comparison set consists of four shots.

The shot parameters were as follows for these experiments. Except for one shot, we used a DPP with a nominally 1 mm beam waist, which we applied in a setup such that the near field was directly on the LEW. This had the benefit of ensuring that the prepulse laser spot is the same width as the main heating pulse at the LEW, but may contribute to self-focusing. They also used a 3.5 ns main heating pulse. Shadowgram probe beam pulse intervals were 4 ns, and the 60 psi helium fills were doped with 5 Torr of neon to enhance low-temperature emissions.

Shadowgrams show the plasma with a magnetic field to be consistently longer. The addition of a magnetic field adds a filamentation feature to the center of the axial end of the plasma at 2.5 ns into laser heating, and seems to remove the region of anomalous opacity. This suggests that the plasma is depositing less energy in the region of the LEW and perhaps heating further

into the gas. The filament feature suggests some self-focusing may be taking place.

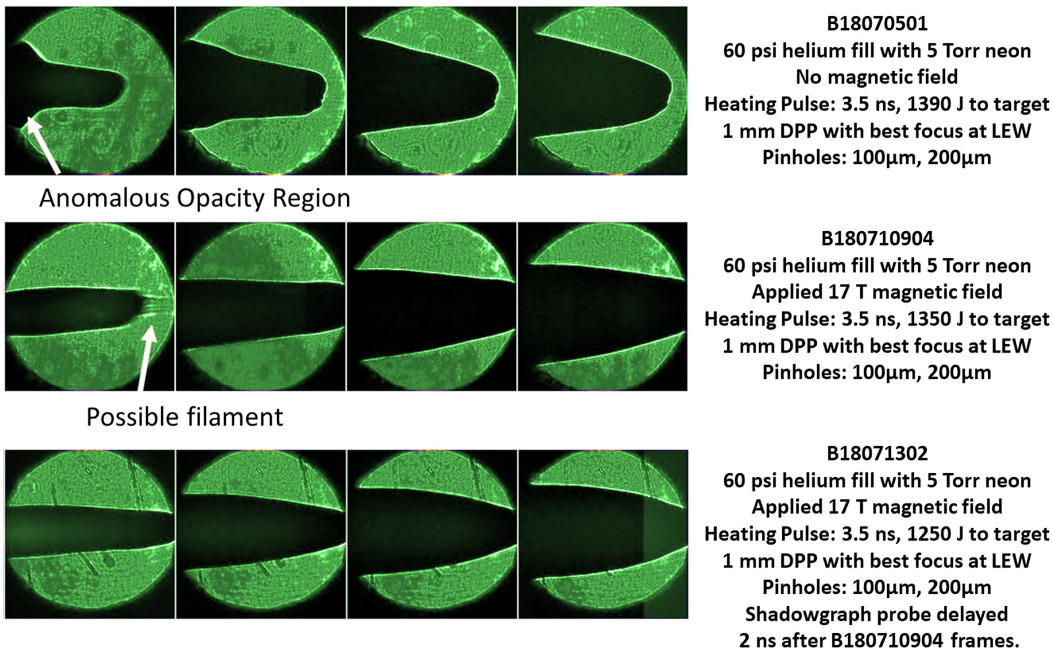

Figure 8.2: These are transverse shadowgrams from three shots, from which sound speed, temperature, and energy density are inferred. We compared two of these sequences with and without magnetic fields in the following sections. We see evidence for a narrow filament from the shadowgram image taken 2.5 ns into the main heating pulse on one of the shot with a magnetic field, which is not present in the non-magnetized shot. The region of anomalous opacity surrounding the LEW is not present with a magnetic field, possibly as a result of reduced radial conductivity causing less LEW material to radiate. Image background subtraction and arrangement by John Porter [39].

The total energy beyond 4 mm on the two shots without a magnetic field was 450 J and 400 J, as measured by the standard methods using the sound speed temperature and average shadowgram radius. With a magnetic

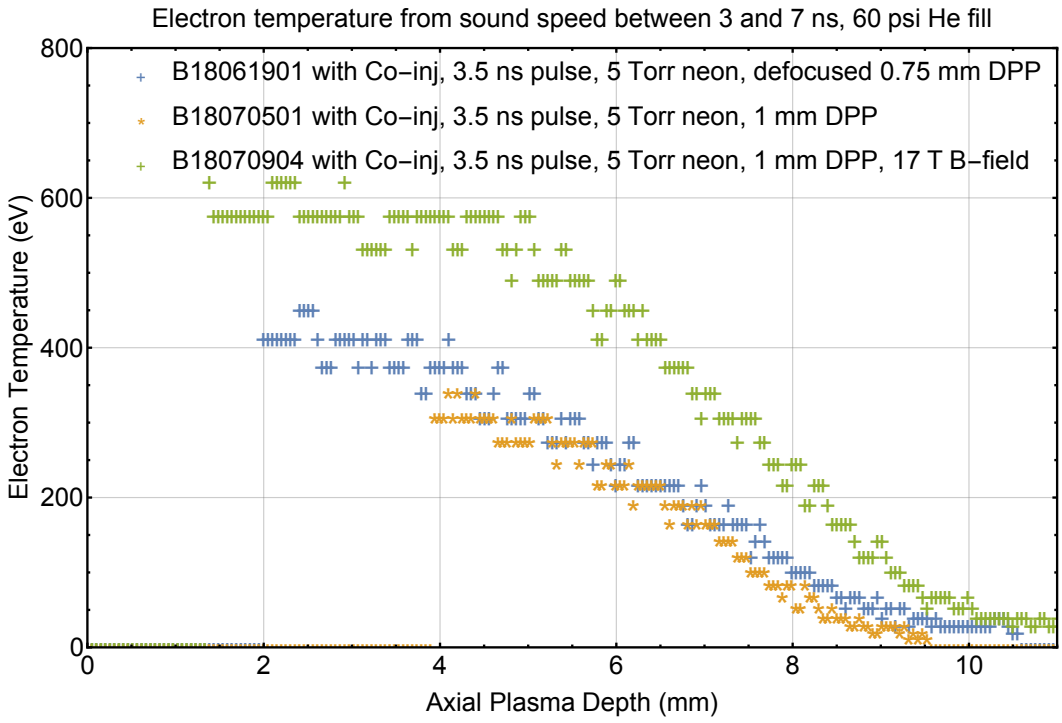

Figure 8.3: Here we compare two shots without a magnetic field to one with a magnetic field. The temperature beyond 4 mm is noticeably higher, and the overall axial penetration of the energy density is higher also. The shadowgram sequence from B18070501 and B18070904 are shown in figure 8.2. All datasets compared here have 4 ns time separation between shadowgram images; having the same time gap and relative timing for comparison is important when neon is cooling the plasma and dropping the sound speed. We could not compare B18071304 here because that shadowgram sequence was at a different time relative to Z-beamlet heating.

field, the total energy beyond 4 mm inferred from this method was 630 J on the shot that provides a meaningful comparison. This is a factor about a 50% increase to the energy delivered beyond 4 mm, although the total energy delivered to the gas may be similar once the region from 0 to 4 mm of axial length is accounted for.

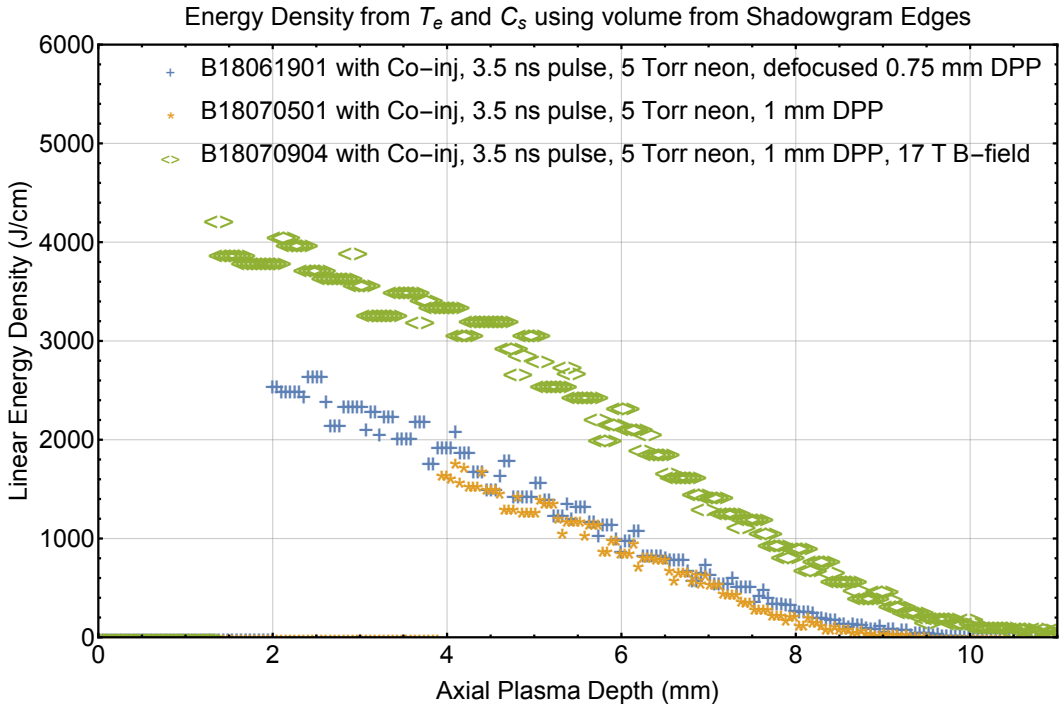

Figure 8.4: These energy densities generally show that the addition of a magnetic field increases the total energy beyond 4 mm, but does not completely eliminate the downward-ramping energy densities which may be indicative of self-focusing. The magnetic field did not make the energy density more uniform in this case.

Analysis of the sound speed from the shadowgram edges indicates these shots exhibited self-focusing behavior similar to that seen in the majority of shots explored in chapter seven. Their energy density profiles shown in figure 8.4 are all descending functions of axial length beyond 4 mm. Additional evidence that the heated regions of the plasma are getting narrower with axial length is apparent in figure 8.5, which shows the transverse x-ray heating sequence from three of these four shots. X-ray emission in the plasma should

correlate with both heated temperature and density, but while the laser is on we expect density changes to be relatively low. This is because the sound speed multiplied by the laser heating time is only a few hundred microns, which is smaller than the plasma width. So during laser heating the x-rays should correspond with the hotter regions of the plasma.

In order to understand these images, it is important describe two effects associated with x-ray emission in the plasma. Neon k-shell emission monotonically increases almost linearly with electron temperature from about 100 eV to about 350 eV. Afterward, the radiated power as a function temperature plateaus and increases slowly from continuum emission from helium. This means that the hottest regions of the plasma up to perhaps 1 keV will not be much brighter than the regions in the range of 400 eV. For more details, see Appendix A.

Qualitatively, the changes in the transverse x-ray emitting profiles are apparent in these shots from the brightest regions of x-ray emission. Compare the first 1-2 ns of laser heating, corresponding to hemisphere B of F0 (frame zero). Without a B-field, the emitting regions begin somewhat narrower than in shots without magnetic field. The heated regions are narrower and longer with a magnetic field. We interpret the 2 mm wide plasma close to the LEW in the absence of a magnetic field as evidence for strong radial thermal transport there, which allows more energy to be deposited by the laser because it cools the regions within the beam width. In the absence of a magnetic field, in frame F1 a 6 mm long tapering cone of relatively uniform x-ray intensity becomes

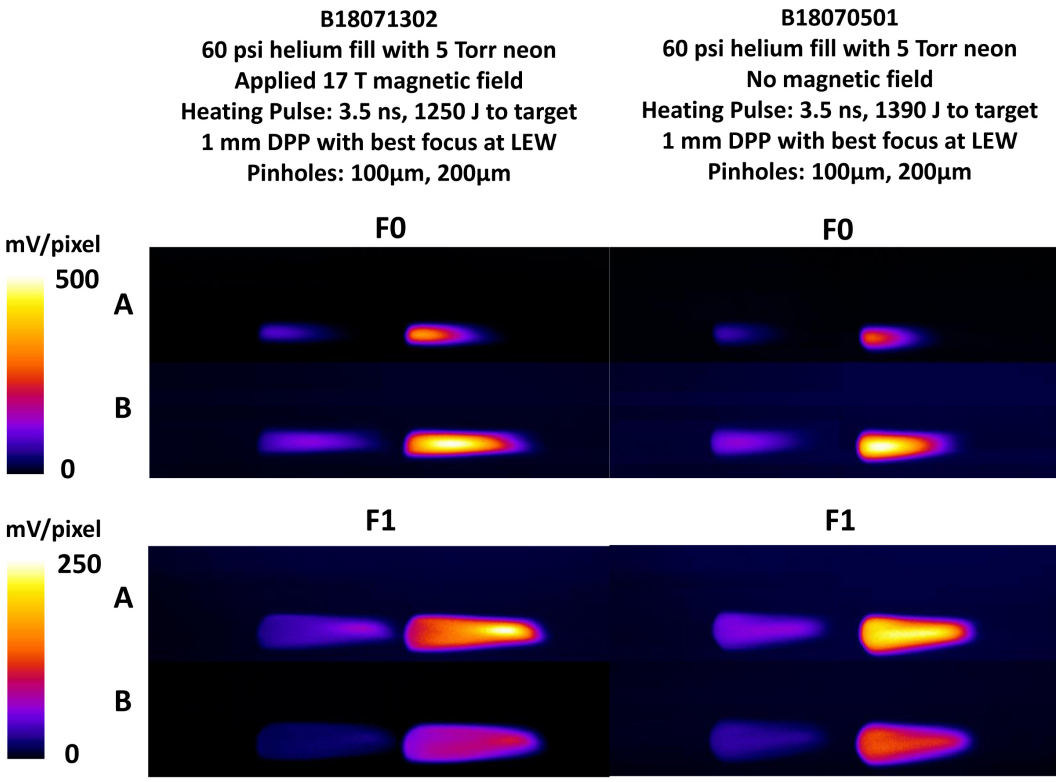

Figure 8.5: Here, we compare two sequences of transverse x-ray self-emission. The two hemispheres A and B in these images are separated by 1 ns in timing. They capture the plasma self-emission during the end of the laser heating, prior to a time at which density may strongly effect x-ray emission. In the shot with a magnetic field, the plasma narrowing in the axial direction is clearly visible compared to the sequence without a magnetic field. Without a magnetic field the plasma is almost 1 mm wider near the LEH. With a magnetic field the temperature-dependent emission is highest beyond about 5 mm into the plasma in the region where the heated column is narrowest. Image background subtraction and arrangement by John Porter [39].

prominent as the 3.5 ns laser heating concludes. Temperature variations may be obscured within this plasma cone as a result of the temperature dependence

of neon emission. In contrast, the brightest emitting regions are in the narrow region toward the end of the axial length between 4-6 mm on shots with a magnetic field, compared to the relatively uniform cone of heating without a field. This suggests that the highest temperatures are present there. The x-ray emission may have dropped close to the LEW in the presence of a magnetic field because sound speed transport has reduced the density there. All of these effects as a result of the magnetic field's radial thermal conduction suppression would reduce the energy deposited close to the LEW.

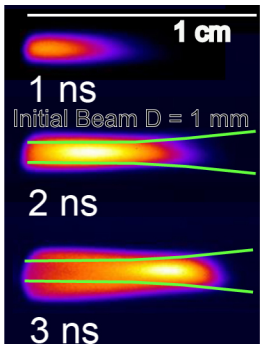

Figure 8.6: We compare transverse X-ray Pinhole sequence images from shot B18071302 during laser heating from 1 to 3 ns to the width of the Beamlet heating beam in vacuum, to scale. The beam is initially 1 mm at the LEW, and will begin enlarging at a depth of about 4 mm in the absence of other effects. Instead, at 2 ns the plasma is relatively uniform out to 6 mm. A hot spot appears in the plasma after 3 ns, just in the location that the beam intensity should be dropping.

The width of the heated region toward at greatest axial length is quite narrow in the last several millimeters with an applied field, as shown in figure 8.5. The fact that the emission region is not wider than the beam is good evidence for electron thermal conduction suppression. The conditioned beam

from the DPP should be uniform in radial profile out to a 0.9 mm diameter, although unfortunately as it diverges hot-spot features appear in the far-field. This may account for the slightly off-axis hot region. The narrower width of the plasma compared to the nominal beam width provides strong evidence for a self-focusing or guiding of the beam, since the beam should diverge in the absence of any other effects.

8.1.2 Comparison with a Longer Pulse Duration and Defocused DPP

Earlier in the history of magnetic field comparisons, we compared shots with and without a magnetic field in which the pulse duration was close to 5 ns. The longer pulse duration intuitively should give the laser more time to overcome energy losses in the LEW region. These experiments used a beam conditioned by a 0.75 mm DPP defocused to about 0.9 mm in width. There was a dramatic difference between these shot with and without a magnetic field, including the longest overall high-temperature-range axial penetration observed so far.

The temperature comparison indicates a 20% higher temperature with a magnetic field in the range of 5-8 mm axially. Other evidence from shadowgrams tells us that the plasma was at least as hot as we infer from sound speeds and probably hotter; neon radiative cooling likely reduces the sound speed before it can be measured, so this temperature is a lower bound. The other lower bound on temperature comes from the shadowgram transparency,

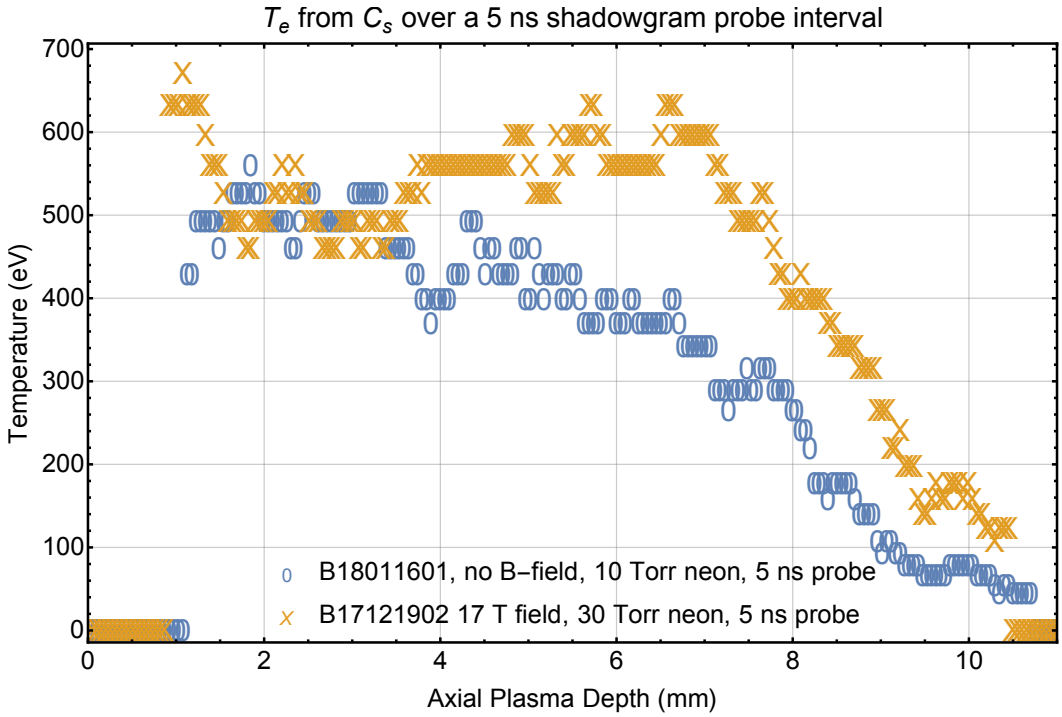

Figure 8.7: These two experiments kept most parameters the same except for the inclusion of a magnetic field in one shot of about 17 T. The shot with magnetic field also had three times more neon dopant, which is important because it causes the sound speed to drop faster. This could give a lower temperature result, yet in this figure the temperatures are comparable, which suggests the temperature is higher past four millimeters with the magnetic field. Both shots used a longer, 4.8 ns pulse at about 1/3 TW power with a total of 1840 J and 1640 J delivered to B17121902 and B18011601, respectively.

which is around 600 eV.

Figures 8.7 and 8.8 demonstrate that a magnetic field has the effect of producing a more uniform temperature and energy density distribution in this configuration. The temperature and energy density are more uniform than the previous comparison with a shorter pulse duration. With the magnetic field,

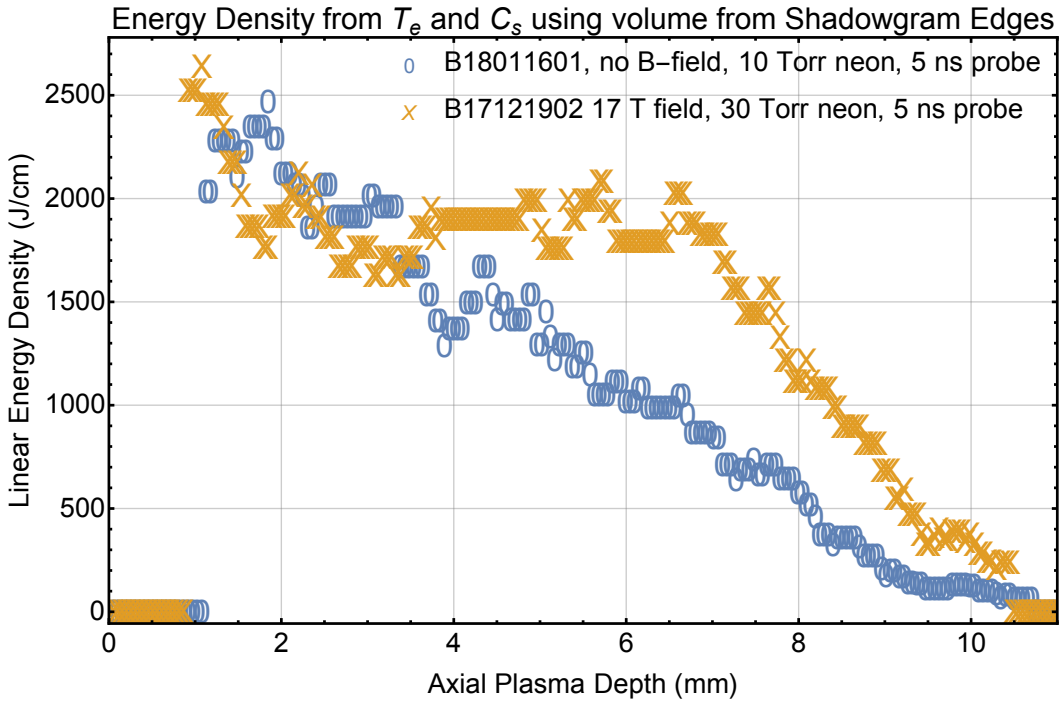

Figure 8.8: The same shots in figure 8.7 are compared using the average radius between shadowgrams to calculate a volume for an energy density. Qualitatively, the shot with the magnetic field had a more uniform energy density and a generally higher energy beyond 4 mm axial length.

we see the energy density and temperature remain uniform to about 8 mm axial length. The total energy from this analysis beyond 4 mm on the B-field shot B17121902 was 860 J, compared to 490 J from B18011601. Using the initially deposited laser energy for each shot, there is a factor of two increase in energy delivered beyond 4 mm with a magnetic field. The more generally uniform temperature and energy density suggests that thermal suppression was limited and the heated plasma remained uniform in cross section. Thermal self-focusing or a plasma waveguide effect must have been occurring still, since

the heating beam was not diverging as it would in vacuum and the heated region is quite narrow, but it must have taken place within the first 4 mm of axial length.

8.2 Constraints on Magnetized Plasma Temperature from Probe Beam Opacity

We can place a lower bound on the temperature in the plasma using the mean free path of shadowgraphy probe beam in the plasma. Collisional absorption mean free paths increase slowly with plasma temperature, like $T^{3/2}$, and strongly with density. At 60 psi helium fill pressure, nearly all shots have been completely opaque to the probe beam, except for B17121902 with an applied B-field, a defocused 750 micron DPP, a co-injected 20 ns early prepulse, and a 4.8 ns main heating pulse. It is possible that electromagnetic noise on this shot accounts for the grayscale pixel counts being higher within the plasma's diameter, but the internal structure would suggest otherwise.

If some of the probe beam light passes through the plasma, this suggests that the collisional absorption mean free path is longer than the plasma width. Based on the fill density, this only occurs for temperatures > 600 eV with a MFP of 3 mm. We do not see partial probe beam transmission on other shots except those carried out at 1/3rd of this density. Since a significant fraction of the plasma is probably lower in temperature while only the core is hot, the temperature is likely significantly higher than this. The transparent shadowgrams in B17121902 are on the order of 1.5 mm in radius. We expect

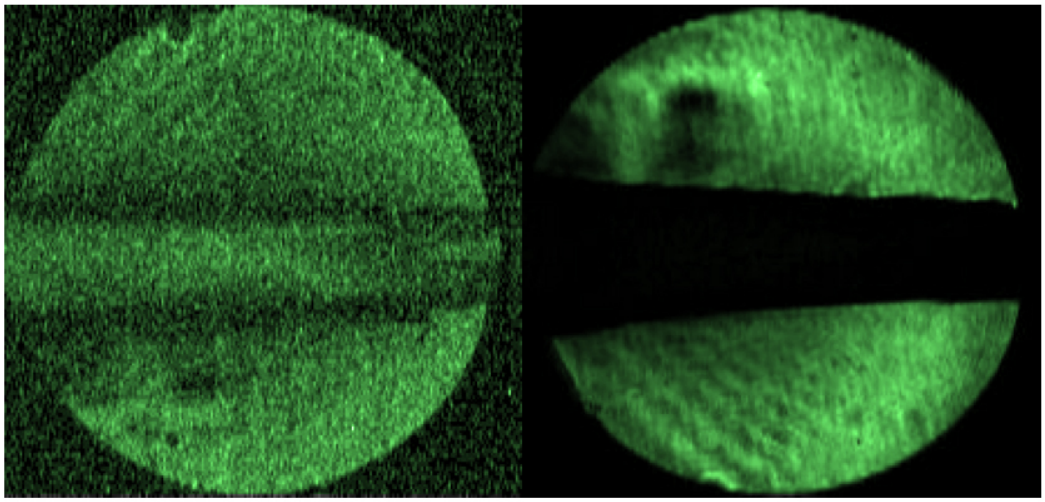

Figure 8.9: Shadowgram frames are compared with and without a magnetic field. These frames are within a few hundred picoseconds of the end of Z-Beamlet's heating pulse on the same shots reported in the energy density comparison in figure 8.7. Notice the qualitative differences in plasma opacity. The shot with a magnetic field produced some sensor noise from EMI, which creates visible reduction in image quality. The shot with the magnetic field is slightly narrower, but by less than 0.5 mm.

a hot plasma approximately half that wide. This is evidence that this plasma is hotter than other preheat plasmas we have produced, although there may be other reasons why probe beam light could pass through the plasma.

Based on the sound speed, we expect a temperature of about 600 eV on the same shot, B17121902, at 3.5 mm axial depth. The averaged temperature is most likely higher than this since neon is cooling the plasma while it is transporting at the sound speed, so we will measure a smaller speed later in time from what it is initially. The sound speed indicates a similar temperature

of about 700 eV on B18011602. On another comparison shot, B18020201 shown in the x-ray profile figure 8.10, we infer a temperature from sound speed of about 900 eV, although this shot had a shorter shadowgraph probe interval while it was radiatively cooling so this temperature cannot be compared.

We strongly suspect that the temperature is much higher than 600 eV because the hot plasma regions are surrounded by a low temperature radiative thermal wave region greater than 0.5 mm thick which strongly absorbs photons at the probe beam wavelength, so collisional absorption cross sections in the hot regions must be quite low.

8.3 Influence of Magnetic Field on Radius X-ray Emitting Regions

We have two comparisons between similar experiments with and without a magnetic field which can be compared using their transverse x-ray emission. In one set of shots the x-ray emission is visible throughout the length of the plasma. In the other experiment we can only compare at 3.5 mm axial depth.

8.3.1 Comparison Of X-ray Radial Profiles with and without Magnetic Fields

Initially, we were able to compare the x-ray radial profiles viewed transversely only at an axial length in the range of 3 to 4 mm. This region was visible through a narrow slit opening in the side of the gas cell. The compari-

son for the long-pulse shot B17121902 with a similar shot without a magnetic field is presented in figure 8.10.

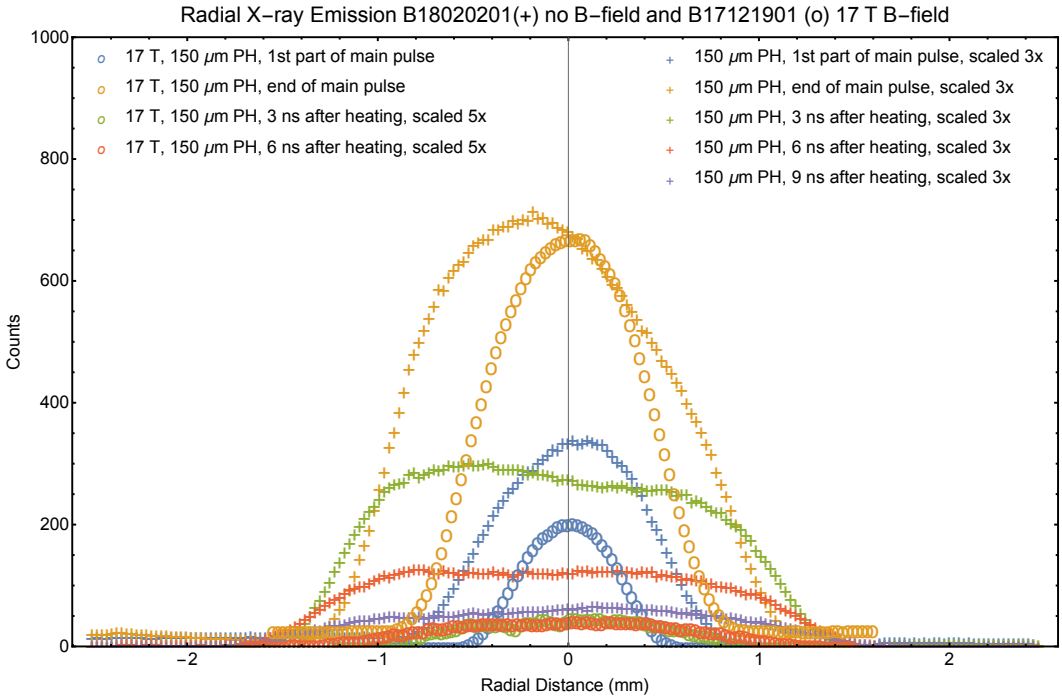

Figure 8.10: We compare two sequences of x-ray self-emission radial profiles captured by a transverse x-ray pinhole camera on two shots different shots. One shot used the magnetic field, while the other did not, but most other parameters are kept the same and the energy of the shots is within 100 J of the same overall energy. The axial position at which these measurements were taken is 3.5 mm into the plasma from the LEH window. Importantly, the neon dopant was 6 times higher density than B17121902 with a B-field, so we scaled the non-field shot x-ray emission by a factor of 3, and increases in detector sensitivity may also have played a role. These two x-ray profiles are not from the same shots as are compared in figures 8.6 and 8.7, since we chose to compare two shots with similar neon density of 30 Torr each.

Transverse line-outs in figure 8.9 indicate a 50% narrower plasma with a magnetic field at 3.5 mm axial depth, as measured by the half-maximum.

Surprisingly, the x-ray self-emission intensity from the narrower plasma with the B-field present is not much higher, which may indicate that it has entered a regime in which neon's k-shell emission is a roughly constant function of temperature. Regardless, the narrower plasma is strong evidence for radial electron thermal conduction suppression. It may also suggest changes to the dynamics of laser thermal self-focusing. The full-width half-maximum (FWHM) of the emitting region profiles at the sensor is about 900 microns, which is more or less identical to the width of the heating beam at the LEW.

8.4 Comparison of X-ray Radial Data with Gaussian Temperature Profile in a Magnetic Field

We were able to calculate the expected signal at the UXI sensor from a hypothetical radial temperature profile in the plasma. We modeled initial electron temperature distributions based on work from chapter four. We can test temperature distributions such as a thermal wave solution, a constant-temperature pedestal distribution, or a pseudo-Gaussian temperature profile.

Next, we modeled x-ray emission from the neon-helium mixture, including the effect of aluminum and polyimide filters. Doing so requires knowledge of the spectrum of emission from the mixture, which we obtained from PrismSPECT codes and is shown in Appendix A [40]. From there, we numerically summed an emission profile from a cylindrical geometry, effectively including a discrete Abel transform. Then we find the total radiated power delivered to a pinhole and spread over the sensor with 25 micron pixels. The analysis is

not complete; we did not develop a method for calculating spatial smoothing based on the optical transfer function of the pinhole camera. The spectral data gives delivered power per steradian, and with the pinhole size we can calculated total delivered power. Knowledge of the UXI sensor detection lets us calculate signal counts on the detecter at each pixel from the local total absorbed power over 2 ns frame time. All of these details are discussed in some detail in Appendix 1.

Our method for calculating a mock image on the sensor is limited to early time, before mass transport is very important. Mass transport alters the density of the emitters in the plasma. The emitted power is a strong function of the electron density. It also increases linearly with the neon dopant fraction, up to a point when the neon dopant would begin to significantly increase the overall electron density.

We used a Gaussian test temperature profile to compare to the data at the end of the main heating pulse from figure 8.9. The other options including a thermal wave function might fit better to the data without a magnetic field, although we ran out of time to test this. The radial image line-out from x-ray images on shot B17121902 appear to fit closely to a Gaussian profile already, so a Gaussian test temperature profile was a reasonable hypothesis. Recall from chapter four that a Gaussian profile is also a solution to the diffusion equation with a constant coefficient of thermal diffusion. This was the zeroth-order approximation to the diffusion behavior in a magnetic field, which increases up to a maximum around 100 eV electron temperature and changes slowly after-

ward. For the comparisons we will show here, we used a diffusion coefficient of 10 m^2/s, which corresponds to the approximate coefficient of diffusion beyond 100 eV in a magnetic field of approximately 10 T.

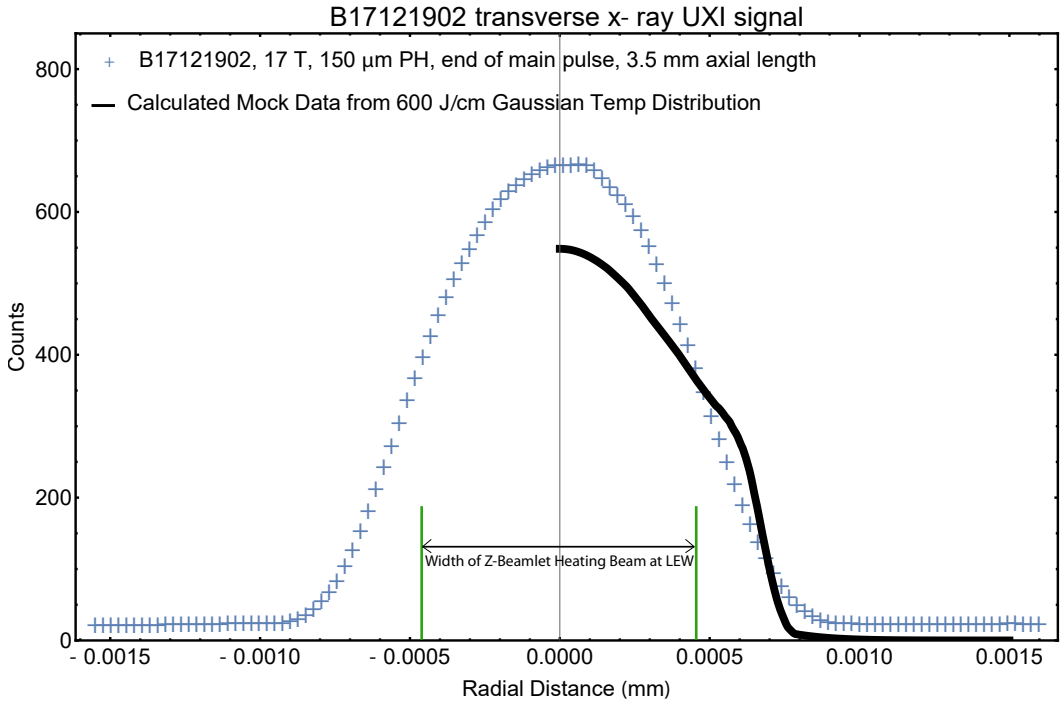

Figure 8.11: This figure includes the radial x-ray line-out data from the end of laser heating on shot B17121902, which is also depicted in figure 8.9. It also includes a continuous curve of mock-data, generated from the Gaussian test temperature profile in figure 8.12. The mock data needed to be scaled by a factor of 3.1 to match the actual data.

We used the same parameters for the shot to calculate the mock data. Parameters included 30 Torr of neon which is six times the baseline calculation, a 150 micron pinhole at a distance of 0.5 m from the target, an integration time of 2 ns, 6 microns of aluminum filter material, and 2 microns of polyimide filter material. We performed many iterations of the of the initial temperature

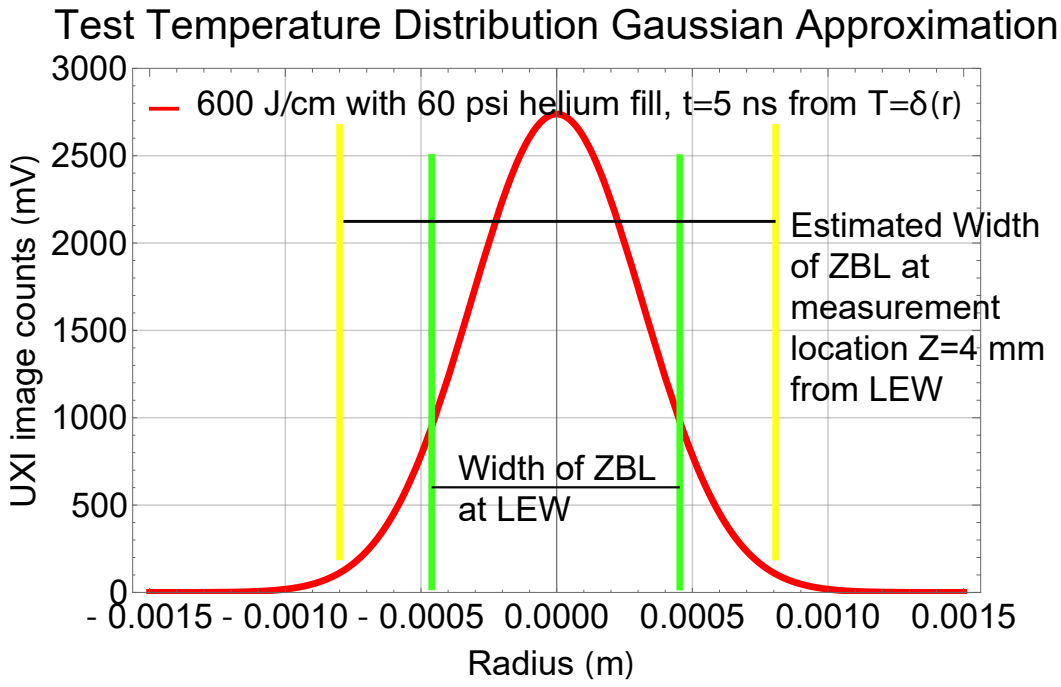

Figure 8.12: The test temperature distribution is a solution to the diffusion equation for a constant specific heat. It is a Gaussian distribution with an energy density chosen to match that which was inferred from shadowgram analysis of later-time sound speeds. This temperature distribution is strongly centrally peaked, and narrower than the heating beam at the LEW and much more narrow than the beam would be if it continued to defocus and enlarge in width as it would in vacuum. Comparison widths are shown in the figure, which are approximately 900 microns and 1400 microns.

profile to match the width and approximate height of the data. Overall energy per unit length as well as the width of the Gaussian temperature profile were varied to give a result that approximately matched the experimental data. Ultimately we settled on the temperature profile in figure 8.12. Unfortunately, the resulting mock data was lower intensity by a factor of three compared to the real data. The plotted mock data curve in figure 8.10 was scaled by a

factor of three.

Since we could model the initial energy per unit length in the test temperature distribution as we iterated to improve the match, we explored distributions with central temperatures in the range from 600 eV all the way to 3 keV. For the comparison above, we chose an energy per unit length of 600 J/cm, which was what we measured from the shadowgram energy density methods at this axial length of about 4 mm. Extremely high central peak temperatures over 2.5 keV are required to get an energy per unit length of 600 J/cm with a Gaussian temperature profile as narrow as the data. Recall that the shadowgram data most likely over-estimates the energy per unit length. However, even with an extremely high central temperature of over 2.5 keV, we were unable to get a central peak emission intensity as high as that from the data. The mock data was still a factor of three smaller and needed to be scaled.

Some of this factor of three discrepancy may be from the lack of spectral data at high temperatures. Calculations of expected detector signals did not include spectral data for plasmas above 1 keV, because we were not expecting temperatures that high. We also do not have spectral data for continuum emission beyond 3 keV in photon energy. However, as temperatures approach 1 keV this spectral range may be important, and it passes through the filters without much attenuation. These two inadequacies of our model mean that the emitted x-ray power as a function of electron temperature rises very slowly with temperature in the 1 keV range, and mathematica extrapolated emission

from there. So, it required very high temperatures in the test distribution in order to generate mock data close to what we observe. Another possible explanation for the factor of three discrepancy in x-ray data on this shot might be the presence of higher-Z contaminants in the plasma, such as from the LEW, which will also produce some x-ray radiation. With numerous uncertainties, we consider a factor of three to be reasonable for absolute estimates of x-ray signal strengths.

If we had time to complete the Bessel transfer function smoothing of the expected data, we expect that the calculated mock data would more closely resemble real data in spatial dependence, because it would be more smoothed. Features such as the sharp outer boundary in the mock data curve, and the inflection point in the curve at half-maximum would be smoothed out on the 100 micron scale. Correct account for pinhole smoothing would give a more accurate rendering of mock data that would be more smoothed and approximately Gaussian.

Overall, the data points to a very centrally peaked temperature distribution, with the highest temperatures in the range of at least 1.5 keV over a cylindrical region with a radius of about 200 microns. The central peak temperature is significantly narrower than the expected laser width at that axial depth, especially considering that this shot used a defocused DPP. The sound speed at 2 keV temperature is a surprisingly high 200 microns per nanosecond, which means that the density may be changing dramatically in this region while the laser is on. For deuterium this sound speed would be 300 microns

per nanosecond. A factor of four drop in density would lead to a factor of two change in refractive index, which is more than sufficient to act as a waveguide for the plasma and facilitate self-focusing.

8.5 Comparison of X-ray Radial Data with Electron Thermal Waves

We find that, in the absence of a magnetic field, a thermal wave temperature profile with a dominantly Spitzer-Harm electron thermal conductivity matches well with the x-ray profile data, as we will see shortly in figure 8.13. The absolute x-ray emission can be modeled with temperatures in the range from 100 to 400 eV. We explored comparisons between data and models on shot B17122002, which used 30 Torr of neon, a 20 ns early prepulse, and a higher delivered energy and power than most shots, totaling 2400 J to the target.

Figure 8.13 compares mock data to real data. The mock data was generated using temperature distributions in figure 8.14, which are thermal wave solutions to the diffusion equation with dominant Spitzer thermal conductivity given in chapter four. The temperature model is given by

$$T(r) = T_c \left(1 - \left(\frac{r}{R_f}\right)^2\right)^{2/5} \tag{8.1}$$

where the exponent is determined by the reciprocal of the temperature dependence in Spitzer electron thermal conductivity. The match is close but not perfect, partly because of the non-zero x-ray background. This x-ray profile

from a shot without B-field is the same as that shown in figure 8.9, and in that figure we see that the profile is actually not symmetric. The thermal wave model is not a good match on the left side of the distribution. Non-axially-symmetric heating must be occurring, perhaps due to off-axis filamentation. Regardless, electron thermal conductivity seems effective at smoothing the temperature profile over length scales greater than the laser width.

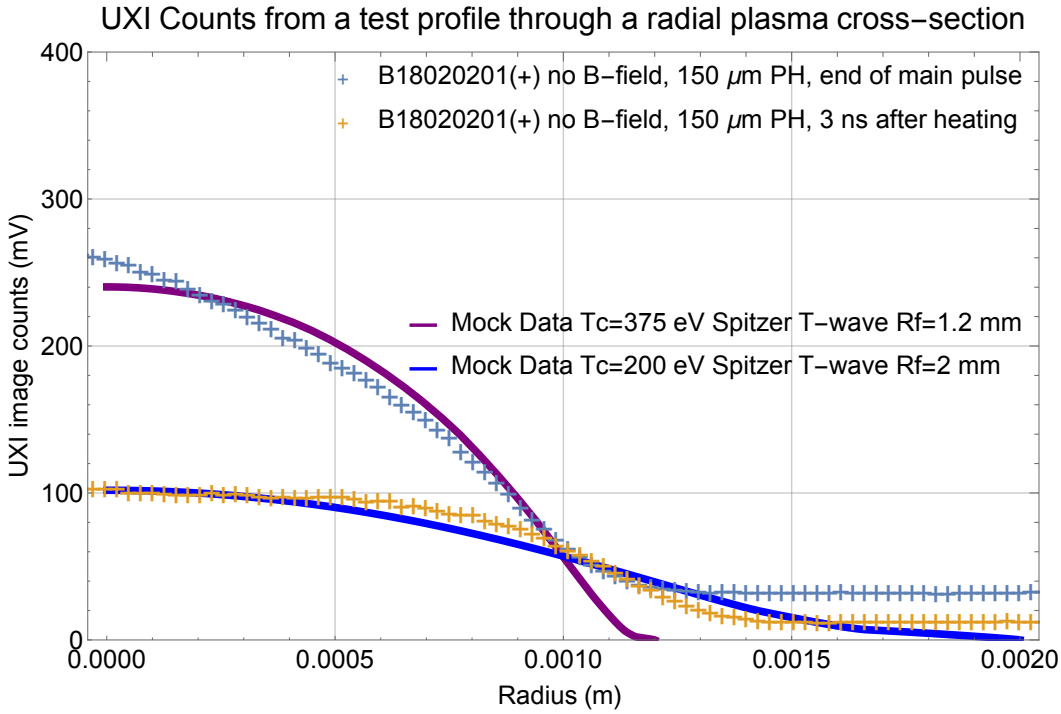

Figure 8.13: Here we show mock data compared to real data from a shot without a magnetic field. The central peak temperature and radius of the thermal wave model were iterated to produce mock data that matched the most closely with real data. In to generate the data for this case, the detector is sensitive to soft x-rays in the range of 1 kV to 1.5 kV, before the aluminum k-edge.

The energy density in each of the thermal wave models in figure 8.14

is given by equation 4.35, which we originally derived from the integral of the temperature distribution. For the earlier-time distribution the energy per unit length is 390 J/cm. For the later time distribution it is 575 J/cm. This discrepancy can be partially explained by the asymmetric distribution in the real data; earlier in time, more energy was on the left side of the distribution. However, the first temperature distribution might also be hotter and produce similar data, since beyond 400 eV the emitted power does not change much (see Appendix A).

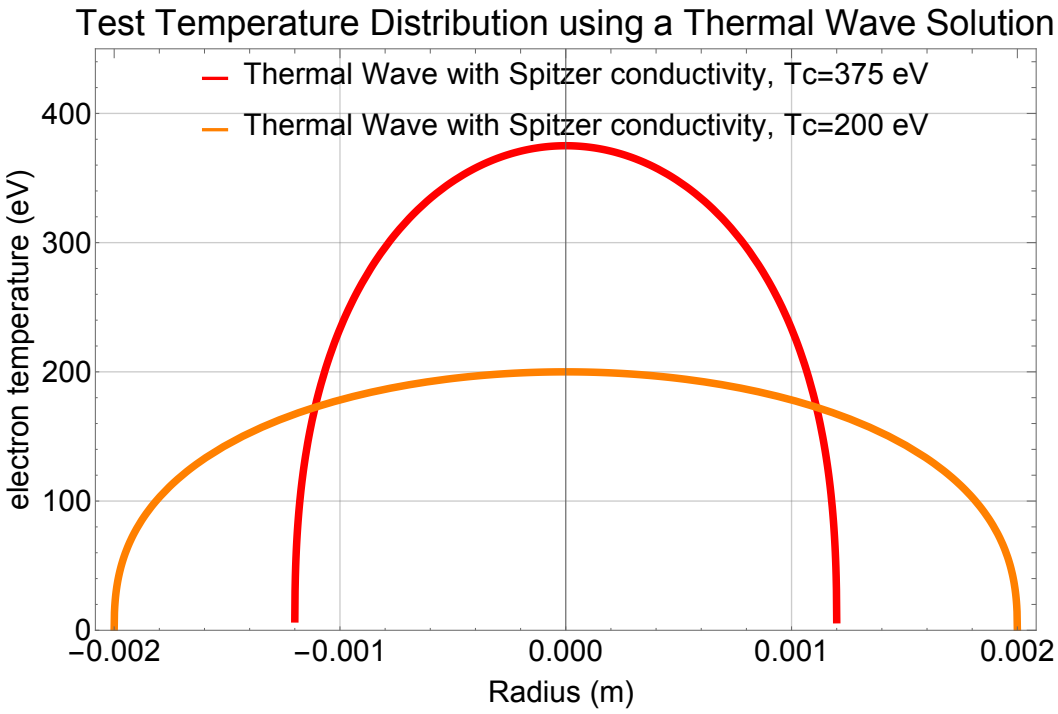

Figure 8.14: We see the temperature profiles which produced the mock data in figure 8.13. These profiles are thermal waves, modeled after equation 8.1, which are based on the derivation we did in chapter four.

We expect a thermal wave solution to be an accurate model for the

temperature while transport is not dominated by hydrodynamic motion. Since we have thermal wave models at two different times, we can find the expansion speed of the thermal wave front. The expansion of the thermal wave in this comparison is 0.8 mm in 3 ns, or 260 km/s. This is a rapid expansion rate that is higher than usual sounds speeds. Such a sound speed suggests an unrealistic driving temperature of 3 keV! So the thermal wave model is still valid here; it has yet to slow to within Mach two. This result suggests that within the first few nanoseconds of laser heating, the thermal wave will transport heat faster than hydrodynamic motion.

What this suggests is that the thermal wave is essentially inhibited with a magnetic field present.

8.6 Conclusions and Future Work

There is strong evidence that the magnetic field reduces radial electron thermal diffusion, such that hydrodynamic transport become the more dominant form of energy transport away from the heating beam. Without a magnetic field we see x-ray profiles that are well modeled by an electron thermal wave. The magnetic field suppresses that thermal wave, and in doing so reduces the heated width of plasma close to the LEW. In the absence of a magnetic field, energy density is strongly biased toward the LEW, since electron thermal conduction carries heat radially away from the beam's heated area and allows more energy to be deposited there. Suppression of an electron thermal wave transporting heat away from the beam width causes the beam

to deposit more energy beyond 4 mm compared to before 4 mm. It is unclear if the total amount of energy in the plasma is greater with a magnetic field, but it is clear that radial thermal conduction has been substantially reduced.

The reduction in the thermal wave transport lengthens the heated region, narrows the plasma, and increases the overall peak temperature. Evidence for a higher temperatures comes from shadowgram transparency and sound speed also. With a magnetic field, the energy density is increased beyond 4 mm by up to a factor of two.

For the purposes of understanding MagLIF preheat, the magnetic field makes a significant difference in the peak temperature and energy density distribution results. Studying total delivered energies without a magnetic field present might be useful to understand specific effects, such as laser-plasma interactions. However, we have demonstrated that any experiments without magnetic fields will give quite different energy density distribution results and will not an adequately simulate MagLIF preheating.

Heating beam self-focusing is likely occurring with the magnetic field present and possibly also without a magnetic field. This is clear from the narrow, high temperature regions imaged with x-ray pinhole cameras, which give temperature distributions that peak in a region narrower than the beam should be. We also see visual evidence for filamentation on shadowgram diagnostics, like in figure 8.1; filaments are created by thermal self-focusing. Self-focusing must be occurring very early, within the first 2 mm of axial length, because changes to the laser heating diameter are not apparent beyond that length.

To increase the amount of energy delivered to the plasma, it would help to increase the laser spot size further. If self-focusing to a certain critical size is happening, then perhaps the dynamics of heating can be changed, for example with an annular beam. We can also attempt to counter self-focusing by reducing the laser intensity and using a beam that is already diverging focused in front of the LEW, possibly with a shorter focal length. Finally, it is possible to reduce self-focusing by using spectral dispersion smoothing, although this technique would be technically challenging to implement on Z-beamlet.

Significant further analysis could be done, including particularly with the x-ray emission transverse PHC images. These images can be analyzed similarly to the shadowgram images, to extract radial information from the emission profiles at each axial depth. This would give information about the heated volume that is much more accurate and informative than the shadowgrams, since the shadowgrams relies on the outer edge of a radiative thermal precursor rather than the hottest part of the plasma. Estimates of plasma energy density could be much more tightly constrained by estimating plasma volume and temperature both with sound speed and absolute emission profiles. We could also infer the strength and dominance of thermal transport via diffusion and hydrodynamic motion.

Future experiments might explore the magnetic field in the plasma and further constrain the thermal transport coefficients. It might be possible to measure magnetic fields in the plasma or outside of it with faraday rotation

or pickup coils inside the gas cell. The Nernst effect and plasma diamagnetic effect are of great interest to the community and poorly measured experimentally.

Chapter 9

Summary and Implications for MagLIF

In this work we've explored the laser preheat process of MagLIF through surrogate experiments. The preheat process is a necessary step to deposit energy prior to compression and heating, and in chapter one we learned the ideal characteristics of a preheat plasma and what motivates those characteristics. The more energy the laser deposits in the gas, the better, up to about 6 kJ with existing implosion techniques. The preheat also benefits from certain energy distribution characteristics, specifically an axially uniform distribution. The radial distribution of temperature is also important, because it insulates heat loss from the liner walls and facilitates the flux compression and implosion dynamics.

We wanted to be able to diagnose the temperature, energy density, shape, size, and evolution of the preheat plasmas. This will better inform simulations of MagLIF, and allow us to explore setup parameters to optimize delivered energy and energy uniformity in an effort to improve MagLIF preheat. To our knowledge, we present the first indirect measurements of preheat temperatures in the target gas via sound speed methods. We were able to estimate the total energy beyond 4 mm of axial length, and concluded that

increasing the prepulse delay and adding heating pulse length increased total energy delivered beyond this length by up to an order of magnitude over initially low values. We were also able to characterize the effects of a magnetic field on the plasma, finding that it significantly narrowed the temperature distribution, raised temperatures, and caused the plasma to lengthen axially. The magnetic field has such a significant effect that conducting experiments in the absence of a magnetic field may be of less utility to understanding MagLIF preheat.

9.1 Experimental Platform

Chapter two outlines the experimental platform we developed to explore MagLIF preheat-related measurements. The platform included a newly outfitted target chamber on the Z-beamlet laser, with the capability to field gas cell targets. We fielded x-ray and visible light diagnostics. And we developed a magnetic field system, adapted from an LDRD to do cluster fusion in a magnetic field. Chapter three explains the main diagnostic we used in these experiments: transverse visible light shadowgraphy with multi-frame techniques. The images capture regions of the plasma that are ionized and opaque due to collisional absorption of the probe beam as well as refractive scattering outside of the collection optic. The shadowgraphy probe laser is absorbed by low temperature plasmas even down to the ionization thresholds, so they will be sensitive to areas that are ionized by lower-temperature radiative precursors outside of the range of the hottest parts of the plasma. However,

there is evidence that the precursors follow consistently ahead of the hotter regions in the plasma, so interpreting them for hydrodynamic motion is likely valid as long as the interior plasma remains hotter than the precursor.

We used helium for our experiments for safety reasons, but helium is more strongly radiative than deuterium and we expect a radiative thermal precursor to be more important. Also, the difference in ionization energy will create a larger discrepancy in energy required to create the plasma. Collisional absorption cross sections are somewhat higher in helium as a result of the higher Z, so this creates a shorter plasma under identical conditions otherwise. Finally, the sound speed will be 30 to 40% higher in deuterium, so hydrodynamic effects such as mass transport at the sound speed, as well as thermal self-focusing, will be more important in MagLIF than what we observe.

9.2 Plasma Transport

Understanding plasma energy transport is important for explaining our experiments. Chapters four, five, and six explained the transport physics of three different modes of energy transport. Namely, these are thermal diffusion and hydrodynamic motion at the sound speed and in blast waves. In chapter four, we described the important modes of energy transport via radiation and electron thermal conduction. We briefly mentioned that there are both diffusive, local modes and non-diffusive modes of thermal transport. Our plasmas have diffusive radiative transport only at lower electron temperatures and

photon energies, which supports a radiative precursor that extends out of the plasma's hottest regions. The plasma supports radially expanding cylindrical thermal waves as a solution to the diffusion equation, and in the absence of a magnetic field these thermal waves are likely expanding as a function of time in the manner of a driven thermal wave. With a magnetic field applied, the thermal diffusion is no longer a strong function of temperature beyond a certain threshold, and we approximate the temperature distribution as the solution to the diffusion equation with a constant coefficient of thermal diffusion. This solution is the Guassian heat kernel. We used the Guassian model to compare with x-ray radial line-outs later in chapter eight.

Hydrodynamic transport at the plasma sound speed is important initially, until the plasma doubles in radius and the fraction of energy in electron thermal pressure is roughly equal to radially outward ion kinetic energy. Sound speed transport is another important energy transport mechanism in the plasma, and is more important than thermal diffusion on timescales greater than about 2 ns. We measure a constant sound speed out to more than 20 ns via shadowgram diagnostics when radiative cooling is not important. The sound speed transport transitions to blast wave transport as the acoustic wave sweeps up more ion density and compresses it at the shock boundary by a factor of four. Data demonstrates that the blast wave in pure helium follows closely to a classical Sedov blast wave in a cylindrical geometry.

9.3 Temperature and Energy Density Measurement Methods

We used our understanding of plasma transport to diagnose the plasma temperature and energy density. If a blast wave is adiabatic, as ours proved to be with pure helium, we could use the blast wave to extract an initial energy per unit length. We did this on a few shots in late 2016. However, practical constraints led to a transition to measuring temperature and energy density using the plasma sound speed in the first 15 ns of evolution. This method measures the early time radial expansion speed and finds a temperature of the driving electron pressure. We can then use the average volume between frames combined with the pressure to extract an energy per unit length. We are able to measure distributions by comparing this energy density across the axial length of the plasma. This method likely gives only an upper bound on the overall energy in the plasma, since it assumes that the sound speed temperature is valid across the entire plasma volume represented by the shadowgram images. However, it can still be useful for relative comparison between shots to determine changes in the delivered energy with changes in experimental parameters. The blast wave and sound speed methods gave a similar energy density on a shot where we could compare the two, with the two energy densities differing by 20%. Both methods are only able to account for plasma thermal energy and kinetic energy, and do not factor in the energy lost to radiation and ionization. These losses can total hundreds of joules.

We also fielded x-ray self-emission imaging with time-gated detectors

and a pinhole camera. This enabled 2 ns time exposure 2D images of the hottest parts of the plasma. The x-ray emitting regions are consistently smaller than the shadowgram images by about 0.5 mm in radius. Appendix A describes an approach for predicting an x-ray signal based on an initial temperature and density distribution. We can compare test distributions with actual x-ray data to verify our understanding of the plasma's temperature distribution, as we did in chapter eight.

9.4 Summary of Major Results from Energy Density Analysis

Our early results for energy density in the gas were promising, but after we began exploring laser configuration space we found that there were a range of parameters, some of which have been used for MagLIF, that had relatively low preheat energy.

The plasmas created by these heating processes without a magnetic field typically display a steeply downward ramping energy density profile. This is either indicative of strong radial energy transport creating a tapering cone of heating, or laser thermal self-focusing, or both. Regardless, while these profiles are useful as a diagnostic of certain processes, the energy density profiles are quite different with a magnetic field present, so these profiles are not as useful for MagLIF.

We have seen evidence that the laser deposited merely several hundred Joules into the gas with a 2 ns early prepulse and a beam intensity greater

than $5 * 10^{14}$ W/cm^2 over 3 ns or less. This range of energies may explain why the stagnation columns of initial MagLIF experiments were surprisingly narrow; stagnation columns had too little thermal energy to create outward thermal pressure and larger plasmas.

As the prepulse delay was increased to 20 ns, we saw a factor of three increase in the total energy delivered beyond 4 mm. A beamlet power of 1/3 TW and beam spot size of about 900 microns were necessary to see these improvements. The upper range of improvement in energy penetration came from implementing longer pulses, approaching 5 ns in duration, combined with an early prepulse. A longer pulse seemed to couple most of the energy delivered in the last 1-2 ns of heating beyond 4 mm of axial length. Increasing the pulse duration by about 1 ns at the end of a 3.5 ns heating pulse increased the overall length of the plasma by 1-2 mm. The longer pulse was required to get the highest increase in deposited energy from a co-injected 20 ns early prepulse.

9.5 Effects of an Applied Axial Magnetic Field

In chapter eight we explored the effects of a magnetic field on the preheat plasma. We introduced a magnetic field in the range of 7 to 17 T to simulate the MagLIF seed field and explore plasma transport during and after laser heating.

The magnetic field lengthens the deposited energy in the plasma. For the the range of parameters we explored, this effect increases the heated

plasma's length by 2 mm or about 30 to 40%. We also see an increase in the total energy delivered beyond 4 mm by a factor of 1.5 to 2, some of which is explainable with the increase in length and corresponding decrease in energy deposited between z=0 and z=3 mm. The energy densities are also significantly more uniform with a magnetic field out to about 6 mm with a 3.5 ns pulse and 8 mm with a 4.8 ns pulse. Overall, with a long pulse of 4.8 ns, a 20 ns early prepulse, and a 17 T B-field, we saw a factor of six or more increase in energy delivered beyond 4 mm.

X-ray observations validate the increased plasma length and elucidate the cause: the heated region is narrower. Transverse PHC images indicate that the plasma is narrower and hotter when the external magnetic field is applied. At the end of laser heating, the region near the LEW does not emit significant x-rays out to 1.5 mm radius as it does without a field. The magnetic field reduces radial electron diffusive heat conduction, but it does not reduce transport of energy by hydrodynamic sound speed expansion, so we see a reduction in the central intensity of x-ray emission in the path of the beam close to the LEW as a result of density transport.

We used the radial PHC image line-outs of x-ray emission to make an estimate of the initial temperature distribution created by the heating laser. We found that the a temperature distribution with a very high central temperature, possibly exceeding 1.5 keV, matches the data. However, the x-ray data was higher by a factor of three from what our calculations would estimate. The spatial distribution of x-ray emission with a magnetic field suggests that some

degree of self-focusing must be occurring, because the hottest heated regions are significantly narrower than the conditioned beam on most shops. Some of this effect may be a result of far-field beam hot spot features, but thermal self-focusing due to sound speed transport is only expected to be more significant with a magnetic field applied. Overall, we find a narrow and highly centrally peaked temperature distribution similar to a Guassian matches best to the x-ray emission with a magnetic field, suggesting that radial thermal conduction has been reduced.

9.6 Evidence for Self-Focusing

We saw evidence for filamentation in the plasma via the shadowgram images, which show filaments extending from the axial limit of the plasma. Filamentation is a direct consequence of thermal self-focusing, caused by a dynamic equilibrium condition in which sound-speed transport modifies the plasma refractive index and guides the beam as it transports. We've also seen that, in the presence of a magnetic field, the hottest plasma regions are substantially narrower than the heating beam should be at that axial position, suggesting that either the wings of the beam had been attenuated preferentially or the beam has narrowed as it transported through the plasma.

Although not reported here, the steeply descending axial energy density profiles are best explained if the heated regions of the plasma are decreasing in radius linearly with axial depth. Initial 1D models of collisional absorption with heat transport match the data best when the heated radius is diminishing

linearly with axial length. Those results are from old work which had not been adapted to recent data, and cannot be relied on yet. They may point to a path for possible future work.

Self-focusing may be a limiting factor for delivering more than a certain energy into the gas using existing preheat technology, because it limits the volume of heated gas within the available 1 cm of the target. There some technically challenging ways to counter deleterious effects of thermal self-focusing and filamentation [41] [15]. Smoothing by spectral dispersion (SSD), has been shown to offer improvements by moving hot spot speckles of the DPP faster than the plasma waves speed [15]. Another closely related approach is induced spatial decoherence (ISI), which rapidly smooths the beam via somewhat different methods, but which simulations indicate is much more effective at reducing filamentation than DPP smoothing alone [41]. Simulations indicate that SSD Going to 3ω is also expected to benefit this issue, since the changes to refractive index as a result of density changes would be smaller at shorter wavelengths [15]. We can also imagine using an annular beam with a custom DPP design, such that a central region of unchanged compressed density is created which would guide the beam in an annulus rather than a diminishing filament. All of these approaches would require major technical re-designs of the laser systems.

9.6.1 Laser Preheat Improvement Recommendations

Based on the general trends we observed as presented in chapter seven, we can identify the characteristics of an ideal heating configuration given the current platforms and technological constraints. First, there is a threshold behavior in the delivered energy and pulse duration to overcome heating and radiation losses at the LEW. Low energy coupling efficiency and short axial penetration is correlated with a region of anomalous opacity centered on the LEW. This region is created by energy losses from the LEW and is undesirable, so it is indicative of a threshold energy required to heat the LEW and overcome radiative losses there. The threshold may be reduced with the application of a 20 ns early prepulse, but it does not seem to have been eliminated. We have already seen that there is a threshold time and energy associated with a 1/3 TW pulse over about 2 ns, or approximately 800 J.

The MagLIF program is already pursuing ways to reduce the energy lost at the LEW [39]. This includes a thinner LEW using cryogenic cooling to reduce the fill pressure, and a LEW that breaks away along points of weakness [21]. The simplest improvements are parameters we already explored, including the earlier prepulse and the longer pulse duration.

Thermal conductivity reduction and/or self-focusing in a magnetic field make the heated region quite narrow. The heated width with a magnetic field is less than the heating beam width at the LEW and becomes narrower with axial length. This limits the practical benefit to increasing the pulse duration available energy per unit length and extends deposition to a greater axial

length. The long plasma length with a very narrow beam is a result of very high temperatures strongly reducing collisional absorption. With a magnetic field the plasma may easily become unfavorably long. All energy in the plasma plasma beyond 1 cm it is no longer useful to the implosion and could lead the ablation of solid material from the MagLIF fill tube, so increasing the pulse duration has a practical limit. Fortunately, with a 17 T magnetic field, a 5 ns pulse appears to create a heated region of high energy density that is about 0.9 cm long, at least in helium. This plasma would be slightly longer in deuterium. Regardless, a 5 ns heating pulse or similar heating pulse with a low-intensity temporal pedestal prepulse seems like it would be ideal. If the beam is also widened or we need to deliver more energy to the target by increasing the laser power, then it is possible to increase the pulse duration beyond 6 ns by upgrading the Z-beamlet AWG to give a larger control window. This would allow ZBL to deliver more total energy while maintaining a constant power.

Increasing the width of the laser and the overall delivered energy to create a wider heated plasma would be beneficial, resulting in an overall higher energy per unit length. In magnetic field experiments, we saw a heated width equal to the beam width and narrower, so if the dynamics are the same and intensity remains constant, then increasing the beam width should deliver more energy to the plasma proportional to the beam's cross sectional area. With the intensity of $5 * 10^{13}\ W/cm^2$ that we used on the highest yield experiments, we could increase the beam radius to 0.75 mm (1.5 mm overall width). This would correspondingly require doubling the total beam energy delivered to the

target from the range of 1.5 kJ to 3.5 kJ, which is near the practical limit of Z-beamlet energy. If dynamics remain the same and temperatures approach 2 keV as we saw from x-ray data, Slutz's figure 1.4 places the optimum beam width at 2 mm (1 mm radius). A larger width presents a greater chance of the acoustic wave coming close to the liner before $\beta = 1$ conditions are reached, as we saw in chapter five, but it would probably still be better to couple more energy into the plasma. Presently, the coupled energy and plasma temperatures place existing experiments in the far left of figure 1.4, well off of the optimum delivered energy and beam width. A larger initial laser width would also widen the plasma to counter self-focusing, which we expect to be even stronger in deuterium versus helium as a result of the higher sound speed at the same temperature. This larger beam width would require a new DPP, and an increase in ZBL power from about 1/3 TW to 1 TW.

We might also imaging countering the effects of self-focusing by using a phase plate with the focal plane in front of the LEW rather than at the LEW, so that the laser is diverging as it enters the plasma. Since undesirable hot spot features as well as changes to the relative size of the co-injected prepulse and Z-beamlet heating pulse appear in the far field, this approach may be technically challenging. Perhaps it is possible to condition the beam at a certain location in the far-field, maybe via adaptive optics.

9.7 Directions for Future Work

We see numerous paths to publishable results as well as future methods to extract useful physics information from existing diagnostics. There are also new capabilities we could develop to further explore new physics closely related to what we have done. We will list a few here.

9.7.1 Comparing Energy Densities

In future work and publications we will have access to a broader range of shots over a larger number of parameters. We will need to effectively compare total energy delivered beyond an axial length less than 4 mm. We should be able to add many more shots to comparison figures such as figure 7.10.

We will also need to bound the error that our methods from sound speed expansion give us on total energy and temperature by quantifying radiative energy loss with information in Appendix A. We can use x-ray images to help bound the error on estimated plasma volume.

We might wish to characterize the preheat plasma length scaling as well as overall energy scaling with changes in laser parameters. Examples of might be total energy scaling with a magnetic field as a function of pulse duration, or as a function of magnetic field strength. General empirical scalings with various laser parameters require more shots than we have currently carried out.

9.7.2 Full-length Transverse X-ray PHC Image Sequences

The first recommendation for future work comes from the new capability to image the full length of the plasma with x-rays. Right away this suggests building a functionality similar to that described in chapter five, which uses MATLAB to extract plasma widths at each frame and at each position axially. The x-ray emission will give a much better estimate of the heated plasma volume than shadowgraphy, because only the hotter regions of the plasma are emitting x-rays. We can also compare the sound speed methods from both approaches to bound the size of the radiative precursor that we see in shadowgrams, and perhaps re-calibrate the heated plasma volume to get a better energy density with the sound speed temperature.

The x-ray expansion by itself may be useful for sound speed inference, but we may also be able to use the absolute emission to quantify temperature distributions via methods described in appendix A and chapter eight. This enables an independent measurement of plasma temperature and overall energy density across the full length of the plasma and at each frame in the x-ray sequence. These methods could be improved further to include pinhole camera transfer functions and 2 ns time averaging for expansion. We can also automate the initial test temperature distribution iteration process to obtain the initial temperature profile that matches the x-ray data most closely within a given model. Using these methods, we expect to be able to carefully bound the thermal conductivity both parallel and perpendicular to the magnetic field.

Finally, the x-ray data can be analyzed for line-outs not across the

plasma radially but axially. This will create an axial profile of temperature that could be compared with sound speed methods.

9.7.3 Exploring Self-Focusing

We might investigate thermal self-focusing using the techniques for energy density profiles from x-rays and shadowgraphy already described. The experiment might explore self-focusing by varying the beam profiles and divergences using various lenses, phase plates, or other beam condition methods.

9.7.4 Exploring Solid Target Thin Film Heating With and Without a Magnetic Field

We have the capability to measure changes in the collisional absorption heating and thermal expansion of laser-heated foils similar to the gas cell LEW. We can image these thin windows with x-rays and capture expansion plasmas with shadowgraphy. The magnetic field may change radial heat transport and affect how rapidly the LEW plasma cools, and how much energy is required to achieve transparency. We can also estimate the total radiative energy lost in these LEW plasmas through imaging and methods similar to Appendix A. All of these investigations would inform LEW design for MagLIF and would be particularly important because most experiments with LEW heating have taken place without a magnetic field so far [39].

9.7.5 Future Work with Collisional Absorption Dynamics that Account for Transport

An entire chapter was left out of this dissertation, representing unfinished and unresolved work with models of collisional laser absorption. The author had built a 1D numerical code for collisional absorption and length scaling that included a simple model of radial thermal transport. It could also model a diverging or converging beam, which was important for modeling self-focusing. The work did not capture the effects of hydrodynamic transport, beam ray tracing, or thermal diffusion. These effects turned out to be important. The effects to look for are density changes during laser heating, which lead to self focusing. Thermal transport during laser heating in the absence of a magnetic field may lead to a larger heated volume than the width of the laser, changing the energy density profiles as a function of axial length. Instead of designing the code from scratch we suggest that a more sophisticated numerical code would do better at modeling the plasma for comparison to the existing data, for example the radiative hydrodynamics code FLASH.

9.7.6 Investigation of Diamagnetic Effect and Nernst Effect

We might investigate the magnetic field surrounding the laser plasma with a pickup coil inside the gas cell. These could capture changes to the magnetic flux both around the entire plasma and in the region between the coil and the plasma edge. Such a setup could provide bounds on the plasma diamagnetic effect and Nernst effect that would be important as a benchmark

for MagLIF designers, as well as provide very novel measurements in a unique HEDP environment.

Appendices

Appendix A

Calculating Expected X-ray Pinhole Camera Signals from a Temperature Distribution

We would like to infer an expected signal on our sensors with our pinhole camera viewing x-ray self-emission from the laser-heated plasma. In order to do this, we will need to understand the spectrum of x-ray emission and the effect of filters on the spectrum. We will need to model the total radiated power from the plasma as a function of temperature which will pass through a pinhole. Then we will need to associate the incident radiation power with a signal on the UXI detector. The steps to do this are outlined here.

A.1 X-ray Emission

John Porter ran the Prism Computational Sciences' PrismSPECT software [40] to generate the spectral data for a 60 psi helium fill with 5 Torr of neon. The spectral data gives the radiated power from a mixture of helium at 60 psi, which determines the electron density, and neon at an initial fill pressure of 5 Torr. The electron temperature determines the emission, but so does the electron density and number of neon ion emitters. The emitted x-ray power should scale linearly with the neon dopant density as long as the helium

density determines the overall electron density.

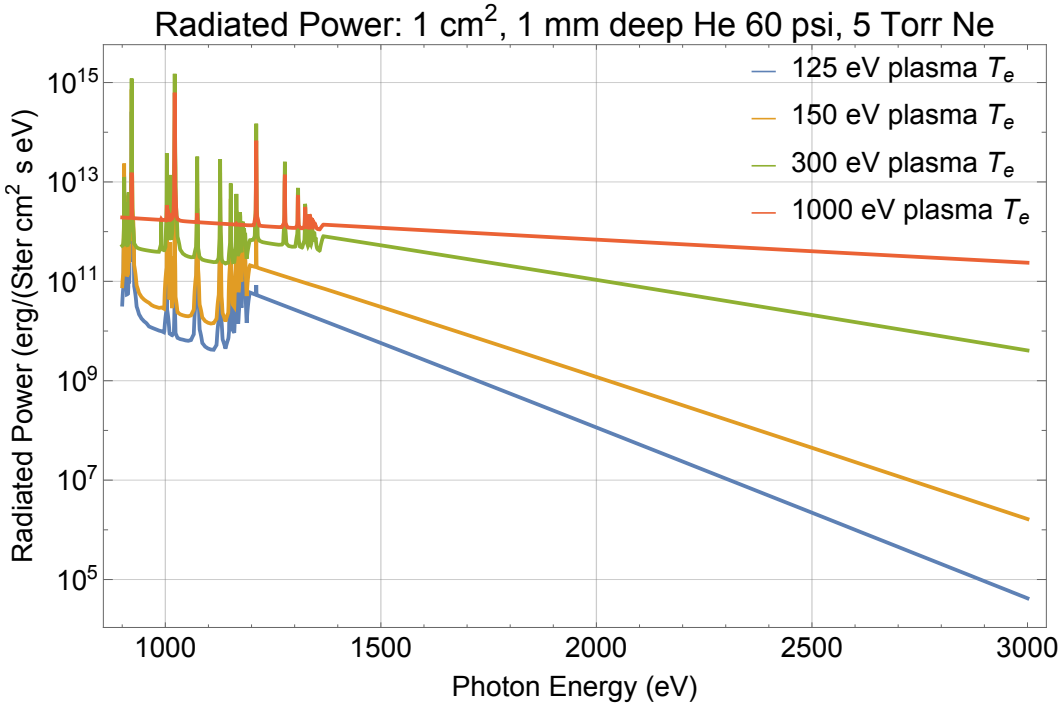

Figure A.1: This spectrum is the baseline spectrum used to calculate emission as a function of temperature, by integrating over the spectrum at each temperature. The spectrum only goes up to 3 keV photon energy, which is not important for most temperatures but might become important beyond 1 keV plasma electron temperature.

We imported the spectral data and filter spectrum data from henke.lbl.gov into Mathematica. From there, we could convolve the spectrum with the filters and do a calculation of the emitted power per ion. The data from PRISM is given from a rectangular geometry of plasma. But we assume that the plasma opacity to x-ray photons is very low. The fact that the plasma is optically thin lets us extract a radiated power per ion by calculating the number of emit-

ting averaged ions in the plasma. The neon k-shell emission will scale linearly with temperature, but helium continuum radiation will remain fixed as neon dopant increases, so a linear increase with added neon dopant fraction is only an approximation that works at low temperatures.

The spectrum most important to us is in the range of 900 eV to 3000 eV photon energy. Below this, very little energy makes it through the aluminum filter. Emission in the range beyond 3 kV becomes more important for higher temperatures in the range of 1 kV or more, but we did not include it because it is still a smaller contribution to the total radiated power. For the range of electron temperatures from 100 to 900 eV, the emission is dominated by neon k-shell emission. The emission spectrum for neon is given in figure A.1.

A.1.1 Filters

The filter attenuation spectrum from a convolution of 6 microns of Al and 2 microns of Polyimide is given in figure A.2. The neon k-shell emission lines make it through the aluminum filter in the range from around 950 to around 1560 eV photon energy.

The convolved spectrum with the filter function applied is plotted in figure A.3.

A.1.2 Radiatied Power with Temperature

After the spectrum data was convolved with the filter data, we used Mathematica to build a second order interpolation function of the filtered spec-

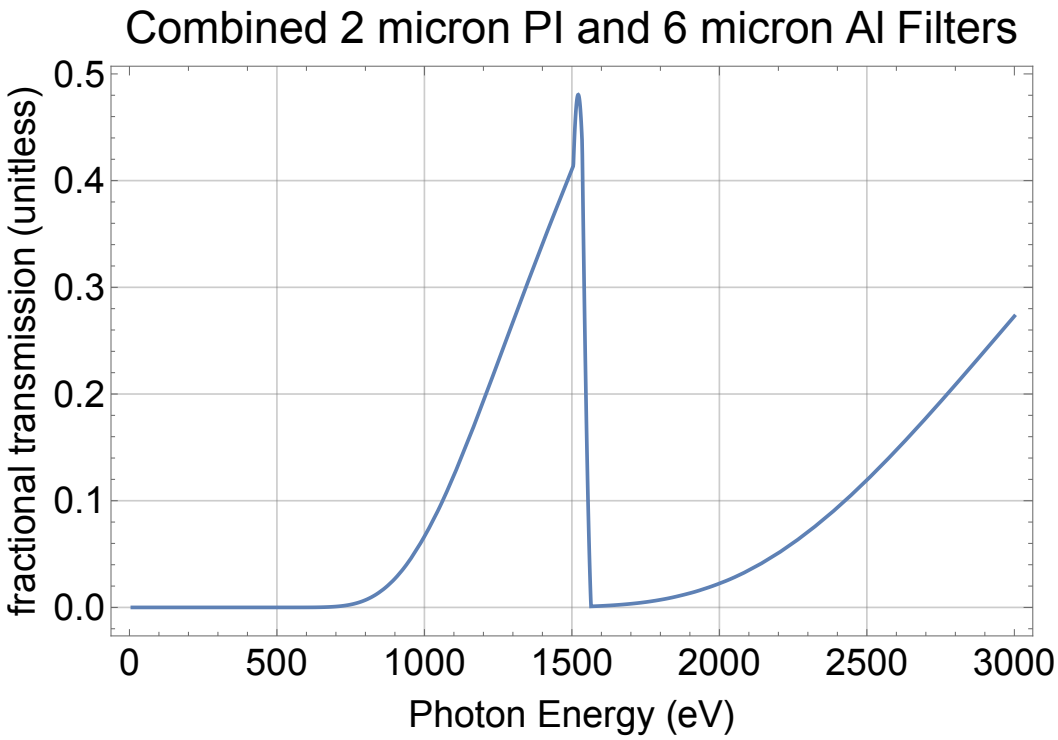

Figure A.2: Filter function from both 6 microns of aluminum and 2 microns of polyimide, as plotted from exported data from henke.lbl.gov. This transmission fraction function closely resembles the filter function of the aluminum filter by itself.

trum at a range of electron temperatures. With this interpolation, we could numerically integrate the total radiated power across the spectrum at each electron temperature. We then used Mathematica to build another interpolation function of the integrated power as a function of electron temperature. The result is plotted in figure A.4.

From figure A.4 it is clear that the radiated x-ray power is a monotonically increasing function of electron temperature up to about 350 eV, so

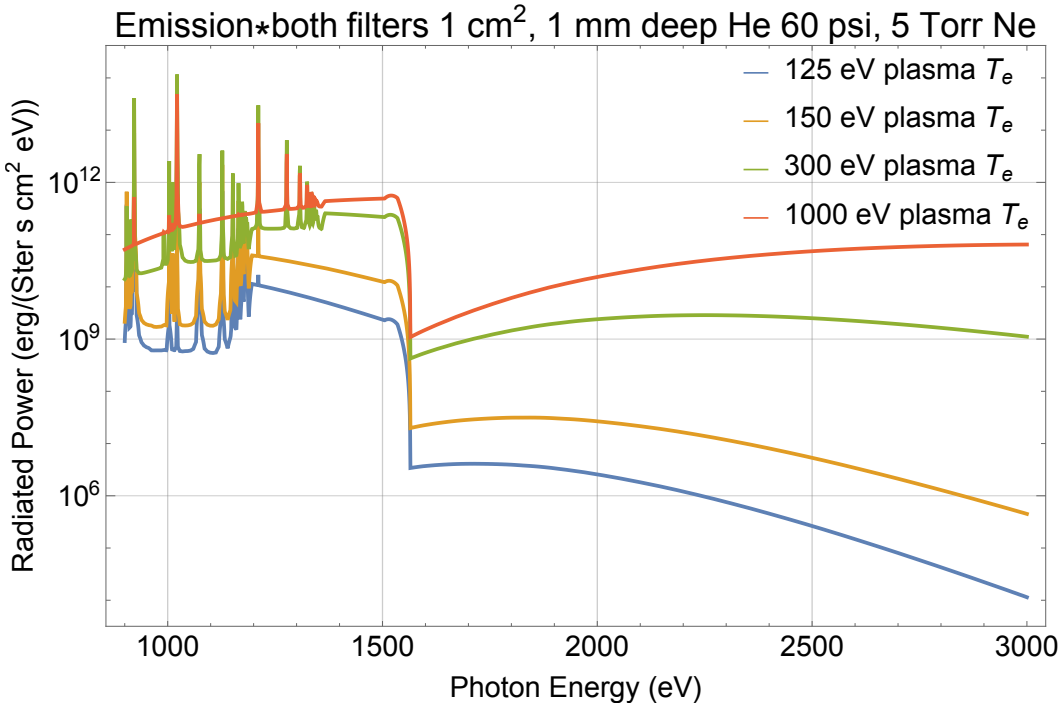

Figure A.3: The filters emphasize the neon k-shell emission range and the portion of the spectrum beyond 2 kV, reducing the rest.

in this region it could be possible to use total power to calculate the plasma temperature if we assume a fixed emitter density. However, the degeneracy in radiated power beyond 400 eV makes it difficult to work backward from the emitted power and infer a temperature if we expect temperatures to be higher than this. This effect tends to flatten the radiated power from an otherwise centrally peaked temperature distribution, and makes it all the more surprising that we saw such a centrally peaked emission profile, as we saw in chapter eight.

We can proceed to calculate the divide by the number of electrons in the

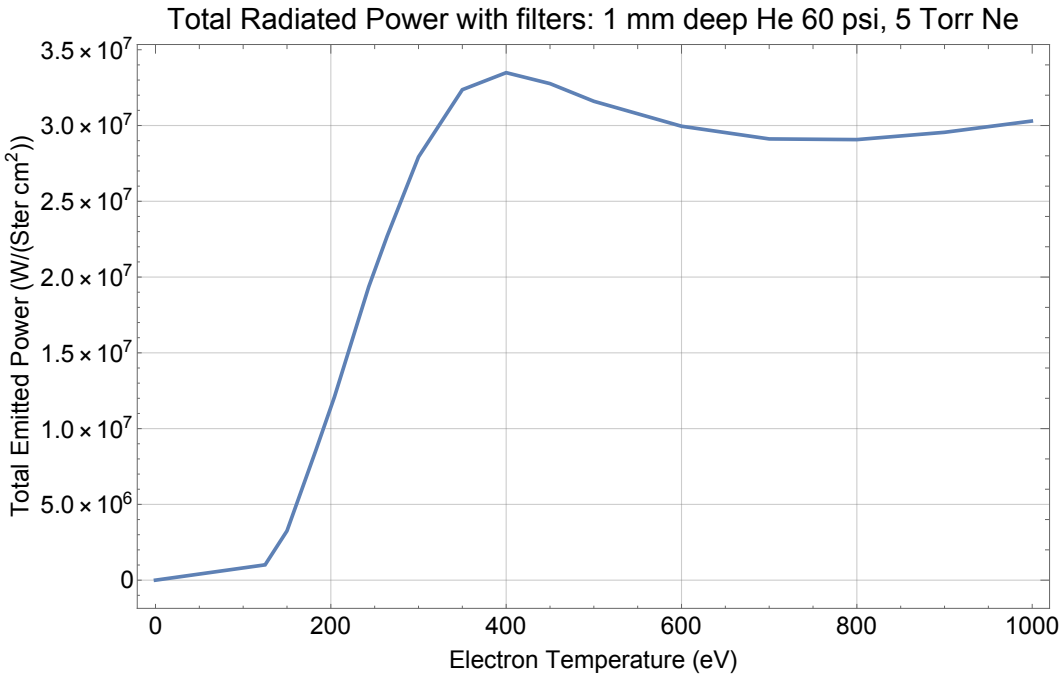

Figure A.4: We see that the neon k-shell emission becomes saturated around 400 eV, and the emitted power with filters included becomes more or less constant with electron temperature. As temperatures approach 1 keV, the continuum emission becomes important. Our model would be inadequate for higher temperatures.

emitting region to estimate the total emitted power per electron. We multiply by $16.242 * 10^{11}$ eV/J, and we divide by $2 * 10^{19}$ electrons per 0.1 cm^3. Also we convert units to nanoseconds for convenience with a factor of 10^{-9} ns/s.

A.2 Pinhole and Detector

At the pinhole detector, we eliminate the steradian units with a factor to account for the solid angle of the pinhole at the appropriate distance. The steradian factor is given by $r_{ph}^2\pi/(4\pi d_{ph})$ where the pinhole radius r_{ph} and

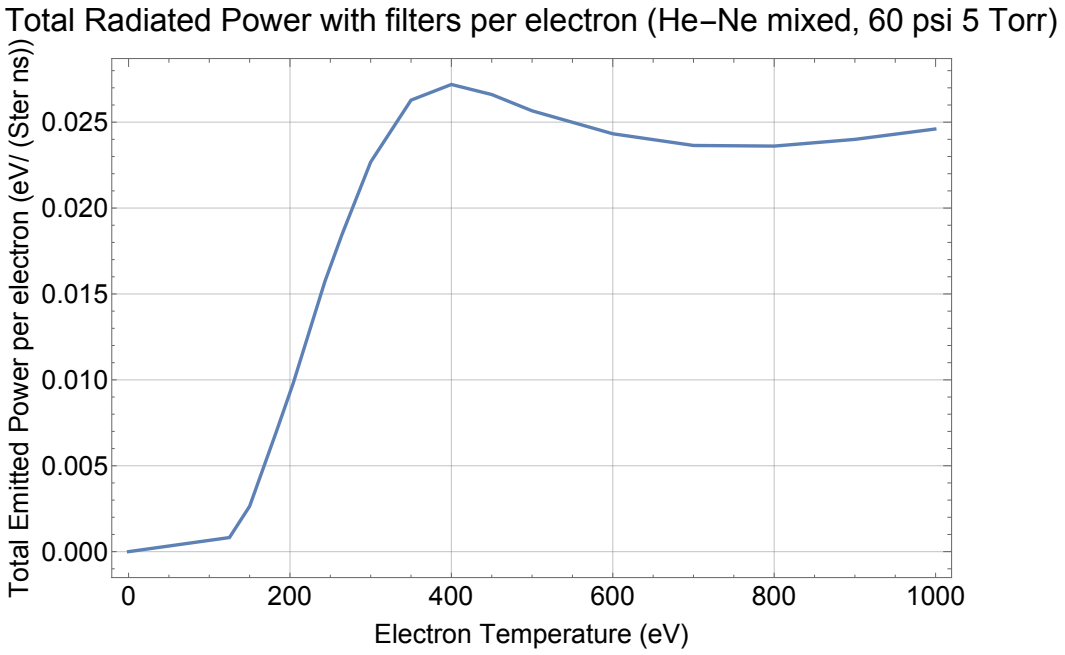

Figure A.5: We have changed the units from figure A.4, to divide by the total number of electrons in the emitting volume modeled from the PRISM data, and convert to eV/(ns Ster).

pinhole distance d_{ph} must be given in the same units.

The next step in the calculation is to do a numerical summation of small 25 micron squares containing a fixed number of electron emitters determined by the density. These emitting boxes are integrated numerically over a range of on the x-axis of the cylindrical plasma with the specific y value fixed to give the numerical equivalent of forward Abel transform from a cylindrical plasma. 25 microns was chosen because with the 1:1 pinhole it was the appropriate volumetric integration size for 25 micron pixels.

The final factor comes from the conversion incident power to detector

counts. The UXI units convert 2 keV of radiated energy striking the detector in each frame to 1 mV of signal count.

Since the output is a specific value at each 25 micron interval, the final result is interpolated using a first order interpolation to give a clean output curve which could be spatially smoothed if desired.

The result of all these calculations can generate a function which is able to calculate a total expected UXI count from an input temperature function, for example, see figures 8.10 through 8.13.

The pinhole transfer function was not properly accounted for. This will tend to smooth spatial data, like a running average. The exact transfer function is a Bessel function, qualitatively similar to a weighting via a Gaussian if numerical simplicity is needed. We did not have time to implement a working version of this spatial smoothing.

Appendix B

Shot Tables and Selected Raw Shadowgram Data

Shot #	Helium Fill (psi)	Neon dopant (Torr)	probe beam pulse interval (ns)	total ZBL energy at target (J)	heating pulse duration (ns)	laser power (TW)	Phase Plate near field 95% (µm	Heating Beam spot size (µm FWHM)	dist defocal (mm)	heating beam intensity (W/cm^2)	Pre-pulse Energy (J)	pre-pulse time gap (ns)	B-field (T)
B17102508	60	0	5	1120	3.5	0.32	730	800	2.5	6.369E+13	72	2	0
B17111401	60	0	5	1215	3.5	0.347143	730	700	0	9.025E+13	83	2	0
B17111505	60	0	5	1382	3.5	0.394857	730	700	0	1.027E+14	30	20	0
B17111603	60	0	5	1090	3.5	0.311429	687.5	950	5	4.396E+13	30	20	0
B17120707	60	0	5	1170	3.5	0.334286	687.5	950	5	4.718E+13	30	20	0
B17121801	60	20	5	1609	3.5	0.459714	687.5	950	5	6.489E+13	106	2	0
B17121902	60	30	5	1860	4.8	0.3875	687.5	950	5	5.47E+13	86	20	17
B17122002	60	30	5	2473	4.8	0.515208	687.5	950	5	7.272E+13	26	20	0
B18010503	60	30	5	1770	4.8	0.36875	687.5	950	5	5.205E+13	30	20	17
B18011601	60	10	5	1640	4.8	0.341667	687.5	950	5	4.823E+13	30	20	0
B18020201	60	5	2	1730	4.8	0.360417	687.5	950	5	5.087E+13	30	20	0
B18061901	60	5	4	1342	3.5	0.383429	687.5	950	5	5.412E+13	30	20	0
B18070501	60	5	4	1391	3.5	0.397429	937.5	980	0	5.272E+13	30	20	0
B18070904	60	5	4	1355	3.5	0.387143	937.5	980	0	5.135E+13	30	20	17
B18071302	60	5	4	1250	3.5	0.357143	937.5	980	0	4.737E+13	30	20	17

Figure B.1: Shot Table showing basic laser parameters and summary notes.

Shot #	Energy Past 3 mm (J)	Energy past 4 mm (J)	low bound Energy from sound speed (J)	Fraction delivered beyond 4 mm	Fraction delivered energy deposited (low bound)	Axial length of post-heating plasma (mm)	Figure Number Mentioned
B17102508		50		0.044643	0	8.9	7.4, 7.5, 7.6,
B17111401		50	200	0.041152	0.16460905	7.8	7.4, 7.5, 7.6
B17111505	80	50	300	0.036179	0.2170767	9.6	
B17111603	211	131	240	0.120183	0.22018349	8.5	
B17120707	540	350		0.299145	0	9	7.4, 7.5, 7.6, 7.7, 7.8, 7.9, 7.13, 7.14, 7.15
B17121801	170	81		0.050342	0	8	7.7, 7.8, 7.9, 7.16
B17121902	1040	860		0.462366	0	11+	8.7, 8.8, 8.9, 8.10, 8.11, 8.12
B17122002	no data	no data			0	11	
B18010503	no data	no data			0	11+	
B18011601	659	448	1060	0.273171	0.64634146	11+	7.8, 7.9, 7.16, 8.7, 8.8, 8.9
B18020201	1170	780	1400	0.450867	0.80924855	11+	7.12, 7.13, 7.14, 7.15, 7.16 , 8.10, 8.13, 8.14
B18061901	660	450	1440	0.33532	1.07302534		7.11, 7.13, 7.14, 7.16, 8.3, 8.4
B18070501	688	401	910	0.288282	0.65420561		7.11, 8.2, 8.3, 8.4, 8.5
B18070904	790	625	1150	0.461255	0.84870849		7.12, 8.1, 8.2, 8.3, 8.4
B18071302	not yet analyzed			0	0		8.2, 8.5, 8.6

Figure B.2: Shot Table showing Energies and Figure References.

Shot #	NOTES
B17102508	large LEW-centered opacity feature, makes energy hard to measure 0-5 mm
B17111401	large LEW-centered opacity feature, makes energy hard to measure 0-5 mm
B17111505	large LEW-centered opacity feature, very similar results to previous shot on 11-14
B17111603	large LEW-centered opacity feature present, makes energy hard to measure 0-5 mm
B17120707	very small LEW-centered opacity feature, improved energy density
B17121801	no bulb feature, seemingly less energy than dec 12 shot without co-injection
B17121902	can't see end of plasma! Dramatic increase in length with B-field
B17122002	plasma is shorter than shot with B-field, missing some shadowgrams
B18010503	not considered, shadowgram data not functional with B-field this time
B18011601	good comparison with B-field shot B17121902
B18020201	high energy density- likely result of 2 ns probe interval giving less time for rad cooling
B18061901	comparison shot for next two experiments- energy density moderately high
B18070501	LEW-centered opacity feature returns after switching to 0.94 mm DPP
B18070904	B-field shot, longer plasma, no opacity feature, filament structure visible
B18071302	B-field shot, longer plasma, different probe timing so not comparable energy with previous

Figure B.3: Shot table with notes.

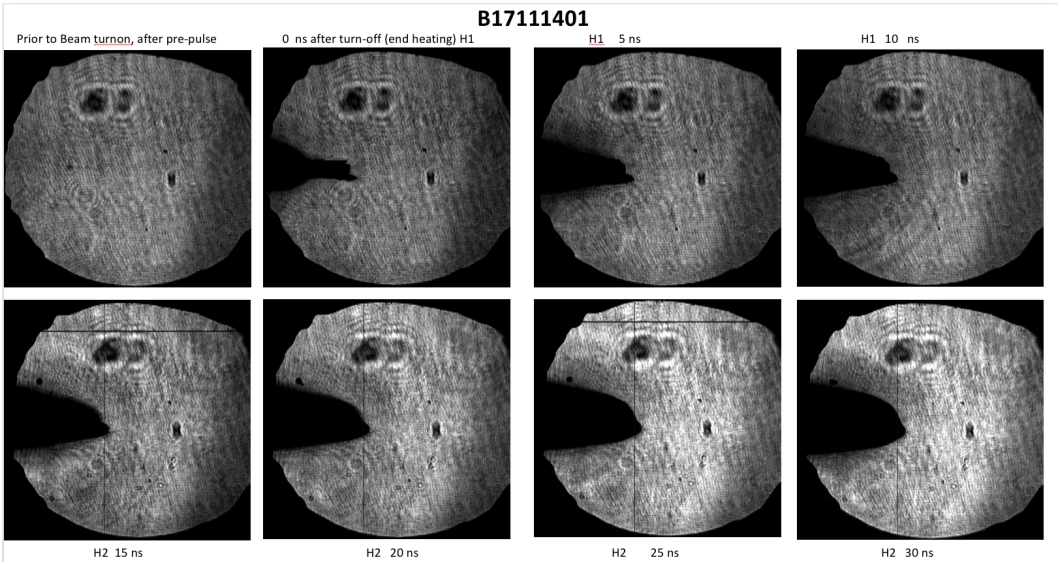

Figure B.4:

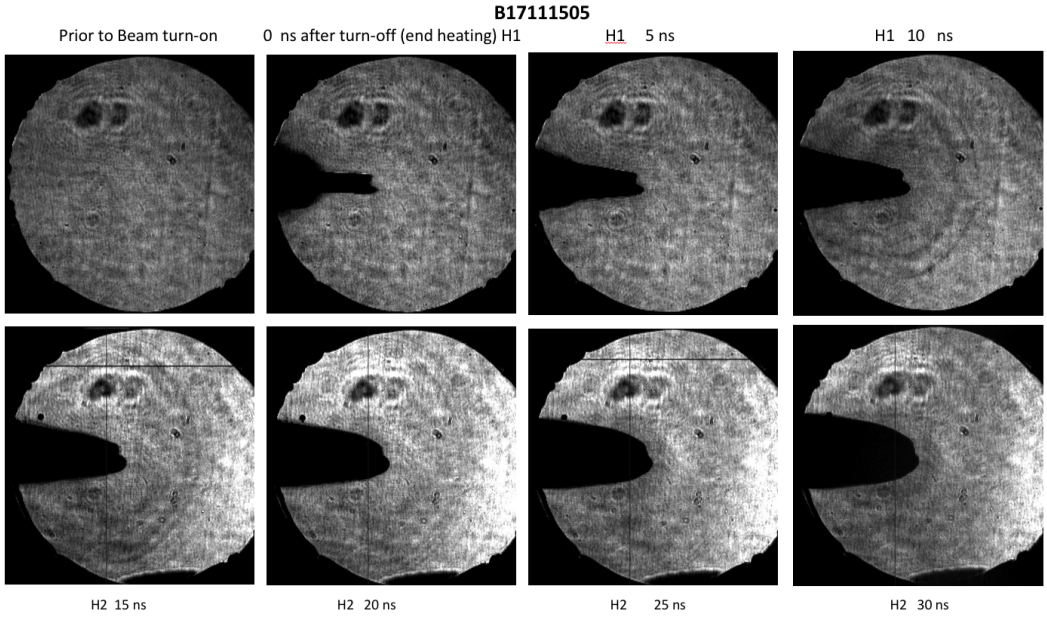

Figure B.5:

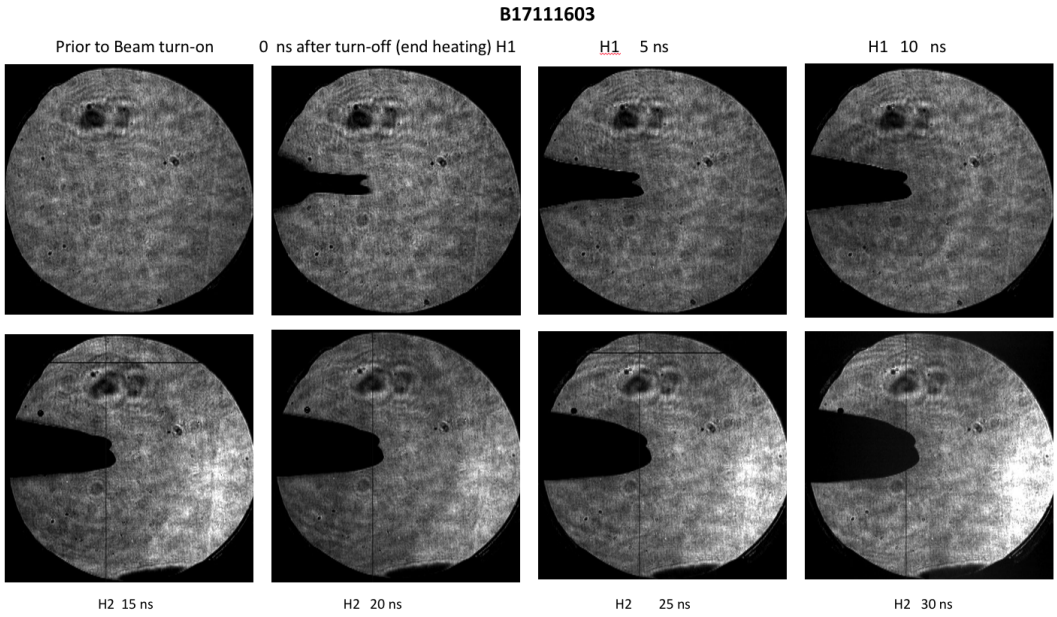

Figure B.6:

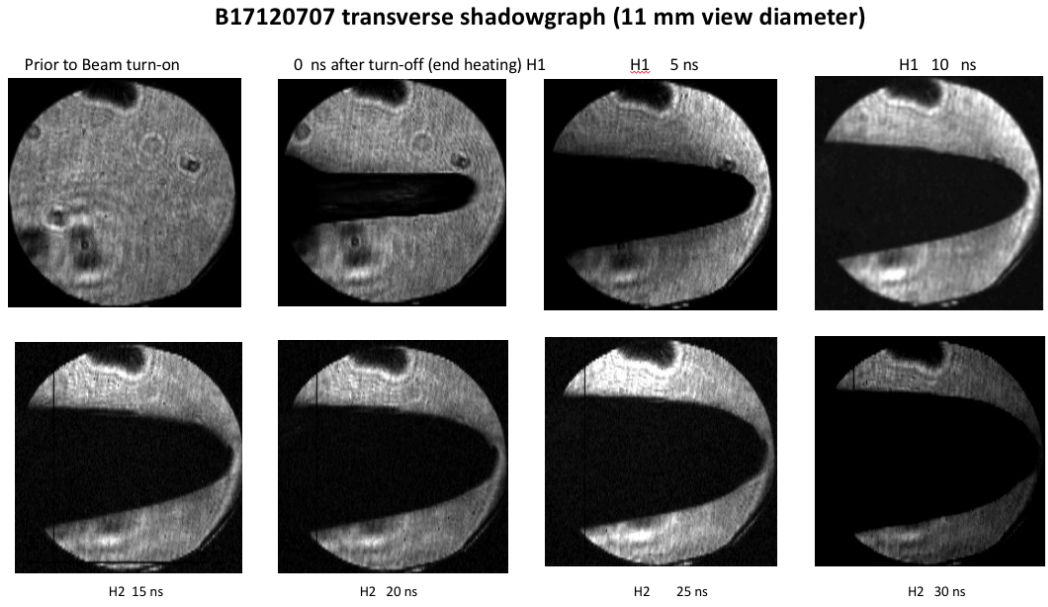

Figure B.7:

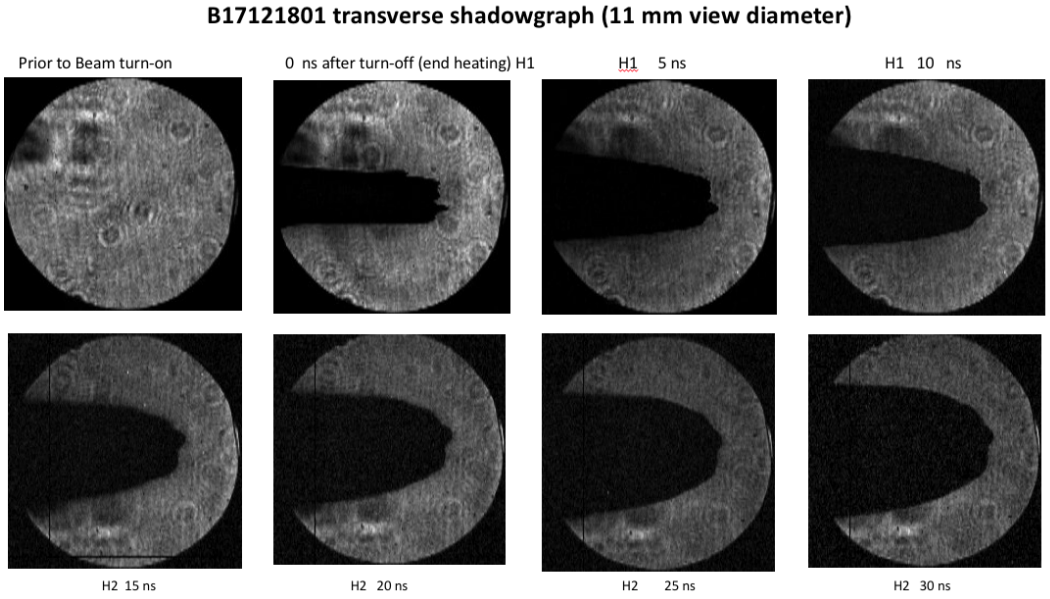

Figure B.8:

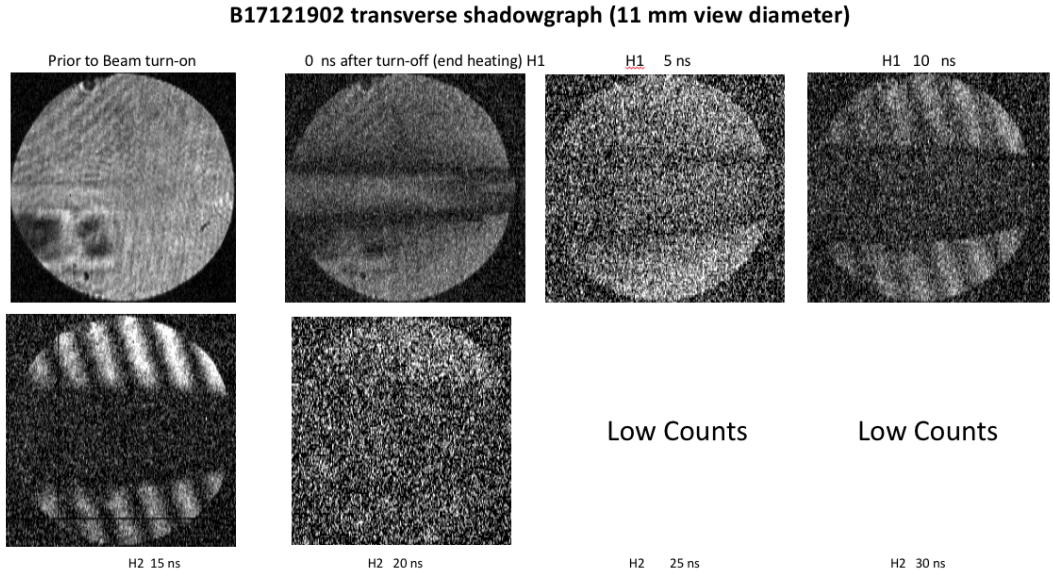

Figure B.9:

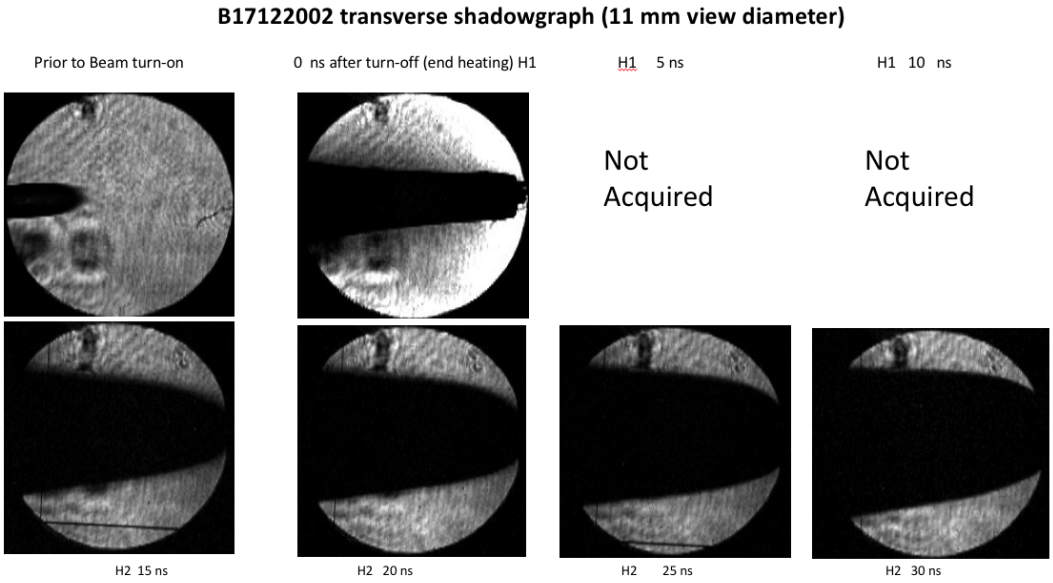

Figure B.10:

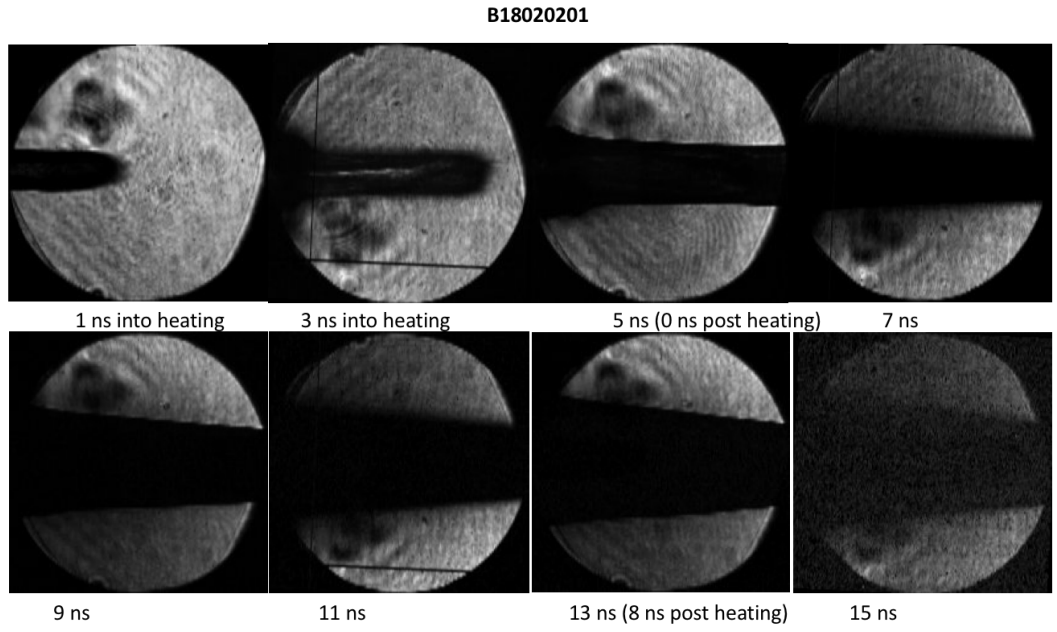

Figure B.11:

Bibliography

[1] S. A. Slutz, M. C. Herrmann, R. A. Vesey, A. B. Sefkow, D. B. Sinars, D. C. Rovang, K. J. Peterson, and M. E. Cuneo, "Pulsed-power-driven cylindrical liner implosions of laser preheated fuel magnetized with an axial field," *Physics of Plasmas*, vol. 17, no. 5, p. 056303, 2010.

[2] M. R. Gomez, S. A. Slutz, A. B. Sefkow, D. B. Sinars, K. D. Hahn, S. B. Hansen, E. C. Harding, P. F. Knapp, P. F. Schmit, C. A. Jennings, T. J. Awe, M. Geissel, D. C. Rovang, G. A. Chandler, G. W. Cooper, M. E. Cuneo, A. J. Harvey-Thompson, M. C. Herrmann, M. H. Hess, O. Johns, D. C. Lamppa, M. R. Martin, R. D. McBride, K. J. Peterson, J. L. Porter, G. K. Robertson, G. A. Rochau, C. L. Ruiz, M. E. Savage, I. C. Smith, W. A. Stygar, and R. A. Vesey, "Experimental demonstration of fusion-relevant conditions in magnetized liner inertial fusion," *Phys. Rev. Lett.*, vol. 113, p. 155003, Oct 2014.

[3] A. B. Sefkow, S. A. Slutz, J. M. Koning, M. M. Marinak, K. J. Peterson, D. B. Sinars, and R. A. Vesey, "Design of magnetized liner inertial fusion experiments using the Z facility," *Physics of Plasmas*, vol. 21, no. 7, 2014.

[4] S. Atzeni and J. Meyer-Ten-Vehn, *The Physics of Inertial Fusion: beam plasma interaction, hydrodynamics, hot dense matter.* International se-

ries of monographs on physics, Great Clarendon Street, Oxford OX2 6DP: Oxford University Press, 2009.

[5] F. F. Chen, *Introduction to Plasma Physics and Controlled Fusion*, vol. 1. Plenum Publishing Corporation, 1984.

[6] Y. C. F. Thio, "Status of the US program in magneto-inertial fusion," *Journal of Physics: Conference Series*, vol. 112, no. 4, p. 042084, 2008.

[7] S. A. Slutz, W. A. Stygar, M. R. Gomez, K. J. Peterson, A. B. Sefkow, D. B. Sinars, R. A. Vesey, E. M. Campbell, and R. Betti, "Scaling magnetized liner inertial fusion on z and future pulsed-power accelerators," *Physics of Plasmas*, vol. 23, no. 2, 2016.

[8] P. F. Knapp, P. F. Schmit, S. B. Hansen, M. R. Gomez, K. D. Hahn, D. B. Sinars, K. J. Peterson, S. A. Slutz, A. B. Sefkow, T. J. Awe, E. Harding, C. A. Jennings, M. P. Desjarlais, G. A. Chandler, G. W. Cooper, M. E. Cuneo, M. Geissel, A. J. Harvey-Thompson, J. L. Porter, G. A. . Rochau, D. C. Rovang, C. L. Ruiz, M. E. Savage, I. C. Smith, W. A. Stygar, and M. C. Herrmann, "Effects of magnetization on fusion product trapping and secondary neutron spectra," *Physics of Plasmas*, vol. 22, no. 5, p. 056312, 2015.

[9] P. F. Schmit, P. F. Knapp, S. B. Hansen, M. R. Gomez, K. D. Hahn, D. B. Sinars, K. J. Peterson, S. A. Slutz, A. B. Sefkow, T. J. Awe, E. Harding, C. A. Jennings, G. A. Chandler, G. W. Cooper, M. E. Cuneo, M. Geissel,

A. J. Harvey-Thompson, M. C. Herrmann, M. H. Hess, O. Johns, D. C. Lamppa, M. R. Martin, R. D. McBride, J. L. Porter, G. K. Robertson, G. A. Rochau, D. C. Rovang, C. L. Ruiz, M. E. Savage, I. C. Smith, W. A. Stygar, and R. A. Vesey, "Understanding fuel magnetization and mix using secondary nuclear reactions in magneto-inertial fusion," *Phys. Rev. Lett.*, vol. 113, p. 155004, Oct 2014.

[10] T. J. Awe, C. A. Jennings, R. D. McBride, M. E. Cuneo, D. C. Lamppa, M. R. Martin, D. C. Rovang, D. B. Sinars, S. A. Slutz, A. C. Owen, K. Tomlinson, M. R. Gomez, S. B. Hansen, M. C. Herrmann, M. C. Jones, J. L. McKenney, G. K. Robertson, G. A. Rochau, M. E. Savage, D. G. Schroen, and W. A. Stygar, "Modified helix-like instability structure on imploding z-pinch liners that are pre-imposed with a uniform axial magnetic field," *Physics of Plasmas*, vol. 21, no. 5, 2014.

[11] M. R. Gomez, S. A. Slutz, A. B. Sefkow, K. D. Hahn, S. B. Hansen, P. F. Knapp, P. F. Schmit, C. L. Ruiz, D. B. Sinars, E. C. Harding, C. A. Jennings, T. J. Awe, M. Geissel, D. C. Rovang, I. C. Smith, G. A. Chandler, G. W. Cooper, M. E. Cuneo, A. J. Harvey-Thompson, M. C. Herrmann, M. H. Hess, D. C. Lamppa, M. R. Martin, R. D. McBride, K. J. Peterson, J. L. Porter, G. A. Rochau, M. E. Savage, D. G. Schroen, W. A. Stygar, and R. A. Vesey, "Demonstration of thermonuclear conditions in magnetized liner inertial fusion experiments," *Physics of Plasmas*, vol. 22, no. 5, p. 056306, 2015.

[12] J. Denavit and D. W. Phillion, "Laser ionization and heating of gas targets for longscalelength instability experiments," *Physics of Plasmas*, vol. 1, no. 6, pp. 1971–1984, 1994.

[13] P. Knapp, "Liner Inertial Fusion (MagLIF) Experiments on Z: Spectroscopy and What's Been Learned About Stagnation," 2015.

[14] R. D. McBride and S. A. Slutz, "A semi-analytic model of magnetized liner inertial fusion," *Physics of Plasmas*, vol. 22, no. 5, p. 052708, 2015.

[15] D. S. Montgomery, "Two decades of progress in understanding and control of laser plasma instabilities in indirect drive inertial fusion," *Physics of Plasmas*, vol. 23, no. 5, p. 055601, 2016.

[16] A. J. Harvey-Thompson, A. B. Sefkow, T. N. Nagayama, M. S. Wei, E. M. Campbell, G. Fiksel, P.-Y. Chang, J. R. Davies, D. H. Barnak, V. Y. Glebov, P. Fitzsimmons, J. Fooks, and B. E. Blue, "Diagnosing laser-preheated magnetized plasmas relevant to magnetized liner inertial fusion," *Physics of Plasmas*, vol. 22, no. 12, p. 122708, 2015.

[17] A. J. Harvey-Thompson, A. B. Sefkow, T. N. Nagayama, M. S. Wei, E. M. Campbell, G. Fiksel, P.-Y. Chang, J. R. Davies, D. H. Barnak, V. Y. Glebov, P. Fitzsimmons, J. Fooks, and B. E. Blue, "Diagnosing laser-preheated magnetized plasmas relevant to magnetized liner inertial fusion," *Physics of Plasmas*, vol. 22, no. 12, p. 122708, 2015.

[18] P. K. Rambo, I. C. Smith, J. L. Porter, M. J. Hurst, C. S. Speas, R. G. Adams, A. J. Garcia, E. Dawson, B. D. Thurston, C. Wakefield, J. W. Kellogg, M. J. Slattery, H. C. Ives, R. S. Broyles, J. A. Caird, A. C. Erlandson, J. E. Murray, W. C. Behrendt, N. D. Neilsen, and J. M. Narduzzi, "Z-beamlet: a multikilojoule, terawatt-class laser system," *Appl. Opt.*, vol. 44, pp. 2421–2430, Apr 2005.

[19] P. Rambo, "Personal communication, Sandia National Laboratories," 2017.

[20] M. Geissel, A. J. Harvey-Thompson, T. J. Awe, D. E. Bliss, M. E. Glinsky, M. R. Gomez, E. Harding, S. B. Hansen, C. Jennings, M. W. Kimmel, P. is, S. M. Lewis, K. Peterson, M. Schollmeier, J. Schwarz, J. E. Shores, S. A. Slutz, D. B. Sinars, I. C. Smith, C. S. Speas, R. A. Vesey, M. R. Weis, and J. L. Porter, "Minimizing scatter-losses during pre-heat for magneto-inertial fusion targets," *Physics of Plasmas*, vol. 25, no. 2, p. 022706, 2018.

[21] M. Geissel, "Personal communication, Sandia National Laboratories," 2018.

[22] L. Claus, L. Fang, R. Kay, M. Kimmel, J. Long, G. Robertson, M. Sanchez, J. Stahoviak, D. Trotter, and J. L. Porter, "An overview of the ultrafast x-ray imager (uxi) program at sandia labs," 2015.

[23] M. Kimmel, "Personal communication, Sandia National Laboratories," 2017.

[24] H. Chung, M. Chen, W. Morgan, Y. Ralchenko, and R. Lee, " FLYCHK: Generalized population kinetics and spectral model for rapid spectroscopic analysis for all elements," *High Energy Density Physics*, vol. 1, pp. 3–12, 2005. Helium Charge State.

[25] I. Zel'dovich and Y. Raizer, *Physics of Shock Waves and High-Temperature Hydrodynamic Phenomena*. Dover Books on Physics, Dover Publications, 2002.

[26] B. S. I., "Transport processes in a plasma," *Rev. Plasma Phys.*, vol. 1, p. 205, 1965.

[27] B. Breizman, "Personal communication, UT Austin," 2018.

[28] G. Barenblatt, *Scaling, Self-similarity, and Intermediate Asymptotics: Dimensional Analysis and Intermediate Asymptotics*. Cambridge Texts in Applied Mathematics, Cambridge University Press, 1996.

[29] L. Spitzer and R. Härm, "Transport phenomena in a completely ionized gas," *Phys. Rev.*, vol. 89, pp. 977–981, Mar 1953.

[30] J. Samson and W. Stolte, "Precision measurements of the total photoionization cross-sections of he, ne, ar, kr, and xe," *Journal of Electron Spectroscopy and Related Phenomena*, vol. 123, no. 2, pp. 265 – 276, 2002. Determination of cross-sections and momentum profiles of atoms, molecules and condensed matter.

[31] T. Ditmire, E. T. Gumbrell, R. A. Smith, A. Djaoui, and M. H. R. Hutchinson, "Time-resolved study of nonlocal electron heat transport in high temperature plasmas," *Phys. Rev. Lett.*, vol. 80, pp. 720–723, Jan 1998.

[32] M. McCormick, A. V. Arefiev, H. J. Quevedo, R. D. Bengtson, and T. Ditmire, "Observation of self-sustaining relativistic ionization wave launched by a sheath field," *Phys. Rev. Lett.*, vol. 112, p. 045002, Jan 2014.

[33] K. A. Keilty, E. P. Liang, T. Ditmire, B. A. Remington, K. Shigemori, and A. M. Rubenchik, "Modeling of laser-generated radiative blast waves," *Astrophysical Journal*, vol. 538, 8 2000.

[34] M. J. Edwards, A. J. MacKinnon, J. Zweiback, K. Shigemori, D. Ryutov, A. M. Rubenchik, K. A. Keilty, E. Liang, B. A. Remington, and T. Ditmire, "Investigation of ultrafast laser-driven radiative blast waves," *Phys. Rev. Lett.*, vol. 87, p. 085004, Aug 2001.

[35] M. Geissel, A. J. Harvey-Thompson, T. J. Awe, D. E. Bliss, M. E. Glinsky, E. M. Campbell, M. R. Gomez, E. Harding, S. Hansen, C. A. Jennings, M. W. Kimmel, P. F. Knapp, S. M. Lewis, R. D. McBride, K. Peterson, M. Schollmeier, D. Scoglietti, A. B. Sefkow, J. E. Shores, D. Sinars, G. A. Rochau, S. A. Slutz, I. C. Smith, M. R. Weiss, and J. L. Porter, "Developing a pre-heat platform for maglif with z-beamlet," in *APS Meeting Abstracts*, p. CO8.005, oct 2016.

[36] I. Smith, "Personal communication, Sandia National Laboratories," 2018.

[37] D. S. Montgomery, B. J. Albright, D. H. Barnak, P. Y. Chang, J. R. Davies, F. G., D. H. Froula, K. J. L., M. J. MacDonald, A. B. Sefkow, L. Yin, and R. Betti, "Use of external magnetic fields in hohlraum plasmas to improve laser-coupling," *Phys. Plasmas*, vol. 22, p. 010703, 2015.

[38] D. H. Froula, J. S. Ross, B. B. Pollock, P. Davis, A. N. James, L. Divol, M. J. Edwards, A. A. Offenberger, D. Price, R. P. J. Town, G. R. Tynan, and S. H. Glenzer, "Quenching of the nonlocal electron heat transport by large external magnetic fields in a laser-produced plasma measured with imaging thomson scattering," *Phys. Rev. Lett.*, vol. 98, p. 135001, Mar 2007.

[39] J. Porter, "Personal communication, Sandia National Laboratories," 2018.

[40] J. Macfarlane, I. Golovkin, P. Woodruff, and P. Wang, "PrismSPECT and SPECT3D Tools for Simulating X-ray, UV, and Visible Spectra for Laboratory and Astrophysical Plasmas," 05 2003.

[41] A. J. Schmitt, "Three dimensional filamentation of light in laser plasmas," *Physics of Fluids B: Plasma Physics*, vol. 3, no. 1, pp. 186–194, 1991.

Vita

Sean Matthew Lewis was originally from Bloomington, IN. Sean attended Indiana University from 2005 through 2009 where he earned B.S. degrees in physics and mathematics. While completing his undergraduate work, Sean worked as a T.A. and worked in two different research groups at the IU Cyclotron Facility and at the Spallation Neutron Source. In 2009 Sean began a physics Ph.D program at the University of Texas at Austin to study plasma physics. The first summer at UT, Sean took an internship at Sandia National Laboratories involved in the construction of a pulsed magnetic field driver. The driver was intended for plasma confinement of cluster fusion on the Texas Petawatt Laser. Under Roger Bengtson, Sean operated the magnetic field pulser at UT Austin with Matt Wisher from 2011 to 2012. He completed a Masters degree in applied physics on the construction and magnetic field measurements from this device. In 2013 Sean returned to Sandia as a full time intern with the Z-Beamlet laser group under John Porter, where he worked with the group to develop capabilities for doing gas cell experiments with magnetic fields. In 2015 he returned to UT to complete research for a doctorate. The work done at Sandia Labs from 2014-2018 resulted in the content of this dissertatiion with Todd Ditmire as supervisor. Sean may be reached via email at sealewis@gmail.com.

Permanent address: Austin, TX

This dissertation was typeset with LaTeX[†] by The Author.

[†]LaTeX is a document preparation system developed by Leslie Lamport as a special version of Donald Knuth's TeX Program.